High Strain Rate Properties of Geological Materials

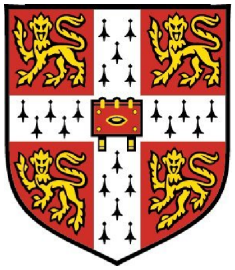

Christopher Braithwaite

Department of Physics and King's College

University of Cambridge

A thesis submitted for the degree of

Doctor of Philosophy

February 2009

I would like to dedicate this thesis to my loving wife Antonia and to my son Joseph, who when he is old enough to be able to read this, probably won't want to.

Acknowledgements

There are many people without whom the writing of this thesis would have been impossible. These range from those offering academic help through to those whose main job has been to keep me sane for the last four years. A hopefully fairly exhaustive list is as follows:

De Beers and Pilbara Iron Company (a subsidiary of Rio Tinto) for sponsoring my work and providing me with samples. Additionally Dr. Alan Guest (formerly De Beers) and Marc Ruest (De Beers) for keeping an eye on me as they pass through to more exotic climes. In the wider HSBM project I would like to thank all the sponsors and people involved, in particular Ted Bearman (Rio Tinto) for providing additional samples, Peter Cundell (Itasca) for making sure I produced the right numbers and of course Gideon (University of Queensland) for making sure I never got carried away on a tangent that I then couldn't explain the relevance of.

At the Cavendish my work has been supervised by Prof. John Field and Dr. Bill Proud and I would like to thank them for the valuable input and guidance that they have given me. My fellow PhD students and postdocs have also been of great help. David Chapman and Dr. Kostas Tsembelis, without whom I would never have managed to complete an experiment, Dr. Geoff Willmott for being an excellent predecessor in the De Beers sponsored work and (the now Dr.) Ed Zaaymann for being excellent company during the Diamond Conference.

The technical staff at the Cavendish have been essential in completing the experiments for this research. Preparation of samples and

maintenance of facilities has been carried out by Dave Johnson, Ray Flaxman and Bob Marrah, amongst others. Much of the cutting of rock cores was carried out at the Earth Sciences department thanks to Keith Gray. Work on mineral identification in samples was performed at the University of Nottingham by Dr. Steve Plint and Prof. Sam Kingman.

Finally I would like to thank all those people whose input was less academic in nature. People who have been in teams, or taken part in sports that have given me a great deal of enjoyment over the past eight years in some cases. My family and other friends who have been very supportive. Last but certainly not least I would like to thank my wife Antonia for everything that she has done that has allowed me to start, finish and everything in between!

Abstract

High Strain Rate Properties of Geological Materials

Christopher Braithwaite

The dynamic response of various geological materials has been investigated through a series of plate impact experiments. The materials involved were supplied from various mines by De Beers and Rio Tinto and were generically termed: sandstone, scilified siltstone, kimberlite, quartz/feldspathic gneiss, biotite schist, amphibolite, amphibolitic gneiss, basalt and iron ore. Investigations into compressional, shear and tensional behaviour were carried out.

This project was part of a larger international study to develop models for the explosive loading of rock in a mining environment. This model is known as the Hybrid Stress Blasting Model, or HSBM. For this model to be accurate and relevant to the mining process it is essential to have dynamic data on the various rock types concerned. This was the purpose of the current project.

The materials were initially characterised statically both through the measurement of density (utilising a volume method) and sound speeds (using a time of flight method with ultrasonic transducers) and also through the use of mineral analysis equipment at the University of

Nottingham (this work was carried out by Dr S. Plint). The materials were found to have a wide range of properties, with a density range of 1.93 - 4.46 $g\ cm^{-3}$ and a range of longitudinal sound speeds of 1.97 - 6.86 $km\ s^{-1}$. Two of the materials were found to be porous, the iron ore and the sandstone. A large number of mineral phases was identified within the specimens.

Dynamic investigations into material properties were carried out at the Cambridge Plate Impact Facility at the Cavendish Laboratory. This facility consists of a well instrumented 50 mm bore single stage light gas gun. The facility has been operating for a number of years and has previously been shown to be suitable for investigations such as the ones presented. The main diagnostic equipment used in the experimental series were commercial manganin stress gauges and a laser interferometer (or VISAR) system. Both of these diagnostics are widely used in the shock physics field and are reliable in the data they provide. In the region of 120 separate plate impact experiments were performed for this thesis. The use of the facility involves many sophisticated techniques, and the author underwent a significant training period in order to learn their correct and safe use. The data analysis is also complex and the author made significant advances with this analysis.

The compressional response of all of the materials was measured. The porous materials demonstrated behaviour dominated by their compaction, with a curved Hugoniot relation for sandstone, and an obvious Hugoniot elastic limit (HEL) at around 3 GPa in the iron ore longitudinal data. Additionally, while not exhibiting porosity, the biotite schist also had a curved Hugoniot. It is postulated that this is due to the presence of clay in the material, something that was shown to be the case in the mineral analysis. The other materials all showed a linear Hugoniot relationship when the data are in σ - u_p space. Additional experiments confirmed that this linear relationship implied

that the shock velocity did not change significantly over the pressure regime studied. As well as the compressional response, the unloading behaviour of a number of the materials was also investigated. It was found that in all loading/unloading cycles there was some irretrievable energy loss. In a number of the materials it appears that the energy lost on loading increases with pressure, as more damage is done to the material. The opposite trend was observed in the biotite schist. Basalt consistently showed a higher percentage of energy lost than the other materials, with the exception of sandstone, where substantial energy loss associated with the collapse of pores occurred.

Shear strength and lateral stress were measured using stress gauges for amphibolite, iron ore, sandstone, quartz/feldspathic gneiss, kimberlite, siltstone and basalt. With the exception of sandstone and biotite schist, all of the materials were found to have an obvious HEL. These ranged in value from 1.3 GPa (gneiss) to 5 GPa (siltstone). This HEL was not obvious in many cases from the longitudinal data as it would be in many other materials. It is speculated that the nature of non-elastic deformation in rocks, namely brittle cracking would possibly account for this observation.

Attempts were made to investigate the dynamic tensile properties of a number of the materials, however this was only successful for kimberlite (21 $\pm$ 4 MPa), siltstone (55 $\pm$ 6 MPa) and biotite schist (one experiment giving 26 MPa). The polycrystalline and inhomogeneous nature of rocks means that fracture is unlikely to occur in the well defined planes that are required for successful plate impact tensile failure experiments. This means that a statistical approach is necessary to determine a spall strength, and a significant number of unsuccessful shots should be expected.

As the material data are destined for use in a computer modelling

programme it was essential to attempt to develop prediction methodologies to avoid the need for expensive dynamic characterisation of any new materials encountered in the mining environment. Much of the static data provided with the materials from De Beers proved of little use in predicting behaviour, although crucially it was not possible to determine sufficient dynamic tensile strengths in this investigation to make comparisons with the De Beers data. More success was found in predicting the slope of the Hugoniot with the elastic impedance of the material (for the non-porous linear Hugoniot materials). A fairly strong trend was found, which was backed up with data from the literature. Additionally some effort at further analysis using mineral data was undertaken. Attempts at predicting the HEL were also partially successful. While no specific quantitative prediction method was found, it was noted that the HEL did seem to scale with grain size, in that the large grained materials had a lower value of the HEL (below 2 GPa) compared with the finer grained materials (around 4 GPa and above).

This dissertation is the result of my own work and includes nothing which is the outcome of work done in collaboration except where specifically indicated in the text. Additionally the word limit has not been exceeded.

5th February 2009

Contents

Nomenclature

Roman Symbols

ΔR	Change in Resistance of Gauge
ΔV	Change in Voltage
a_1	Pressure dependent component of wave velocity
a_2	Pressure dependent component of wave velocity
C_0	Fitted parameter for shock equation of state
c_a	Sound speed on the Hugoniot
c_0	Bulk Sound Speed
c_b	Sound Speed in a Bar
c_l	Longitudinal Sound Velocity
c_s	Shear Sound Wave Velocity
E	Young's Modulus
e	Energy
F	Fringe Number
f	Incident Frequency of Light
f'	Frequency of Light Measured by Stationary Observer

G	Shear Modulus
h	Etalon Length
K	Bulk Modulus
M	Mirror (in VISAR)
n	Refractive Index
P	Hydrostatic Pressure
R_0	Initial Gauge Resistance
as	Fitted parameter for shock equation of state
t	Time
t_d	VISAR Time Delay
u_p	Particle Velocity
U_s	Shock Velocity
V	Volume
Y	Dynamic Compressive Strength
Z	Acoustic Impedance
Z_s	Shock Impedance

Greek Symbols

ϵ	Strain
Γ	Grüneisen parameter
ν	Poisson's Ratio
ϕ	Angle between the extent of 1D strain and the normal
ρ	Density

ρ_0	Initial Density
σ	Stress
σ_x	Longitudinal Stress
σ_y	Lateral Stress
τ	Shear Strength

Subscripts

y	Cartesian y axis
x	Cartesian z axis
z	Cartesian z axis

Acronyms

BS	Beamsplitter
HEL	Hugoniot Elastic Limit
$HSBM$	Hybrid Stress Blasting Model
$JKMRC$	Julius Kruttschnitt Mineral Research Centre
MLA	Mineral Liberation Analyzer
PBS	Polarising Beamsplitter
$PETN$	Pentaerythritol tetranitrate
$PMMA$	Polymethylmethacralate
PMT	Photomultiplier tube
$PVDF$	Polyvinylidene Fluoride
TCS	Triaxial Compressive Strength
UCS	Ultimate Compressive Strength
$VISAR$	Velocity Interferometer System for Any Reflector

Chapter 1

Introduction

1.1 Motivation

1.1.1 Diamonds

Diamonds have been known for a number of millenia. They were first discovered in India, and it has been suggested that by about 400 B.C. there was a well-established pattern of diamond trading [1]. In the Western world, i.e. the Mediterranean, diamonds were probably unknown to both the Egyptians and the Greeks, although it is likely that by the time of the Roman empire they were well-known, and used for, amongst other things, the cutting of different types of gemstone. Diamonds were initially likely to be used in an industrial capacity, utilising their extreme hardness. This was partially due to the lack of the technology and skill required to adequately finish diamonds to gem quality. However by the fourteenth and fifteenth centuries, techniques for cutting and polishing had evolved to the stage where diamonds brought from India could be used for jewellery in Europe. This was the start of the use of diamonds as the high value luxury items that we know them as today.

1.1.2 De Beers

After India, the next big diamond production region was Brazil. However, in both of these countries production was based on alluvial diamonds in rivers, and

other secondary sources. The deposits discovered in South Africa from the middle of the nineteenth century, were by contrast primary deposits, meaning that they were in the original kimberlite pipes and thus able to be mined on a large scale. At first individual miners worked claims on a small scale but this rapidly became inefficient leading to the amalgamation of claims. Consolidation through Cecil Rhodes eventually led to the formation of De Beers Consolidated Mines Ltd, which at one point controlled 90% of the world's diamond production. Today De Beers is still the best known diamond company in the world, and controls much of the sale of rough diamonds.

1.1.3 Blast Mining and HSBM

In the world of modern mineral procurement, it is no longer possible to find diamonds, or many other commodities, simply lying in rivers and streams. Diminishing resources and an ever increasing demand for materials has lead to both an increase in prices and a drive to more efficient mining practices. As a great deal of mining on a large scale is accomplished by a process of blasting with explosives, this is an area where good research can lead to substantive economic gains for mining companies. Dr. Alan Guest, a geotechnical engineer working for De Beers realised that a holistic approach was needed, encompassing both a rock mechanics model and an explosives model. This project, involving specialists from a number of companies and universities came to be known as the Hybrid Stress Blasting Model, or HSBM .

1.2 Methodology

The aim of this thesis is to contribute to the body of knowledge needed to make HSBM a viable tool for use in day to day mining. While the model will deal with arrays of boreholes, to get a feel for the parameters required it is instructional to look at the single borehole case, see fig. 1.1. When a charge is set off in a borehole, there are three distinct regions. This is similar to the work done in polymers (PMMA) by Field and Ladegaard-Pedersen [2, 3]. Around the borehole itself (region 1) is a "crush zone", where the rock is strongly fractured (region

2), this leads to formation of fines and small fragment sizes. Further out from the borehole (region 3) is a zone where radial cracks start to appear. These large cracks do most of the breaking of the rock mass on a large scale in a blast.

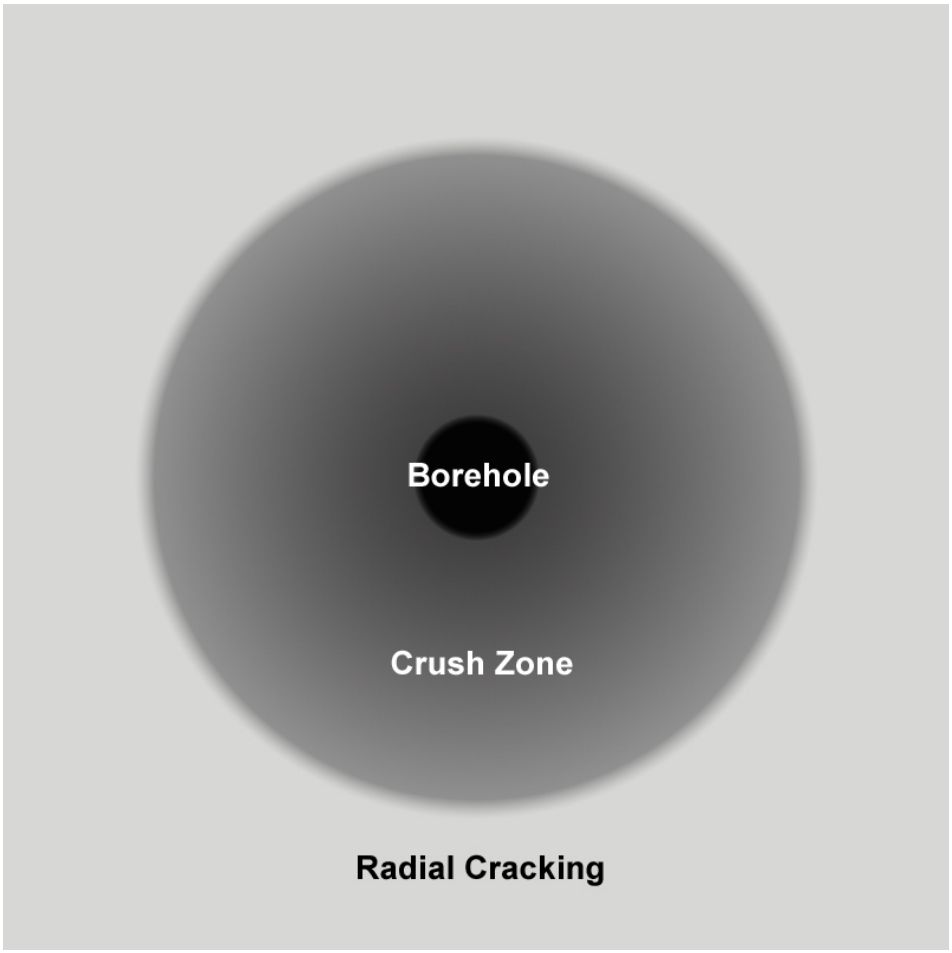

Figure 1.1: A schematic of a borehole showing the cylindrical geometry of blast mining. The shaded zones indicate the borehole itself in the centre, a region close to the borehole where the main method of rock failure would be crushing and a zone further away from the borehole where it would be expected that the rock would fail through radial fracturing.

Figures 1.2 and 1.3 are reproduced from the work of Field and Ladegaard-Pedersen [4]. They show detonations of PETN charges in blocks of PMMA.

The use of PMMA, a transparent material, allows for cracking to be seen clearly. In figure 1.2 there is plastic deformation of the region around the borehole, an annulus of shear failure and a series of radial cracks emanating outwards from the edge of the plastic and shear regions. The gas from the explosion has not been able to enter these cracks. In effect the plastic deformation region has "sealed" the borehole and prevented gas from accessing the crack network and extending the cracks further into the material. In figure 1.3 however the PETN charge has been diluted so the explosive power is reduced. This leads to a reduction in the pressure generated around the borehole. In turn this means that the plastic zone does not "seal" the radial cracks and in fact the cracks can propagate back into the borehole. This gives the gas generated by the explosive access to the cracks in the material, which are then enlarged. Overall therefore the damage from using a diluted explosive is more than from using the full power of the explosive.

The extent of the three zones described, and the characteristics within them are determined by the physical parameters of the materials (rocks in the case of the real-world mining situation) concerned, as well as the explosives, as described above (note that the optimisation of explosives is also being investigated for the HSBM project). Within the crush zone, the key parameters are the compressional and shear strengths, as there is sufficient energy to overcome these strengths and cause significant failure. Further away from the borehole, the energy from the explosive has dissipated to the extent that it is unable to cause compressional or shear failure. At this point however the cylindrical expanding shock wave can overcome the tensional strength of the material (as adjacent areas of material are locally moving away from each other). Therefore it is necessary to examine the tensional, compressional and shear properties of the rocks in order to obtain sufficient information to model the blast mining situation.

In the laboratory it is possible to simulate the stresses and loading types found in the mining situation by using a plate impact facility. This consists of an instrumented gun and uses impact of projectiles rather than explosives to load the rock to high stresses at a high strain rate. It is hoped that this research will not only allow for more accurate modelling to be carried out, but also through

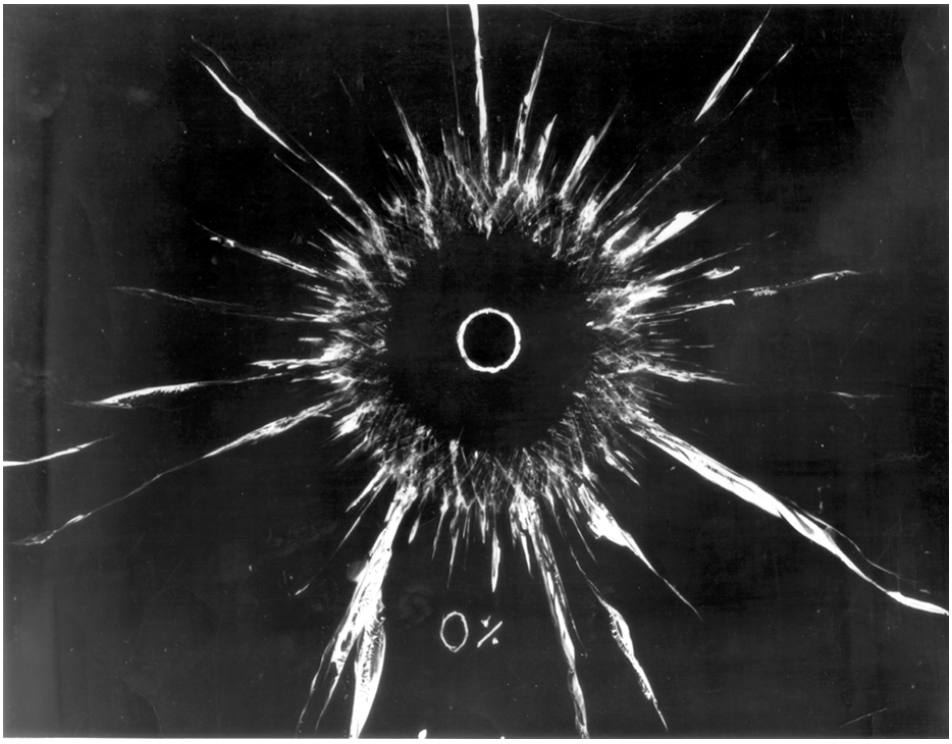

Figure 1.2: Image of a PMMA block subjected to explosive loading from a PETN charge [4]. As the material is plastic, the "crush zone" is in fact a zone of plastic deformation. However the three zones from figure 1.1 are clearly visible. The extent of the plastic deformation has sealed the radial cracks and prevented gases from the borehole entering and enlarging them.

measuring static properties, predict rock behaviour. This ability to predict is important as it allows for the behaviour of rocks not specifically investigated to be modelled with a reasonable level of confidence.

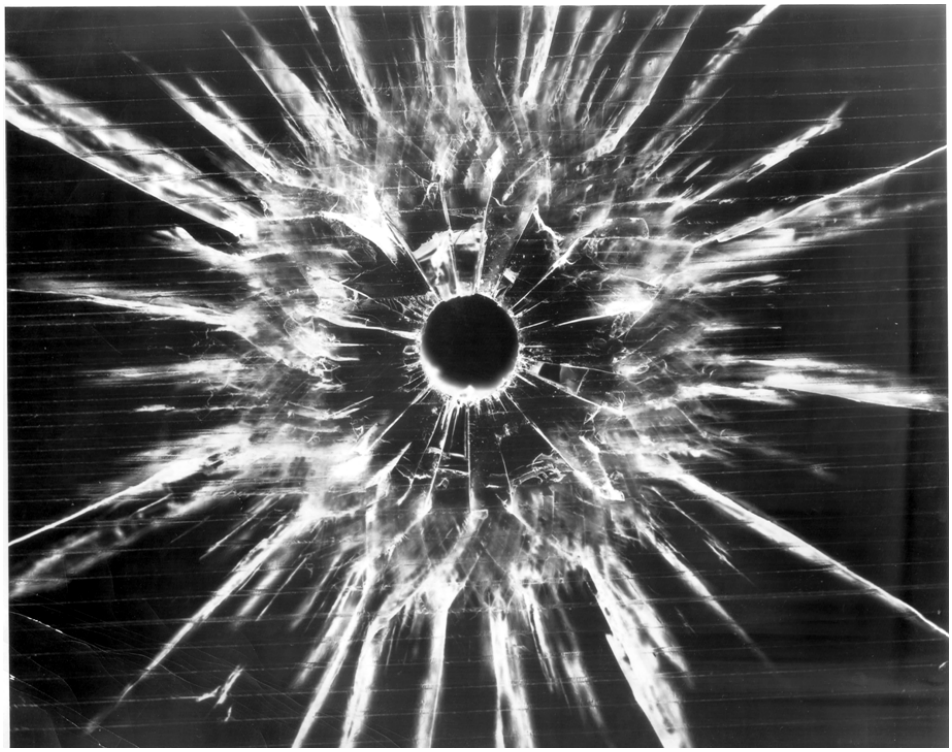

Figure 1.3: Image of a PMMA block subjected to explosive loading from a diluted PETN charge [4]. The situation is similar to that shown in figure 1.2 however the plastic deformation close to the borehole has not sealed the radial crack structure in the same way. Gas from the borehole has entered the crack network and expanded the cracks, increasing the overall damage to the material.

References

[1] Davies, G., *Diamond*, Adam Hilger, Bristol (1984)

[2] Field, J.E. and Ladegaard-Pedersen, A., "Fragmentation processes in rock blasting", *Dechema-Monographien (also Int. J. Rock Mech. and Min. Sci.)*, **69**, (1972), 1–29

[3] Field, J.E. and Ladegaard-Pedersen, A., "The importance of the reflected stress wave in rock blasting", *Int. J. Rock Mech. and Min. Sci.*, **8**, (1971), 213–226

[4] Field, J.E. and Ladegaard-Pedersen, A., "Detonics of High Explosives", in

Detonics of High Explosives, C. Johansson and P.A. Persson, eds., Elsevier, Amsterdam (1970), p. 247

Chapter 2

Materials and Static Properties

2.1 Introduction

The purpose of this section is twofold. Firstly it allows for the presentation of various useful physical property data that were measured statically and therefore do not constitute part of the main experimental thrust of the present thesis. Secondly it is intended to offer as much information about the materials in their initial state as it was possible to obtain. Knowing the material characteristics is of use when comparing the data acquired in this research to other literature data, both already in existence and in the future. The importance of such material data is emphasised by Austin [1] in the following quotation:

" Much of the value of any research in rock materials is related to the degree of description of the test material, and to the apparent degree of reproducibility within the test materials themselves. From these descriptions the reader can determine the extent to which the test materials match or differ from other materials of possible individual interest" .

2.2 Geological Materials

The geological materials which have been researched for this thesis have either been supplied by De Beers Consolidated Mines or Rio Tinto, and have come from a variety of sources, including South Africa. They are, even to cursory inspection, different in their properties, and these differences are emphasised and obviously quantified when the material properties are measured. The static measurements conducted consist of a measure of the density, and both longitudinal and shear sound speeds. From these basic measurements, further useful data can be obtained, for example various moduli. In addition to the numerical data, a mineral analysis was carried out on the materials by Dr S. Plint at Nottingham University. Table 2.1 presents a summary of the numerical physical properties data, and subsequently the experimental methods and the specific materials are described.

Table 2.1: Table of Measured and Calculated Rock Properties

Rock Type	c_l ($mm\ \mu s^{-1}$)	c_s ($mm\ \mu s^{-1}$)	c_0 ($mm\ \mu s^{-1}$)	ρ ($g\ cm^{-3}$)	**G** (GPa)	**K** (GPa)	**E** (GPa)	ν	**Z** ($mm\ \mu s^{-1}\ g\ cm^{-3}$)
Siltstone	6.86 ± 0.11	3.79 ± 0.08	5.28 ± 0.16	2.838 ± 0.007	41 ± 3	79 ± 6	105 ± 5	0.279 ± 0.004	19.47 ± 0.3
Kimberlite	5.53 ± 0.08	2.89 ± 0.04	4.41 ± 0.11	2.76 ± 0.02	23 ± 2	54 ± 4	60 ± 5	0.312 ± 0.007	15.24 ± 0.2
Amphibolitic Gneiss[1]	6.38 ± 0.08	3.88 ± 0.10	4.54 ± 0.13	2.664 ± 0.01	40 ± 3	55 ± 5	97 ± 6	0.206 ± 0.004	17.00 ± 0.2
Amphibolitic Gneiss[2]	6.22 ± 0.10	3.66 ± 0.07	4.56 ± 0.13	2.828 ± 0.005	38 ± 2	59 ± 4	93 ± 4	0.234 ± 0.004	17.58 ± 0.3
Amphibolite	6.61 ± 0.05	3.89 ± 0.04	4.85 ± 0.07	3.001 ± 0.005	45 ± 2	71 ± 4	112 ± 5	0.235 ± 0.002	19.84 ± 0.2
Quartz/Feldspathic Gneiss	5.72 ± 0.19	3.50 ± 0.09	4.05 ± 0.22	2.650 ± 0.002 *	32 ± 2	43 ± 5	78 ± 3	0.201 ± 0.01	15.16 ± 0.5
Sandstone	1.97 ± 0.05	1.36 ± 0.02	1.20 ± 0.05	1.926 ± 0.005	3.5 ± 0.2	2.8 ± 0.3	7.5 ± 1	0.051 ± 0.03	3.8 ± 0.1
Biotite Schist	5.97 ± 0.16	3.53 ± 0.07	4.36 ± 0.19	2.893 ± 0.008	36 ± 2	55 ± 6	89 ± 5	0.231 ± 0.008	17.27 ± 0.5
Basalt	5.02 ± 0.05	2.29 ± 0.02	4.28 ± 0.07	2.675 ± 0.009	14.0 ± 0.8	49 ± 3	38 ± 2	0.370 ± 0.003	13.44 ± 0.1
Iron Ore[3]	6.03 ± 0.20	3.43 ± 0.08	4.55 ± 0.24	4.46 ± 0.16	52 ± 10	92 ± 10	132 ± 25	0.260 ± 0.04	26.9 ± 1.3
Gabbro [2]	6.21 ± 0.01	3.51 ± 0.02	4.71 ± 0.02	2.88 ± 0.02	35 ± 5	64 ± 8	90 ± 12	0.27 ± 0.01	17.88 ± 0.3
Dolerite [3]	5.89 ± 0.07	3.34 ± 0.11	4.45 ± 0.13	2.89 ± 0.03	32 ± 4	57 ± 7	82 ± 8	0.26 ± 0.01	17.05 ± 0.3
Cement Paste [4]	3.70 ± 0.20	2.20 ± 0.20	2.69 ± 0.30	2.00 ± 0.02	10 ± 4	14 ± 6	24 ± 8	0.2 ± 0.1	7.4 ± 0.8
TKB [5]	3.56 ± 0.04	1.85 ± 0.01	2.85 ± 0.05	2.49 ± 0.04	8 ± 1	20 ± 3	22 ± 3	0.32 ± 0.01	8.86 ± 0.2

*For the first cut, later cuts gave a density of 2.748 ± 0.0012g cm^{-3}

1. This was a cut of amphibolitic gneiss with more of the lighter coloured material
2. This was a darker cut of amphibolitic gneiss and was the material used for plate impact experiments
3. The sound speeds and density given in the table are averages, further details are given in the description of the iron ore in section 2.4.9

2.3 Experimental Methods

2.3.1 Density

The density was measured by a simple volume method. The sample dimensions were measured using either a digital Vernier calliper (Mitutoyo) or if the dimensions were sufficiently small, a digital micrometer (Mitutoyo). This gave an accuracy of ± 0.01 mm for the calliper and ± 0.001 mm for the micrometer. In both cases elements of sample roughness meant that scatter in the data was a greater source of error than measurement error. The masses of the samples, if below 110 g, were measured on a precision balance (Sartorius) which was accurate to approximately ± 0.001 g. Above 110 g a simple digital balance (Salter, model 1300), accurate to ± 0.1 g was used. Fairly large samples and careful selection were used in order to ensure that the measured densities were representative of the bulk and to reduce errors. In certain cases the materials showed such a variation in character between rocks that were nominally the same that separate measurements were made.

2.3.2 Sound Speeds

The sound wave velocities were determined from measuring the time of arrival of pulses from ultrasonic transducers. For the longitudinal wave (c_l) velocity the transducers (Panametrics 5 MHz) were coupled to the sample surface using a silicone based grease. When measuring shear wave velocities (c_s) (again using 5 MHz Panametrics transducers) treacle was used as a coupling medium. The transducers were powered by a dedicated power supply, and the signals from the transducers were displayed on a Tektronix 460A digitising oscilloscope. Time of transit was measured using the cursors on the oscilloscope and the sound speed was then calculated after measuring the thickness of the sample with a digital micrometer. Sample thickness was a key factor in these measurements, if the sample was too thick then the attenuation was too great and signal to noise ratio was unacceptably low. Conversely if the sample was too thin, then the disruption and broadening of the wave packet on its transit of the material meant that the

signals on the oscilloscope overlapped leading to ambiguity when measuring transit time. This gave a usable range of sample sizes from about 4-25 mm although this varied from material to material. A series of samples of different thicknesses were then cut and abraded flat to remove saw marks. The gradient of a graph of sample thickness against transit time gives the sound speed. An example of this (for amphibolite) is shown in figure 2.1. The individual points are shown without errors as the scatter in the measurements is the major source of error. To generate each point in the figure a number of repeat measurements were taken of the transit time, and the thickness was measured on a number of points across the specimen. The advantage of this gradient method is that the thickness of the coupling medium does not effect the result as if the measurements are made in a consistent manner the coupling medium will give a constant offset rather than a change in the gradient. It also removes any systematic errors introduced by the experimental set-up.

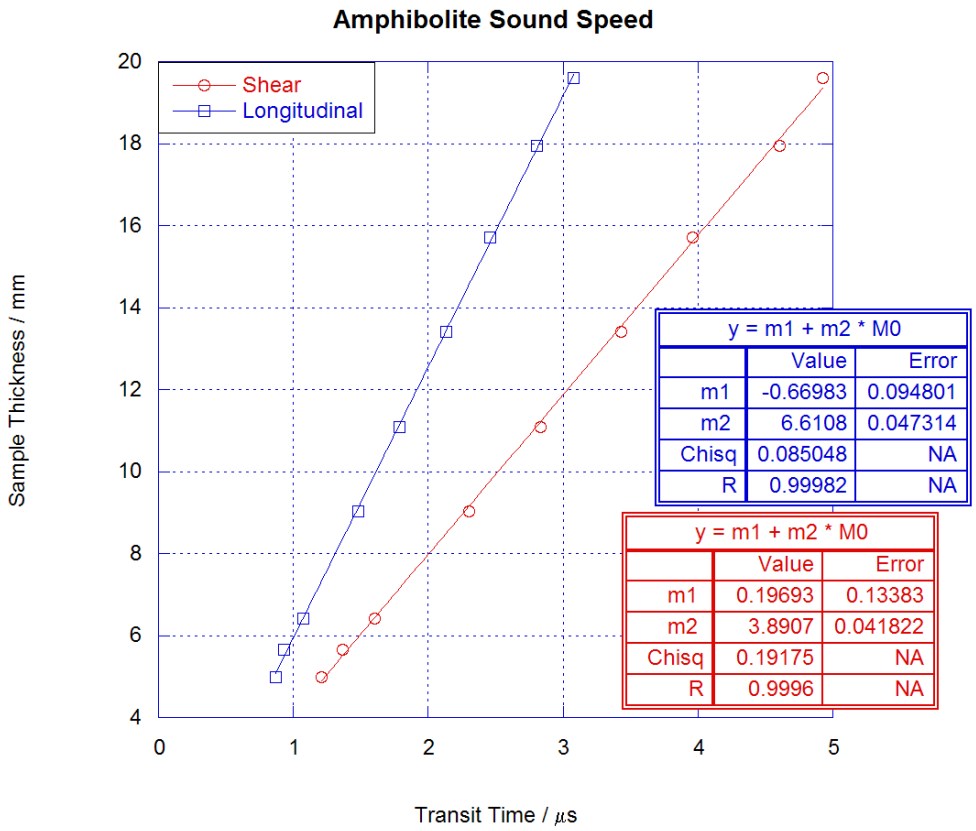

Figure 2.1: Amphibolite sound speeds, both longitudinal and shear. The sound speeds are calculated as the gradients of the lines fitted to the individual data points in each series. The negative intercept of the longitudinal sound speed fit is taken to be indicative of a systematic feature in the experimental set-up, as this was a feature common to all of the sound speeds measured using this particular pair of transducers.

In measuring the sound speeds of specimens no account has been taken of possible anisotropy in the materials. The rock cores were cut perpendicular to the direction which the cores provided were drilled in, to provide disc shaped samples. The number of rock types provided and the additional technical difficulties of cutting specimens at angles meant that it was not possible to examine this aspect of the material behaviour. However as all samples were prepared in the same manner from the core provided, sample to sample consistency (with respect to anisotropy) can be assumed. It is noted however that other authors (for example [6]) do demonstrate anisotropy in geological materials, and this is not something that can be entirely neglected when considering their properties.

2.3.3 Moduli and Derived Parameters

After making the direct measurements described above, it can be helpful to calculate the values of various other useful material properties. The formulae below are taken from Asay [7] and give values for bulk sound speed (c_0) (equation 2.1), bulk modulus (K) (equation 2.2), sound speed in a bar (c_b) (equation 2.3), Young's modulus (E) (equation 2.4), shear modulus (G) (equation 2.5), Poisson's ratio (ν) (equation 2.6) and acoustic impedance (Z) (equation 2.7). Note that ρ is the density and ρ_0 is the initial density:

$$c_0 = \sqrt{c_l^2 - \frac{4}{3}c_s^2}, \tag{2.1}$$

$$K = \rho_0 c_o^2, \tag{2.2}$$

$$c_b = c_s^2 \frac{3c_l^2 - 4c_s^2}{c_l^2 - c_s^2}, \tag{2.3}$$

$$E = \rho c_b^2, \tag{2.4}$$

$$G = \rho_0 c_s^2, \tag{2.5}$$

$$\nu = \frac{3K - 2G}{2(3K + G)}, \tag{2.6}$$

$$Z = \rho_0 c_l. \tag{2.7}$$

2.3.4 Mineral Analysis

The mineral analysis was carried out at the School of Chemical and Environmental Engineering at Nottingham University using a Mineral Liberation Analyser (MLA) designed by JKTech [8]. JKTech is the company responsible for commercial development of research from the Julius Kruttschnitt Mineral Research Centre (JKMRC) and the Sustainable Minerals Institute at the University of Queensland, Australia. The method uses back scattered electron image analysis to build up a grey-scale image of the sample where the different minerals within a particle are assigned a different grey-scale value. Subsequently x-ray analysis is used for specific identification of mineral phases. This allows an image of the sample to be created where mineral phases can be given a false colour to make them easier to identify. The machine can scan particles up to a circular section of 27 mm in diameter. As the scan is a surface scan it is necessary, if mineral percentages are required, to make sure that samples are representative of the bulk and that multiple samples are scanned to reduce errors. While strict mineral percentages are not key to this thesis, care was taken to ensure a representative sample was scanned. In some of the larger grained materials this was more difficult owing to the presence, in some cases, of material grains larger than the sample mount. In order to make the reading of this section easier, a mineralogical glossary can be found in appendix B.

2.4 Material Specifics

2.4.1 Amphibolite

Amphibolite is a rock composed mainly of the mineral amphibole and can be either igneous or metamorphic in origin [9]. The samples tested in this research are more likely igneous in origin as they lack the typical plagioclase elements of metamorphic amphibolite and are also smaller grained than would be expected for metamorphic specimens. These features can be seen clearly in the MLA pictures (Figs. 2.2 and 2.3). The MLA pictures have been false coloured in order to give good contrast between the different mineral types present. It should be noted that for the different rock types there is no colour correlation, minerals have been assigned colours to give better contrast in individual images rather than to allow identification of the minerals between images of different rock types. The natural colour of the amphibolite is almost black when polished as can be seen in Figs. 2.2, 2.3, 2.4 and 2.5. There are however small flecks of material which reflect light and give a slight sparkle. These can, thanks to the MLA work, be associated with some of the mineral inclusions, such as prenhite, muscovite and anorthite.

In some sections of the rock cores, there are significant areas of inclusions that are identified as quartz grains. With this exception, however, the rock is reasonably uniform and shows little in the way of big variations in appearance through the cores supplied. An image of one of the cores is shown in figure 2.6. It is noticeable both from this image and the image in figure 2.5 that there is little in the way of directionality within the material, in contrast to some of the other materials. The amphibolite samples are the densest rocks in this study and have one of the highest sound speeds. It is noted that in general a high density implies a lower sound speed (with sound speed being proportional to the square root of the ratio of modulus and density) so it is the high modulus of the material that is the cause of the high sound speed.

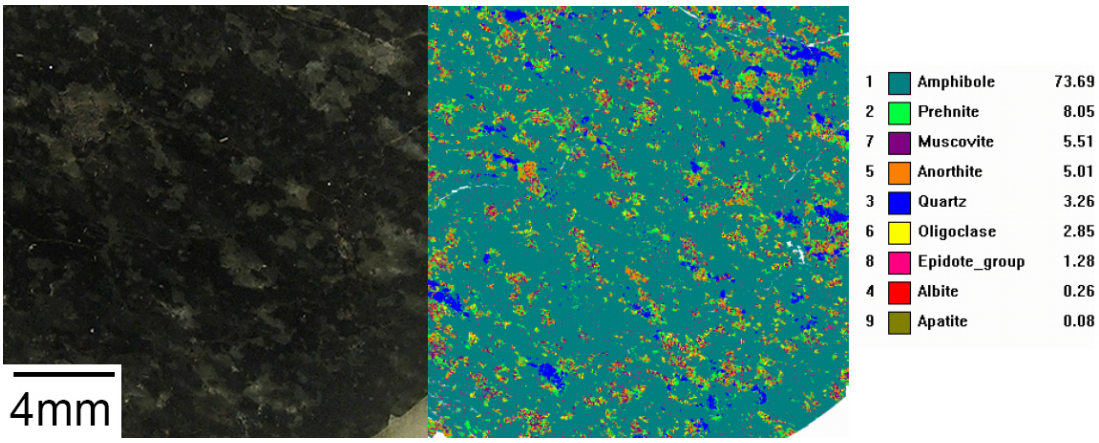

Figure 2.2: Images of an amphibolite sample. The left panel shows an optical photograph of the sample, the middle a false coloured MLA image and the right panel a breakdown of the percentage abundances of the various minerals found on the surface of the specimen. The left and middle panels are of the same section of the same sample. As would be expected amphibole is the dominant mineral, however there are significant amounts of other minerals present.

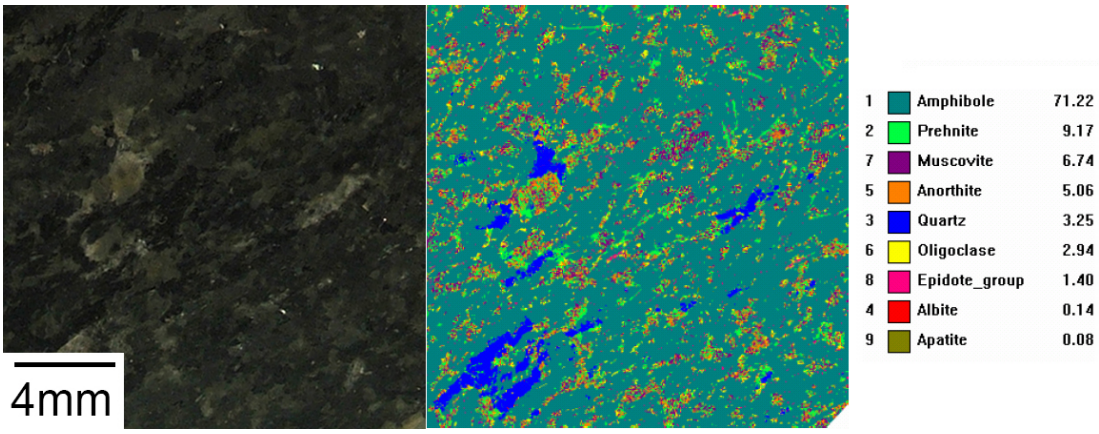

Figure 2.3: Amphibolite sample. When compared to figure 2.2 it can be seen that the overall percentage of amphibole in the sample is smaller, with most of the difference being made up with an increase in the percentages of prehnite and muscovite. Note that the quartz has clumped somewhat when compared with figure 2.2, though the overall percentage is similar

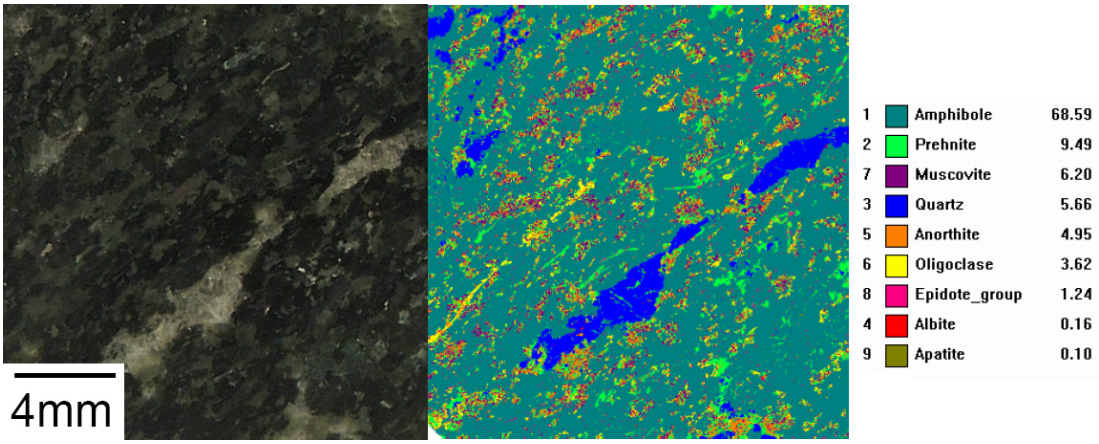

Figure 2.4: Amphibolite sample. When compared with figures 2.2 and 2.3, the most immediately obvious difference is a change in the percentage of quartz. This is largely due to the two large quartz inclusions that are evident in the optical photograph.

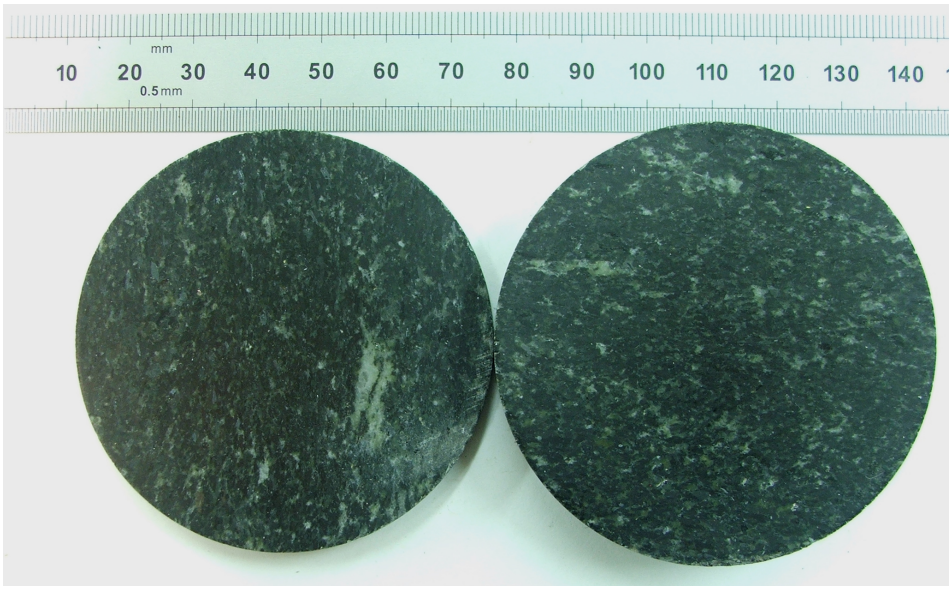

Figure 2.5: Amphibolite samples with scale bar. This wider view gives an indication, when compared with the wide view images of the other materials in this chapter, of the level of inhomogeneity in the samples used in the plate impact experiments. On the whole, while containing quartz inclusions and other minerals, the amphibolite was one of the more homogeneous materials examined.

Figure 2.6: Amphibolite core sample. There is no obvious banding on the drilled cores, as there is with some of the other materials. The relatively homogeneous nature of the material can also be seen in the lack of large crystal inclusions on the outer surface of the core.

2.4.2 Amphibolitic Gneiss

Gneiss is a fairly general term that can encompass a wide range or rocks with differing mineral compositions. It is a metamorphic rock, which while it is likely to display distinct banding, has little tendency to split along particular planes [9]. It is not possible to see banding in the cut samples, as in figures 2.7 and 2.8, but it can clearly be seen in the long sections of cores supplied by De Beers (an example is shown in figure 2.11). There is significant variation in samples cut from different sections of the core, mainly due to differences in the quartz content The different cuts of the material can be seen in figures 2.9 and 2.10. For the most part however, the samples look similar to the amphibolite (and it was these samples that were used for the dynamic testing of the material). Additionally, the MLA images reveal that the main constituent mineral in the samples, after the plagioclase matrix, is amphibole. The rock is significantly less homogeneous than

the amphibolite however, with the MLA data showing less than 50% abundance of the most prevalent mineral, as opposed to above 70% for the amphibolite. A final similarity to the amphibolite is the relatively high density, modulus and sound speeds compared with other rock types investigated. The banding in the rock cores suggests possible anisotropy. It has not been possible to examine this further however.

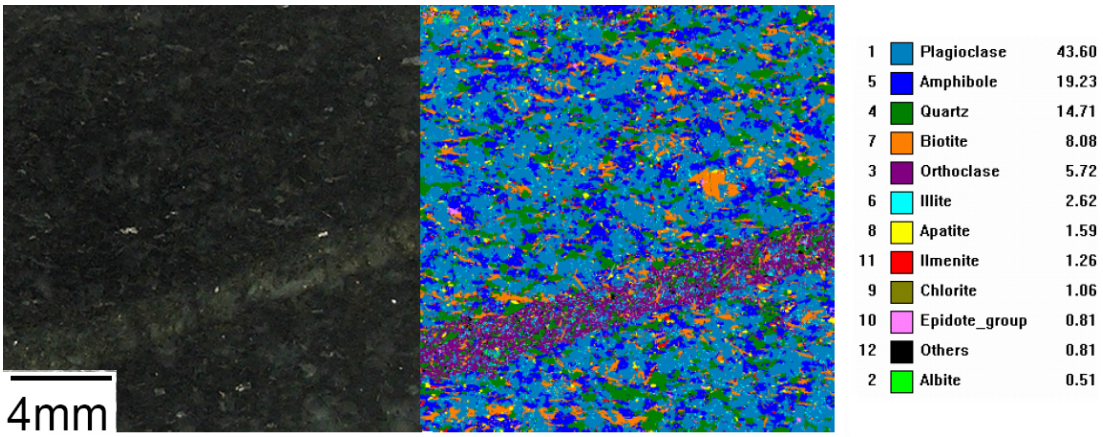

Figure 2.7: Amphibolitic gneiss sample. In the MLA image there is shown to be a clear band of orthoclase inclusions. The band of orthoclase is also seen in the photograph on the left of the figure. These bands were not an uncommon feature of the material, although they were not present in all samples. In general the material can be viewed as a plagioclase matrix with significant amounts of amphibole and quartz.

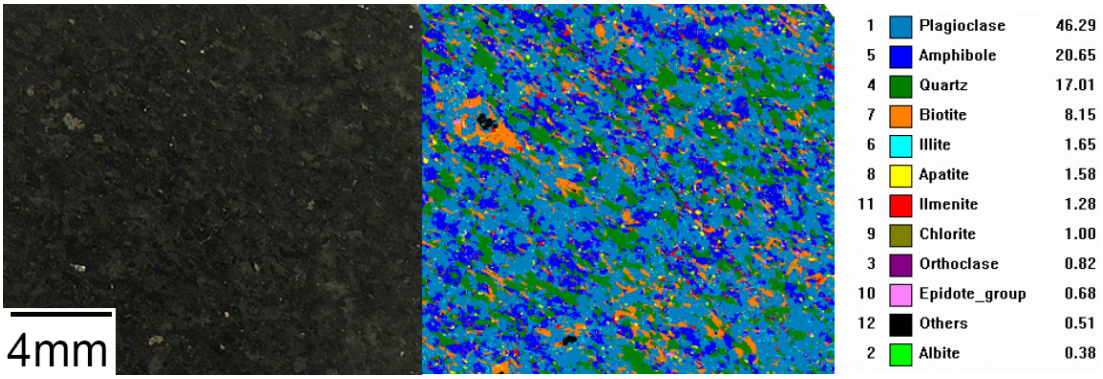

Figure 2.8: Amphibolitic gneiss sample. There is no orthoclase banding in this sample, as there is in the one shown in figure 2.7. In fact the proportion of orthoclase has decreased significantly, suggesting that the orthoclase in the material may be largely present in localised bands rather than distributed evenly throughout the rock.

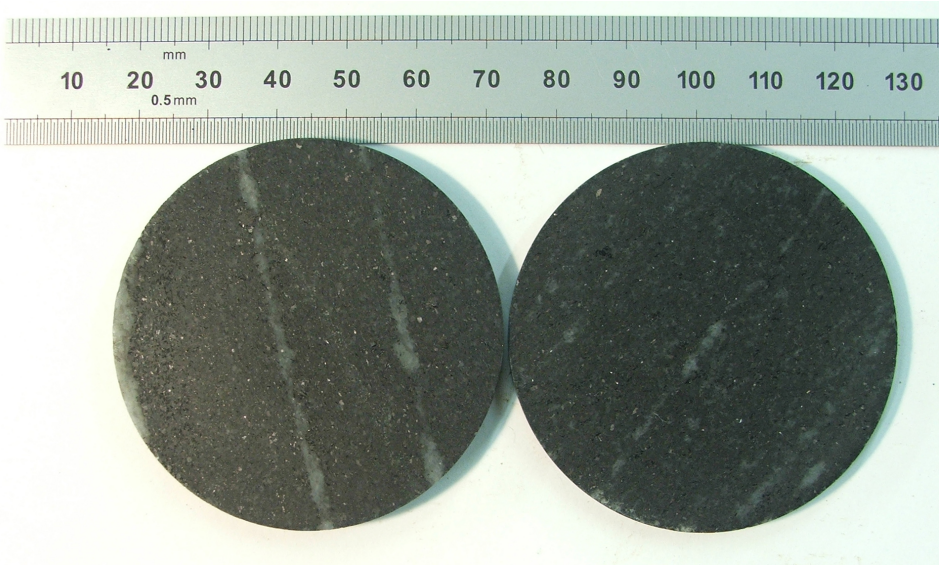

Figure 2.9: Amphibolitic gneiss samples. This wide view shows two samples of the darker cut of the material. Bands of inclusions are clearly visible, and are likely to be orthoclase, similar to those shown in figure 2.7. The bands cross the entire specimen in the cases shown in this figure. In the handling of the samples it was not noticed that there was any particular weakness along these bands.

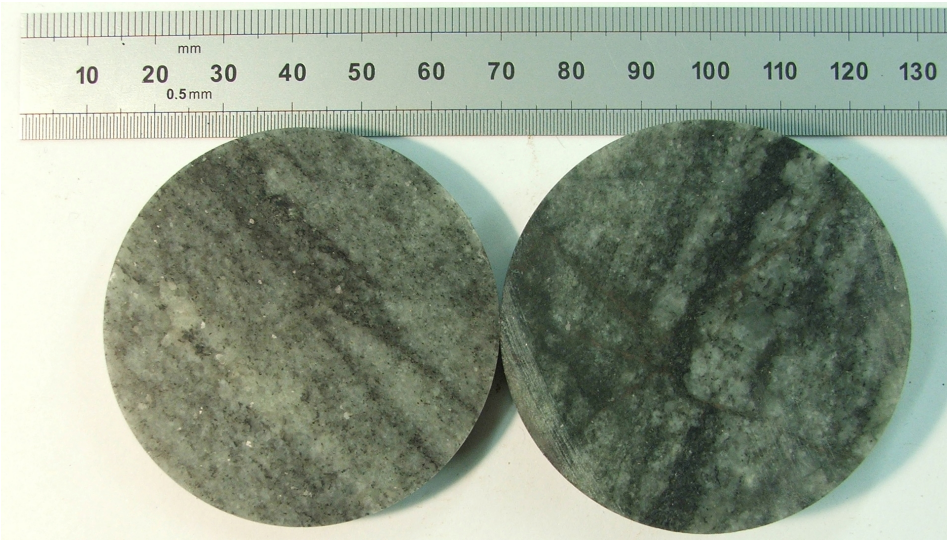

Figure 2.10: Amphibolitic gneiss samples. This wide view should be compared with the images of the "dark" samples in figure 2.9. The lighter cut of the material was not subjected to the MLA analysis, nor was it used for the plate impact experiments. However it was cut from the same core as the darker material. It could be speculated that the material has a much higher orthoclase content.

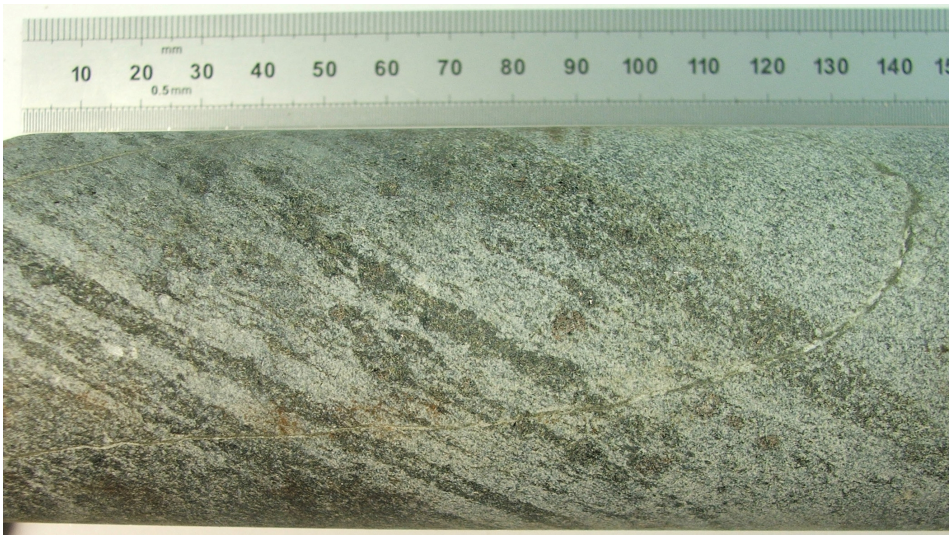

Figure 2.11: Amphibolitic gneiss core, showing clear banding. The banding on the core is almost certainly indicative of the directional banding in the cut samples. It may also be that the banding suggests directions for possible anisotropy. However it was not possible to investigate potential anisotropy due to time constraints.

2.4.3 Quartz/Feldspar Rich Gneiss

The composition of the second type of gneiss in this study is significantly different to the amphibolitc gneiss already described. There is no amphibole, and significantly less plagioclase. The main constituents are quartz, and albite and orthoclase, two different feldspars. The large orthoclase crystals give rise to the significant pink colouration in some of the samples. Again, as seen in Fig. 2.16 the banding typical of gneiss is easily visible, though it is not so clear on the cuts from across the cores. However, different sections of the cores look significantly different, with varying amounts of white and pink colouration. This can be seen most clearly in figure 2.15 where two of the samples are side by side. However the MLA data in figures 2.12 - 2.14 demonstrate that the percentages of the minerals present do not change significantly from specimen to specimen. This change in colouration does not have a significant affect on on sound speeds although the density is 2.650 $\pm$ 0.001 g cm^{-3} with the more white colouration and 2.748 $\pm$ 0.0012 g cm^{-3} for the pinker sections. The density, modulus and sound speeds are lower than the amphibole based rocks and also the siltstone.

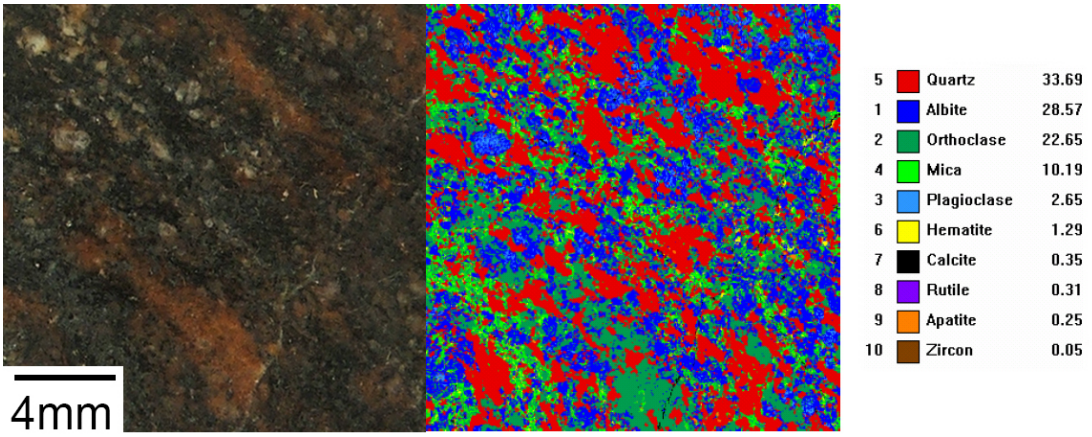

Figure 2.12: Gneiss sample composed largely of quartz and feldspars. It is noticeable that the material appears to be a relatively even mixture of the three main constituents. This is even clearer when figure 2.13 and 2.14 are considered. This mixture composition is in comparison, for example, with the amphibolite, which is mainly amphibole with inclusions of other minerals.

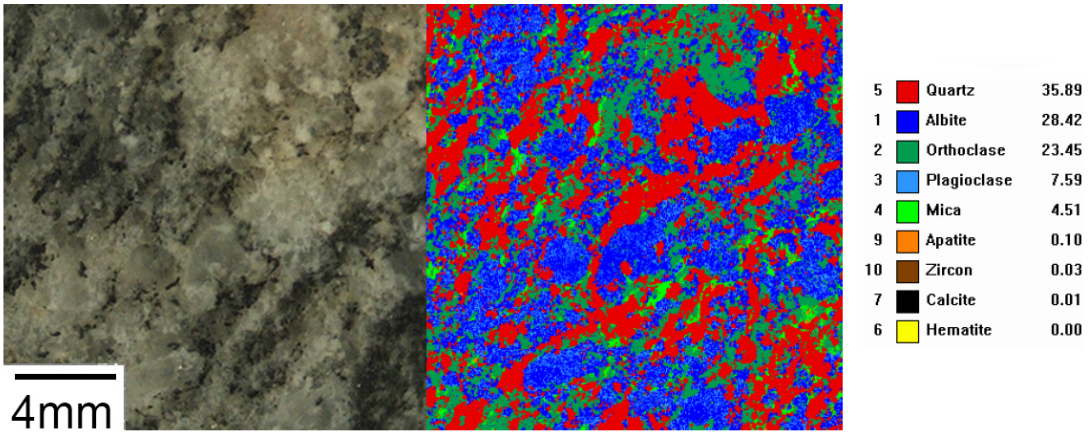

Figure 2.13: Quartz/feldspar rich gneiss sample, showing small variation in composition between samples. The lack of variation in mineral content is slightly surprising considering the distinct difference in the appearance of the samples in the photographs on the left of the figures.

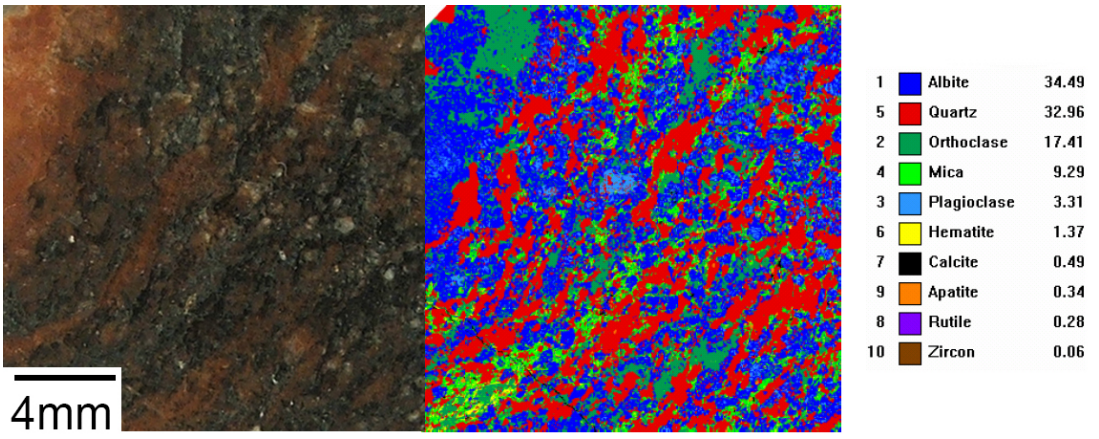

Figure 2.14: Quartz/feldspar rich gneiss sample with slightly higher percentage of albite. Again it should be noted that the mineral composition is reasonable consistent across the samples shown in this figure, figure 2.12 and figure 2.14. Additionally, while the material is fairly large grained and inhomogeneous, the grain size is also reasonably consistent from sample to sample.

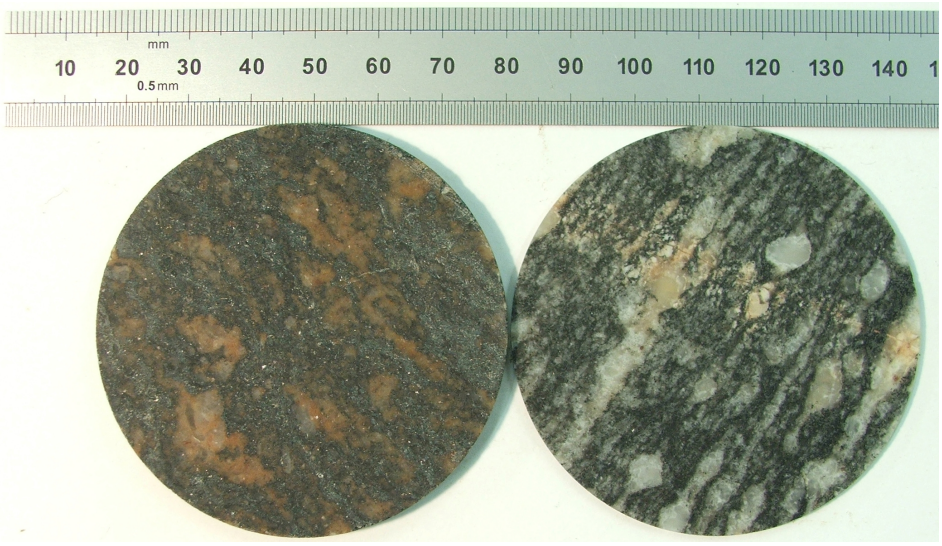

Figure 2.15: Quartz/feldspar rich gneiss samples showing the two different cuts of material. As shown in figures 2.12 and 2.13 the mineral percentages are similar, though the lighter coloured sample has a greater percentage of mica.

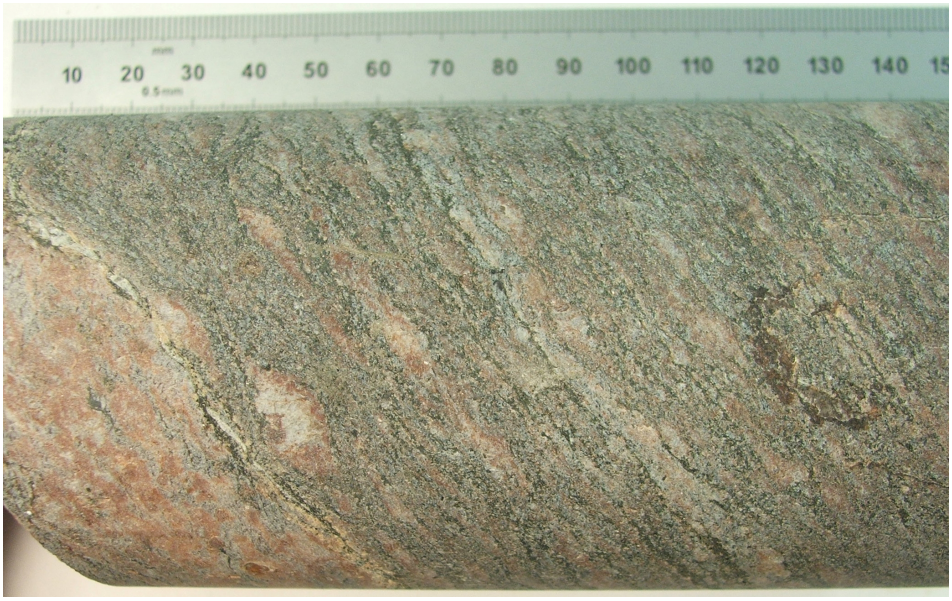

Figure 2.16: Quartz/feldspar gneiss cores showing banding. The banding in the cut samples is most evident in the right sample in figure 2.15. As with other materials presented in this investigation, it was not possible to investigate whether this banding was an indication of anisotropy in the material.

2.4.4 Biotite Schist

Schist is described [9] as having highly developed schistocity, i.e. a tendency to split into layers. Additionally banding, as seen in the gneiss specimens, is less of a feature, this can be seen in figure 2.17 and figure 2.18. Splitting tests have not been carried out in this research. The main constituents are biotite, which is typical for a schist, and quartz, which is slightly atypical. The MLA pictures (figures 2.19 - 2.21) show the presence of fairly large garnet crystals and also some clay inclusions. While the clay is not particularly soft to the touch, it is possible that it is slightly more porous or compressible than the solid mineral crystals that make up the majority of the rock. This in turn may have an effect on the physical properties.

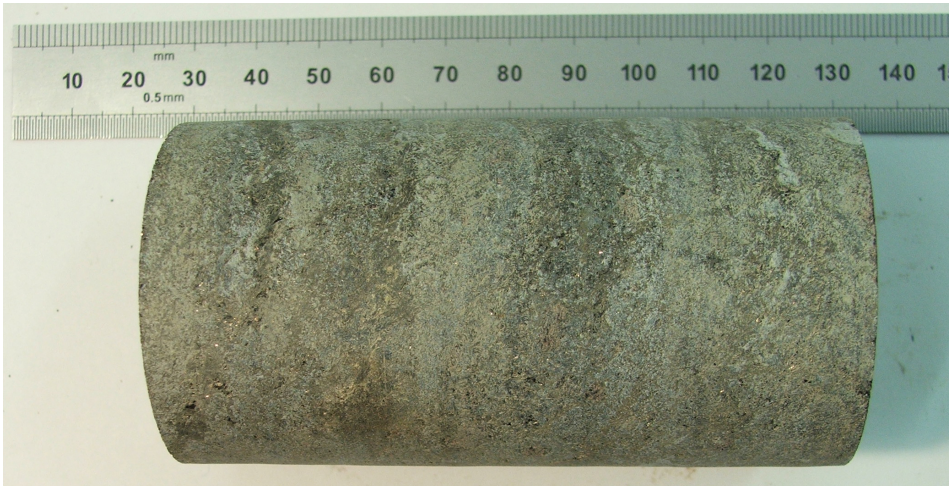

Figure 2.17: Schist core showing a lack of banding. While the material had a number of large inclusions in the cut samples, no inclusions are visible on the surface of the drilled core pictured. In the handling of the material, schistocity was not particularly noticeable.

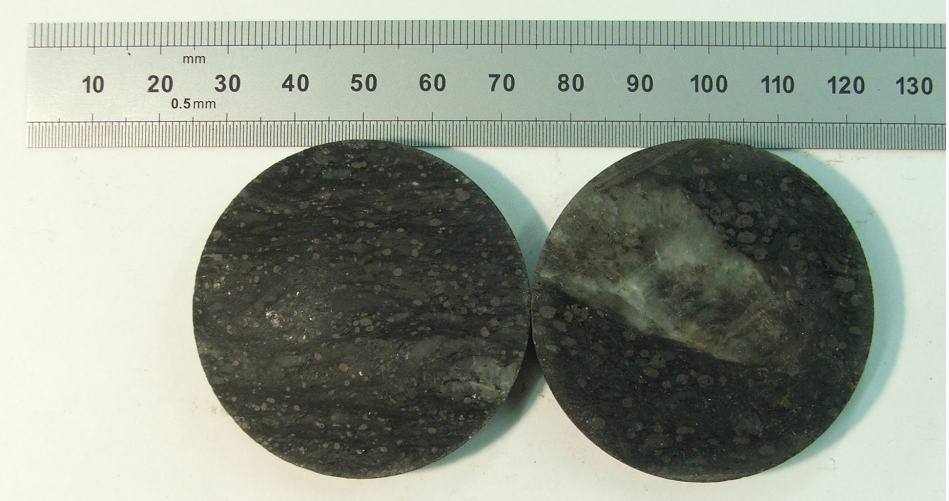

Figure 2.18: Schist samples showing a large inclusion in one of the samples. While the material generally resembled the sample of the left of the figure, there were a number of samples with large inclusions. As can be seen in figure 2.19 it is not possible to identify these inclusions with any one mineral phase.

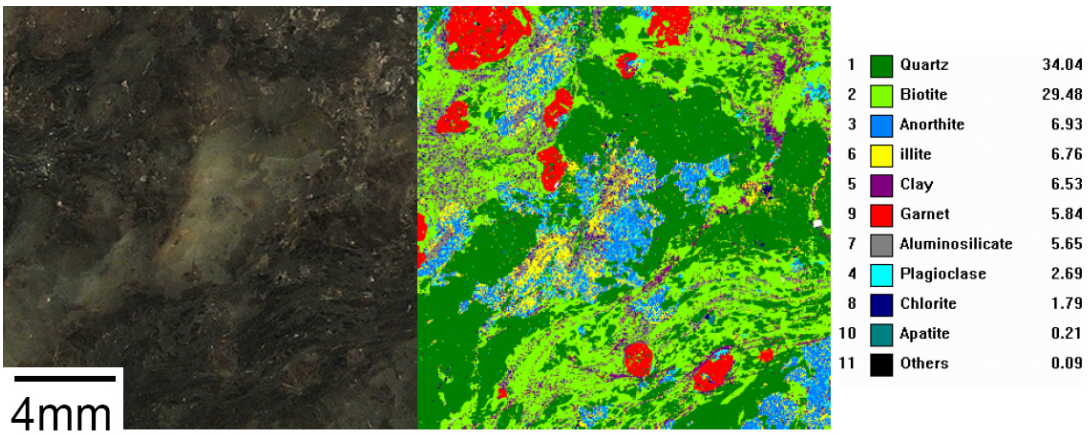

Figure 2.19: Schist sample showing that the main constituents of the material are quartz and biotite. The inclusion in the centre of the sample appears to be (from the MLA image) a mixture of anorthite and illite. When considering the samples shown in figures 2.20 and 2.21 it appears that this sample is slightly atypical with quartz being the most abundant mineral. However it should be noted that three samples is not enough to reach a general conclusion.

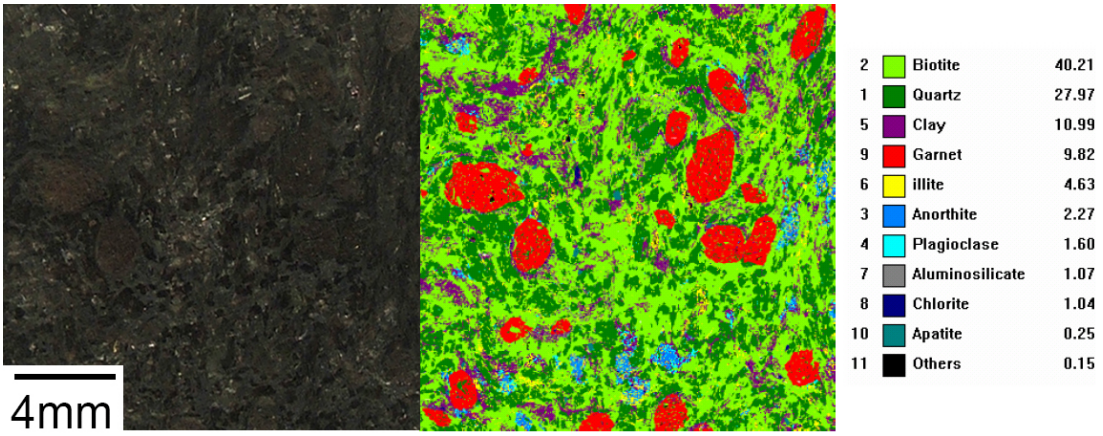

Figure 2.20: Biotite schist sample. This sample has a larger proportion (compared with figure 2.19) of both garnet inclusions, and also clay, which is distributed relatively evenly throughout the sample. As opposed to the sample with the inclusion shown in figure 2.19, this sample is more typical of the majority of the cut samples.

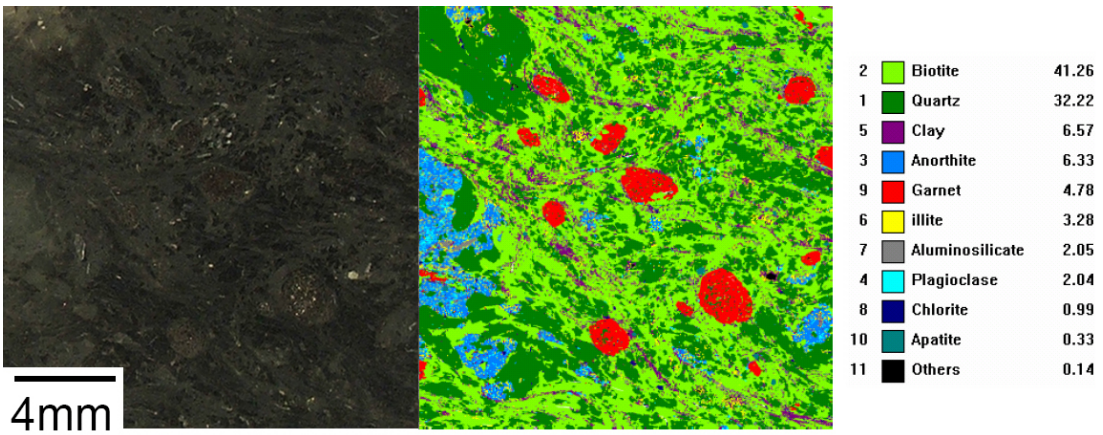

Figure 2.21: Biotite schist sample. There is a good similarity in terms of the percentage abundance of minerals between this sample and that shown in figure 2.20. While there is clay present in this material, as shown in all three samples, the clay is not obvious in terms of softness on handling the samples.

2.4.5 Siltstone

Siltstone is a hardened sedimentary rock [9] and not easily split into layers. An image of the core showing no discernable banding can be seen in figure 2.22. It can be described as hard and durable, which is in contrast to some other more common sedimentary rocks, such as certain sandstones and limestones. The density, modulus and sound speeds are reasonably high, and the rock is not obviously porous. The samples provided have a swirly patterning, which is very evident in figure 2.24. The patterning could be evidence of the typical siltstone trait of structures resulting from current flow [9]. The mineralogy of the samples is slightly less varied than the other materials shown, consisting almost exclusively of dolomite and quartz as can be seen in figures 2.23 and 2.25, with very small levels of other impurities.

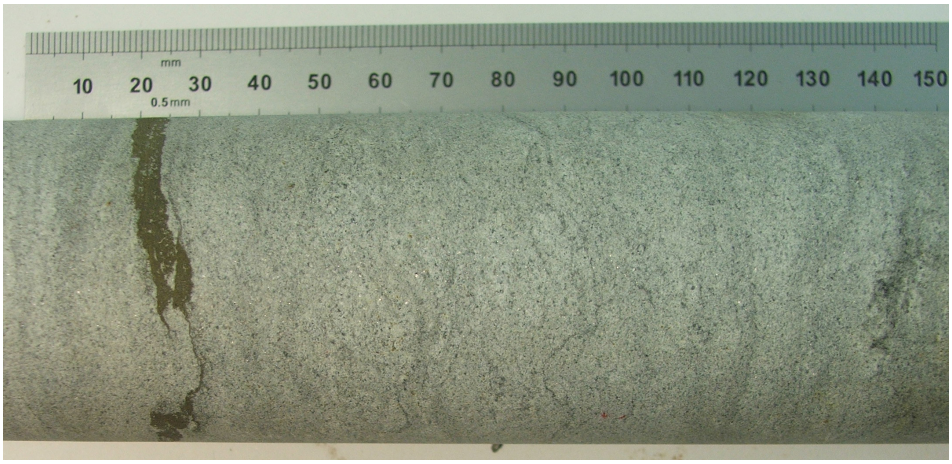

Figure 2.22: Siltstone core showing a lack of banding. It is possible to see some of the swirly patterning that is more evident in the cut samples, on the outer surface of the core.

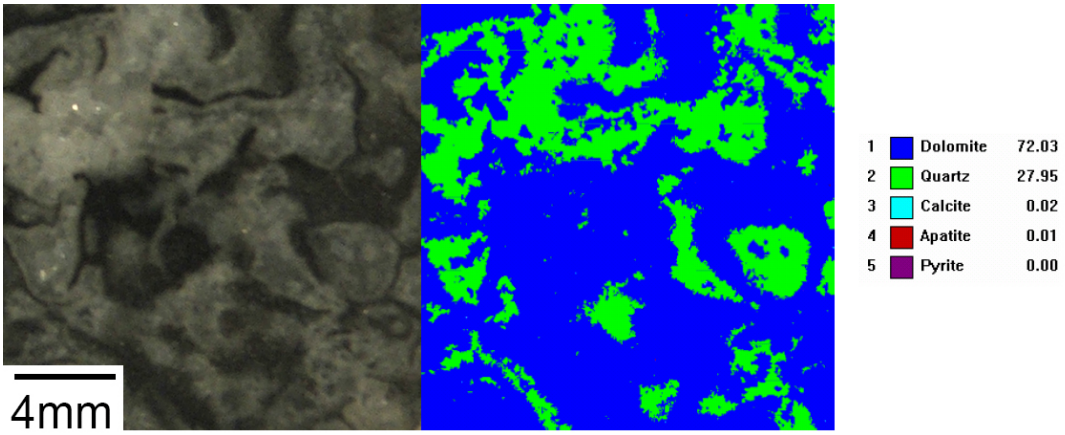

Figure 2.23: Siltstone sample consisting mainly of dolomite, but with significant quartz inclusions. As can be seen (the effect is clearer when examining the actual samples) when comparing this figure with figure 2.25 the quartz inclusions have a glossy finish when polished as opposed to the matte appearance of the majority of the material (which is shown to be dolomite by the MLA analysis).

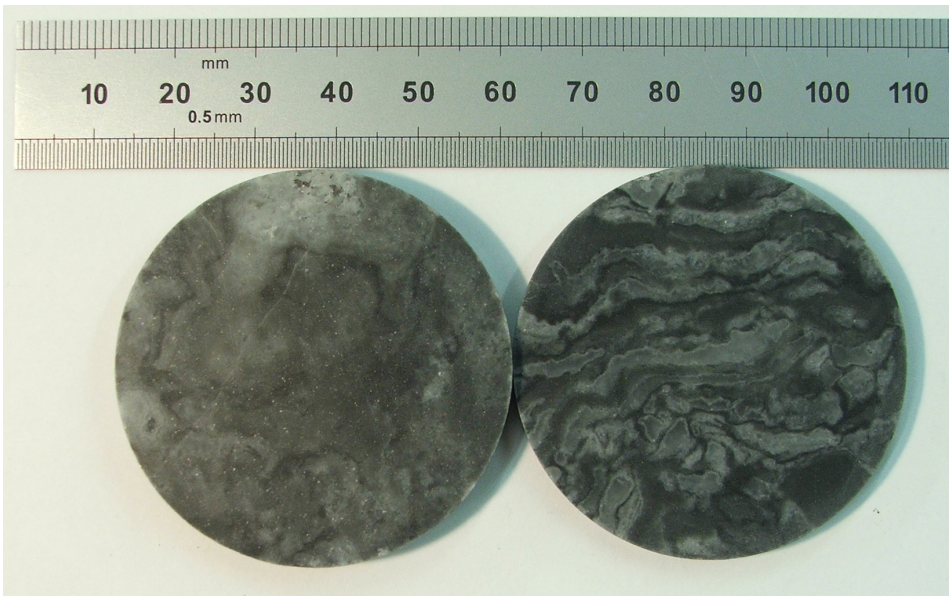

Figure 2.24: Siltstone samples showing distinctive swirly patterning. It is likely, given the MLA results in figures 2.23 and 2.25 that the more matte sample on the left of this figure is almost exclusively dolomite, whereas the sample on the right has significant amounts of quartz present.

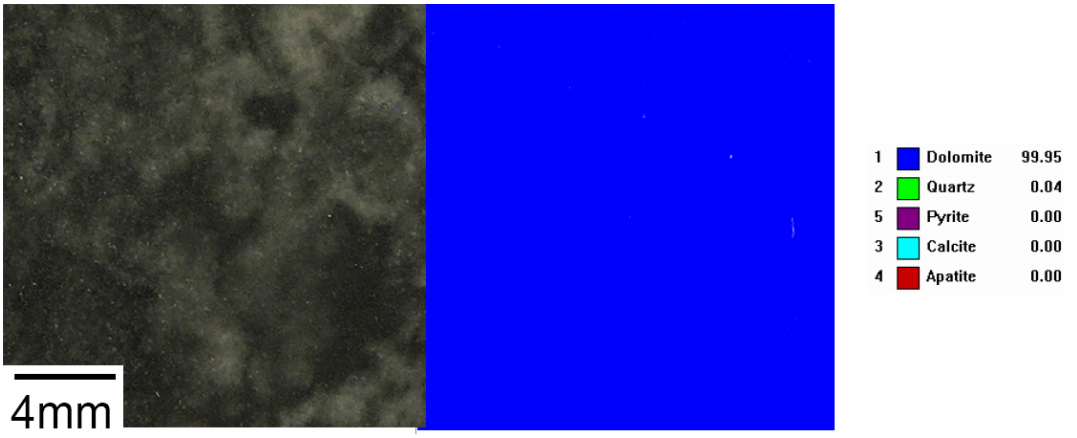

Figure 2.25: Siltstone sample with far smaller quartz inclusions. The photograph on the left of this figure is typical of the majority of the siltstone used for the plate impact experiments. As is shown in the MLA image, this material is almost exclusively dolomite.

2.4.6 Kimberlite

Kimberlite is named after the town of Kimberly in South Africa and is mainly known for its properties as a diamond bearing rock. It is an intrusive igneous rock. The principal constituent of kimberlites is olivine, though this can sometimes be altered to serpentine [9]. This seems, from the MLA pictures (figures 2.26 and 2.27), to be the case with the samples of hyperbyssal kimberlite in this series of experiments. While the other main constituent is phlogopite there are many other inclusions that give the material a distinctly conglomerate appearance. This conglomerate appearance is shown in figures 2.28 and 2.29, the latter of which gives an indication of the large size that inclusions in this material can reach. The minerals can differ in their abundance, as shown in Figs. 2.26 and 2.27. The kimberlite is lower in density, modulus and sound speeds than all of the other samples with the exception of the sandstone and the basalt. It does not however appear to be significantly porous. It is to be expected however that rocks of a lower density would start to demonstrate an obvious porosity.

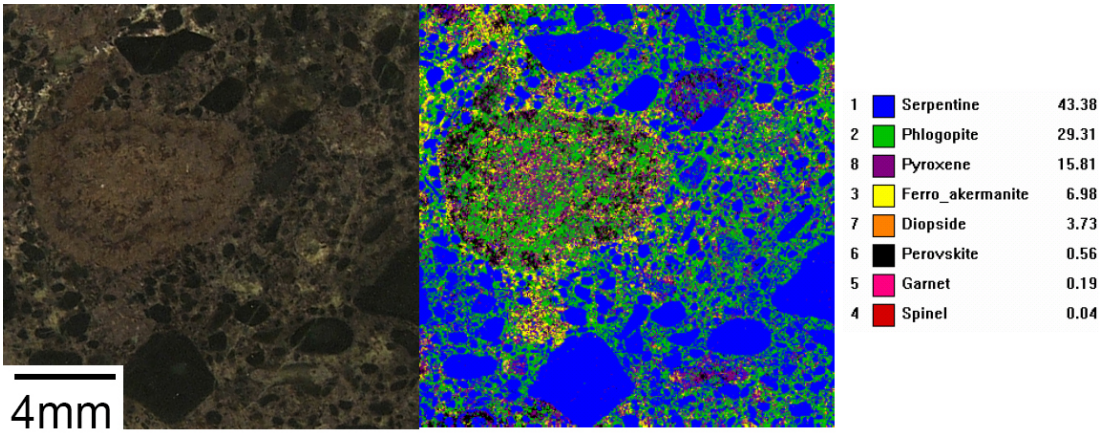

Figure 2.26: Kimberlite sample showing serpentine grains is a phlogopite matrix. The serpentine grains had a wide size distribution, and contributed to the overall inhomogeneity of the kimberlite samples. In addition to these serpentine grains, there is also a large inclusion which consists of a mixture of different minerals in small grains. This inclusion can be seen in both the optical and MLA images.

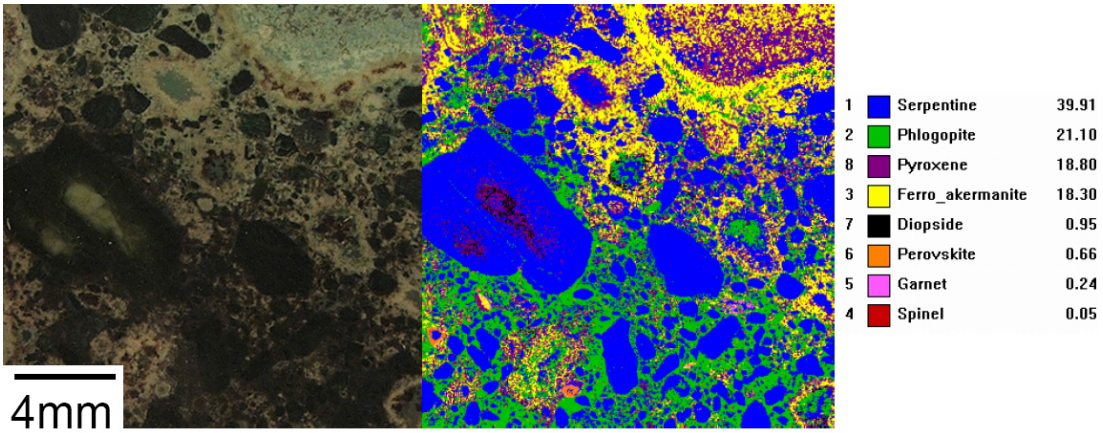

Figure 2.27: Kimberlite sample with higher percentage of ferro akermanite inclusions. These greenish ferro akermanite inclusions were common within the samples, and were, at times in the range of centimetres in size (see figure 2.29). These inclusions were a large source of heterogeneity in the kimberlite samples.

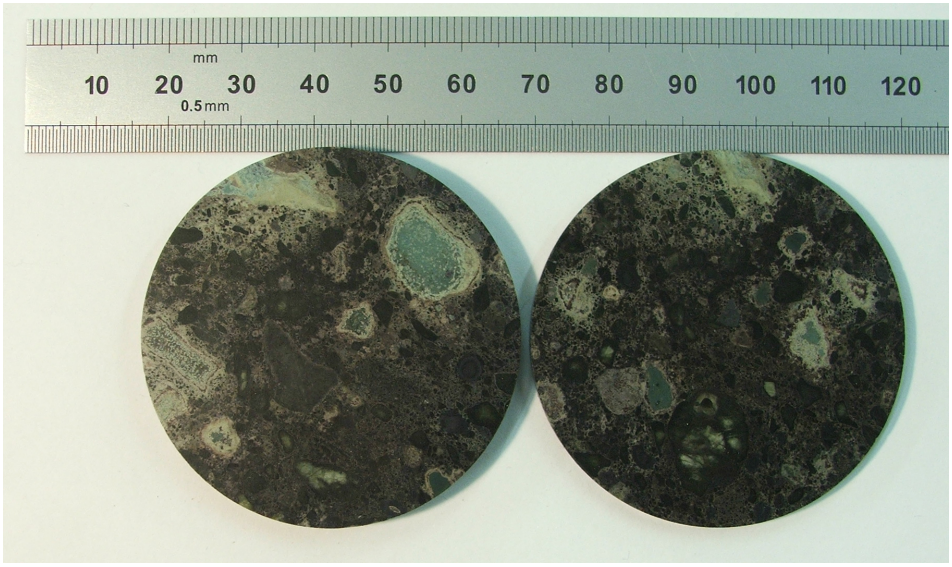

Figure 2.28: Kimberlite samples showing multiple inclusions and a conglomerate appearance. Both the greenish ferro akermanite inclusions and the size range of the serpentine grains are evident in the two samples shown.

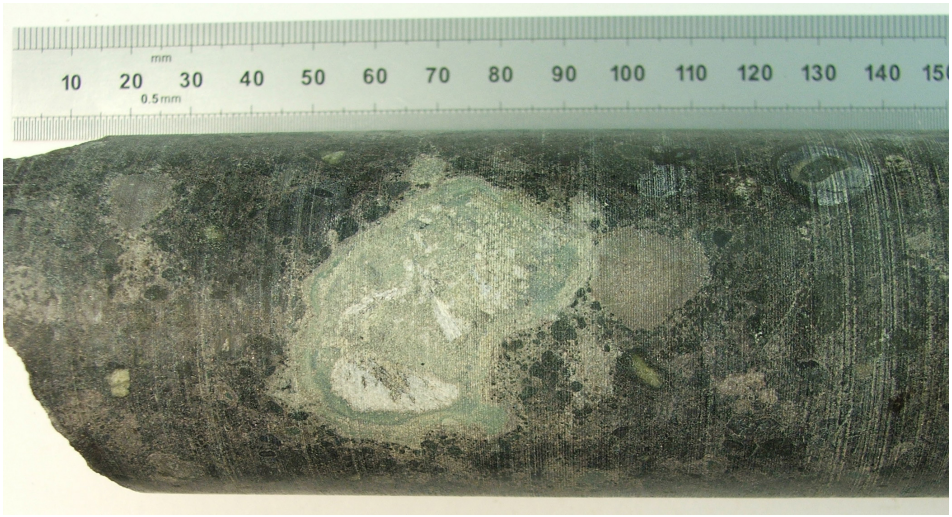

Figure 2.29: Kimberlite core with large ferro akermanite inclusion. In this larger scale image, it is clear that the level of heterogeneity in the kimberlite is much greater than in the other materials present in the current investigation. There is also no noticeable directionality in the core samples.

2.4.7 Sandstone

The sandstone samples are very different from the other samples in this research. The samples are significantly porous. Porosity was tested by submerging the samples in water for a period of 48 hours and then measuring the wet density and comparing it to the dry density. While this is not exhaustive, it does at least indicate whether an interconnected pore network exists within the sample. For all of the rock types, with the exception of the sandstone, it was found that wet and dry density were the same (note that this measurement was not performed on the iron ore as the flaws were of too great a size in many cases). For the sandstone, the dry density was 1.926 $\pm$ 0.005 g cm^{-3} and the wet density 2.12 $\pm$ 0.01 g cm^{-3}. This suggests significant porosity. The sandstone is fragile and crumbly and has a fairly coarse grain size. MLA work was not performed on the sandstone samples as they are likely to be almost entirely silicon based. In addition, the fragile nature of the samples meant that preparation would have been difficult. A macro photo of a typical sample is shown in Fig. 2.30, a wider angle shot of two samples in figure 2.31 and a core in figure 2.32.

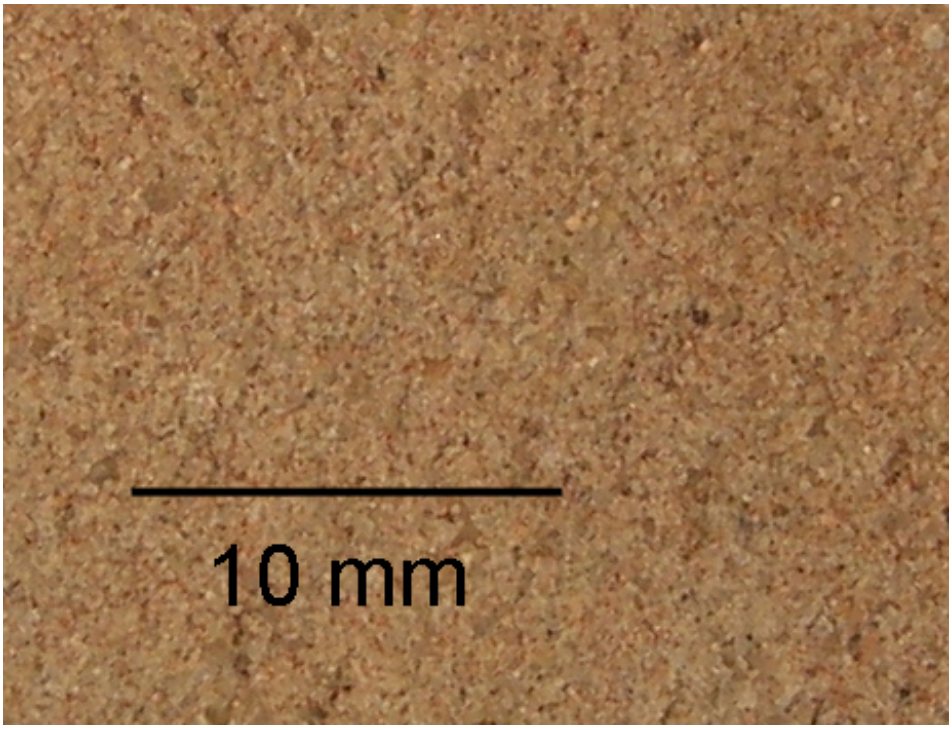

Figure 2.30: Sandstone Sample. The grains are reasonable coarse when compared with other sandstones, though as can be seen they are of a sub mm scale. Even in the slightly magnified image shown, the material appears reasonably uniform in appearance.

Figure 2.31: Sandstone Samples with scale bar. The wider angle image demonstrates that it was not possible to polish or finish the sandstone samples to the same extent as the other materials.

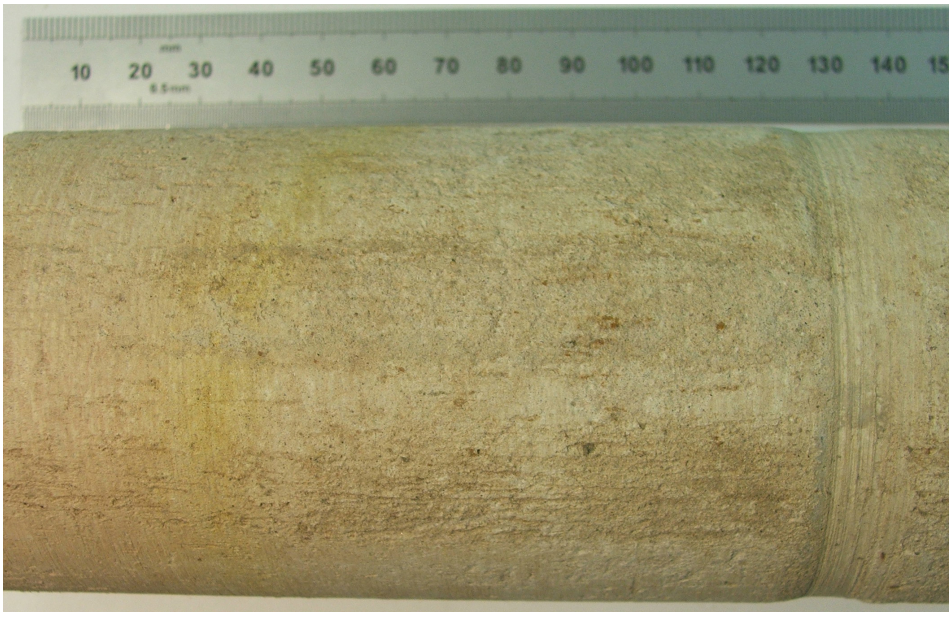

Figure 2.32: Sandstone core. The main point to notice is a lack of any large scale structure, or inclusions. There were some lines of weakness in the material, but any samples where these occurred were discarded as they failed to hold together under cutting.

2.4.8 Basalt

Unlike the previous materials discussed in this chapter, the basalt was provided by Rio Tinto rather than De Beers. It was provided as cut samples so there are no core photographs The MLA data shows that saporite and plagioclase are the main components. The MLA data and the photo are not of the same side of the specimen in this instance. Basalt is a generic name which can be used for a wide variety of igneous rocks that can have significantly different properties. The basalt has the lowest density of all of the materials examined that do no show any obvious porosity. The sound speed is also lower than all of the other rock types bar sandstone. The material tended to have lines of white coloured material running through it that lead to significant weakness. These lines can be seen easily in the sample on the right of figure 2.34, while the sample to the left has already failed along one such line.

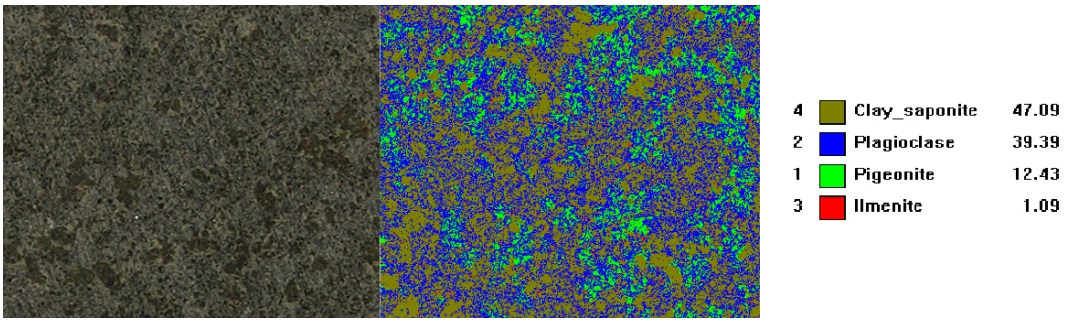

Figure 2.33: Basalt samples. In this image the photograph is a representation of the basalt at a similar scale to the MLA image. This is opposed to the other (apart from the iron ore) MLA images, where the photograph and the MLA image ore of the same sample. This was due to the sample being scanned at short notice. This also accounts for the lack of scale bar, although each of the images is approximately 20 mm across. It can be seen that the basalt is small grained and relatively uniform. It also has a relatively simple mineralogy when compared with many of the geological materials in this investigation.

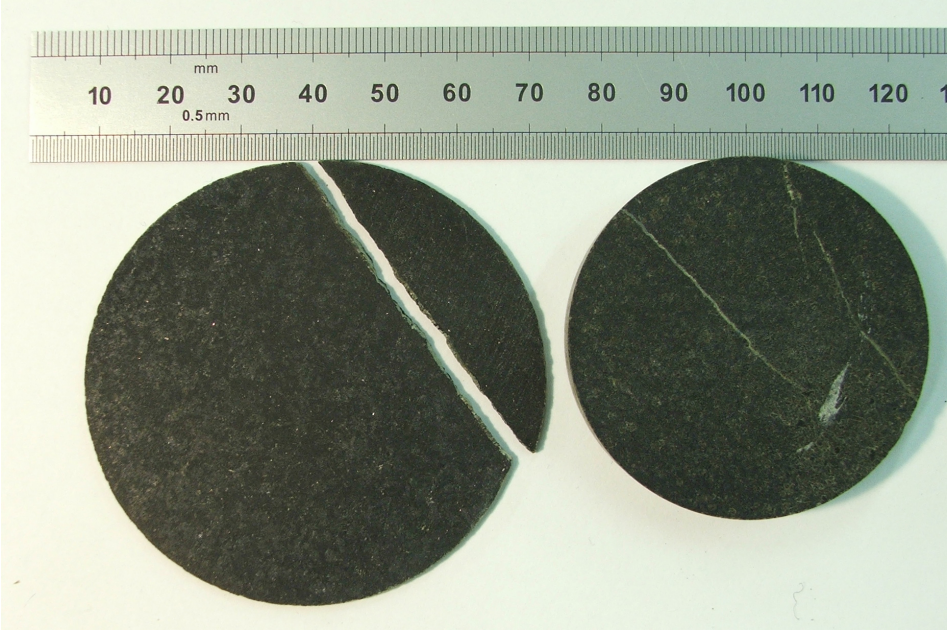

Figure 2.34: Basalt samples showing lines of white included material in the right hand sample. As there was no MLA scan of one of these lines it is impossible to give any indication of the mineral type. However it was noticed on handling that these white inclusions were points of weakness in the samples. A sample which has split along one such line during handling can be seen on the left of the figure.

2.4.9 Iron Ore

As with the basalt, the iron ore was obtained through Rio Tinto and came in cut samples rather than cores. The material is mainly goethite and haematite as can be seen in the MLA data in figure 2.35 (note that in this case the photo and the MLA data are not of the same side of the sample). The purpose of mining iron ore is to obtain iron for use in manufacturing and engineering. The ore in this case is significantly more dense than the other materials in this thesis, due to a high metal content. To the naked eye there appears a shine to the samples when polished (this can be seen in figure 2.36), suggesting iron is abundant, indeed the samples, in some cases look more akin to metal samples than rock. The other indication of the presence of iron is the large amount of rust present on samples left exposed to air for a period of time. While being the most dense of the materials available it is also somewhat porous with a large range of void sizes

(from sub mm to approximately 5 mm). This porosity is likely to have a large effect on dynamic properties. It is noticeable that the voids are not uniformly distributed either within a sample or between samples (where the differences can be quite marked). This is shown up in the large error present in the static measurements of both sound speed and density. Both the presence of rust and the large cracks/voids in the sample are very evident in figure 2.37.

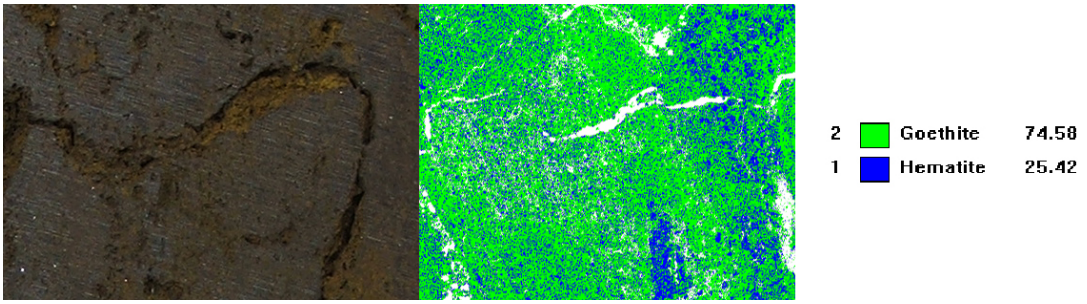

Figure 2.35: Iron ore MLA sample. As with the basalt sample in figure 2.33 the photograph on the left of the image is not the same as the MLA image in the middle. Again the images represent samples approximately 20 mm across. Cracks are visible in both images. The MLA scan reveals that there are two components to the iron ore, with the majority of the material being goethite.

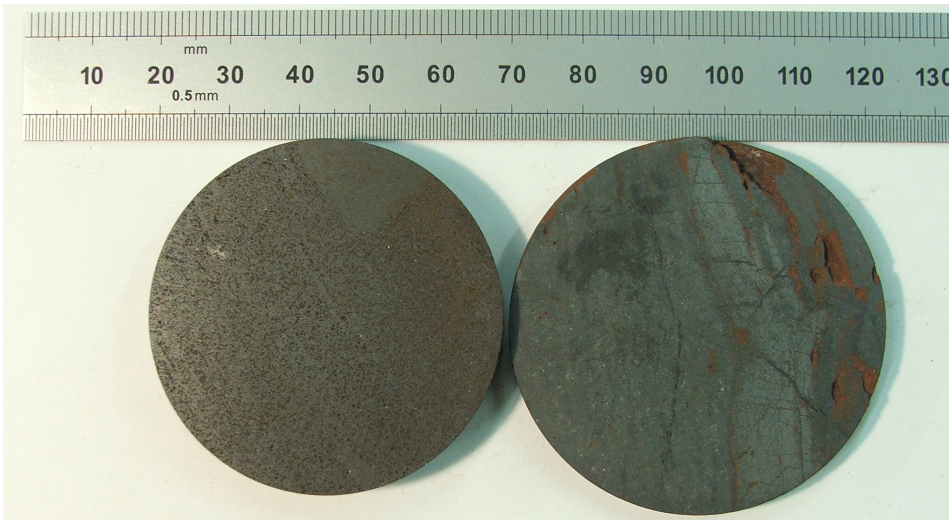

Figure 2.36: Iron ore samples showing a metallic appearance. In the sample on the left we can see a surface patterning that in fact is caused by the material having a significant amount of small scale porosity. This is largely absent from the sample on the right, which instead has a number of large voids.

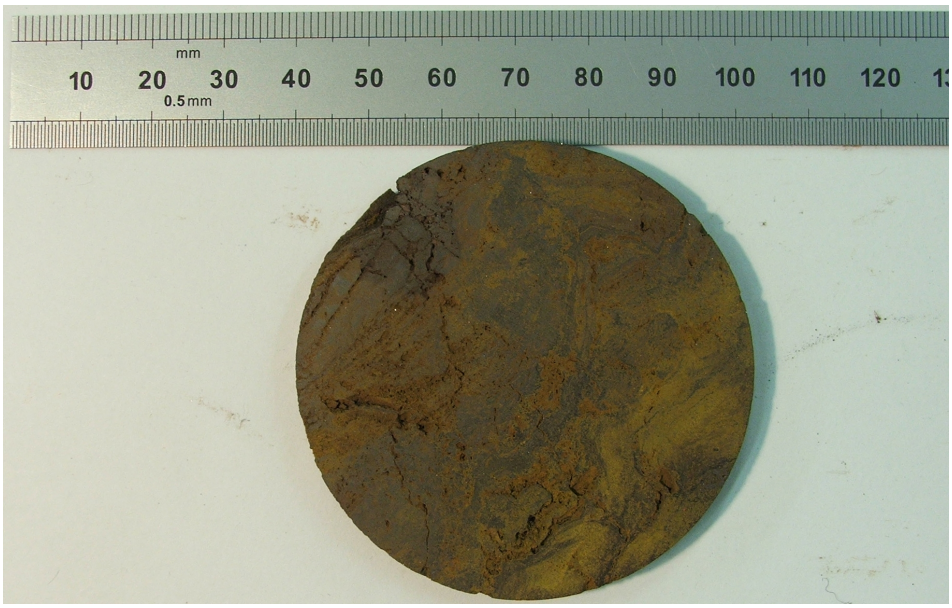

Figure 2.37: Iron ore sample showing rust and significant cracks/voids. These cracks made it difficult to ensure sample to sample consistency in experiments as they are not uniformly distributed between samples (this is clear when comparing the sample in this figure and those in figure 2.36.

2.5 Summary

- Numerous rock types have been provided for investigation.
- Various static properties have been measured including sound speeds and density.
- Further parameters have been calculated from the measured material properties.
- Mineral analysis has given an indication of the percentages of different minerals present.
- The kimberlite, siltstone, amphibolitic gneiss, amphibolite, biotite schist, quartz/feldspathic gneiss and basalt were all found to be hard non porous polycrystalline materials.
- The kimberlite and the quartz/feldspathic gneiss are fairly coarse grained materials, frequently containing grains of about 5 mm in size. The other materials have a much finer grain structure, though most contain random larger inclusions within the cores.
- Iron ore and sandstone samples show significant porosity.

References

[1] Austin, C.F., Cosner, L.N. and Pringle, J.K., "Shock Wave Attenuation in Elastic and Inelastic Rock Media", *Transactions of the Society of Mining Engineers*, (1966), 16–31

[2] Millett, J.C.F., Tsembelis, K. and Bourne, N.K., "Longitudinal and lateral stress measurements in shock-loaded gabbro and granite", *J. Appl. Phys.*, **87**, (2000), 3678–3682

[3] Tsembelis, K., Proud, W.G. and Field, J.E., "The principal Hugoniot and dynamic strength of dolerite under shock compression", in *Shock Compression*

of Condensed Matter - 2001, M. Furnish, N. Thadhani and Y. Horie, eds., American Institute of Physics, Melville, NY (2002), pp. 1385–1388

[4] Tsembelis, K., Proud, W.G. and Field, J.E., "The dynamic strength of cement paste under shock compression", in *Shock Compression of Condensed Matter - 2001*, M. Furnish, N. Thadhani and Y. Horie, eds., American Institute of Physics, Melville, NY (2002), pp. 1414–1417

[5] Willmott, G.R., *Shock Studies of Kimberlite, Diamond and Brittle Embedded Particles*, Phd, Cambridge (2004)

[6] Tonon, F. and Amadei, B., "Stresses in anisotropic rock masses: an engineering perspective building on geological knowledge", *International Journal of Rock Mechanics and Mining Sciences*, **40**, (2003), 1099–1120

[7] Asay, J.R. and Shahinpoor, M., *High-Pressure Shock Compression of Solids*, Springer-Verlag, New York (1993)

[8] Gu, Y., "Automated Scanning Electron Microscope Based Mineral Liberation Analysis - An Introduction to JKMRC/FEI Mineral Liberation Analyser", *Journal of Minerals and Materials Characterization and Engineering*, **2**, (2003), 33–41

[9] *Encyclopedia Britannica*

Chapter 3

Literature Review

3.1 Introduction

The process of mining with explosives is one where the properties of the geological materials encountered are of paramount importance. It is necessary to know these properties to understand the likely fracture, breakage and throw of the rock, in order to maximise yield, the convenience of handling the comminuted material, and minimise adverse safety implications. Whilst mining with explosives has been going on since the 1600's [1], interest in the measured, quantitative, properties of geological materials as a scientific endeavour is a much more recent phenomenon. This is true of both static and low strain rate experimentation at high pressure and especially with regards to high strain rate measurements.

The beginning of interest in measuring properties of geological materials at high pressure in a systematic way would appear to be in the 1920's. Adams and Williamson [2] note that, "Very little information has been available concerning the elastic properties of rocks and their constituent materials at high pressures". Naturally the aim of their paper is to address this lack of information, and the theme is continued by Adams, as well as other researchers [3–5]. The rationale given for conducting such research is that the information acquired is "Of use in connections with problems of geophysics , among which may be mentioned the tidal deformation of the earth, the elastic yielding of the crust due to loads such as mountain masses or ice sheets, the propagation of earthquake waves and the

effect of pressure on the stability of materials" [2]. It should be noted that these early papers, while dealing with high pressures, were either static or quasi-static in terms of the loading methods used.

It was not until after WW2 and the aftermath of the Manhattan Project that the shock response (that is to say the high strain rate loading) of materials was investigated thoroughly. The nuclear era, specifically the need for nuclear testing, meant that data pertaining to material response at high pressures and strain rates were suddenly of great import. Previously such experimental conditions had been unattainable by artificial means. This resulted in an entirely new branch of science (Shock Physics) and many different experimental techniques and diagnostics were developed by, and eventually outside of, military research projects. The initial research, reported by Walsh and Christian [6], used Hugoniots to describe the shock states of materials. This paper was followed by a review by Rice, McQueen and Walsh [7] which set down much of the theory behind the experimentation. Initially shock wave physics was closely tied to nuclear weapons programmes, and the results from early experiments reflect this, with works such as Marsh [8] (which although it was published as a collection in 1980, includes data from many earlier experiments conducted in support of nuclear testing programmes) reaching pressures of 400 GPa and more. In addition to weapons research, extreme high pressure studies are of use to those looking at extraterrestrial impact events and these have also been the subject of numerous papers [9–11].

Less research has been carried out at the lower pressures (below about 20 GPa) which are more applicable to mining applications. However, compression data are available, including some in Marsh [8] and others. Dynamic tensile data are widely found at low pressures owing to the ease with which rock fractures. This means failure can be achieved, in a spall configuration for example, at a much lower pressure than for a metal such as tantalum. Much data from the literature, if collated carefully, can be of use to the mining industry, particularly to people employed in modelling rock response to explosives. As Ahrens and Petersen [12] comment, "In general the shock wave research on various solid materials, including that on rocks and minerals, has been directed towards answering one

of the following questions. (i) How do the characteristics of the material affect the propagation of shock waves? (ii) What is the net effect of the passage of the shock wave disturbance on the material?" These questions are obviously ones that need answering in order to model the blasting process.

3.2 General Rock Properties

There are many factors that affect the mechanical properties of geological materials. The first topic to consider is the physical structure of the material at the scale of the grain structure. The minerals that make up the overall rock have a big part to play. If oriented randomly we can consider these minerals to create an isotropic situation, with the rock properties as a whole taking a value of approximately the average of the constituent mineral properties [13]. This averaging method could be considered best applied to for rocks made up of interlocking crystalline grains, such as granite, gneiss, and rhyodacite. For rocks which are composed of particles in a matrix, such as sandstone and kimberlite, there are other factors to be considered, including type of cementing and porosity. However, such an averaging process can only ever be a guide to the mechanical properties (it would obviously apply to measurements such as density for example). It has been noted however that the flat sections of magmatic type rock Hugoniots can possibly be attributed to this averaging process [14].

The averaging of material properties and the predicting of Hugoniot curves, as well as other material properties, has been set out in a number of papers. This is of limited use however for mining purposes, as research is concentrated at higher pressures, and after conversion to high pressure phases has occurred. At these higher pressures it is easier to form relations that will predict behaviour, and in addition the Hugoniot curves are much more concurrent than they are at lower pressures (the materials will behave hydrodynamically and material strength can be neglected). Good examples of papers looking at high pressure predictions include Trunin et al. [15] which looks at experimental results in the range 100-400 GPa and Telegin et al. [16] where the investigated u_p values are in the range 2-4 km s^{-1}. Note that in both of these cases the data are above the useful pressure

range for mining, and also well in excess of the pressures achievable in the Cambridge plate impact facility.

The random nature of rocks, as well as the wide range of different compositions of minerals that can be classified under a single name can lead to wide variations in properties [17]. It is certainly not the case that two granite samples from disparate geographical areas will behave in the same way. This implies a need to do detailed studies of any particular rock mass before one can say with absolute certainty what its properties under various conditions will be. However, for a predictive model of the mining process it is necessary to be able to deal successfully with any rock type that is encountered. In order to achieve this, some method of estimating relevant parameters is desirable, if not essential, as reliable high strain rate data are both time-consuming and expensive to obtain. Ideally, simple static or quasi-static tests could be used to categorise a rock, and then a series of formulae would relate these properties to high rate properties. To realise this goal of predicting high rate properties, it is advantageous to validate the formulae used as rigorously as is possible, over as wide a variety of rocks as can be realistically researched. The previous literature on the subject becomes invaluable at this point, allowing a breadth of knowledge that would be impractical to obtain from self-supported experimentation.

Due to the structure of rocks, the testing of geological materials has inherent problems when compared with, for example, the testing of metal samples. An example of this is that flaws can exist in the rock mass on much larger scales than that which can be sampled in the lab. Whether such size effects are of importance, would appear to depend somewhat on the nature of the experiment being performed. Pratt [18] brings up the issue of disagreement when pointing out that previous results for compressive strength measurements have suggested; a decrease in strength (or shear strength) with specimen size [19–23], an increase (though only for small specimen sizes) [22] or indeed no effect at all [24, 25]. One possible mechanism for explaining the results suggesting strength decrease is a strain energy reserve system. This is put forward rather than a Weibull effect (i.e. that the larger sample size would contain a greater number of larger flaws)

which would likely be the case in tensional rather than compressive failure. Pratt himself found that the maximum compressive strength supported dropped by a factor of 10 with increasing specimen size for some rocks (see fig 1). Brace [26], in his review, says that this strength decrease (in soft rocks) occurs at a length scale of about 1m, and at larger sizes the strength remains constant. This decrease cannot be put down to the variation in elastic modulus, which has much weaker size dependence. Further examples of size effects have been reported, including Lin and Heuze [27], who demonstrated a difference in excess of 200% in dynamic stiffness coefficients between laboratory and field measurements, and Mereu's investigation into attenuation of high amplitude waves [28].

The results reviewed above are static or low strain rate experiments. There is less data on size effects in shock compression, owing to the difficulties of doing accurate experiments on a very large scale. However Trunin [14] comments that laboratory tests and underground nuclear explosion testing produced coincident Hugoniots when they were compared. This result however should be treated with a little caution. Firstly it is possible that Trunin was lucky in not having any large flaws in the underground test rock mass, thus negating any size effect present. Secondly, it is possible that the extreme rates and pressures concerned negate the effect that such features might have. There may not have been sufficient time to activate and grow large flaws under these conditions. This second view is backed up by other evidence, for example the previously mentioned research on extremely high pressure Hugoniots [15, 16].

Another manifestation of size effects can be seen in the experimental scatter from various data sources. Willmott [29] comments that the Marsh [8] data for rocks have significantly greater scatter than the scatter for other more homogeneous materials also reported in the book. However, this scatter is much less that that seen in some static tests [30]. Setting aside for a moment possible strain rate effects, some of this reduction in scatter might be due to the size of sample that is able to be investigated, which may be smaller in the static tests than for the dynamic ones. In order to be representative of the rock, it is necessary for any sample to contain a sufficient number of grains. A similar situation can be

found when comparing the use of Hopkinson bars apparatus and plate impact equipment for investigating geological materials. The size of the apparatus, and therefore the size of sample that can be tested will affect the strain rates that can be achieved (in general smaller sample sizes allow for higher rates and pressure). If testing at a specific loading rate is required, then it is possible that smaller and less representative samples might have to be chosen, thus leading to more scatter. Whilst there must inevitably be a trade off, and the techniques can be made to work well [31], caution must be exercised.

As well as size effects relating to the size of samples tested and the size of the apparatus used for testing in relation to grain size it is important to consider whether the testing method itself introduces any further bias to the results. It is noted by Field and Pickles [32] for example, that a Hertzian indenter produces a stress field, the intensity of which falls off rapidly with depth. A brittle material with a distribution of flaws will only fail completely if the applied stress field creates a critical stress intensity at the flaw tip. A small stress field may be unable to apply a stress at the tip of a large flaw, especially if the flaw is larger than the stress field. If the flaws are all below the size of the stress field a Weibull distribution would be appropriate, however the smaller the stress field, the closer the measured value of stress is to the theoretical yield and fracture limits (as it is less and less dominated by the flaw distribution in the material). A similar situation occurs with stress or shock waves in that if the duration of the shock pulse is not sufficiently long to encompass the full length of a defect then the strength of the material will appear higher.

Machining, both in the laboratory and in the field, is another difficulty that has to be taken into account when considering the properties of geological materials. Evidence of this is given in Heuze [33] where damage to a pillar during cutting led to a large reduction in Rock Quality Designation values. Similar issues may well arise in smaller scale preparations for lab work, and it is certainly an area where care is required. Furthermore, techniques involving complicated sample geometries may be difficult or impossible to use due to fabrication issues that

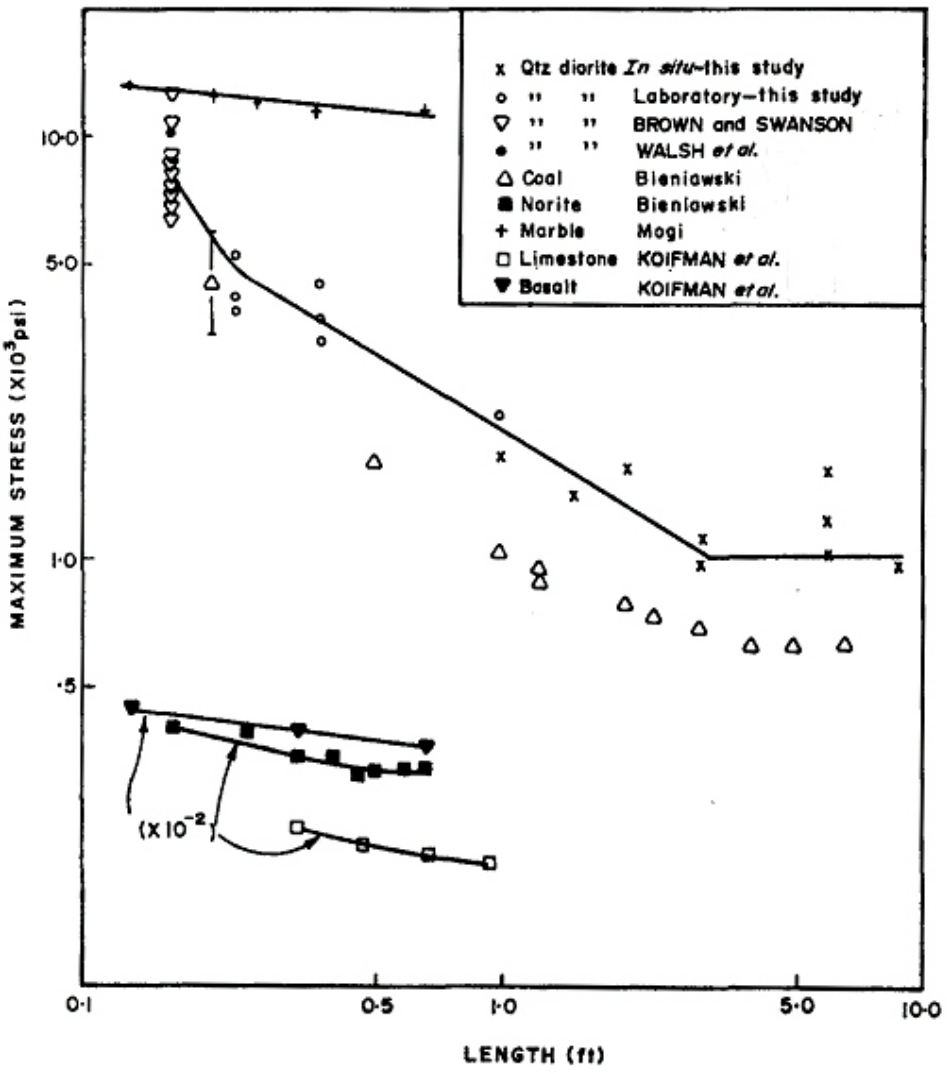

Figure 3.1: From Pratt [18] showing the size effects in rocks. Note that the Brown and Walsh papers do not attempt to show size effects and so are not referenced separately here. There is a stronger size dependence in the coal and the diorite than in the other materials. However is is also the case that these materials have been tested over a wider range of sizes. In general however there is a trend of decreasing strength with size.

simply do not arise with metals or polymers.

It is clear that there are a number of issues that have to be considered when applying the results of laboratory testing of geological materials to field situations. However, if care is taken to apply results in the regime tested rather than extrapolating merely for the sake of convenience, then laboratory testing can give extremely valuable data that would be otherwise unavailable.

3.3 Static Testing

Static testing is, in general, much more inexpensive and less time consuming than high rate dynamic tests. Coupled with the fact that the techniques are more established, this means that there are data available for a much wider variety of rocks at static rates. The most commonly measured static properties are sound speeds, density and various elastic constants, although data are available on hardness and other properties, for example Grabco et al [34].

As well as being *de rigueur* for categorisation of rocks for shock experiments, measurements of sound velocities have been the subject of much study in their own right, for example Birch [17, 35] and Christensen [36, 37]. In these works, as elsewhere, the density of samples is measured by a simple mass/volume method and the velocities by transit time of pulses from a transducer. With measurements of velocity, Birch comments that it is important to look at the first arrival when examining compression waves, to avoid inadvertent measurement of bulk sound speed, or bar sound speed. The measurements reported deal with the dependence of sound velocity on pressure up to 1 GPa and shows that for the majority of rocks there is an increase in sound velocity with pressure, both in terms of compressional waves [17, 35, 36] and also in shear [37]. Notable exceptions include marble and limestone, which show anomalous behaviour relating to calcite phase changes, as detailed by Wang [38]. Additional to experimental results, some modelling has been undertaken on elasticity in order to try and understand the processes behind various observations. Examples include using an integral method [39] and examining the pressure dependence in relation to the closing of pore space and

micro-cracks [40]. The low pressure (e.g. 10 Bar) values of sound speeds however, especially in Birch [35], are very similar, where direct comparison is possible, to the P = 0 values quoted in McQueen [41]. Another important result of these papers is that there is significant anisotropy in the sound speeds of various rocks including certain limestones and also a number of metamorphic rocks [36, 37]. Similar anisotropy is shown in Woeber et al [42]. The impact of such anisotropy on shock experiments however does not appear to have been significantly studied.

The static test data from the literature strongly suggest that one of the main characteristics of a geological material that determines mechanical properties is the density. As many rocks are made of similar minerals, often the density is very closely related to the porosity. The porosity can strongly influence whether a rock will behave elastically or merely compact when subjected to a compressive stress, either static or dynamic. Walsh and Brace [43] note that for low porosity rocks even very high pressure deformation is recoverable. Similar to the porosity argument, it can also be demonstrated that crystal vacancies have a significant effect on compressibility [44]. A further issue of note with respect to porous materials is that the presence of water in crack tips can, with the action of stress cause the elongation of defects.

3.4 Fracture and Fragmentation

The process of fracture and fragmentation in rock is one that is fraught with difficulties when it comes to predicting behaviour. Equations for failure such as the Griffith criterion rely on the size of initial flaws present in the material for predicting failure. For some homogeneous materials we can make a reasonable estimate of these parameters, but in the case of rocks it can be difficult to determine what microstructural features to associate with these initial flaws. Hatzor and Palchik [45, 46] carried out a study of dolomites and the effects that grain size and porosity had on the fracture initiation stress. While it might be expected in a polycrystalline material that the grain size would be a good indicator of the initial flaw size it was found that this was in fact two or three orders of magnitude too low. Such a result can be explained when the porosity of the rock is taken

into effect. With a porous rock the vacant areas act as initial flaws of much larger dimensions than the crystal grains. It can be shown therefore that in rocks of low porosity the fracture initiation stress is much more sensitive to the grain size than for rocks with a high porosity.

The amalgamation of a number of factors affect the fracture initiation stress and it has been shown that the stress is proportional to the elastic modulus, the grain size and the porosity of the rock. The traditional assumption that the grain size will determine fracture initiation is only valid in a low porosity, low grain size material. Hatzor and Palchik go on to develop a microstructure based failure criterion for dolomites [46].

3.5 Quasi-Static and Intermediate Strain Rates

There are a number of ways in which the dynamic strength of a geological material can be measured, encompassing a wide range of apparatus, loading geometries and strain rates. Many of these are detailed in a comprehensive review by Field et al. [47]. If tensile properties are required for example, it is possible to cause fracture by using the impact of a pendulum on a sample [48]! This is not a very common method however, with the preferred methods of generating tensile failure being the split Hopkinson Bar apparatus, the Brazilian Test and three point flexural bending.

The split Hopkinson Bar apparatus can be used in combination with the effects of spalling to determine the dynamic tensile strength of the specimen as described by Cho et al. [49]. The apparatus usually consists of a striker bar which is propelled (either by compressed gas or explosive charges) into an incident bar. The specimen is then sandwiched between this incident bar and the output bar. In the set up used by Cho et al., however, the specimen and the output bar are replaced with a long cylindrical sample. As the compression wave reflects from the far end of the sample, it creates a rarefaction. This travels back down the bar causing an increase in tension, leading ultimately to the failure of the material if this tensile stress is high enough. Gauges are used to determine the stress in the

system. It is from this that we can discern the dynamic tensile strength. With Hopkinson Bars it is possible to achieve a range of strain rates, typically up to 10^3 s^{-1}. With miniaturised Hopkinson bars even greater rates are obtainable, as high as 10^5 s^{-1} (though the extent to which the sample is representative of the whole then becomes an issue). It is also possible to achieve the same spalling effect by having a sample that has been initially compressed on all three axes and then releasing the ends rapidly [50]. This then leads to a situation of tension in the centre of the specimen.

The Brazilian Test was developed as a static test for concrete strength, but can now be applied in a dynamic set up with a variety of loading rates [51], typically 10^{-1} - 10^3 MPa s^{-1}. The Brazilian Test involves compressing a circular disc between two contact areas across a diameter of the circle. As the circle is squeezed, the sample is forced outwards perpendicular to the force acting on it and ultimately causing a tensile failure in the centre of the specimen. It is possible to embed a strain gauge in the specimen to allow for the recording of *in situ* measurements. There are also optical techniques that can be employed to determine strain and displacement maps. These might include speckle metrology and the fine grid method. It is also possible for the test to be carried out using a modified Hopkinson bar apparatus and a circular notched specimen [52].

Three point flexural bending is a very simple test which can either be performed statically or dynamically. A maximum rate of 104 MPa s^{-1} was achieved using the three point flexural method by Zhao and Li [51]. It should be noted that while the trend of increasing tensile strength with loading rate was observed to be the same for both the Brazilian and Three Point tests, the flexural method gives values for tensile strength of approximately two and a half times that measured using the Brazilian set up. It is not made explicitly clear from the literature why the three point test gives higher values but it is likely that it is due to the volumes of material under tensile stress being different. A differing volume of material under stress would possibly have an effect on the size of flaws sampled in the experiment in the same way as for a Hertzian indenter.

For compressional strength tests there are a number of methods available to an experimenter. Examples of these include drop weights, Hopkinson Bars and plate impact (for shock work). This gives a range of strain rates from 10^2 s^{-1} - 10^8 s^{-1}. It is noticeable that there appears to be less available data for intermediate rate compression of geological materials. However, Shan et al. [53] give a good description of the use of the Split Hopkinson bar to determine a full stress-strain relationship (including post failure characteristics) for granite and marble. Other methods have been utilised to find full stress-strain relationships, including piston loading [54] and also tensional loading [55]. The latter data was modelled successfully by Zhou [56] using a model based on the deformation of the undamaged matrix and the interactions of microcracks within the material.

3.6 Shock Compression

High strain rate and shock compression results are the most useful data from the point of view of modelling the mining situation. For dynamic compressive strength under shock conditions, the Hugoniot is one of the most important properties of a material. It givess the locus of all states that can be reached by a single shock loading of a particular material. The Hugoniot is described by two of the following parameters; stress (σ), density (ρ), volume (V), particle velocity (u_p) and shock velocity (U_s) . It is possible to determine the Hugoniot in a number of ways therefore, as there are a number of parameters that can be measured. In addition to direct measurements made within a material it is possible to use conservation equations [6] and materials of known properties to indirectly infer the values of the other parameters. Numerous methods exist for the measurements of the various parameters.

Data from Los Alamos, including Marsh [8] and McQueen [41] were obtained using a method of measuring shock speed in both the material of interest and the "reference" material with either a smear camera or shorting pins. Using the shock equation of state (equation 3.1) particle velocity in the reference material (chosen such that equation 3.1 has well defined values of C_0 and s for the material) was calculated and then the particle velocity in the material of interest

is found by impedance matching. Note that the shock equation of state, as a first order polynomial, is empirically observed to hold for many materials, but in some materials further orders in the polynomial are required. C_0 and s are fitted parameters, but are related to physical properties; C_0 can be approximated as the bulk sound speed and it can be shown [57] that the constant s is related to the first pressure differential of the zero pressure bulk modulus.

$$U_s = C_0 + su_p. \tag{3.1}$$

Other parameters are then derived using the Rankine-Hugoniot equations [6]. Other methods of determining Hugoniot properties include velocity interferometry (VISAR) (e.g. [58, 59]), which gives a measure of particle velocity, and manganin stress gauges (e.g. [60]). Whilst each, in the end, should lead to the same Hugoniot curve, it is important to realise that each of the methods have advantages and disadvantages depending on precisely the information that is required and the material involved. VISAR has excellent time resolution, but monitors only the material surface, giving no "in-material" data. In addition, with a traditional VISAR system, only particle velocity is measured, although with newer multi-point systems [61] and stepped targets it is possible to measure shock velocity by a time of arrival method. Manganin gauges offer in material results, and with the use of more than one gauge per sample the opportunity to measure shock velocity simultaneously. In addition, the cost of gauges is significantly less than that of a VISAR system, although the later requires little other than the initial outlay. However it has been demonstrated that for certain geological materials the noise associated with gauge traces is sufficient to warrant using a reverse impact configuration and VISAR to obtain more reliable results [62, 63]. There is further discussion of this issue in chapter 6 regarding whether the source of the noise is straining of the gauge element or electromagnetic emissions [64] from the sample. Quartz for example, which is a component of many rock types, is a piezo-electric material.

While there are much more data corresponding to very high pressures, there are a number of studies, or parts of studies that are useful for looking at pressures

associated with mining. These include: McQueen [41], Boslough and Ahrens [65], Shang, Shen and Zhao [51] (Bukit Timah granite), Takazawa et al. [66] (jadeite), Nakazawa et al. [67] (basalt) and Tsembelis et al. [60] (dolerite). There are also examples of cement paste and concrete studies, which have some similarities with naturally occurring geological materials. Examples of these studies are those carried out by Tsembelis et al. [68, 69].

One of the key points that is brought out by the literature is that there is often significant scatter on the measurements that are taken. Experimental uncertainty, amongst other factors, can lead to the "blurring" of such key features as the Hugoniot Elastic Limit (HEL) [60], though this (specifically the blurring of the HEL) can be attributed to other issues, such as the shock impedance and elastic impedance of the material being studied. If the two impedances are similar then it leads to a change in slope at the HEL that is only slight and can therefore be difficult to determine. Scatter is somewhat unavoidable due to the inhomogeneity of the samples. Most studies, for example Shang [70], carry out up to 10-15 experiments to build up a better picture of the Hugoniot.

Another important aspect of the literature is that in places there is a lack of available data. Certain rock types are tested more often than others, with the trend being driven by the aim of the research (e.g. oil shale), or the types of materials that are readily available. An example of this is in Tsembelis et al. [60] where it is mentioned that no previous results are available and the only comparison that can be made is with analogous igneous materials. A further complication comes from papers that do not publish a description (or mineral breakdown) of the rocks that were studied. An example is Millett et al. [71] where only a grain size is given. This makes effective comparison between different papers even harder and hinders any attempt to categorise or predict shock properties by mineral content. Additionally, due to the cost of testing it is often not possible to undertake repeat measurements, making it difficult to determine whether particular features in the data are indeed significant.

It is possible, despite not all possible rock types being tested, to draw some general conclusions about the Hugoniot properties of geological materials:

Low density rocks below approximately 2.5 g cm^{-3}, such as tuff [8], TKB [72] and sandstone [73], have behaviour dominated by their porosity. Porous materials generally have a downwards sloping Hugoniot (in $U_s - u_p$ space) in the region where pore crushing is occurring, but above this pressure relationship is often linear, an example is shown in figure 3.2 although the initial curved section is indistinguishable due to a lack of data in that stress regime. There are other complications such as the effects of phase changes, which are particularly common (at low pressures) in calcite rocks such as limestone [59]. Furnish comments that below 4 GPa in saturated limestone strength effects dominate behaviour. The effect of porosity is limited by the filling of pores with water.

At intermediate densities, approximately 2.5-3.0 g cm^{-3}, it is common to find a very weak relationship between shock speed and particle velocity [60, 71], and indeed to within experimental error and statistical scatter shock velocity remains initially constant with respect to increasing particle velocity (or pressure). For magmatic rocks, it is suggested [14] that the initial part of the Hugoniots of such rocks is governed by averaging of mineral grain properties, while steeper sections at higher pressures correspond to the Hugoniots of the constituent minerals. An example of this type of Hugoniot is given in figure 3.3.

At high densities, above 3 g cm^{-3}, rocks such as dunite [41], bronzitite [41] and jadeite [66] for example exhibit behaviour that is much more akin to the Hugoniots of their constituent minerals. These minerals often have fairly strong linear relationships between shock velocity and particle velocity. At higher pressures than are really applicable for mining, the effects of phase changes are seen as changes in slopes of the Hugoniots. An example of a high density rock, Dunite (density 3.31 g cm^{-3}), is shown in figure 3.4, along with the Hugoniot of single crystal periclase (MgO, density 3.58 g cm^{-3}) [73]. The dunite is 57.1 mole per cent MgO and 34.9% SiO_2 [41], the SiO_2 probably accounting for the dunite

Hugoniot lying below that of periclase, as it has a lower density.

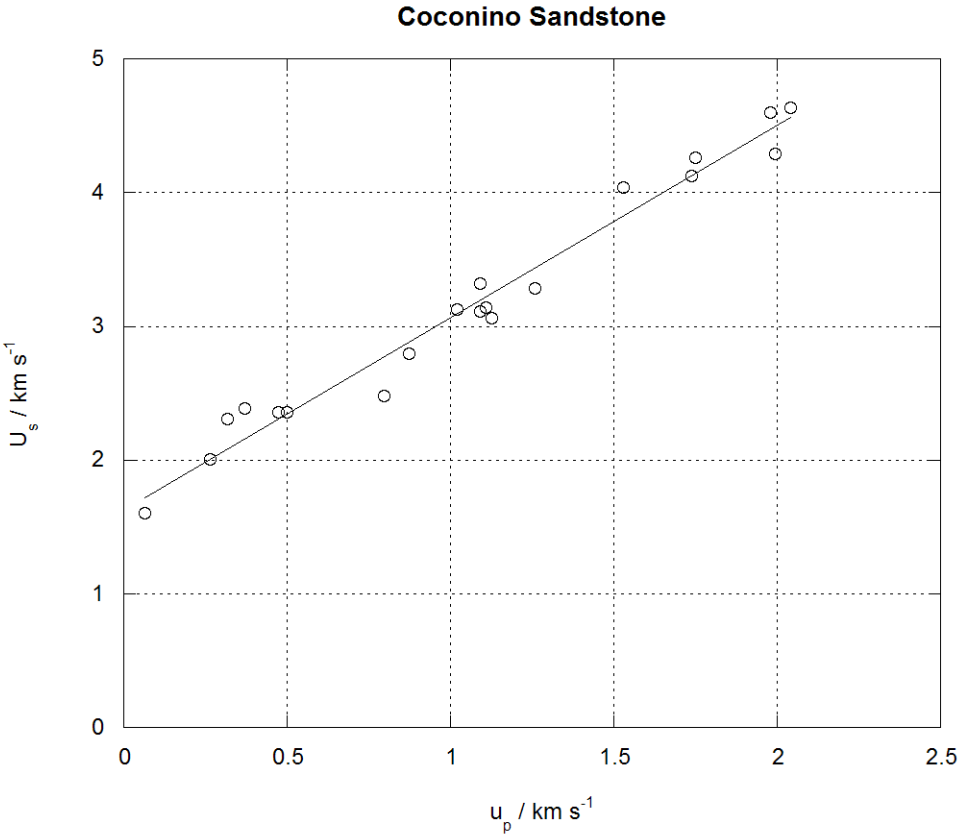

Figure 3.2: Hugoniot for Coconino Sandstone from van Thiel [73]. The overall trend in the material is one of a linear relationship in $U_s - u_p$ space. Any potential low pressure deviations from this are difficult to discern owing to a lack of data in the low stress regime, and additionally, significant scatter in the experimental results.

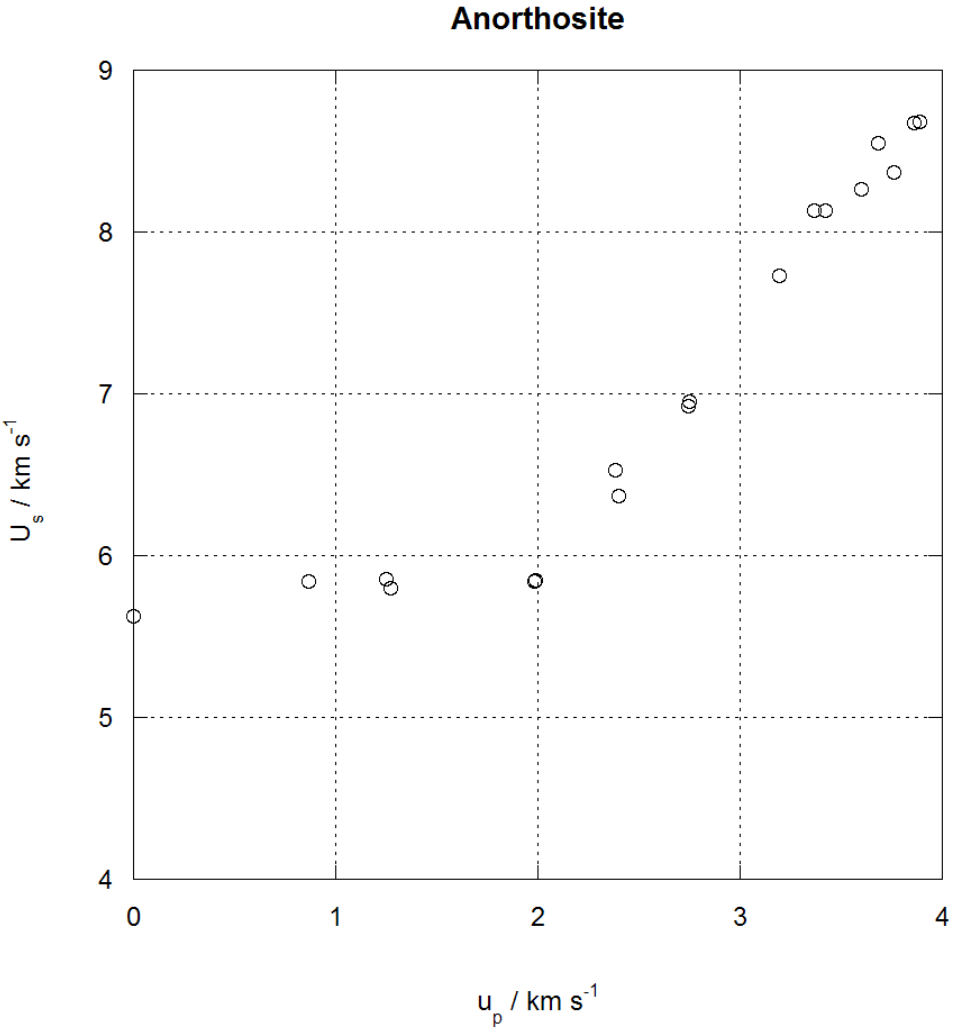

Figure 3.3: Hugoniot for Anorthosite from McQueen et al. [41]. There is an initial section where as the particle velocity increases, the shock velocity remains relatively constant. At a particle velocity of about 2 km s^{-}1 the behaviour changes to a relationship of linearly increasing shock velocity with particle velocity.

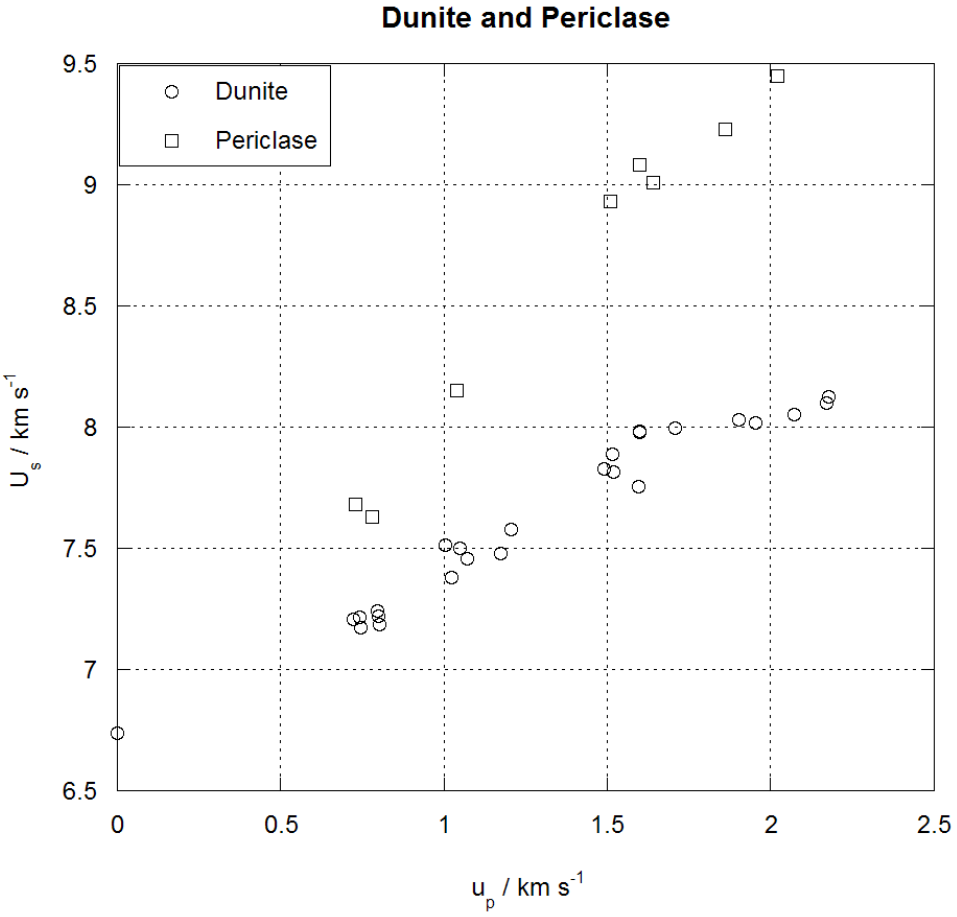

Figure 3.4: Dunite [41] and periclase [73] Hugoniots. Although the datasets are lacking somewhat in low pressure data, there is a trend of linearly increasing shock velocity with particle velocity. It is possible that at values of particle velocity lower than those measured there is an initial flat section, however bearing in mind that the flat section in figure 3.3 extends to 2 km s^{-}1, this seems unlikely.

3.7 Release Behaviour

Loading behaviour in rocks is only the first part of the response to a shock pulse. A rock loaded to high pressure by a pulse will then release this pressure in some way. This is a consequence of the finite nature of the loading pulse. Note that in the experimental section of this thesis measurements are made on well defined one dimensional, longitudinal releases from either the rear of the target or the rear of the flier (one should not forget the existence of lateral releases). Different rock types will respond to releases in different ways depending on the minerals involved and the pressures reached. Sekine et al. [74] looked at high pressure release in granite and discuss the existence of a metastable high pressure phase that quenches to a diaplectic glass at about 10 GPa. Of more use to mining is a study by Petersen et al [75] looking at alluvium, novaculite and tonalite at pressures up to 5 GPa. The alluvium was a low density (1.8 g cm^{-3} and porosity 30%) pressed powder and therefore irreversibly compacted under compression. As the density of the sample upon release is greater than the initial density, velocities of the rarefaction waves were found to be (initially) twice the shock velocity. Petersen notes that this means that in the field they would cause rapid attenuation of the shock wave. A similar, although less pronounced effect was seen in the tonalite, again showing that at a density of 2.56 g cm^{-3} and porosity of 6.6% the porosity is the dominant factor in determining material properties. Even at low pressures there is irreversible compaction occurring, and the rock essentially demonstrates no elastic behaviour. Novaculite, in contrast to the other materials in the study has essentially zero porosity (and a higher density 2.63 g cm^{-3}), and if shocked to below its elastic limit (given as 9.7 GPa in [76]) releases essentially along the same path as the Hugoniot. This behaviour is typical of materials behaving in an elastic manner.

Other studies show results that agree with the conclusions of Petersen. The limestone tested by Furnish [59] demonstrates hysteretic releases that are attributed to a combination of strength effects and phase transitions. Further work by Furnish [77, 78] on tuff, rhyolite and quartzite, amongst others, lend further weight. It is noted in the case of Pennsylvania slate that the hysteretic behaviour of the

releases below 30 GPa returns to normal release behaviour about 60 GPa, something which is described as typical between 40 and 60 GPa in rocks. A final important note is made by Jeanloz and Ahrens [79], regarding approximating releases. If we assume that the release is an approximately isentropic process, then we can estimate it by the reverse (reflected horizontally about the shock state) of the Hugoniot. It shown that this is a valid approximation for shocked, non-porous, geological materials (oxides and silicates).

3.8 The Hugoniot Elastic Limit

The concept of an elastic limit, or looking at it the other way around, the onset of non-elastic behaviour, is an important material property for mining and other applications. To give an example of the importance that such a property would have in a mining situation it is worth considering that materials shocked below their elastic limit are undamaged on loading, in so much as the release is essentially elastic. Damaged rock, through the action of a previous shock wave (for example from explosions in adjacent boreholes) is demonstrated by He and Ahrens to be approximately a factor of two weaker, when considering static failure strength [80].

The concept of the Hugoniot Elastic Limit (HEL) was initially one developed for metals, as with the majority of shock physics. In metals, the idea of plastic deformation, with dislocation movement, flow, strain hardening and so on gives a strong meaning to the HEL, and the HEL is often easily discernable in both gauge records (as two wave structure) and in slope changes on the Hugoniots. This is often much less clear in geological materials, where fracture and cracking is likely to be significantly more important than flow and dislocations. However many examples of HEL values are quoted in the literature, and are arrived at by various means.

One common way of determining a HEL value is to look at the amplitudes of elastic precursor waves in diagnostic records. Examples of this method include Ahrens and Gregson [76], (who quote HEL values of 4-9 GPa in quartzite and

novaculite, 4-5 GPa in plagioclase rocks, 1.5-2.5 GPa in calcite and marble and approximately 0.5 GPa for limestone and sandstone) and Takazawa et al. [66] (who quote 6 GPa for jadeite). It should be noted that Ahrens [76, 81] demonstrates a reduction in amplitude of elastic waves (HEL) with propagation distance of about 0.33 GPa mm^{-1}. This is mainly attributed to intrinsic attenuation in a stress-relaxing elastoplastic material.

Many researchers do not see two wave structure in their diagnostics and find the HEL by other means. Nakazawa et al. [67] interpret a change in slope in the Hugoniot at 5 GPa as corresponding to the HEL in basalt. If neither two wave structure or a change in slope is seen in the data, some researchers have used measurements of shear strength to determine deviation from elastic behaviour and infer an HEL. A change in slope for example might not be seen due to similarities in the elastic and shock impedances of the material, as suggested by Millet and Tsembelis [60, 71].

The shear strength of a material can be, and most usually is, determined by looking at the longitudinal and lateral stresses. The relation (equation 3.2 as quoted in Millet et al. [71] is:

$$2\tau = \sigma_x - \sigma_y, \tag{3.2}$$

where τ is the shear strength and σ_x and σ_y are the longitudinal and lateral stresses respectively (σ_x and σ_y can be measured in plate impact experiments, using lateral and longitudinal stress gauges). Tsembelis et al. [60] estimate the HEL of Dolerite to be 4.3 GPa using this method and TKB has an estimated HEL of 0.9 GPa according to Willmott [72, 82]. It is commented [60] that the method of using longitudinal and lateral stress gauges to calculate shear stress is superior to previous methods, which required calculation of the hydrostat of the material.

There are some caveats relating to this method however. These revolve around a potential problem with the current calibration of certain types of lateral gauges.

This has been the subject of a number of recent papers, for example Rosenberg et al. [83]. Whilst the method of using lateral gauges has not been invalidated per se, the absolute values of some of the results may require slight alteration when a completely robust calibration has been found.

The fact that HEL's have been calculated via the use of a number of different methods depending on available data is both a blessing and a curse. While it does mean that multiple methods exist and therefore finding an HEL value should always be possible, it also means that it is not possible to make a direct comparison across all data. There appears to be no direct evidence that the HEL's found using the different methods agree, and indeed, for example the 9 GPa quoted by Ahrens [76] seems somewhat higher than HEL's reported for what might seem similar rocks using the shear strength method.

3.9 Dynamic Tensile Strength

Much of the fracture and fragmentation of the rock mass which takes place in mine blasting is a dynamic process. In the mining situation, the borehole has a radial geometry, and the mode of radial fracturing is described by Field and Ladegaard-Pederson [84]. This situation is at least a two dimensional problem, but more likely three dimensional. In the laboratory testing of geological materials however it is much more common to use a plate impact facility to achieve the high strain rates required in a spall configuration. Examples of the methods can be found in Grady and Hollenbach [85] and Ai and Ahrens [86]. A good description of the theory behind the methods, and of data analysis from both VISAR and gauge records can be found in Grady and Kipp [87]. It should be noted when using such data in a model, that the plate impact environment is designed to be one dimensional.

The spall process depends on overlapping release waves creating an area in the rock which is under tension. This will then fail in a tensile manner if the additive magnitude of the releases exceeds the tensional strength of the material. For homogeneous materials, this process is a very reproducible one and therefore metals

will often have a well-defined spall strength (although quite possibly a strain rate dependent one). In an inhomogeneous material however, by definition, different grains and minerals in the case of rocks will have different properties. In order to initiate spall, it is not necessary that the "bulk" tensional strength is exceeded (if indeed such a concept is a helpful one for geological materials) merely that local tensional strength is exceeded. In terms of percentage therefore, this means that spall experiments tend to have a greater statistical scatter of results than other dynamic strength measurements. More experiments are needed to get a reliable statistical average for spall strength. A good example of this is seen in the different values reported for the spall strengths for Solenhofen limestone in two different papers by Grady [85, 88]. In 1979 [85], the value is reported as 53 MPa. This however was on the basis of one experiment. In 2000 [88], after further experimentation this value was revised to the significantly higher value of 77 MPa.

In terms of variation of spall strengths between rock types, there are, as with other mechanical properties, significant differences. Grady and Hollenbach [85] have values as low as 10 MPa for sandstone and as high as 130 MPa for basalt. Ai and Ahrens [86] have a range of 22 MPa (sandstone) to 150 MPa (gabbro). There is no strong correlation in the data between static data such as density and the measured spall strength. It is possible however that a relation between HEL and spall strength could be found, analogous to the one that exists for other brittle materials [89].

3.10 Strain Rate Effects

As with many other materials, rocks do not respond the same way to impulses at different rates, that is to say that they exhibit strain rate dependence. This strain rate dependence does not occur completely uniformly however and would appear from the literature to depend on absolute strain rate, and also possibly on loading geometry. Blanton [90] notes that there is no significant strain rate dependence at low rates in triaxial bend tests. Chong and Boresi [91], again at low rates find that while there is little rate dependence of Poisson's ratio, Young's modulus is strongly rate dependent. Grady et al, demonstrate a factor of 10 increase in

yield strength of dolomite dynamically compared with statically. A factor of 4 increase in longitudinal modulus is found for clay shale by Bless and Ahrens [92]. Interestingly Brace and Jones [26] indicate that strain rate dependence is also dependent on rock type, with granite having concurrent stress-strain curves in static and dynamic tests, and tonalite showing significant differences.

It also should be noted that the dynamic and static tensile strengths are, in general, not the same. It has been shown in some studies that the dynamic strength can be as much as four times [48] as high as the equivalent static strength. Other studies have put the figure as high as ten times [93]. Even at low strain rates there is a measurable rate dependence, as shown by Goldsmith et al. [94]. Cho et al. set out reasoning for the increase in dynamic tensile strength at higher strain rates. They argue that the increasing strain rate increases the number of microcracks formed in the material. This leads to releasing of stress from nearby microcracks and therefore interferes with the formation of a fracture plane. This therefore gives us a higher dynamic tensile strength.

3.11 Concrete

Concrete is a man-made material consisting of a matrix of cement, sand and water, binding together aggregates composed of various geological materials. Due to extensive use as a building material much research has been carried out into properties of concrete and its constituent parts. This body of work includes, for example shock and release properties [68, 69, 95–97], HEL [98], shear [99, 100] and spall [99, 101]. It is concluded that much of the behaviour of concrete is determined by the matrix properties, and is therefore more often than not dominated by the porosity that is introduced during the manufacturing process.

Given the fact that it is possible to control the properties of concrete, it would be a natural choice as a simulant for geological materials. However this is only likely to be the case in a certain subset of cases where the behaviour of the natural material is also likely to be dominated by porosity. In the case of the majority of the materials in the present thesis, porosity is not an issue, as the materials are

hard, non-porous materials made up of interlocking mineral crystal grains. For a study into lower density materials it would almost certainly be advantageous to use concrete as a well characterised natural analogue.

3.12 Summary

- Accurate measurement of material properties is important in a mining context.
- Although data on geological materials are available, the dataset would benefit from further experimental investigations.
- Rocks are complex polycrystalline materials where the response is often further complicated by manifestations of other physical characteristics such as porosity.
- The non uniformity of geological materials and especially sample to sample variation means that a statistical approach must be taken.
- A number of size and sampling effects must be considered when interpreting results.
- Data exist across a range of strain rates, from static to shock studies.
- Shock compression data indicate three broad types of response; porosity dominated compression, polycrystalline rock compression and high density, mineral dominated rock compression.
- At low levels in non porous materials, the release demonstrates elastic behaviour, however this is not the case at higher pressures, where there might be significant hysteresis.
- While HEL data are available they are not particularly consistent and multiple methods are used to obtain data.
- Dynamic tensile strength is difficult to measure accurately and shows significant sample to sample variation.

References

[1] Eloranta, J., "An Explosion in Mining", *61st Annual Mining Symposium*

[2] Adams, L.H. and Williamson, E.D, "On the Compressibility of Minerals and Rocks at High Pressure", *Journal of the Franklin Institute*, **195**, (1923), 474–529

[3] Adams, L.H. and Gibson, R.E., "The Compressibilities of Dunite and of Bassalt Glass and their Bearing on the Composition of the Earth", *Proceedings of the National Academy of Sciences*, **12**, (1926), 275–283

[4] Zisman, W.A., "Comparison of the Statically and Seismologically Determined Elastic Constants of Rocks", *Proceedings of the National Academy of Sciences*, **19**, (1933), 680–686

[5] Ide, J.M., "Comparison of Statically and Dynamically Determined Young's Modulus of Rocks", *Proceedings of the National Academy of Sciences*, **22**, (1936), 81–91

[6] Walsh, J.M. and Christian, R.H., "Equation of state of metals from shock wave measurements", *Phys. Rev.*, **97**, (1955), 1544–1556

[7] Rice, M.H., McQueen, R.G. and Walsh, J.M., "Compression of solids by strong shock waves", *Solid State Physics*, **6**, (1958), 1–63

[8] Marsh, S.P., *LASL Shock Hugoniot Data*, University of California Press, Berkeley, California (1980)

[9] Ahrens, T.J. and O'Keefe, J.D., "Equations of state and impact-induced shock-wave attenuations on the Moon", in *Impact and Explosion Cratering*, D. Roddy, R. Pepin and R. Merrill, eds., Pergamon, Oxford (1977), pp. 639–656

[10] Silver, L.T. and Schultz, P., "Geological Implications of Impacts of Large Asteroids and Comets on the Earth", *The Geological Society of America*

[11] Sharpton, V.L and Ward, P.D., "Global Catastrophes in Earth History; An Interdisciplinary Conference of Impacts, Volcanism and Mass Mortality", *The Geological Society of America*

[12] Ahrens, T.J. and Petersen, C.F., "Shock wave data and the study of the earth", in *The Application of Modern Physics to the Earth and Planetary Interiors*, S. Runcorn, ed., Wiley-Interscience, London (1969), pp. 449–461

[13] *Encyclopedia Britannica*

[14] Trunin, R.F., *Shock Compression of Condensed Materials*, Cambridge University Press, Cambridge (1998)

[15] Trunin, R.F., Simakov, G.V., Dudoladov, I.P., Telegin, G.S. and Trusov, I.P., "Rock compressibility in shock waves", *Phys. Solid Earth*, **24**, (1988), 38–42

[16] Telegin, G.S., Antoshev, V.G., Bugaeva, V.A., Simakov, G.V. and Trunin, R.F., "Calculated determination of Hugoniot curves of rocks and minerals", *Phys. Solid Earth*, **16**, (1980), 319–324

[17] Birch, F., "The velocity of compressional waves in rocks to 10 kilobars. Part 2", *J. Geophys. Res.*, **66**, (1961), 2199–2224

[18] Pratt, H.R., Black, A.D., Brown, W.S. and Brace, W.F., "The effect of specimen size on the mechanical properties of unjointed Diorite", *Int. J. Rock Mech. Min. Sci.*, **9**, (1972), 513–529

[19] Bieniawski, Z.T., "The effect of specimen size on compressive strength of coal", *Int. J. Rock Mech. Min. Sci.*, **5**, (1968), 325–335

[20] Mogi, K., "The influence of the dimensions of specimens on the fracture strength of rocks: Comparison between the strength of rock specimens and that of the Earth's crust", *Bull. Earthquake Res. Inst.*, **40**, (1962), 175–185

[21] Koifman, M.I., "The Size Factor in Rock-Pressure investigations", in *Mechanical Properties of Rocks* (1969), pp. 109–117

[22] Koifman, M.I. and al, et, "Investigation of the Effect of Specimen Dimensions and Anisotropy on the Strength of some Coals in Donets and Kuznetsk Basins", in *Mechanical Properties of Rocks* (1969), pp. 118–129

[23] Il'nitskaya, E.I., "Effect of Rock Specimen Size on Mechanical Properties in Shear Tests", in *Mechanical Properties of Rocks* (1969), pp. 57–63

[24] Hodgson, K. and Cook, N.G.W., "The Effects of Size and Stress Gradient on the Strength of Rock", *Proceedings of the Second Congress of the International Society of Rock Mechanics*, **2**, (1970), Paper 3–5

[25] Obert, L., Winder, S.L. and Dervall, W.I., "Standardised Tests for Determining the Physical Properties of Mine Rock", Technical Report 3891, U.S. Bureau of Mines Report of Investigation (1946)

[26] Brace, W.F., "The Effect of Size on Mechanical Properties of Rock", *Geophysical Research Letters*, **8**, (1981), 651–652

[27] Lin, W. and Heuze, F.E, "Comparison of in Situ Dynamic Moduli and Laboratory Moduli of Mesaverde Rocks", *International Journal of Rock Mechanics and Mining Sciences and Geomechanical Abstracts*, **24**, (1987), 257–263

[28] Mereu, R.F., "The attenuation of high-amplitude waves in rocks", *Canad. J. Phys.*, **42**, (1964), 526–534

[29] Willmott, G.R., *Shock Studies of Kimberlite, Diamond and Brittle Embedded Particles*, Phd, Cambridge (2004)

[30] Guest, A.R., *Private Communication*

[31] Li, X.B., Lok, T.S., Zhao, J. and Zhao, P.J., "Oscillation elimination in the Hopkinson bar apparatus and resultant complete dynamic stress-strain curves for rocks", *Int. J. Rock Mech. Min. Sci.*, **37**, (2000), 1055–1060

[32] Field, J.E. and Pickles, C.S.J., "Strength, fracture and friction properties of diamond", *Diamond and Related Materials*, **5**, (1996), 625–34

[33] Heuze, F.E., "Sources of Errors in Rock Mechanics Field Measurements and Related Solutions", *International Journal of Rock Mechanics and Mining Sciences*, **8**, (1971), 297–310

[34] Grabco, D., Palistrant, N., Shikimaka, O., Zhitaru, R., Rahvalov, V. and Zugravescu, D., "Hardness and Brittleness of Rocks Studied by Microindentation Method in Combination with the Registration of Acoustic Emission Signals", *Proceedings of the 8th European Conference on Nondestructive Testing*

[35] Birch, F., "The velocity of compressional waves in rocks to 10 kilobars. 1", *J. Geophys. Res.*, **65**, (1960), 1083–1102

[36] Christensen, N.I., "Compressional wave velocities in metamorphic rocks at pressures to 10 kilobars", *J. Geophys. Res.*, **70**, (1965), 6147–6164

[37] Christensen, N.I., "Shear wave velocities in metamorphic rocks at pressures to 10 kilobars", *J. Geophys. Res.*, **71**, (1966), 3549–3556

[38] Wang, C.Y., "Velocity of compressional waves in limestones, marbles, and a single crystal of calcite to 20 kilobars", *J. Geophys. Res.*, **71**, (1966), 3543–3547

[39] Domany, E., Gubernatis, J.E. and Krumhansl, J.A., "The elasticity of polycrystals and rocks", *J. Geophys. Res.*, **80**, (1975), 4851–4856

[40] Greenfield, R.J. and Graham, E.K., "Application of a simple relation for describing wave velocity as a function of pressure in rocks containing microcracks", *J. Geophys. Res.*, **101**, (1996), 5643–5652

[41] McQueen, R.G., Marsh, S.P. and Fritz, J.N., "Hugoniot equation of state of twelve rocks", *J. Geophys. Res.*, **72**, (1967), 4999–5036

[42] Woeber, A.F., Katz, S. and Ahrens, T.J., "Elasticity of Selected Rocks and Minerals", *Geophysics*, **28**, (1963), 658–663

[43] Walsh, J.B. and Brace, W.F., "Elasticity of rock in uniaxial strain", *Int. J. Rock Mech. Min. Sci.*, **9**, (1972), 7–15

[44] McCormick, T.C., Hazen, R.M. and Angel, R.J., "Compressibility of Omphacite to 60 kbar: Role of Vacancies", *American Mineralogist*, **74**, (1989), 1287–1292

[45] Palchik, Y..H..Hatzor and V., "The influence of grain size and porosity on crack initiation stress and critical flaw length in dolomites", *International Journal of Rock Mechanics and Mining Sciences*, **34**, (1997), 805–816

[46] Palchik, Y..H..Hatzor and V., "A Microstructure-based Failure Criterion for Aminadav Dolomites", *International Journal of Rock Mechanics and Mining Sciences*, **35**, (1998), 797–805

[47] Field, J.E. and Ladegaard-Pedersen, A., "Review of Experimental techniques for High Rate Deformation and Shock Studies", *International Journal of Impact Engineering*, **30**, (2004), 725–775

[48] Bacon, L., "A Method of Determining Dynamic Tensile Strength of Rock at Minimal Loading", *USBMRI 6067*, **22**

[49] Cho, S.H., Ogata, Y. and Kaneko, K., "Strain-rate dependency of the dynamic tensile strength of rock", *Int. J. Rock Mech. Min. Sci.*, **40**, (2003), 763–777

[50] Gran, J.K., Gupta, Y.M. and Florence, A.L., "An Experimental Method to study the Dynamic Tensile Failure of Geological Materials", *Mechanics of Materials*, **6**, (1987), 113–125

[51] Zhao, J. and Li, H.B., "Experimental determination of dynamic tensile properties of a granite", *Int. J. Rock Mech. Min. Sci.*, **37**, (2000), 861–866

[52] Ross, C.A., Thompson, P.Y. and Tedesco, J.W., "Split-Hopkinson pressure tests on concrete and mortar in tension and compression", *ACI Mater. J.*, **86**, (1989), 475–481

[53] Shan, R., Jiang, Y. and Li, B., "Obtaining dynamic complete stress-strain curves for rock using the split Hopkinson pressure bar technique", *Int. J. Rock Mech. Min. Sci.*, **37**, (2000), 983–992

[54] Schock, R.N., Heard, H.C. and Stephens, D.R., "Stress-strain behavior of a granodiorite and two graywackes on compression to 20 kbar", *J. Geophys. Res.*, **78**, (1973), 5922–5941

[55] Okubo, S. and Fukui, E., "Complete Stress-Strain Curves for Various Rock Types in Uniaxial tension", *International Journal of Rock Mechanics and Mining Sciences and Geomechanical Abstracts*, **33**, (1996), 549–556

[56] Zhou, X.P., "Analysis of the localization and the complete stress-strain relation for mesoscopic heterogeneous brittle rock under uniaxial tensile loading", *Int. J. Solids Structures*, **41**, (2004), 1725–1738

[57] Ruoff, A.L., "Linear Shock-Velocity-Particle-Velocity Relationship", *J. Appl. Phys.*, **38**, (1969), 4976–4980

[58] Barker, L.M. and Hollenbach, R.E., "Laser interferometer for measuring high velocities of any reflecting surface", *J. Appl. Phys.*, **43**, (1972), 4669–4675

[59] Furnish, M.D., "Dynamic compression and release experiments on Indiana limestone", in *Shock Compression of Condensed Matter - 1989*, S. Schmidt, J. Johnson and L. Davidson, eds., Elsevier, Amsterdam (1990), pp. 625–628

[60] Tsembelis, K., Proud, W.G. and Field, J.E., "The principal Hugoniot and dynamic strength of dolerite under shock compression", in *Shock Compression of Condensed Matter - 2001*, M. Furnish, N. Thadhani and Y. Horie, eds., American Institute of Physics, Melville, NY (2002), pp. 1385–1388

[61] Barker, L.M., "Multi-beam VISARs for simultaneous velocity vs. time measurements", in *Shock Compression of Condensed Matter - 1999*, M. Furnish, L. Chhabildas and R. Hixson, eds., American Institute of Physics, Melville, New York (2000), pp. 999–1002

[62] Braithwaite, C.H., Field, J.F. and Proud, W.G., "The Hugoniots of Rocks and their Applications to Diamond Mining", in *De Beers Diamond Conference*, Oxford (2005)

[63] Guest, A.R., Braithwaite, C.H., Field, J.F. and Proud, W.G., "The Shock Hugoniot Properties of Geological Materials and Relationship to Static Properties", *SCCM 2007 Hawaii (in Press)*

[64] Yoshida, S. and Ogawa, T., "Electromagnetic Emissions from Dry and Wet Granite Associated with Acoustic Emissions", *Journal of Geophysical Research*, **109**, (2004), B09,204

[65] Boslough, M.B. and Ahrens, T.J., "Shock wave properties of anorthosite and gabbro", *J. Geophys. Res.*, **90**, (1985), 7814–7820

[66] Takazawa, E., Sekine, T., Kobayashi, T. and Zhu, Y., "Hugoniot equation of state and high-pressure transformation of jadeite", *J. Geophys. Res.*, **103**, (1998), 12,261–12,268

[67] Nakazawa, S., Watanabe, S., Kato, M., Iijima, Y., Kobayashi, T. and Sekine, T., "Hugoniot equation of state of basalt", *Planet. Space Sci.*, **45**, (1997), 1489–1492

[68] Tsembelis, K., Proud, W.G. and Field, J.E., "The shock Hugoniot of cement paste up to 5 GPa", in *Proc. 12th DYMAT Technical Meeting: Impact Damage of Composite Materials*, J. Cirne, ed., DYMAT, Arcueil, France (1999), pp. 90–94

[69] Tsembelis, K., Proud, W.G., Willmott, G.R. and Cross, D.L.A., "The shock Hugoniot properties of cement paste and mortar up to 18 GPa", in *Shock Compression of Condensed Matter - 2003*, M. Furnish, Y. Gupta and J. Forbes, eds., American Institute of Physics, Melville NY (2004), pp. 1488–1491

[70] Shang, J.L., Shen, L.T. and Zhao, J., "Hugoniot equation of state of the Bukit Timah granite", *Int. J. Rock Mech. Min. Sci.*, **37**, (2000), 705–713

[71] Millett, J.C.F., Tsembelis, K. and Bourne, N.K., "Longitudinal and lateral stress measurements in shock-loaded gabbro and granite", *J. Appl. Phys.*, **87**, (2000), 3678–3682

[72] Willmott, G.R., Proud, W.G. and Field, J.E., "Shock properties of kimberlite", in *Shock Compression of Condensed Matter - 2003*, M. Furnish, Y. Gupta and J. Forbes, eds., American Institute of Physics, Melville NY (2004), pp. 1492–1495

[73] vanThiel, M., "Compendium of shock wave data (Vols 1, 2, 2(suppl.))", Technical Report UCRL-50108, Lawrence Radiation Laboratory (1966)

[74] Sekine, T., Rubin, A.M., Duffy, T.S., Ahrens, T.J. and Anderson, W.W., "Shock compression and isentropic release of granite", *Geophys. J. Int.*, **120**, (1995), 247–261

[75] Petersen, C.F., Murri, W.J. and Cowperthwaite, M., "Hugoniot and release-adiabat measurements for selected geologic materials", *J. Geophys. Res.*, **75**, (1970), 2063–2072

[76] Ahrens, T.J. and Gregson, J.V.G., "Shock compression of crustal rocks: Data for quartz, calcite, and plagioclase rocks", *J. Geophys. Res.*, **69**, (1964), 4839–4874

[77] Furnish, M.D., "Measuring the dynamic compression and release behavior of rocks and grouts associated with HYDROPLUS", Technical Report SAND92-0984, Sandia National Lab. (1993)

[78] Furnish, M.D., "Measuring the dynamic compression and release behavior of rocks associated with HYDROPLUS (Part II)", Technical Report SAND95-1472, Sandia National Lab. (1995)

[79] Jeanloz, R. and Ahrens, T.J., "Release adiabat measurements on minerals: The effect of viscosity", *J. Geophys. Res.*, **84**, (1979), 7545–7548

[80] He, H. and Ahrens, T.J., "Mechanical properties of shock-damaged rocks", *Int. J. Rock Mech. Min. Sci. and Geomech. Abstr.*, **31**, (1994), 525–533

[81] Ahrens, T.J. and Duvall, G.E., "Stress relaxation behind elastic shock waves in rocks", *J. Geophys. Res.*, **71**, (1966), 4349–4360

[82] Willmott, G.R., Proud, W.G. and Field, J.E., "Shock properties of diamond and kimberlite", *J. Phys. IV France*, **110**, (2003), 833–838

[83] Rosenberg, Z., Bourne, N.K. and Millett, J.C.F., "Calibration of commercial gauges of varying geometry to measure the lateral component of stress", in *Shock Compression of Condensed Matter - 2005*, M. Furnish, M. Elert, T. Russell and C. White, eds., American Institute of Physics, Melville, NY (2006), pp. 1207–1210

[84] Field, J.E. and Ladegaard-Pedersen, A., "Fragmentation processes in rock blasting", *Dechema-Monographien (also Int. J. Rock Mech. and Min. Sci.)*, **69**, (1972), 1–29

[85] Grady, D.E. and Hollenbach, R.E., "Dynamic fracture strength of rock", *Geophys. Res. Letts*, **6**, (1979), 73–76

[86] Ai, H.A. and Ahrens, T.J., "Dynamic tensile strength of terrestrial rocks and application to impact cratering", *Meteor. Planet. Sci.*, **39**, (2004), 233–246

[87] Grady, D.E. and Kipp, M.E., "Dynamic fracture and fragmentation", in *High-Pressure Shock Compression of Solids*, J. Asay and M. Shahinpoor, eds., Springer-Verlag, New York (1993), pp. 265–322

[88] Grady, D.E., "Spall properties of Solenhofen limestone and Dresser basalt", in *Shock Compression of Condensed Matter - 1999*, M. Furnish, L. Chhabildas and R. Hixson, eds., American Institute of Physics, Melville, New York (2000), pp. 1255–1258

[89] Rosenberg, Z., "On the relation between the Hugoniot elastic limit and the yield strength of brittle materials", *J. Appl. Phys.*, **74**, (1993), 752–753

[90] Blanton, T.L., "Effect of strain rates from 10-2 to 10 s-1 in triaxial compression tests on three rocks", *Int. J. Rock Mech. Min. Sci.*, **18**, (1981), 47–62

[91] Chong, K.P. and Boresi, A.P., "Strain rate dependent mechanical properties of New Albany reference shale", *Int. J. Rock Mech. Min. Sci. and Geomech. Abstr.*, **27**, (1990), 199–205

[92] Bless, S.J. and Ahrens, T.J., "Measurements of the longitudinal modulus of Pierre Clay Shale at varying strain rates", *Geophysics*, **42**, (1977), 34–40

[93] Rinehart, J.S., "Dynamic fracture strength of rocks.", in *Proc. 7th Symp. on Rock Mechanics. Vol. 1*, American Institute of Mining, Metallurgical and Petroleum Engineers, New York (1965), pp. 205–208

[94] Goldsmith, W., Sackman, J.L. and Ewerts, C., "Static and Dynamic Fracture Strength of Barre Granite", *International Journal of Rock Mechanics and Mining Sciences and Geomechanical Abstracts*, **13**, (1976), 303–309

[95] Hall, C.A., Chhabildas, L.C. and Reinhart, W.D., "Shock Hugoniot and release in concrete with different aggregate sizes from 3 to 23 GPa", *Int. J. Impact Engng*, **23**, (1999), 341–352

[96] Tsembelis, K., Proud, W.G. and Field, J.E., "The dynamic strength of cement paste under shock compression", in *Shock Compression of Condensed Matter - 2001*, M. Furnish, N. Thadhani and Y. Horie, eds., American Institute of Physics, Melville, NY (2002), pp. 1414–1417

[97] Grady, D., "Shock equation of state properties of concrete", in *Structures under Shock and Impact IV*, N. Jones, C. Brebbia and A. Watson, eds., Computational Mechanics Publications, Southampton (1996), pp. 405–414

[98] Grady, D.E., "Impact compression properties of concrete", Technical Report SAND- 93-0013C, Sandia National Laboratories (1993)

[99] Grote, D.L., Park, S.W. and Zhou, M., "Experimental characterization of the dynamic failure behavior of mortar under impact loading", *J. Appl. Phys.*, **89**, (2001), 2115–2123

[100] Tsembelis, K. and Proud, W.G., "The dynamic behavior of micro-concrete", in *Shock Compression of Condensed Matter - 2005*, M. Furnish, M. Elert, T. Russell and C. White, eds., American Institute of Physics, Melville, NY (2006), pp. 1496–1499

[101] Kipp, M.E., Chhabildas, L.C. and Reinhart, W.D., "Elastic shock response and spall strength of concrete", in *Shock Compression of Condensed Matter - 1997*, S. Schmidt, D. Dandekar and J. Forbes, eds., American Institute of Physics, Woodbury, New York (1998), pp. 557–560

Chapter 4

Experimental Methods

4.1 The Plate Impact Facility

All of the high strain rate experiments described in this thesis were carried out using the plate impact facility at the Cavendish Laboratory, Cambridge University. The facility consists of a single stage light gas gun which was built in house [1]. It has previously been demonstrated to be suitable for the testing of geological materials with work being carried out on granite and gabbro [2], dolerite [3] and tuffistic kimberlite breccia [4] amongst others.

The gun, shown in figure 4.1, can either use air or helium as a propellant and can be charged to a pressure of 350 Bar. This allows for velocities of up to 1100 m s^{-1} to be achieved. The barrel has a length of 5 m and a bore of 50 mm, with an example of a projectile shown in figure 4.2. The projectile shown is drilled to reduce weight and therefore achieve a higher velocity. The metal ring on the front (at the right of the photo) is added to non conducting flier materials so that the velocity measurement system, which consists of four pairs of sequentially shorted pins, functions correctly.

The firing procedure for the gun is shown schematically in figure 4.3. A projectile, such as the standard one overlaid in the photograph is inserted into the breech (the hole in the breach, between the reservoirs, is clearly visible in figure 4.1), the breech plug placed in the end of the barrel and a vacuum of below

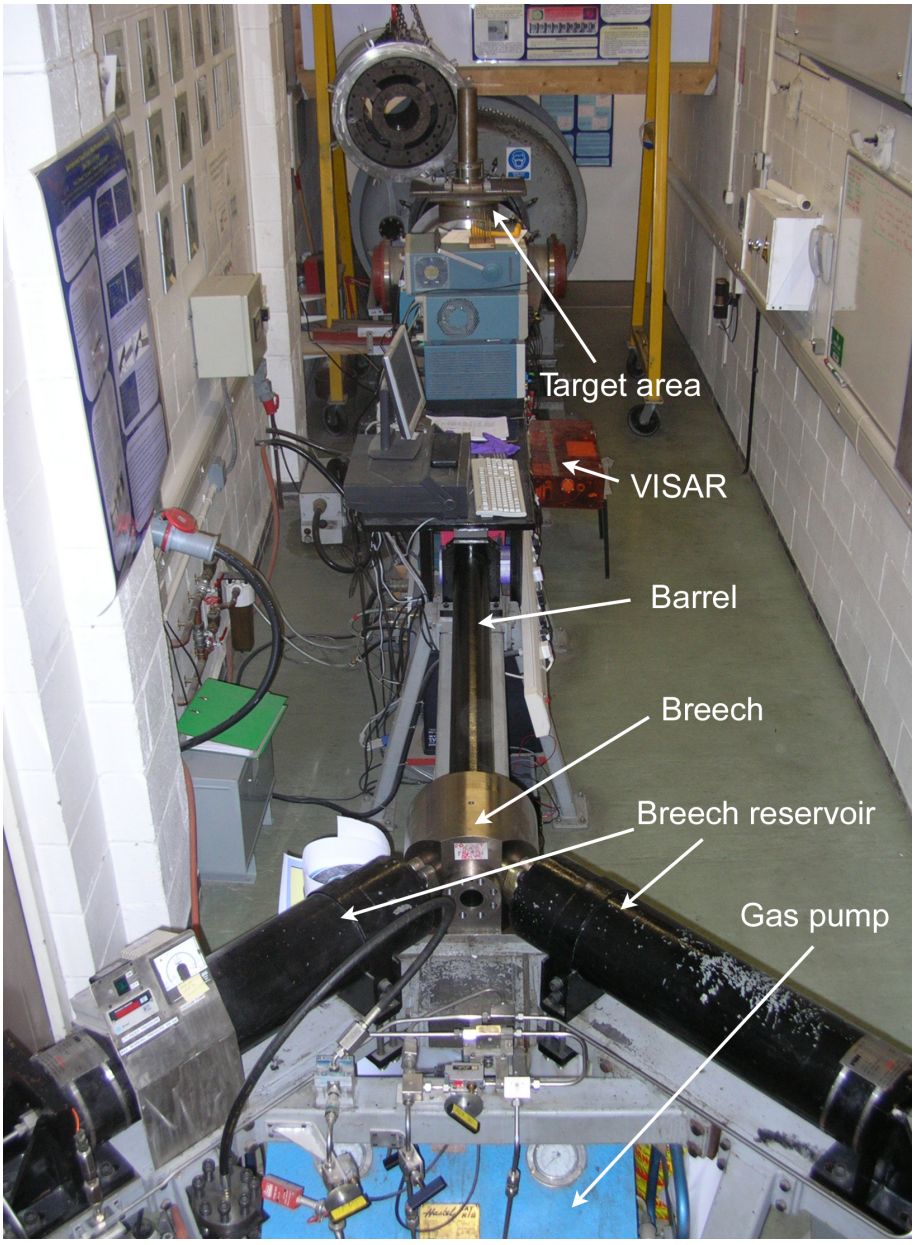

Figure 4.1: View down the barrel from the breech in the foreground to the target chamber in the background. The oscilloscopes for data acquisition can be seen above the barrel. In the foreground are the controls for filling the gas reservoirs. The hole into which the projectile is loaded can be seen in the foreground end of the breech block.

0.1 mbar is drawn behind the projectile, preventing it from moving down the barrel. This keeps the projectile in place while the gas reservoirs are charged for firing. To reduce the chance of air shock ahead of the projectile, eliminate after-firing over-pressure and to reduce noise, the barrel and expansion chamber are also evacuated, but not to the same extent, about 20 mbar. The o-rings on the projectile, shown in figure 4.3, which sit in the grooves shown in figure 4.2 seal the reservoirs while the charging process occurs. The gun is fired by allowing air in behind the projectile, breaking the vacuum and letting the projectile drift down the barrel. Once the rear seal clears the opening to the gas reservoirs the pressure in them is released, accelerating the projectile down the barrel. The velocity achieved is easily predicable thanks to extensive calibration over a large number of shots. The author has made a significant contribution to this predictive capability through formulating a new calibration curve for heavier projectiles.

The design of the sabot is important in the operation of the gun and also the reliability of the data obtained. Each sabot is constructed such that there is a fairly tight fit to the barrel. This, along with the aspect ratio, ensures that there is no significant deviation from a horizontal trajectory upon the sabot leaving the barrel. Obviously the velocity of the sabot and the distance of travel from the end of the barrel (which is minimised) also play a part in this. It is important to have a horizontal trajectory in order to achieve a planar impact. As well as the drilled out sabot shown in figure 4.2 there is a standard non-drilled version for intermediate velocity shots and a low velocity version which is bored out and then has brass weight added. The reason for the heavier low velocity sabot is that the gun fires at a more reproducible velocity with a higher charging pressure. All of the sabot designs have a recess in the front which allows for the release wave from the flier plate to come from an rough vacuum interface rather than a polycarbonate one. A small hole allows this recess to be equal in pressure to the vacuumed pressure of the barrel.

At the target end of the barrel, there is significant scope for instrumentation of various types. The velocity interferometry system for any reflector or VISAR can be seen in figure 4.1 and also in more detail in figure 4.9. This system, which

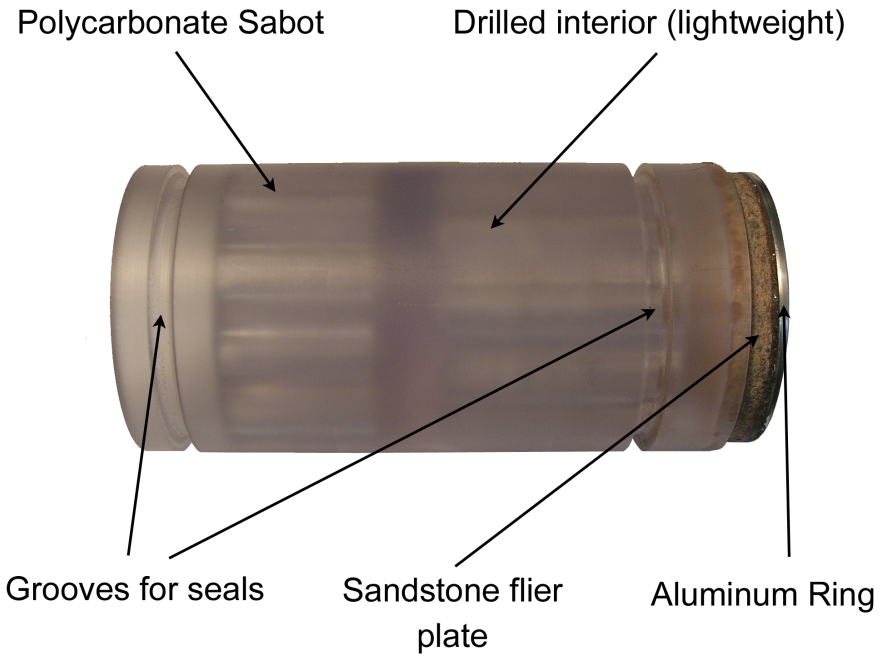

Figure 4.2: Sabot with sandstone flier. The sabot shown is a lightweight sabot, the inside has been extensively drilled out to reduce weight and allow for a higher velocity to be achieved for the same gas pressure (the maximum pressure of the system is limited for safety reasons). The grooves are fitted with o rings for firing. The aluminium ring allows for velocity to be measured by a series of shorting pins (the ring is only used therefore with non conducting flier materials).

allows for the measurement of free surface velocity is discussed in more detail in section 4.2.2. The main other diagnostic used in this thesis is manganin gauges, which connect out of the gun via the port labelled in Figs. 4.4 and 4.5. Data for both of these diagnostics are recorded on the oscilloscopes that can be seen in figure 4.1. It is possible to use a number of other diagnostics either separately, or in conjunction with those already mentioned. It is possible to see a tube for holding an x-ray head in figure 4.4 and windows/ports for high speed photography in Figs. 4.4 and 4.5. These diagnostics have not been used in this thesis however.

In operation, the central section of the expansion chamber can be removed to

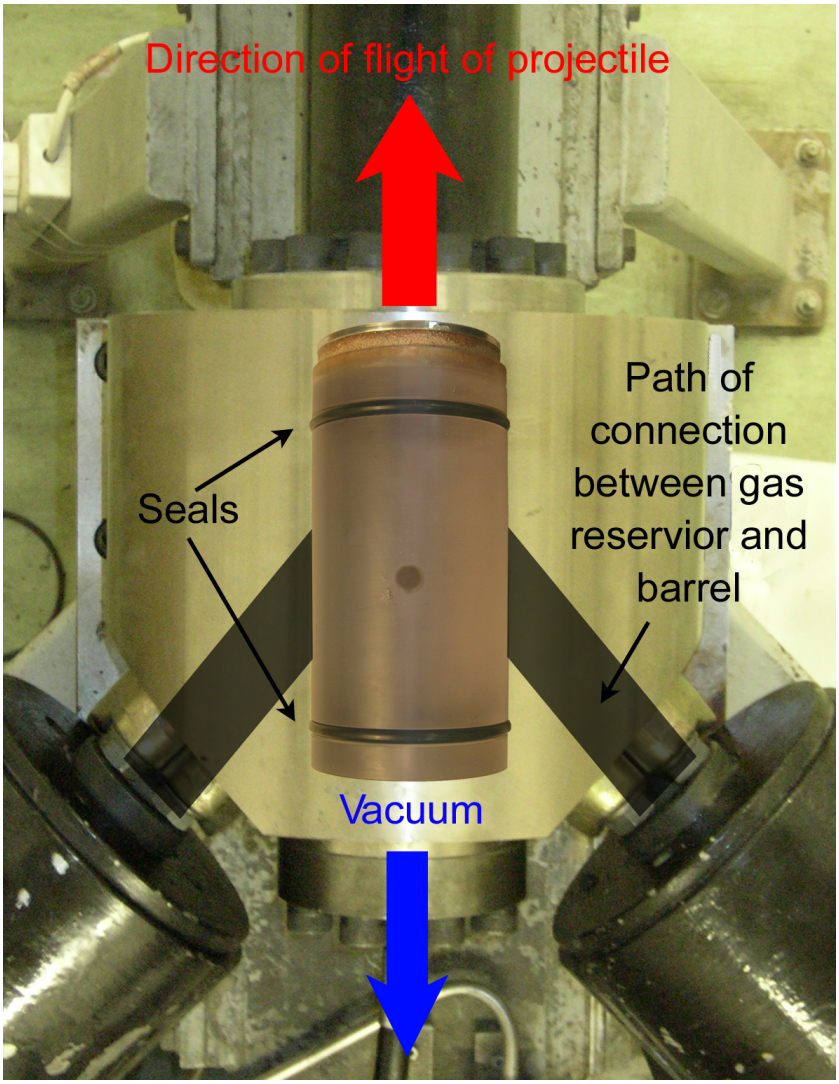

Figure 4.3: Diagram of the breech showing mechanism for firing. For illustrative purposes a photograph of a standard sabot has been overlaid on a photograph of the breech in the position it would roughly be inside the breech. The vacuum behind the projectile prevents it from moving down the barrel while the gas reservoirs are filled. The seals on the projectile seal these reservoirs. To fire the gun, the rear vacuum is broken and the projectile drifts down the barrel until the rear seal is broken. When this occurs, the reservoirs empty behind the projectile, accelerating it down the barrel.

allow easy access and to facilitate both setting up the gun prior to firing and cleaning up afterwards. The wall thickness is sufficient to prevent fragments from samples penetrating the sides of the pressure vessel.

At the end of the barrel an alignment system allows for samples to be aligned with an error of less than 1 mrad. The system consists of a plate mounted on three adjustable screw threads, allowing a full range of tilt to be accessed. A plug is inserted into the end of the barrel with a flat machined end. This provides a reference to which the separate target mount can then be made parallel. In order to determine the correct distances for the screw threads, a dial gauge which fits in the specimen mount is used.

The shorting pins for determining the velocity sit just behind the specimen mount (as seen from the target) at the end of the barrel. The pins, four pairs, are either made of brass (for high velocity shots above about 500-600 m s^{-1}) or graphite (for low velocity shots). The pins have a constant power supply and are instrumented in such a way that a sharp spike is recorded on an oscilloscope when the pins are shorted by a projectile leaving the barrel. The distance between the pins is known to a good accuracy, and therefore by measuring the time difference on the oscilloscope the velocity can be determined to an accuracy of $\pm$ 0.5 %.

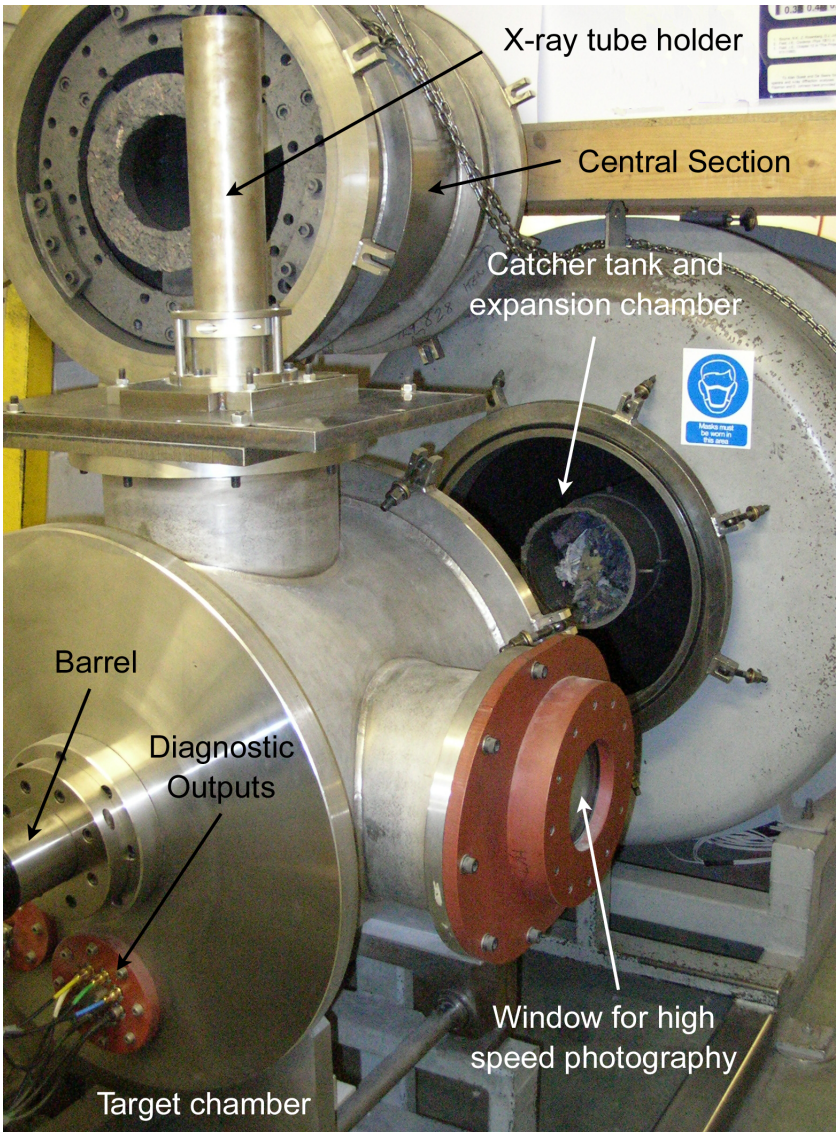

Figure 4.4: Catcher tank and expansion chamber with central section removed. The removable section allows for easy access to the target area. The target chamber itself is also on rails, so that it can be retracted before the central section is raised or lowered (with the aid of a gantry crane). Various fittings to accommodate different diagnostics are labelled in the photograph.

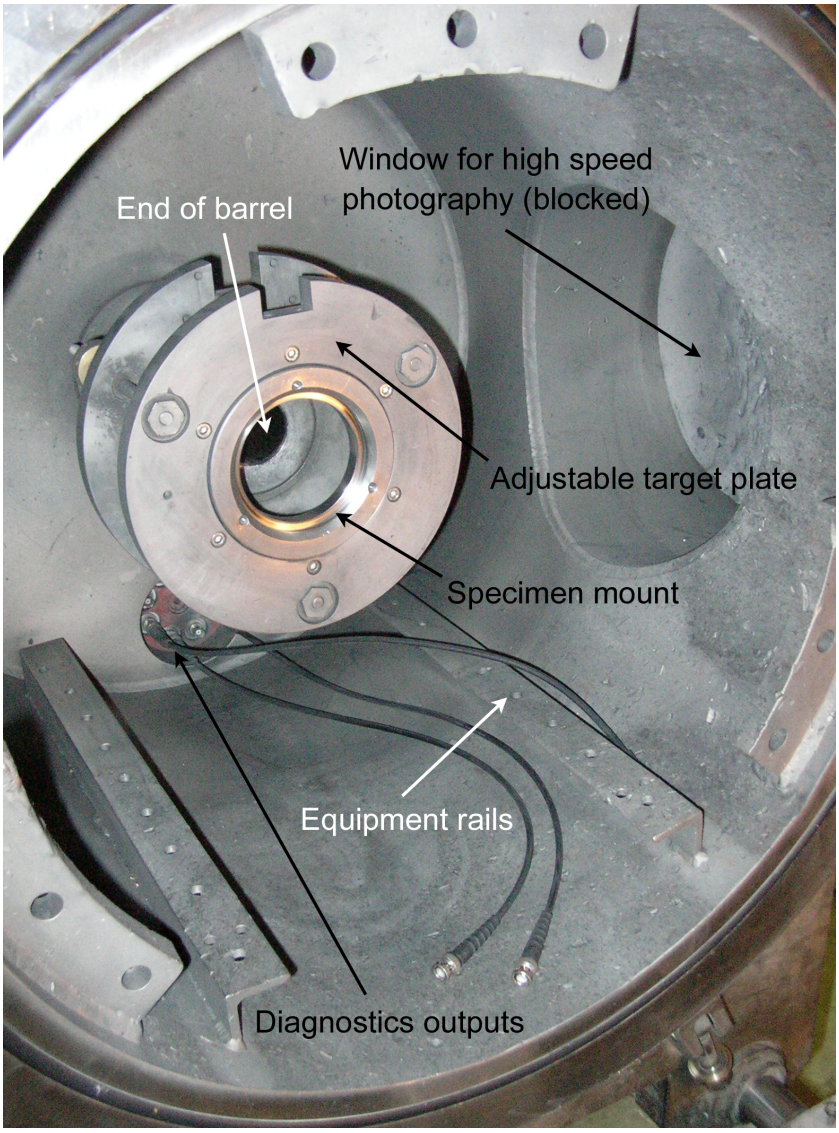

Figure 4.5: Target chamber of the plate impact facility. The specimen mount can be adjusted by means of three screws, the end nuts of which can be seen coming through the target plate. As well as a window for high-speed photography and a general diagnostic output port, there are also two parallel equipment rails that allow for a variety of devices (for example sample recovery devices [5]) to be bolted securely to them.

4.2 Diagnostics

4.2.1 Gauges

Stress gauges can take a number of forms and be made from a number of different materials. In the case of these experiments, in material stress was measured using piezoresistive manganin gauges (possible alternatives to manganin gauges would be carbon resistor gauges [6], quartz gauges [7] and PVDF gauges [8]) such as the one shown in figure 4.6. Manganin is an alloy of copper, manganese and nickel (abundances 84%, 12% and 4% respectively). It is a good material for a stress gauge as it has a good piezoresistive response without having either a high sensitivity to temperature or undergoing any phase transitions. The gauges used are commercially available through the company Micromeasurements. This type of gauge is used extensively in the shock physics community [2, 3] and has been the subject of numerous papers intended to provide calibration or improve material knowledge [9–11].

The stress gauges work on the principle that as the manganin is stressed and subsequently elastically or plastically deformed, the gauge resistance changes. This loading should be planar to the gauge, uniaxial and homogeneous. If this is not the case then the gauge can be subjected to strain and the results will be unreliable.

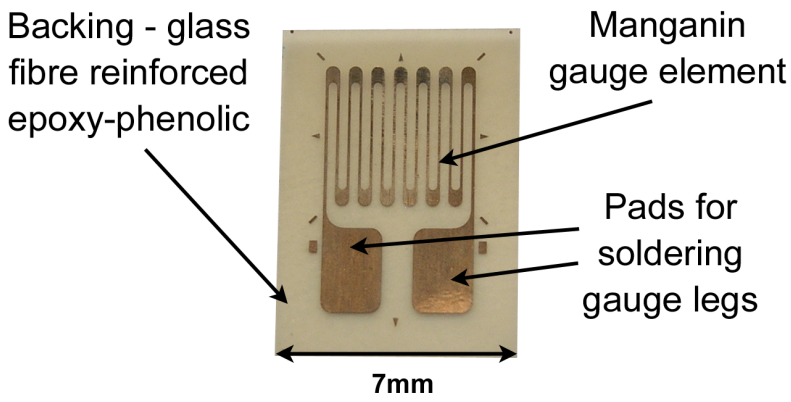

Figure 4.6: A manganin grid gauge - Micro-Measurements LM-SS-125CH-048. The gauge is not encapsulated, but deposited on the plastic backing substrate. In order to be functional, "legs" consisting of brass shim have to be soldered to the pads labelled in the photograph. In order to keep the thickness of the gauge and legs to a minimum, indium alloy solder is used. The gauge is then set into the sample using a slow setting two part epoxy, and insulated from any conducting samples using 25 μm Mylar sheet.

The gauges can be placed in two distinct geometries, longitudinal and lateral, depending on the component of stress which is required to be measured, these are shown in figure 4.7. In the figure, the red face shows the impact face, the blue surface the longitudinal gauge plane (with a grid gauge in a longitudinal orientation) and the green surface the lateral gauge plane (with both longitudinal and 't' gauges). In order to embed the gauges in the correct planes, they are encapsulated in a low viscosity two part epoxy resin. Gauges are insulated by sheets of 25 μm mylar and at each stage of glueing the samples are pressed to ensure an absence of air bubbles. Overall, a gauge package has a typical thickness of 150 μm. It is important that gauge packages are as thin as possible so as not to reduce the time resolution of the gauge (a number of transitions and reflections through the gauge package are required for the gauge to reach equilibrium with the surrounding material).

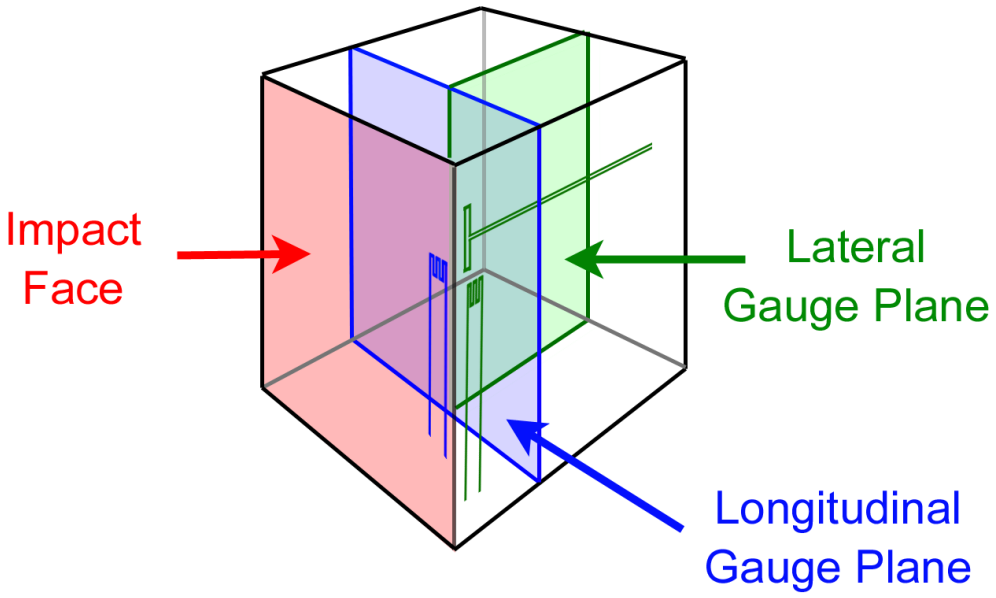

Figure 4.7: Schematic of gauge positions, showing two grid gauges and a 't' gauge. The impact face is parallel to the plane into which longitudinal gauges are inserted, and perpendicular to the plane where lateral gauges are placed. The orientation of the longitudinal gauges is unimportant provided that the gauge lies flat in the plane. For the lateral gauges it is important that the gauges are used in the orientations shown, as misalignment can lead to, for example, longer rise times (as the shock takes a greater time to traverse the misaligned gauge)

In operation, the gauges need to be connected to a constant current power supply. This power supply is set up such that the gauge forms one leg of a Wheatstone bridge circuit. This gives a greater sensitivity to changes in resistance. In addition, to avoid damage to the gauge, the power supply is pulsed using a capacitor, to only supply the required current over the period of interest. When setting up the gauges, the Wheatstone bridge is balanced to give zero output, and subsequently the voltage output of the bridge is calibrated by connecting it to a succession of different resistances in series. The output from the gauges during an experiment is recorded on a Tektronix digital storage oscilloscope (TDS 7054) as a voltage time trace.

In order to calculate the stress from the voltage-time trace, it is necessary to use a calibration, such as the one due to Rosenberg [12] for longitudinal gauges. This calibration takes the form of a 4^{th} order polynomial (Equation 4.1, and has an error of approximately $\pm$ 2 %:

$$P = A_0 + A_1\left(\frac{\Delta R}{R_0}\right) + A_2\left(\frac{\Delta R}{R_0}\right)^2 + A_3\left(\frac{\Delta R}{R_0}\right)^3 + A_4\left(\frac{\Delta R}{R_0}\right)^4. \qquad (4.1)$$

It is assumed that the hydrostatic pressure (P) is equal to the longitudinal stress. ΔR is the change in resistance and R_0 is the initial resistance of the gauge. A_0, A_1, A_2, A_3, A_4 are fitting constants with values of 0.572 GPa, 29.59 GPa, 95.20 GPa, -312.774 GPa and 331.77 GPa respectively. As the measurement made is one of voltage (ΔV) and the calibration requires resistance change the following formula (equation 4.2) is used, with the constants determined by fitting the data derived from connecting the gauge to different resistances.

$$\Delta R = A\Delta V + B\left(\Delta V\right)^2. \qquad (4.2)$$

While gauges in the lateral configuration function in exactly the same way, there are a couple of significant differences in the set-up and calibration. Firstly, it should be noted that the initial resistance of the gauge is only approximately 25 Ω for the 't' gauge. This is an issue because the sensitivity of the gauge power supply is optimised at about 50 Ω, roughly the value of R_0 for the grid gauges used in the longitudinal (and some of the lateral) experiments. In order to get around this problem a resistor is connected in series with the gauge, bringing the total to as near to 50 Ω as is possible. The second difference is that the calibration is different from the longitudinal gauges, irrespective of whether grid or 't' gauges are used.

The initial calibration of the gauge, converting the voltage change to resistance is the same as for the longitudinal situation, as this is a property of the manganin and the gauge geometry rather than the material geometry and environment.

The calibration that is then used is also due to Rosenberg [9]. This calibration accounts for elastoplastic deformation of the manganin above its yield strength. In the longitudinal geometry the gauge is assumed to behave in an elastic, perfectly plastic manner. Further work on the calibration of lateral gauges has been carried out by Rosenberg [11, 13, 14] as well as others, for example Gupta [15, 16]. At the current time there is some discussion as to the absolute validity of these calibrations, for example, some modelling has suggested the 't' gauges are not representative of the bulk material [17]. Above a value of approximately 3 GPa and for brittle materials, the calibration seems to be accepted (in other materials the measured stress may be incorrect by up to 0.25 GPa. This means that the investigations in this thesis should be valid in using the latest Rosenberg calibration.

4.2.2 VISAR

VISAR is a development of the wide angle Michelson interferometer [18] and allows, through defocussing, the formation of fringe patterns after reflection from a diffuse surface as opposed to a specularly reflecting surface (although the system can be used with both types of surface finish). The VISAR systems in the Cambridge plate impact facility consist of a single beam model and a multi beam model (in this case with three beams), both manufactured by Valyn. Valyn was founded by L. Barker who developed the original VISAR in the 1970's [19].

4.2.2.1 Theory

The main physical phenomenon that allows the VISAR system to work is that of Doppler shift. As a surface is moving away or towards an observer, or observation equipment , the light reflected, or given out by that object or surface, has a different frequency, when measured by the observer, depending on the relative speeds. When we neglect the effects of special relativity, the relationship between incident light frequency (f) and the frequency measured by the stationary observer (f') is given by equation 4.3, where c is the speed of light:

$$\frac{f'}{f} = \frac{c + 2u_p}{c}. \tag{4.3}$$

In order to see this frequency shift, the reflected light from the sample is split, one leg has a known delay introduced by glass etalons, and the beams are recombined. The recombining of the beams causes an interference pattern to be set up. The fringe number, F , is related to the frequencies and the delay time t_d as shown in equation 4.4. To calculate the delay time in the etalon leg we can use Equation 4.5, where h is the length of the etalon and n the refractive index. Combining equations 4.3 and 4.4 we can get an expression for particle velocity (Equation 4.6). If a window material is used, then the change in refractive index under shock has to be accounted for in a material dependent correction factor of $\Delta f/f_0$, see Equation 4.7. Additionally there is a factor of $(1 + \delta)$ which accounts for the change in refractive index with frequency. The factor of $\frac{1}{2}(1+cos\theta)$ was presented as an amendment to the original formula in 1997 [20] and relates to the fact that while the incident light is perpendicular to the surface, the collected light will have an angle associated with it (owing to the collection and incident fibres having a spatial separation). Correction for this angle was carried out separately to the VISAR analysis through a routine developed by Chapman [21]. Note that $t - t_d$ centres the velocity timing with the fringe count. Initial work on window materials was carried out by Barker and Hollenbach [22].

$$F = t_d f' - t_d f, \tag{4.4}$$

$$t_d = \frac{2h}{c}(n - 1/n), \tag{4.5}$$

$$u_p = \frac{\lambda}{2t_d} F, \tag{4.6}$$

$$u_p(t - \tfrac{1}{2}t_d) = \frac{\lambda F(t)}{2t_d(1 + \Delta f/f_0)\frac{1}{2}(1 + cos\theta)(1 + \delta)}. \tag{4.7}$$

4.2.2.2 Practicalities

In operation, the VISAR works much as can be seen in figure 4.8. The light reflected from the sample is collimated and polarised. This means that the light reflecting from the first mirror is half P-polarised and half S-polarised. The main beamsplitter, labelled BS in figure 4.8, then splits the light so that half goes through the etalon and is delayed, and half is reflected from the mirror M* and misses the etalon. M* is mounted on three piezoelectric elements, which can be adjusted by a ramp generator to ensure that the best possible fringe pattern is formed. The purpose of the $\frac{\lambda}{8}$ wave plate is to give the P-polarised component a 90°phase delay. At the beamsplitter, on recombination, the P and S polarised fringe patterns are then 90°out of phase. The fact that there are two fringe patterns improves fringe resolution and allows the direction of surface acceleration to be determined. The left and right beams, as shown in the diagram, have a 180°phase difference due to the additional reflection at the beamsplitter for the left hand beam. Each of the left hand and right hand beams are also split into P and S polarised components, giving four outputs that are focussed into photomultiplier tubes. This four output configuration is known as a 'push-pull' VISAR and was initially proposed as a modification by Hemsing [23]. The outputs of these are then fed into a digital storage oscilloscope. Most of these internal components of the VISAR system are labelled in figure 4.9.

The VISAR analysis [23] involves initially subtracting one of the P - polarised signals from the other, and similarly one of the S - polarised beams from the other (this can either be done manually, or by a differential amplifier prior to data acquisition). As the two signals are in anti-phase, this both doubles the output signal and also reduces incoherent self light in the signal. This operation leaves two data sets which have fringe patterns that are 90°out of phase. From this point, the analysis is performed by a computer program supplied by Valyn, which essentially follows the principles laid down by Dolan [24].

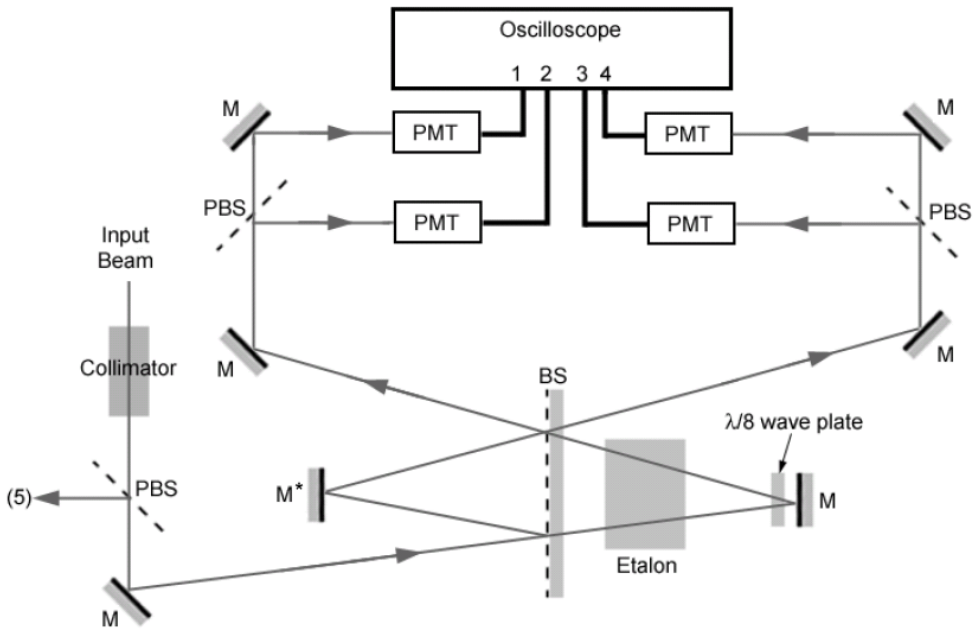

Figure 4.8: Schematic of a single beam VISAR (from [5] with permission). M denotes a mirror, BS a beamsplitter, PBS a polarising beamsplitter and PMT a photomultiplier tube. The output labelled (5) is a reference beam to monitor intensity. The ray path shows light entering the system, being split at the main beamsplitter, and then recombining after one leg has been delayed. The output light is further split by a polarising beamsplitter to give four outputs.

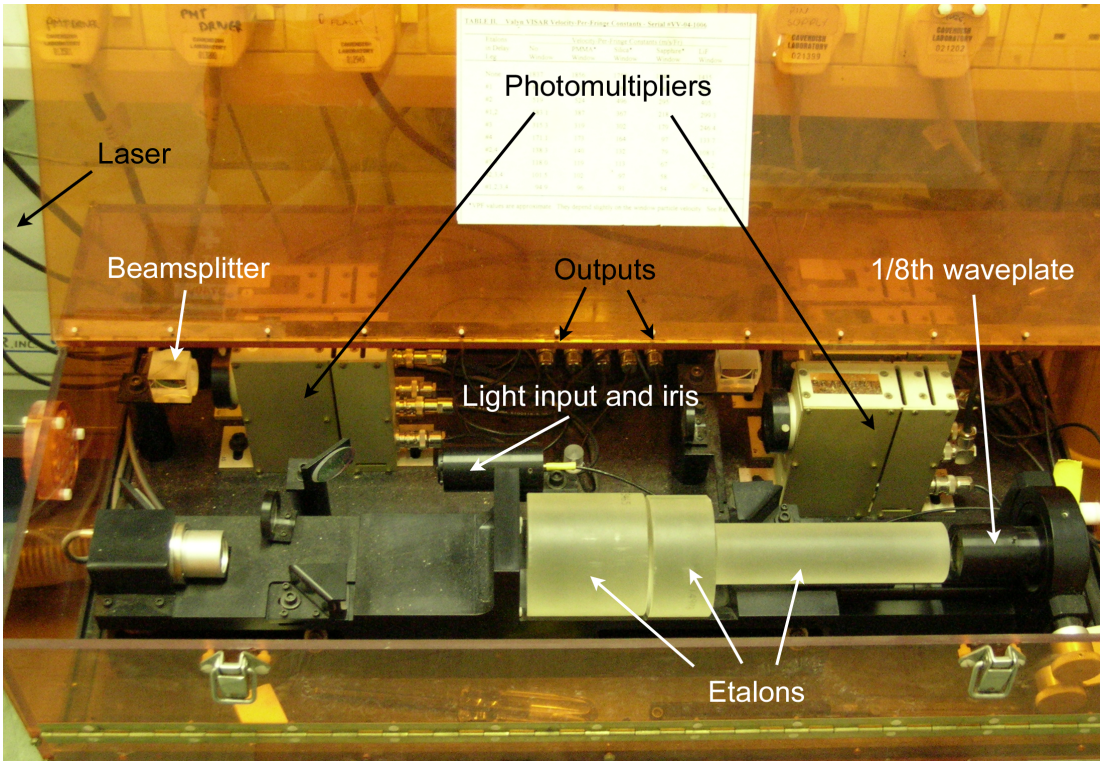

Figure 4.9: Modified Valyn VISAR system. The orange case is designed to prevent any stray laser light becoming a health hazard. Immediately to the left of the etalons is the main beamsplitter. The glass cube beamsplitters are the polarising beamsplitters that transmit the light to the PMT outputs. Some VISAR systems use differential amplifiers in conjunction with the PMTs, but these are absent from the system shown.

4.2.2.3 Multi-point VISAR

The main principals of a multi-point VISAR [25] are the same as for a single push-pull VISAR system. The main difference is that while a conventional system has only one measurement point, a multi-point system might have up to seven. The system at the Cambridge plate impact facility has three. This allows for averaging of properties across inhomogeneous materials for example, and also for example measuring of shock velocity with the use of stepped targets [25].

4.3 Summary

- A well characterised plate impact facility has been used to collect data for this investigation.
- Both of the main diagnostics, VISAR and manganin gauges widely used in the shock physics community and are accepted standard techniques (excepting a slight note of caution over the use of lateral gauges in certain circumstances).

References

[1] Bourne, N.K., Rosenberg, Z., Johnson, D.J., Field, J.E., Timbs, A.E. and Flaxman, R.P., "Design and construction of the UK plate impact facility", *Meas. Sci. Technol.*, **6**, (1995), 1462–1470

[2] Millett, J.C.F., Tsembelis, K. and Bourne, N.K., "Longitudinal and lateral stress measurements in shock-loaded gabbro and granite", *J. Appl. Phys.*, **87**, (2000), 3678–3682

[3] Tsembelis, K., Proud, W.G. and Field, J.E., "The principal Hugoniot and dynamic strength of dolerite under shock compression", in *Shock Compression of Condensed Matter - 2001*, M. Furnish, N. Thadhani and Y. Horie, eds., American Institute of Physics, Melville, NY (2002), pp. 1385–1388

[4] Willmott, G.R., Proud, W.G. and Field, J.E., "Shock properties of kimberlite", in *Shock Compression of Condensed Matter - 2003*, M. Furnish, Y. Gupta and J. Forbes, eds., American Institute of Physics, Melville NY (2004), pp. 1492–1495

[5] Willmott, G.R., *Shock Studies of Kimberlite, Diamond and Brittle Embedded Particles*, Phd, Cambridge (2004)

[6] Ginsberg, M.J. and Asay, B.W., "Commercial carbon composition resistors as dynamic stress gauges in difficult environments", *Rev. Sci. Instrum.*, **62**, (1991), 2218–2227

[7] Ingram, G.E. and Graham, R.A., "Quartz gauge technique for impact experiments", in *Proc. Fifth Symp. (Int.) on Detonation*, I. Rudin, ed., Office of Naval Research, Arlington, Virginia (1970), pp. 369–386

[8] Lee, L.M., Graham, R.A., Bauer, F. and Reed, R.P., "Standardized Bauer PVDF piezoelectric polymer shock gauge", *J. Phys. France Colloq. C3 (DYMAT 88)*, **49**, (1988), 651–658

[9] Rosenberg, Z. and Partom, Y., "Lateral stress measurement in shock-loaded targets with transverse piezoresistance gauges", *J. Appl. Phys.*, **58**, (1985), 3072–3076

[10] Rosenberg, Z., Partom, Y., Mayseless, M. and Falcovitz, J., "Determination of stress-time histories in axially symmetric impacts with the two-gauge technique", *J. Appl. Phys.*, **56**, (1984), 1434–1439

[11] Rosenberg, Z., Bourne, N.K. and Millett, J.C.F., "Calibration of commercial gauges of varying geometry to measure the lateral component of stress", in *Shock Compression of Condensed Matter - 2005*, M. Furnish, M. Elert, T. Russell and C. White, eds., American Institute of Physics, Melville, NY (2006), pp. 1207–1210

[12] Rosenberg, Z. Yaviz, D. and Partom, Y., "Calibration of foil-like manganin gauges in planar shock wave experiments", *J. Appl. Phys.*, **51**, (1980), 3702–3705

[13] Rosenberg, Z. and Partom, Y., "The pressure dependence of the yield strength of shock-loaded Manganin gauges", *J. Appl. Phys.*, **57**, (1985), 5084–5086

[14] Rosenberg, Z. and Brar, N.S., "The influence of the elasto-plastic properties of piezoresistive gauges on their loading-unloading characteristics as lateral shock stress transducers", *J. Appl. Phys.*, **77**, (1995), 1443–1448

[15] Gupta, Y.M., "Stress measurements using piezoresistive gauges: modeling the gauge as an elastic-plastic inclusion", *J. Appl. Phys.*, (1983), 6256–6266

[16] Haggerty, S..E., "Piezoresistance response of longitudinally and laterally oriented ytterbium foils subjected to impact and quasi-static loading", *J. Appl. Phys.*, (1985), 2464–2473

[17] Winter, R.E. and Harris, E.J., "Perturbations caused by lateral stress gauges", in *Shock Compression of Condensed Matter - 2007*, M. Elert, M. Furnish, R. Chau, N. Holmes and J. Nguyen, eds., American Institute of Physics, Melville, New York (2007), pp. 295–298

[18] Zwick, H.H. and Shepherd, G.G., "Defocusing a Wide-Angle Michelson Interferometer", *Applied Optics*, **10**, (1971), 2569–2571

[19] Barker, L.M. and Hollenbach, R.E., "Laser interferometer for measuring high velocities of any reflecting surface", *J. Appl. Phys.*, **43**, (1972), 4669–4675

[20] Barker, L.M., "The Accuract of VISAR Instrumentation", in *Shock Compression of Condensed Matter - 1997*, S. Schmidt, D. Dadekar and J. Forbes, eds., American Institute of Physics, Woodbury, New York (1997), pp. 833–836

[21] Chapman, D.J., Phd, Cambridge (2009)

[22] Barker, L.M. and Hollenbach, R.E., "Shock-wave studies of PMMA, fused silica, and sapphire", *J. Appl. Phys.*, **41**, (1970), 4208–4226

[23] Hemsing, W.F., "Velocity sensing interferometer (VISAR) modification", *Rev. Sci. Instrum*, **50**, (1979), 73–78

[24] Dolan, D.H., "Foundations of VISAR analysis", Technical Report SAND2006-1950, Sandia National Laboratories (2006)

[25] Barker, L.M., "Multi-beam VISARs for simultaneous velocity vs. time measurements", in *Shock Compression of Condensed Matter - 1999*, M. Furnish, L. Chhabildas and R. Hixson, eds., American Institute of Physics, Melville, New York (2000), pp. 999–1002

Chapter 5

Shock Physics

5.1 Shock Waves

A shock wave can be defined as a "travelling wave front across which there is an adiabatic, discontinuous jump in state variables" [1] or alternatively "the ubiquitous result of matter moving at velocities faster than the speed at which adjacent material can move out of the way" [2]. In practice, this means that a true shock-wave should travel at at least the sound speed of the surrounding medium. In a plate impact experiment, or in a mine blast, the initial shock will be a compressive one. However, as a compressive shock is reflected, either from a free surface, or from a boundary with a material of lower impedance, it will be reflected as a rarefaction wave, known as a release wave.

5.1.1 Conservation Equations

In a simplified system, such as the piston driven one shown in figure 5.1 it is possible to derive a series of conservation equations and a mathematical description of the shock process, subject to a number of assumptions:

- Body forces, such as gravity can be neglected
- Both initial and final states are in mechanical equilibrium
- There is a state of steady flow

- There are no reactions or phase changes (though these can be dealt with through various methods)
- The material is assumed to have zero strength and shear modulus

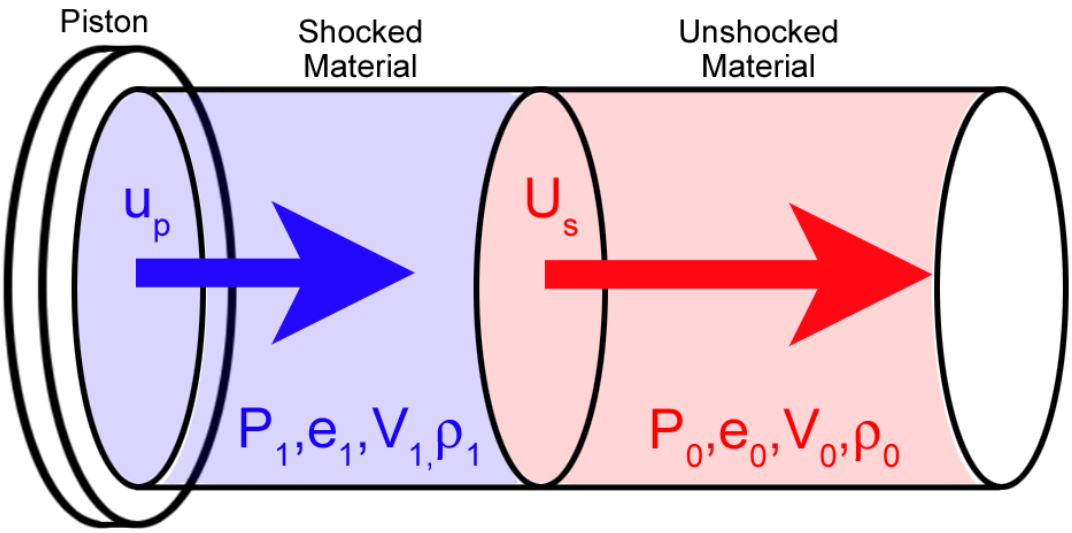

Figure 5.1: Piston driving shocked material into unshocked material. The shock front, moving at U_s is at the boundary between the unshocked (red) and shocked (blue) material. Across the shock front there is a change in state variables as denoted by the change of subscript from 0 to 1. The material behind the shock front, and the piston, move at the particle velocity u_p

In the diagram (figure 5.1) the subscript 0 refers to the original state of the material, and the subscript 1 to the shocked state. P, V and ρ have their normal meanings and e is the energy. Mass, momentum and energy are all conserved across the shock front, thus leading to the following equations for their conservation, equations 5.1, 5.2 and 5.3 respectively:

$$\rho_0 U_S = \rho_1 (U_s - u_p), \tag{5.1}$$

$$P_1 - P_0 = \rho_0 U_s u_p, \tag{5.2}$$

$$P_1 u_p = \tfrac{1}{2}(\rho_0 U_s u_p^2) + \rho_0 U_s (e_1 - e_0). \tag{5.3}$$

While these are the principal governing equations, it should be noted that we can simplify them to give slightly more practical relations. Firstly, by combining equations 5.1-5.3, eliminating the velocities and writing the densities in terms of specific volumes ($V' \equiv 1/\rho$) we arrive at the Rankine Hugoniot equation (equation 5.4). Additionally, in a shock process, usually $P_1 >> P_0$, such that P_0 can be neglected. Finally, as internal energy is a thermodynamic state function, it can arbitrarily be referenced to any initial state, thus meaning e_0 can also be set to zero. This simplifies equations 5.1-5.3 to the forms given in equations 5.5-5.7:

$$e_1 - e_0 = \tfrac{1}{2}(P_1 + P_0)(V_0' - V_1'), \tag{5.4}$$

$$\rho_0/\rho_1 = 1 - u_p/U_s, \tag{5.5}$$

$$P_1 = \rho_0 U_s u_p, \tag{5.6}$$

$$e_1 = (P_1/2)(V_0' - V_1'). \tag{5.7}$$

If we combine equations 5.5-5.7 with an equation of state giving the internal energy as a function of pressure and specific volume then we can get a full definition of the state of the material in five dimensional parameter space. One typical equation of state is the Mie-Grüeisen equation (5.8) where Γ is known as the Grüneisen parameter.

$$(P - P_0) = \frac{\Gamma}{V}(E - E_0). \tag{5.8}$$

Through experimentation we can measure one or two of the variables (if only one is measured, another will need to be inferred, for example from impedance matching) and construct a curve, which gives the locus of all the possible attainable end states from a given starting state. This is known as the Rankine-Hugoniot curve, or more usually just the Hugoniot. If it is centred on an initial state at standard conditions then it is termed the principal Hugoniot. Usually the curve is projected onto two axes to make it easier to interpret. The most common axes are $P - V$, $P - u_p$ and $U_s - u_p$. The loading path is not the Hugoniot itself, but the Rayleigh line, a chord connecting the initial and final state [2]. Note that if the Hugoniot has a cusp then it is not possible for a single chord to be used to connect the initial and final states and consequently two chords and a two wave structure is needed and observed. The gradient of the Rayleigh line in $P - u_p$ space is given by the shock impedance $Z_s = \rho_0 U_s$.

5.1.2 Isentropic Approximation and Release Waves

Occasionally the Hugoniot might be referred to as a shock adiabat. While the shock process in general might be sufficiently fast that heat transfer to the surroundings is impossible, it does not imply that the 'adiabat' takes it's usual meaning of a reversible thermodynamic path. Such a path would entail no change in the entropy, and therefore would be an isentropic path. However it is not generally true that an adiabatic change is isentropic. An isentropic curve can be represented by a curve known as an isentrope.

It can be shown [2] that a material will have an isentrope that is identical to the Hugoniot to the third order in strain. That we can approximate the Hugoniot by the isentrope, particularly for small shocks, is maybe of less importance than the fact that the reverse is also true. This allows us to approximate the release, or unloading path, by using the Hugoniot, which is often what has been experimentally determined.

If the loading and unloading cycle is represented in $P - V$ space, as shown in Figure 5.2 then it is possible to determine the energy lost as a result of the

process. The gain in energy on loading can be represented as the area under the Rayleigh line (though it should be noted that the area bounded by V_0, V_f, P_0 and the V axis is the specific internal energy rather than a gain in kinetic energy). The energy released back to the surroundings on unloading is the area under the Hugoniot (or release curve if different). The shaded grey area in figure 5.2 is known as the waste heat and is the energy lost during the cycle.

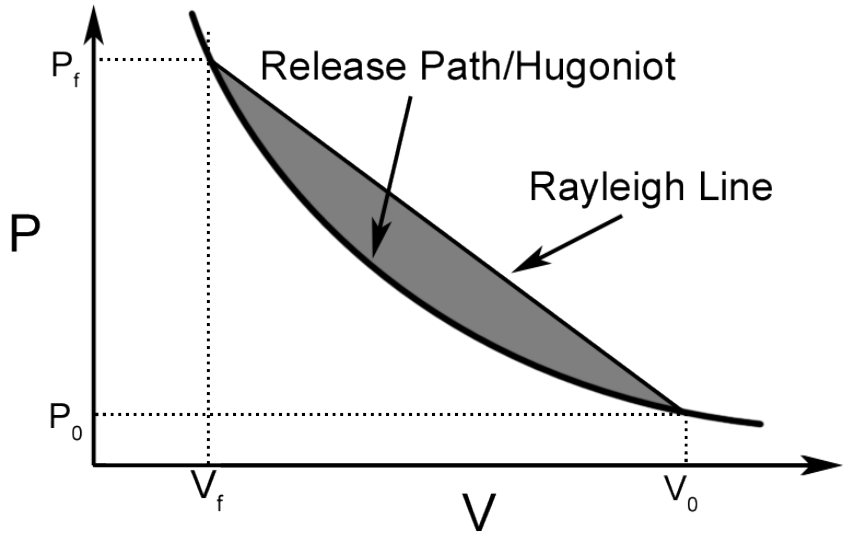

Figure 5.2: Loading and unloading cycle, showing waste heat. The material is loaded along the Rayleigh line and then released along the release path (which can in some cases be approximated by the Hugoniot). The difference between the areas under these lines is the energy difference in the cycle, and is shaded in the figure. Note that in most shock experiments P_0 is sufficiently smaller than P_1 to be negligible.

5.1.3 Wave Profiles

One of the key physical principles underlying large amounts of shock physics theory is the stability and formation of shock waves. In the majority of solids sound speed is an increasing function of pressure (an exception for example would be some forms of quartz where the shock speed falls slightly with increasing

particle velocity at one point on the Hugoniot [3]). This means that a compression wave with a finite rise time will steepen into a shock because the components of the wave at higher pressure will catch up the lower pressure ones, owing to them travelling at a higher speed. This is demonstrated graphically in Figure 5.3. In the figure u_p is the particle velocity, i.e. the velocity at which the wave moves as a whole with respect to the laboratory frame and a_1 and a_2 are the velocity at which certain parts of the wave move with respect to the rest of the wave (this is pressure dependent). The shock will never become a true discontinuity, as there are dissipative effects such as heat transport and viscosity, but above about 10 GPa, it is a reasonable approximation [2]. At lower pressures, steady shocks will form, but the rise times will be longer, and in the range detectable by experimental methods. The condition of shock stability is essentially equivalent to the statements that:

- The shock is supersonic with respect to the material ahead of it. This is equivalent to stating that the slope of the Rayleigh line must be initially greater than that of the Hugoniot/isentrope
- The shock is subsonic with respect to the material behind it (in other words the already shocked material). This is equivalent to the Hugoniot being of greater slope than the Rayleigh line at the final state.

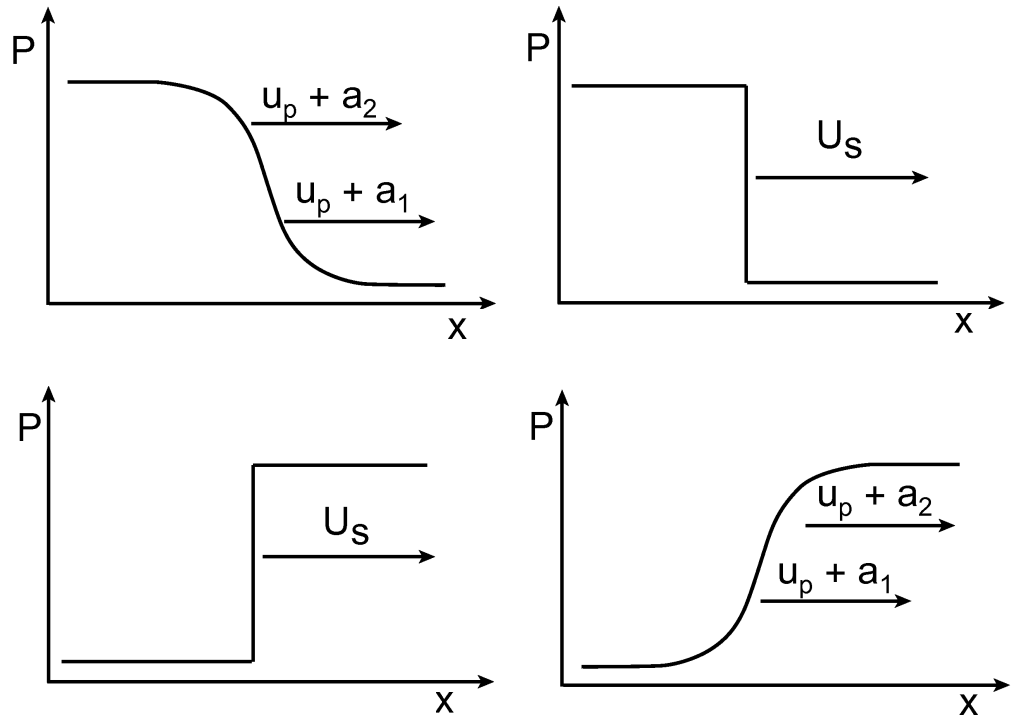

Figure 5.3: $P - x$ diagrams showing wave profiles at two distinct times (left and right) for a shock (top) and a release (bottom). In the top of the diagram, while the whole wave is moving at a velocity of u_p with respect to the laboratory frame, there are also pressure dependent components of the velocity governing the velocity at which parts of the wave move with respect to each other. For most materials the higher pressure components travel at a higher velocity and the wave sharpens into a shock. However the situation is reversed when the wave is reflected as a release (bottom section of the diagram). The release lowers the previously high pressure. The high pressure components of the wave still move faster than the low pressure ones and so the release spreads out.

While shock stability is possible for most solids, there are a few examples where issues arise. In fused silica at low pressures for example, the sound speed decreases with pressure. In elastic-plastic materials, the Hugoniot will have a cusp, and a single Rayleigh line will be unable to join the start and end states. In this situation, there will be two shocks, an elastic and a plastic wave. While each wave will be stable in itself, the two together are not stable, in that the elastic and plastic wave velocities are not the same.

In order to return to the pressure of the surroundings, it is necessary to have waves which reduce the pressure built up in a shock process. Such waves are termed rarefaction or release waves. They occur through interaction of shocks with free surfaces and zero stress boundaries. As release waves are lowering the pressure within the material, and as stated before, the sound speed increases with pressure, a release wave will spread out, as shown in the bottom half of Figure 5.3. While a shock will steepen until dissipative mechanisms become dominant, there are, in a fluid, no significant dissipative mechanisms in a release. Therefore a release can, in many circumstances be treated as an isentropic process. If there is significant plastic deformation however then this will dissipate energy, leading to a non isentropic release and the "waste heat" construction described earlier.

5.1.4 1D Strain and Lateral Stress

The object of a plate impact experiment is to conduct experiments in a regime of 1-D strain. This implies that the material can only deform in the direction of the propagation of the compressive stress pulse, and as such, the material is inertially confined. If we take the direction of the propagation of the compressive pulse (which will also be the direction the projectile travelled) to be the x direction of a cartesian coordinates system then by symmetry the y and z directions will be equivalent. In terms of stress and strain 1-D strain can be defined as stated in Equations 5.9 - 5.11. The subscripts indicate the cartesian directions and ϵ is the strain.

$$\epsilon_x \neq 0, \tag{5.9}$$

$$\epsilon_y = \epsilon_z = 0, \tag{5.10}$$

$$\sigma_y = \sigma_z. \tag{5.11}$$

If the amplitude of the compression wave is small then the material response will be elastic. From the conditions of 1-D strain we can then derive Equation 5.12 [4]:

$$\sigma_x = \frac{1-\nu}{\nu}\sigma_y. \tag{5.12}$$

From Equation 5.12 and the definitions of hydrostatic pressure (Equation 5.13) and shear stress (Equation 5.14), we can derive an expression for the stress in terms of these parameters. This explains why, in a fluid or in an overdriven shock it is possible to approximate the longitudinal stress by the hydrostatic pressure, namely that the shear strength is sufficiently negligible that it can be taken to be zero. Equations 5.12 and 5.14 can then be used to derive the theoretical shear stress for an elastic wave, Equation 5.15.

$$P = \frac{\sigma_x + \sigma_y + \sigma_z}{3}, \tag{5.13}$$

$$2\tau = \sigma_x - \sigma_y, \tag{5.14}$$

$$\tau = \frac{1-2\nu}{2(1-\nu)}\sigma_x. \tag{5.15}$$

As the amplitude of the shock increases, the elastic wave description no longer holds, and some form of non-elastic deformation occurs. The Hugoniot Elastic Limit (HEL) defines this onset of plastic deformation, and can be related to the dynamic compressive strength (Y) by the relationship given by Rosenberg [5] in Equation 5.16. If the shock is overdriven, well beyond the point of the onset

of the plastic deformation then we find that the empirical "shock equation of state" (Equation 3.1) holds well for many materials [3]. In the middle region of shock amplitude, behaviour will differ from material to material depending on the nature of the plastic deformation involved. If the material response is termed "elastic, perfectly plastic" then we assume that there is no strain hardening and that additional shear stresses cannot be supported. This description however does not apply well to some metals, which exhibit significant strain hardening.

$$\sigma_{HEL} = \frac{1-\nu}{(1-2\nu)^2} Y. \tag{5.16}$$

The constants in the shock equation of state (Equation 3.1) are empirical constants, however they can be tied to certain physical realities. The constant C_0 can be approximated as the bulk sound speed, which is equivalent to the shock speed at zero pressure. It can be shown [6] that the constant s is related to the first pressure differential of the zero pressure bulk modulus.

As the analysis is based on a 1-D strain environment, it is important that such an environment is maintained. The main concern in a plate impact geometry is releases from the various free surfaces in the experiment. Releases from the rear surface of the flier plate and the rear of the target are fairly easy to account for. More complicated are the lateral releases that move into the sample from the edges. One way of estimating the extent of 1-D strain is to use Equation 5.17, quoted in Willmott [1]. This states that a gauge embedded in a sample which is struck by a flier of radius r will still be in a state of 1-D strain if the inequality in Equation 5.17 holds.

$$r \geq c_l t. \tag{5.17}$$

Recent work by Swift and Kraus [7] has suggested an alternative to the above formula (Equation 5.18), and suggests that a 45° angle of erosion of the 1-D stress state is not always appropriate. The angle ϕ is the angle between the extent of the 1-D strain region and the normal, i.e. the direction of propagation of the plane shock:

$$tan\ \phi = \frac{1}{U_s}\sqrt{c_a^2 - (U_s - u_p)^2}, \tag{5.18}$$

where c_a is the sound speed on the Hugoniot, or the slope of the isentrope in $\sigma - \rho$ space.

5.2 Derivation of Data and Experimental Design

5.2.1 General Sample Preparation

All of the samples in this study were ground flat and parallel to a tolerance of approximately $\pm 0.01mm$. Gauges were encapsulated with slow setting epoxy that was left overnight to cure. To ensure flat planar gauge packages with minimal thicknesses, samples were pressed between glass blocks supported in a custom designed sample press. Where necessary, gauges were insulated by mylar sheets inserted between the gauge and the sample. Where the use of VISAR was appropriate, the stand-off distance required was either achieved through the use of a PMMA holder attached to the back of the sample, or through affixing the fibre to the rear of a PMMA window on the back of the target. The laser light was reflected from either brass shim (0.002 inch), the copper witness plate (in the case of the reverse impact configurations) or from a layer of silver dag painted on the surface of the specimen.

Most of the consumable materials for the experiments, with the exception of the rock samples themselves, were supplied by Pope and Meads Ltd. This included the aluminium sample rings, the sabots and the metal stock. The metal stock has been tested and found to be in good agreement with the Hugoniot values used in subsequent data analysis [8].

5.2.2 Principles of Data Derivation

Deriving data from plate impact experiments relies on measuring, either directly or indirectly two of the five parameters necessary to achieve a full description of the material response to shock loading. An example of a direct measurement would be an embedded stress gauge, which, when calibrated, gives a direct output of the stress in the material of interest. An indirect measurement would be to deduce the particle velocity of a flier by measuring the free surface velocity of the target using a VISAR system. It is then possible to use some simple principles to calculate one of the other parameters. The main principle used in this thesis is that at the interface between the impactor and the target it is not possible to sustain a discontinuity in either particle velocity or stress. If this was the case then the materials would either move apart instantaneously, or merge into each other.

A useful way of describing this principal of conservation of stress and particle velocity is graphically, in stress-particle velocity space. If two materials impact each other and are in a state which is equal in terms of stress and particle velocity, then graphically there must be an intersection of the Hugoniots of the two materials. This is evident from the fact that from a given initial condition, the Hugoniot describes the locus of the possible final attainable states for the material. In a plate impact experiment, the initial conditions are fairly easily described. The initial stress or pressure is effectively zero, both due to the fact that the apparatus is evacuated and the fact that atmospheric pressure is negligible compared with the pressures reached during impact. The initial particle velocity of the target, in the lab frame of reference is zero. The initial particle velocity of the flier is measured less than 500 μs before impact by sequential shorting pins, as shown in the schematic in Figure 5.4.

Figure 5.5 shows a graphic representation of a plate impact experiment. The initial velocity is determined and used as the x-axis intercept for the flier Hugoniot. As the impact will decelerate the flier (decreasing u_p) and accelerate the target (increasing u_p) it is clear that the directions of the two Hugoniot curves

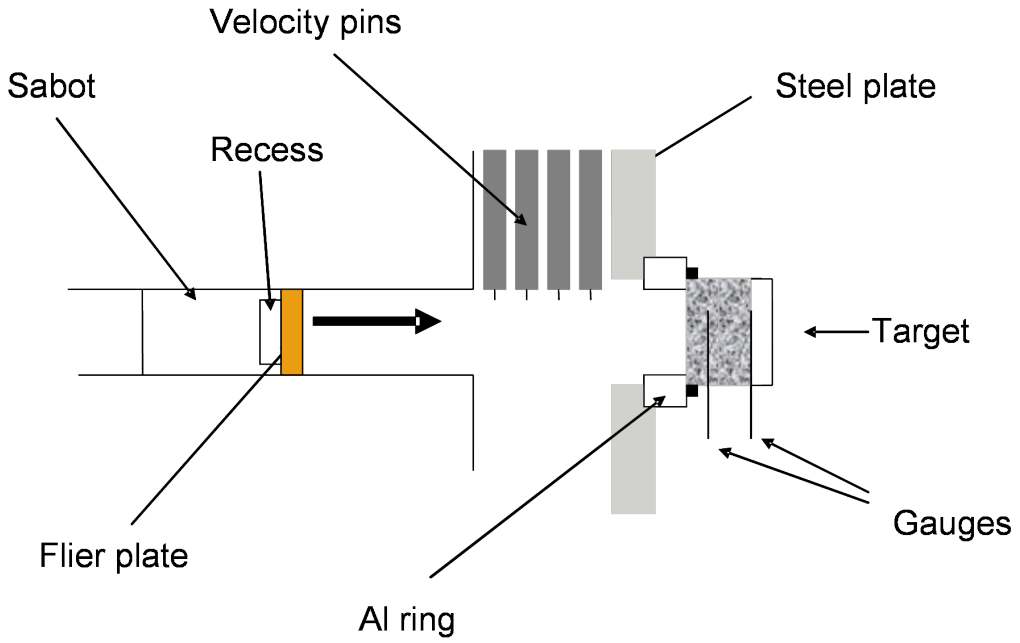

Figure 5.4: Schematic of an experiment in the plate impact facility. The sabot moves from left to right, and the impact velocity is measured by a series of shorting pins as the flier passes them. The flier then impacts the target which is mounted on an aluminium sample ring. The sample ring is in turn lightly fastened so that it is flush with a steel plate. This steel plate is shown in figure 4.5 and can be aligned to ensure that the impact is planar. The shock wave that is produced by the impact is then detected by the gauges and recorded on an oscilloscope.

will be opposite. If we have a knowledge of one of the Hugoniots before we start the experiment, and know the impact velocity then Figure 5.5 shows graphically that only one measurement is needed to determine a point on the Hugoniot of the material of interest. In the case of symmetric impact (where the target and the flier are made of the same material), the well characterised material is not required. We know from the geometry that the particle velocity will be half of the impact velocity, and a measurement of stress is sufficient to ascertain the shock state.

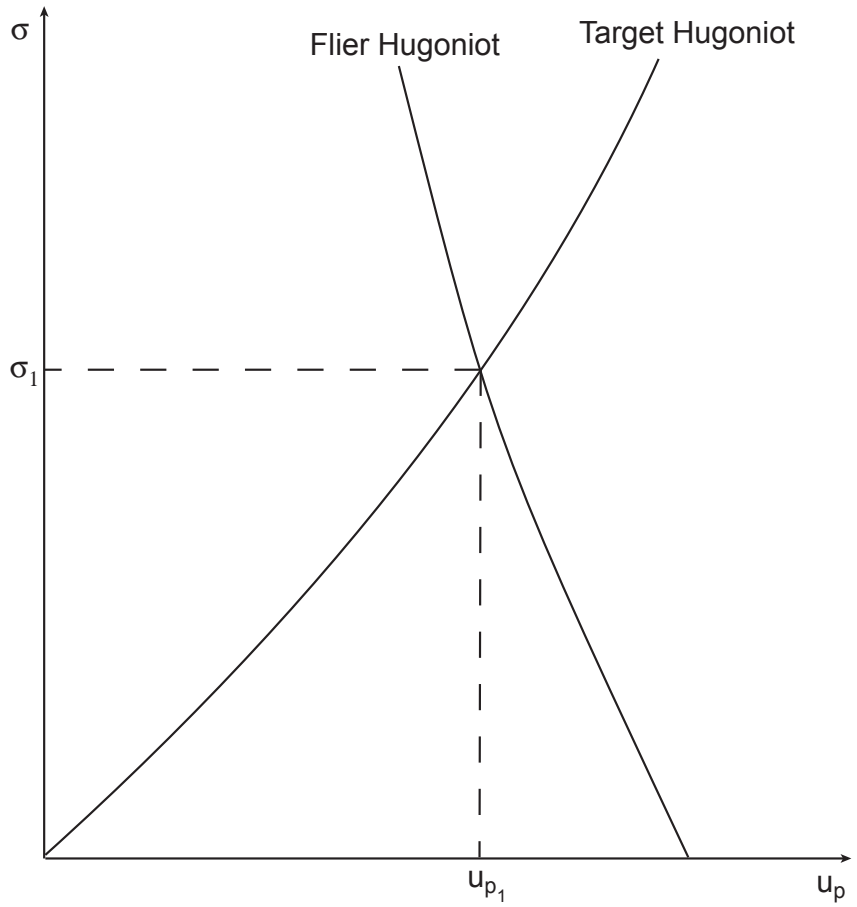

Figure 5.5: Derivation of shock state through the use of a graphical method. The initial state of the target is zero particle velocity and stress. Similarly the initial stress of the flier is zero, but the particle velocity is the (measured) impact velocity. The target will be stressed and accelerated by the impact, the flier stressed and decelerated, hence the flier Hugoniot has a negative slope and the target a positive slope. If either σ_1 or u_{p_1} are measured, knowledge of the Hugoniot of either plate will allow for a point on the other material Hugoniot (in $\sigma - u_p$ space) to be determined.

5.2.3 Compressional Data - Hugoniots and Releases

In this thesis, there have been three different types of longitudinal experiments performed. The two main impact configurations are shown in Figure 5.6. The top diagram shows a conventional impact and the bottom diagram a reverse impact. The reason for the two types of experiments is partially that initial results with direct measurements of stress with gauges led to a high level of experimental error, and partially that the reverse configuration allowed for release data for the materials to be collected simultaneously. The third type of longitudinal experiment was designed primarily to measure the shock speed and involved a rock sample between two gauge containing aluminium anvils (this is shown in 5.11).

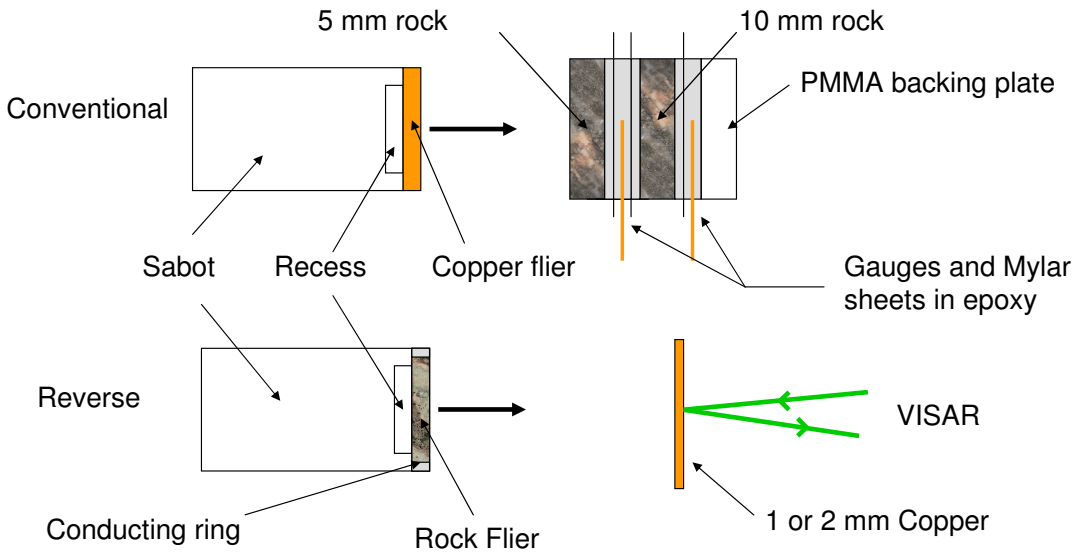

Figure 5.6: Diagram for the two main longitudinal impact configurations showing conventional impact (top) and reverse impact (bottom). The conventional impact configuration allows for the measurement of stress and shock velocity within the one experiment. It also directly measures stress in the material, and does not need to infer this from the knowledge of the copper Hugoniot. While the reverse impact configuration does not measure in-material information, it does allow for the release properties of the flier material to be examined as well as determining a point on the Hugoniot.

In the conventional experimental configuration the graphical interpretation is very similar to that in Figure 5.5, in particular in the embedded gauge (i.e. the gauge package sandwiched between two rock discs). The back surface gauge is slightly more complicated, but still fairly easily explained, as shown in Figure 5.7. The initial impact means that the rock between the two gauges is in the state described by the crossing point of the target and flier Hugoniot. As this interacts with the rear surface material (PMMA in these experiments), a release (if the rear surface material is of lower impedance to the rock) propagates back into the rock and the rear surface material is shocked up to the state marked 2 in Figure 5.7. The rear surface gauge shown in Figure 5.6 will record a value of σ_2. It should be noted however that this analysis assumes that the release in the rock is the reverse of the Hugoniot. Whether this is the case can, in theory be determined by this sort of experiment as the rear surface gauge must record a state which lies on both the rock release curve, and the rear surface material Hugoniot.

To obtain release data, a reverse experimental configuration is used with a thin "witness" plate. The schematic for the experimental set up is shown in the bottom of figure 5.6 while figure 5.8 shows an $x - t$ diagram of the experiment. In the $x - t$ diagrams in the current study the frame of reference is the interface between the flier and the target, such that the interface remains in a constant position with respect to the horizontal axis (which denotes distance). The vertical axis represents time. Initially a shock travels back into the flier and forward into the copper target plate. These shocks are both reflected as releases from the free surfaces. The release from the rear of the flier, due to the relative thickness of the flier and the target plate, is irrelevant to the remainder of the experiment. The wave in the copper plate then reflects back and forth within the plate as a series of shocks and releases. As there must be continuity of pressure and particle velocity at the rock-copper interface the reloading of the copper is characteristic of the release state in the rock. This can be illustrated by looking at the plot in Figure 5.9.

At position 1 in the diagrams, the rock and the copper are shocked up to a particular level. This level is the intersection of the two Hugoniots in figure 5.9.

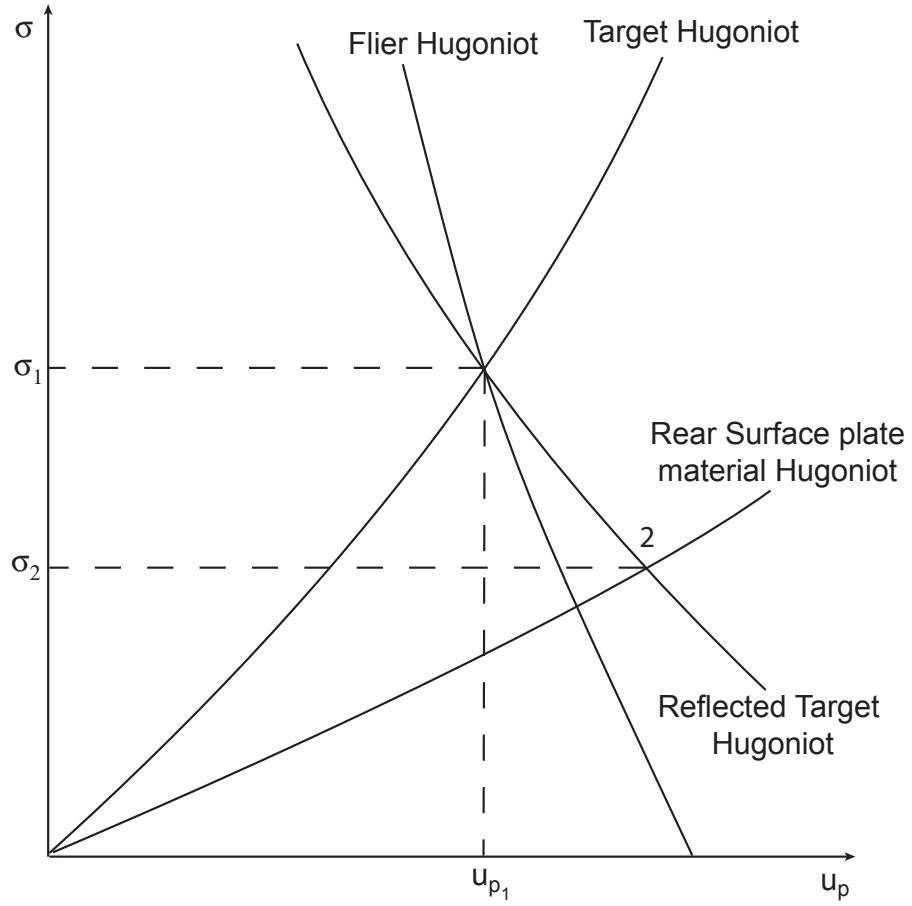

Figure 5.7: Showing data derivation with a rear surface gauge. The initial impact creates a situation that is described in figure 5.6. After this both the flier and the front target plate are in the shock state denoted by σ_1 and u_{p_1}. This front plate then interacts with the rear plate, made of a material that is still at rest, hence the positive sloping rear plate Hugoniot. This material is shocked, and so the particle velocity and stress both increase. As the rear plate material is of lower impedance, the interaction causes the front plate to be released. Therefore the shock state measured by a rear surface gauge is both on the Hugoniot of the rear surface material and the release path of the target plate Hugoniot (which in certain circumstances is well approximated by the reverse of the Hugoniot). The rear surface gauge therefore measures the state denoted by σ_2 and u_{p_2}

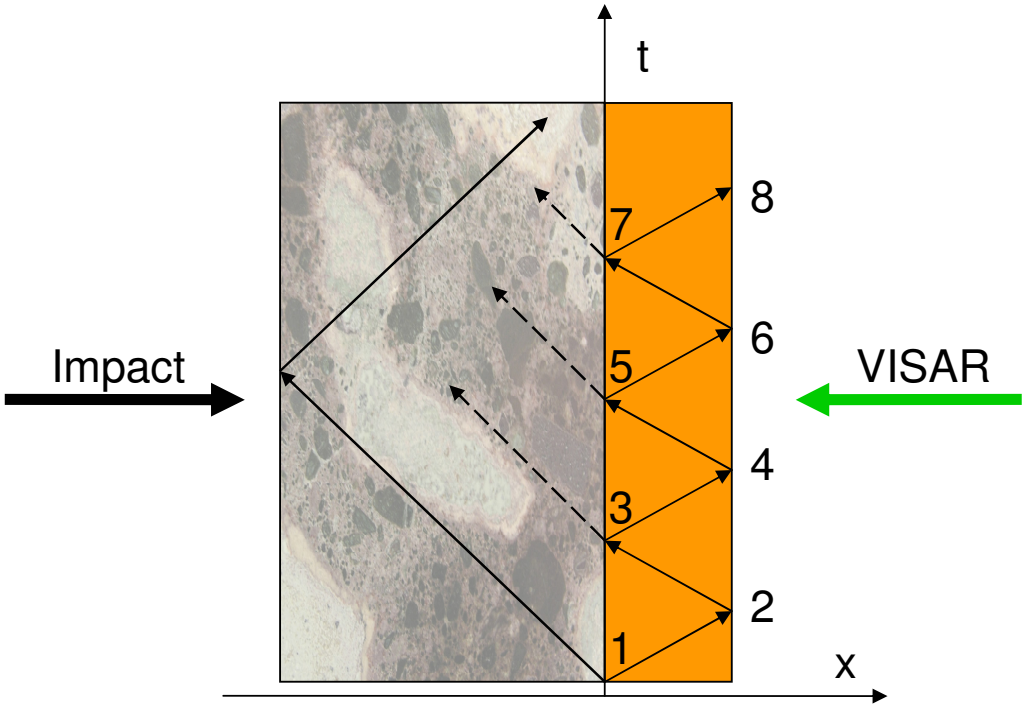

Figure 5.8: $x-t$ diagram showing shocks and releases in the copper witness plate. As there is a continuity of stress and particle velocity across the interface, each of the reverberations measured in the copper contains information about the release state in the rock flier. Multiple reverberations allow for a series of points on the release curve of the rock to be obtained.

Position 2 is where the copper has released from it's rear surface, and the stress returns to zero. It is assumed that the release of the copper in Figure 5.9 is merely the reverse of the Hugoniot. It has been demonstrated by Chapman [8] that this is a reasonable assumption for the specific copper stock used in these experiments. As the rear surface releases, it acquires a particle velocity which can be recorded by the VISAR. This value is labelled 2 in figure 5.10 and allows the calculation of the Hugoniot point for the experiment. After interacting with the rock again, at point 3, a shock is again propagated into the copper, reloading it to a new state in stress and particle velocity. At the rock copper interface, a release propagates into the rock, meaning that the shock reflected back into the

copper has the characteristics of the rock release.

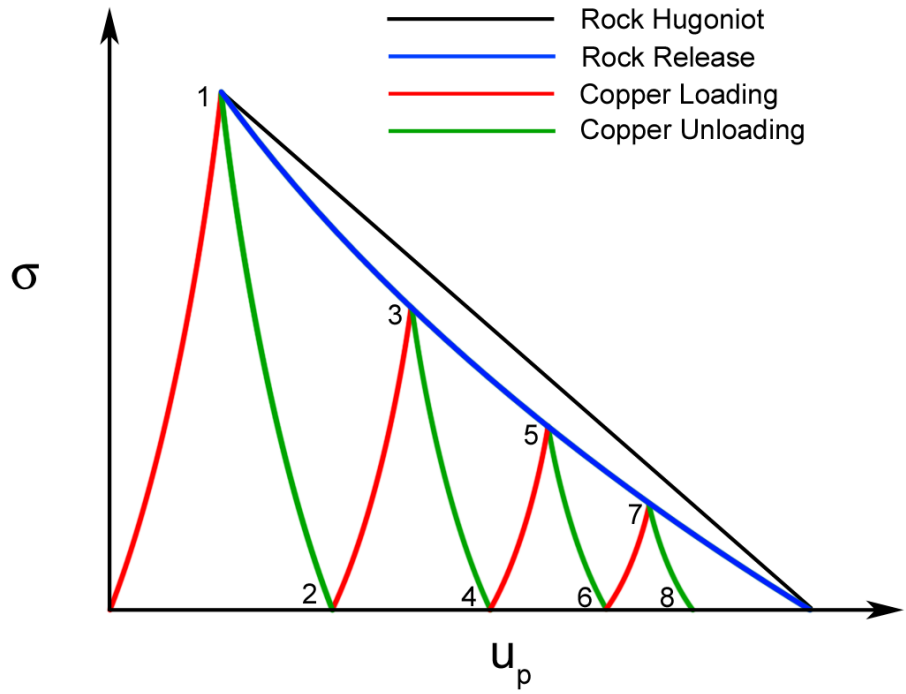

Figure 5.9: Plot in stress-particle velocity space showing the determination of a release path. The method is essentially the same as that described in figure 5.7 except that the rear surface is now a vacuum which has a Hugoniot concurrent with the horizontal axis. It is the value of particle velocity denoted 2 that is measured by the VISAR, as the VISAR monitors the free surface velocity. This will be twice the particle velocity in state 1, provided that the copper release can be approximated by the reverse of the Hugoniot. With the material now in state 2, the process is essentially repeated, such that state 4 is measured by the VISAR and used, along with a knowledge of the copper Hugoniot to derive the shock state denoted 3 in the figure.

When the shock is again reflected, this time from the rear face of the copper, it means that the copper receives a further boost in particle velocity, labelled 4 in Figures 5.8 - 5.10. Using the information from the VISAR signal, and a

knowledge of the copper Hugoniot it is possible to determine the stress and particle velocity of the state labelled 3 in Figure 5.9. When sufficient experiments have been conducted it is possible to decide whether or not this state lies on the Hugoniot or not. The shock and release reverberations continue in the same manner, through the labels 5-8 in the diagrams. It is therefore possible from the VISAR experimental record shown in Figure 5.10 to obtain not only a Hugoniot point, but a number of points on the unloading curve. The exact number of points is determined by the number of levels that can be distinguished in the VISAR record. As the rock becomes more and more fully released, the steps in the VISAR trace become progressively smaller and this therefore limits the number of points before the release from the rear of the flier (or indeed lateral releases from the edges of the projectile) completely invalidates the measurement.

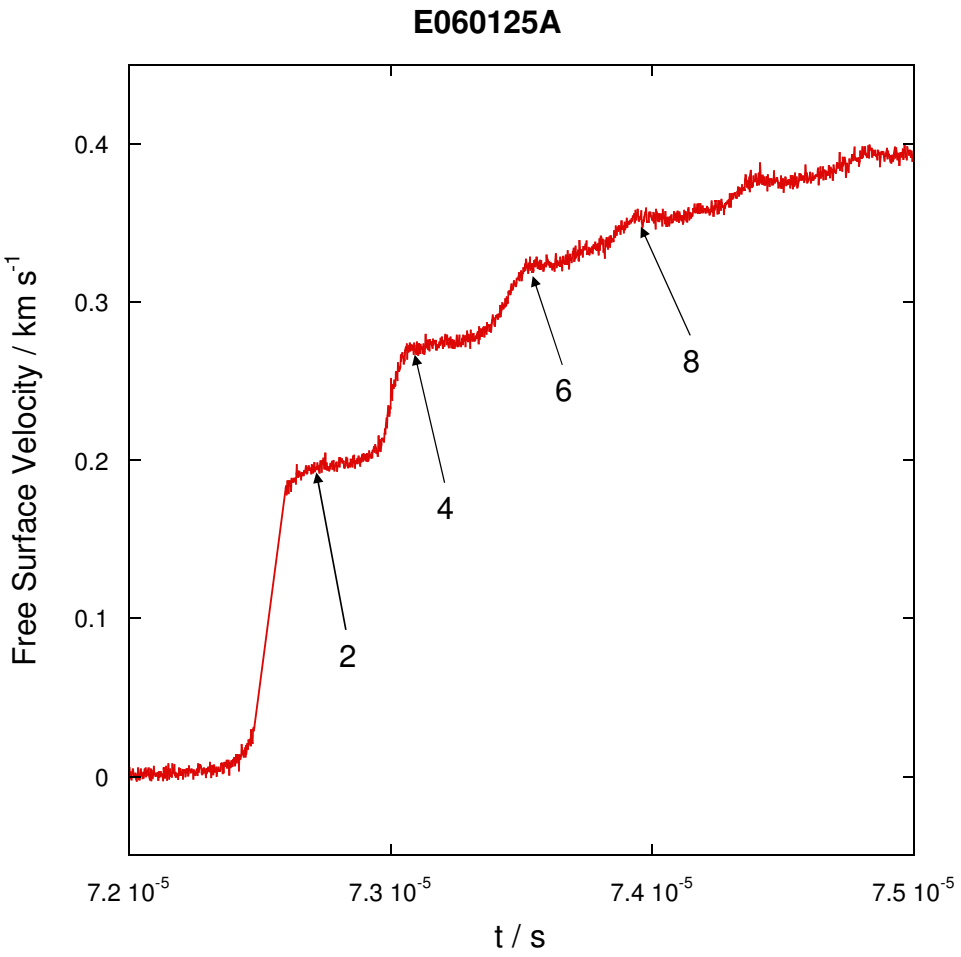

Figure 5.10: Typical VISAR trace for a reverse impact experiment. The numbers denote the shock states as labelled in figures 5.8 and 5.9. To determine the Hugoniot and release points, the plateau values are determined and then used in conjunction with the copper Hugoniot.

5.2.4 Shock Speed Measurements

A further measurement that it is possible to make to help determine the Hugoniot is that of shock speed. This can be measured, as it is in many of the Marsh [3] datasets using a streak camera or high speed framing camera. It is also possible to measure shock speed using the time of arrival of the shock pulse at diagnostics such as stress gauges. The experimental set up shown in Figure 5.6 will allow for this although it is possible to refine the design somewhat to give more reliable results. A concern with the design in Figure 5.6 is that the heterogeneous nature of the rock will cause the rise of the gauges to be noisy and therefore the time of arrival will be difficult to determine. It is advantageous therefore to have a design that allows for the gauges to be in a more favourable environment with a transition through the rock between two protected gauges. With improved rise times and with the shock speeds in the "anvil" material and epoxy able to be calculated from literature values, it is therefore possible to calculate the shock speed in the rock with a good degree of accuracy.

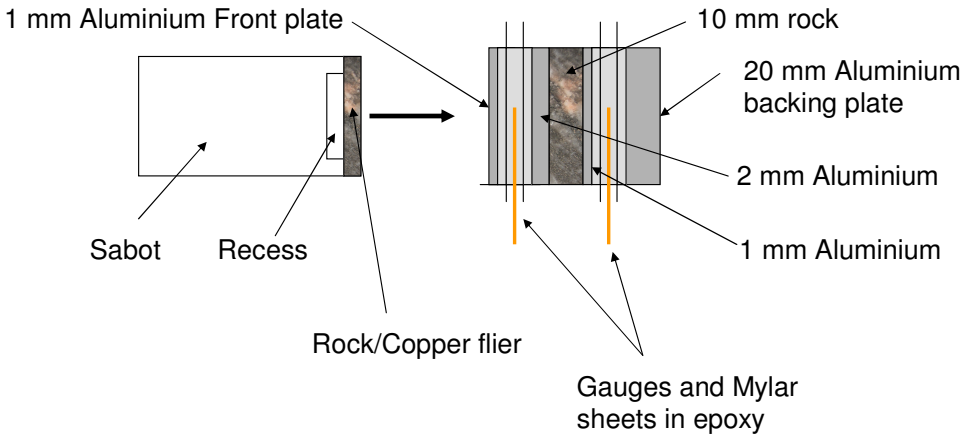

Figure 5.11: Experimental design for measuring shock speed with aluminium anvils (i.e. the gauge is placed between two aluminium plates). The purpose of the anvils is to eliminate any effect of inhomogeneity from the rock material.

If a rock impactor is used, then as with the reverse impact design described above, it is possible, through knowledge of the aluminium Hugoniot to derive points on

the rock Hugoniot in addition to the measurement of shock speed.

5.2.5 Waste Heat Measurements

In section 5.1.2, brief detail was given that a knowledge of the shock state and the release states of a material allow for the calculation of "waste heat", namely the energy that is irretrievably lost in shockloading a material (i.e. it is not released back to the environment upon unloading). This was diagrammatically represented in figure 5.2. In the experimental designs that have been described in the previous section (with the exception of the ability to measure shock velocity as described in section 5.2.4) all measurements are either of particle velocity or stress. This means that the final data is in $\sigma - u_p$ space and requires transformation into $\sigma - V$ space before any calculations on the waste heat are attempted. It should be noted that this conversion is approximate, and as such approximations such as the equivalence of P and σ (not strictly true except in cases where material strength is zero) are used. The limiting approximation in the calculation is the lack of points in $\sigma - V$ space to which a curve can be fitted to give an accurate release path. The fact that this is a major source of error means that approximations in the transformation of data from $\sigma - u_p$ are of less importance.

In the book High-Pressure Shock Compression of Solids [2] equation 5.19 (note that the subscript 0 denotes the initial conditions) is derived from the jump conditions and relates the pressures, particle velocities and volumes across a discontinuity such as a shock wave. It is further noted that in the limit of small discontinuities equation 5.20 holds generally, and is therefore valid on release curves. If it is assumed that the initial conditions are ambient conditions and that the initial specific volume is merely the inverse of the density, it is possible to convert the data derived from the experiments into $\sigma - V$ space. Whilst a full integration along the release path would be the ideal for data reduction, given the other potential sources of error in determination of the release path, equation 5.19 was used in a step-wise manner on the data obtained to give a release path in $\sigma - V$ space. The initial point on the release is the Hugoniot point, where stress

and particle velocity are known, and the volume can be found by applying equation 5.19 to initial conditions of zero pressure and particle velocity. Subsequent points on the release can be transformed into σ - V space in a similar manner. This can be considered a first order approximation.

$$u - u_0 = \sqrt{(P - P_0)(V_0 - V)} \tag{5.19}$$

$$du = \pm\sqrt{dPdV}. \tag{5.20}$$

After converting the data into a suitable space the aim is to find the areas under the loading and unloading paths and the difference between them. The area under the loading path is easy to determine as the loading path is merely a straight line joining the initial conditions and the Hugoniot point. The unloading line is slightly more problematic. Depending on how easy it is to determine the level on the appropriate VISAR trace, the number of points on the release curve is variable, but unlikely to be above five. The final point on each release is derived from the final velocity of the witness plate in the experiment. It is then necessary to fit some function to these points to allow the area under such a function to be calculated. As the data are experimentally derived it cannot be expected that all of the points will fall exactly on a line which is easy to fit a function to, and with so few points, one slightly anomalous point will cause a major discrepancy in any waste heat calculation. In order to slightly alleviate this problem, the analysis has been carried out with two separate methods of fitting the release points. The two methods used were the fitting of a second order polynomial and the trapezium rule. While smooth curve fitting is the ideal, and hence the use of the polynomial fit, with so few points it is easy to end up with a physically unrealistic plot, for example giving a negative volume. In such case it is useful to use the trapezium rule which does not suffer from the same problem.

5.2.6 Lateral Stress and Dynamic Shear

As mentioned previously, measuring the lateral stress is accomplished by embedding gauges in a lateral orientation within the sample, as shown in Figure 5.12.

Often two gauges are used per sample in order to give an indication as to whether any significant attenuation is taking place over the distance of travel in the sample. Having a layer of epoxy parallel to the direction of travel of the projectile means that it is possible for epoxy be compressed preferentially down this layer, termed jetting. This would lead to erroneous results. To prevent this from happening, a cover plate is used on the front of the sample. With some of the rock types it is not possible to cut a thin enough sample to make a coverplate and therefore a copper cover plate (matched to the projectile) is used. The differences between these two methods are illustrated in the two halves of Figure 5.12.

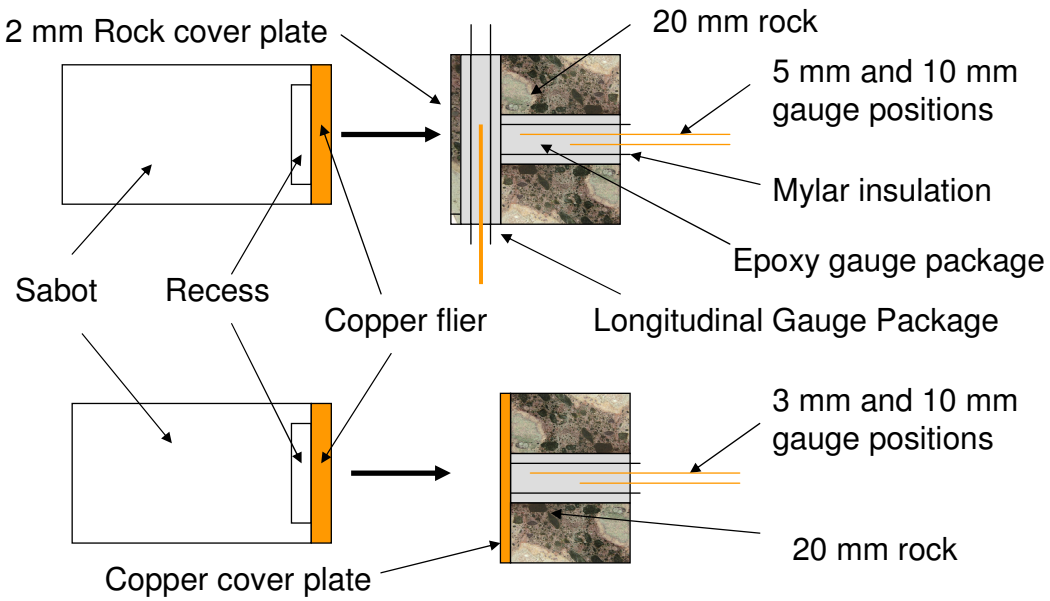

Figure 5.12: Experimental design for lateral gauge experiments. While the lateral gauges were the main diagnostics for these experiments (and can be seen in both the top and the bottom of the figure), in certain materials it was possible to obtain additional longitudinal data through the placement of a longitudinal gauge behind a cover plate made of the rock under investigation. In some cases, either the material was unable to be cut into thin enough discs for cover plates, or the gauge data was deemed unlikely to be sufficiently reliable/useful, in which cases, a copper cover plate was used.

When a rock cover plate was used it was possible to use a longitudinal gauge in the target as well to try and obtain additional information about the Hugoniot of the material concerned. This did not affect the lateral experimental set up, and was placed so that the gauge was not over the epoxy layer joining the two halves of the lateral section together.

5.2.7 Spall and Dynamic Tensile Strength

A measurement of the spall strength of a material can be taken as a measure of the dynamic tensile strength of the material. The way that this is achieved in a plate impact experiment is through the interaction of release waves. This is shown schematically as an $x-t$ diagram in Figure 5.13. The impactor is moving from left to right in the diagram and at impact a shock propagates into both the flier and the target, putting both materials into the state labelled 2. This is shown in red in the diagram. From the previous graphical representation of crossed Hugoniots (Figure 5.5) it is clear that the shock raises the particle velocity in the target and reduces it in the flier. As the shocks are reflected as releases (which are shown in blue), the particle velocity increases further in the target, and decreases further in the flier, which is state 3. The release in the flier propagates into the target as well. At this stage there is a right going release decelerating material to the left, and a left going release accelerating material to the right. As these waves interact (denoted by the deeper blue coloured region) there is a movement to pull the material apart. If this pulling force exceeds the dynamic tensile strength of the material then a spall plane will be formed and material breaks up.

Two distinct experimental set-ups (shown in Figure 5.14) were utilised in finding the spall strengths of geological materials in this thesis. While in essence they create the spall in the same way (i.e. the wave interaction described above) there are subtle differences in both the design of the targets and the extraction of data from the experiments. The target design shown in the top half of Figure 5.14 has a silvered surface painted onto the rear of the target and uses VISAR to directly monitor the free surface velocity of the rear face of the target. The target design in the bottom half of Figure 5.14 was used after the initial design

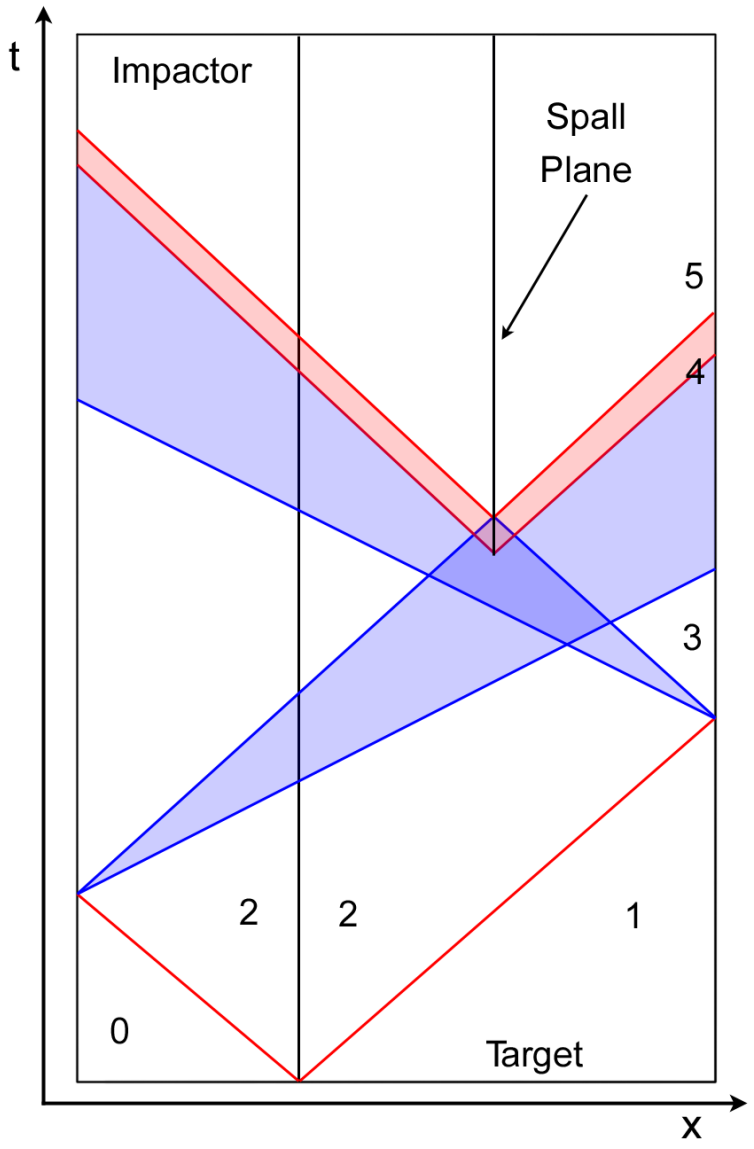

Figure 5.13: $x - t$ diagram of spall. Red indicates shocks, and blue releases. Initially, both the target and the flier are shocked up to state 2. Releases are then propagated from both the rear of the impactor and the rear of the target. As these releases interact in the centre of the material, they can cause the material to fail (if the tensile strength is exceeded). The failure of the material causes a re-shock to be propagated towards the rear surface, from the spall plane. The interactions of this series of waves with diagnostics at the rear of the target (either VISAR or gauges) causes a distinct profile, as can be seen in figure 5.16.

seemed to be failing to produce consistent results. The revised design has a 1mm layer of PMMA intended to prevent fragments from being ejected from the rock material prematurely. Additionally there is both a stress gauge and VISAR as diagnostics. This gives a back-up should one of the diagnostics fail to capture the data required. This is similar to the experimental set-up used by Grady [9] in his 1979 paper on spall in rock. ence they create the spall in the same way (i.e. the wave interaction described above) there are subtle differences in both the design of the targets and the extraction of data from the experiments. The target design shown in the top half of Figure 5.14 has a silvered surface painted onto the rear of the target and uses VISAR to directly monitor the free surface velocity of the rear face of the target. The target design in the bottom half of Figure 5.14 was used after the initial design seemed to be failing to produce consistent results. The revised design has a 1mm layer of PMMA intended to prevent fragments from being ejected from the rock material prematurely. Additionally there is both a stress gauge and VISAR as diagnostics. This gives a back-up should one of the diagnostics fail to capture the data required. This is similar to the experimental set-up used by Grady [9] in his 1979 paper on spall in rock.

To derive data from the spall experiments, it is necessary to look at the stress or particle velocity history of the rear surface or the interface of the material and the window. The wave interactions are the same in the case with and without a window material, as the window impedance is generally lower than the target material impedance. This is also the case with the rough vacuum inside the gun, which nominally has an impedance of zero. The diagrams in Figures 5.13 and 5.15 allow an understanding of the method of data analysis. In the initial compression, the flier and the target are shocked from states 0 and 1 until they are both in state 2. However this is not registered in any diagnostics until it reflects as a release from the interface or the free surface. This is state 3 in the diagrams. If there is a free surface and not a window then the release will take the material in state 2 all the way to zero pressure and the VISAR will measure a free surface velocity peak of approximately twice the u_p value of state 2. If a window is present then the diagnostics will register the pressure and particle

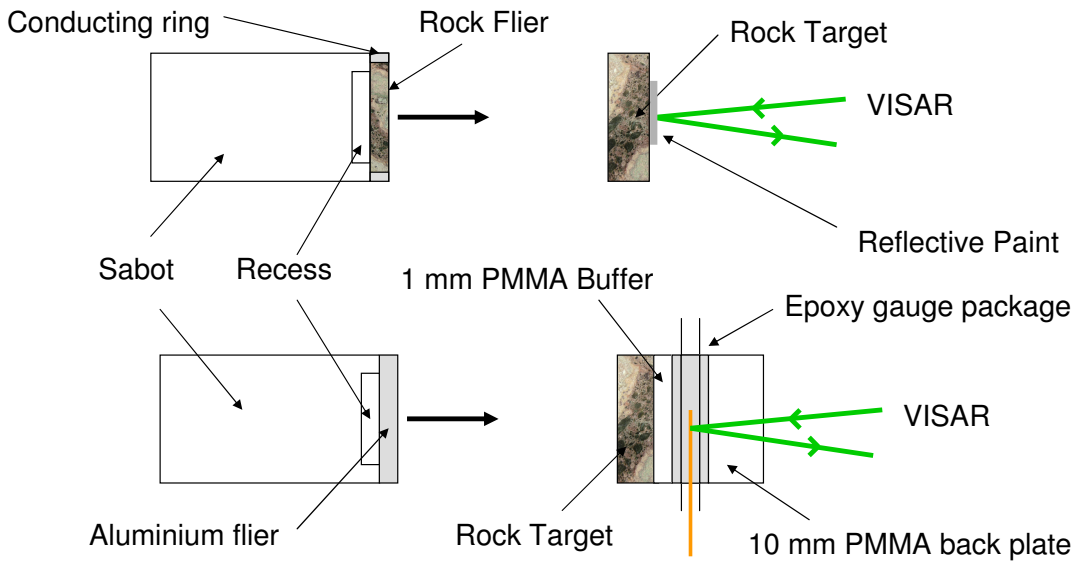

Figure 5.14: Schematics of spall experimental set-ups, with and without windows. Whilst the symmetric impact monitored with VISAR (top of figure) is the simplest set-up, it was speculated that the more complex design shown in the bottom half of the figure would produce more consistent results. This more complex design has multiple diagnostics and a thin PMMA buffer plate designed to prevent potential fragments from the rear of the target damaging the diagnostics.

velocities denoted as σ_{max} and u_{max} in Figure 5.15.

After the initial rise in pressure and particle velocity at the rear of the sample, the next interaction seen at the interface/free surface is the release that propagates from left to right in Figure 5.13. This reduces the particle velocity and the stress. This wave is only registered in the diagnostics after interaction with the free surface or window material. This means that while the target releases along the release path for the target material, the diagnostics record along the window or vacuum Hugoniot. This means that while the target reaches state 4 the diagnostics measure σ_{min} and u_{min}. If there is no spall, then the rock will fully release (at the rear edge) back to a state of zero stress and particle velocity. If spall occurs and a new surface is created then the release will not be complete. After the spall has occurred, the left going release wave shown in Figure 5.13

reflects from the free surface as a compression wave. When this interacts with the free surface/window interface, it is detected in the diagnostics as a reloading signal. Under the reload the rock will attain state 5 in Figure 5.15, where stress is zero. If no window is present then this particle velocity is measured as u_0. If a window material is present then the values recorded are σ_0 and u_0 as shown in the figure.

In the simple case that the Hugoniots are straight lines and that the release waves can be approximated by the Hugoniot, it is possible to derive simple analytic solutions to find the spall strength. If the Hugoniot and release characteristics are more complicated, then the analysis is more involved. However in the case of low velocity impacts into brittle materials, such as the rocks described in this thesis, this is of negligible concern as the stresses involved are small and there is little chance of plastic behaviour. The following formulae can then be easily derived to give the spall strength σ_T. There are slightly different formulations depending on whether a window is present (Equations 5.21 - 5.24) or not (Equation 5.25), whether stress (Equations 5.21 and 5.23) or particle velocity (Equation 5.22 and 5.24) is measured and whether the drop caused by the release (Equations 5.21 and 5.22) or the height of the rebound signal (Equations 5.23 and 5.24) is the most appropriate measure of spall. Kipp and Grady [10] comment that expressions using u_0 and u_{min} are more appropriate when $u_0 - u_{min}$ or $\sigma_0 - \sigma_{min}$ is small compared with $u_{max} - u_0$ or $\sigma_{max} - \sigma_0$.

$$\sigma_T = \frac{1}{2}\left(\frac{Z_s}{Z_w} - 1\right)\sigma_{max} - \frac{1}{2}\left(\frac{Z_s}{Z_w} + 1\right)\sigma_{min}, \tag{5.21}$$

$$\sigma_T = \tfrac{1}{2}(Z_s - Z_w)u_{max} - \tfrac{1}{2}(Z_s + Z_w)u_{min}, \tag{5.22}$$

$$\sigma_T = \frac{1}{2}\left(\frac{Z_s}{Z_w} + 1\right)(\sigma_0 - \sigma_{min}), \tag{5.23}$$

$$\sigma_T = \tfrac{1}{2}(Z_s + Z_w)(u_0 - u_{min}), \tag{5.24}$$

$$\sigma_T = \tfrac{1}{2}Z_s\left(u_{min} + u_{max}\right). \tag{5.25}$$

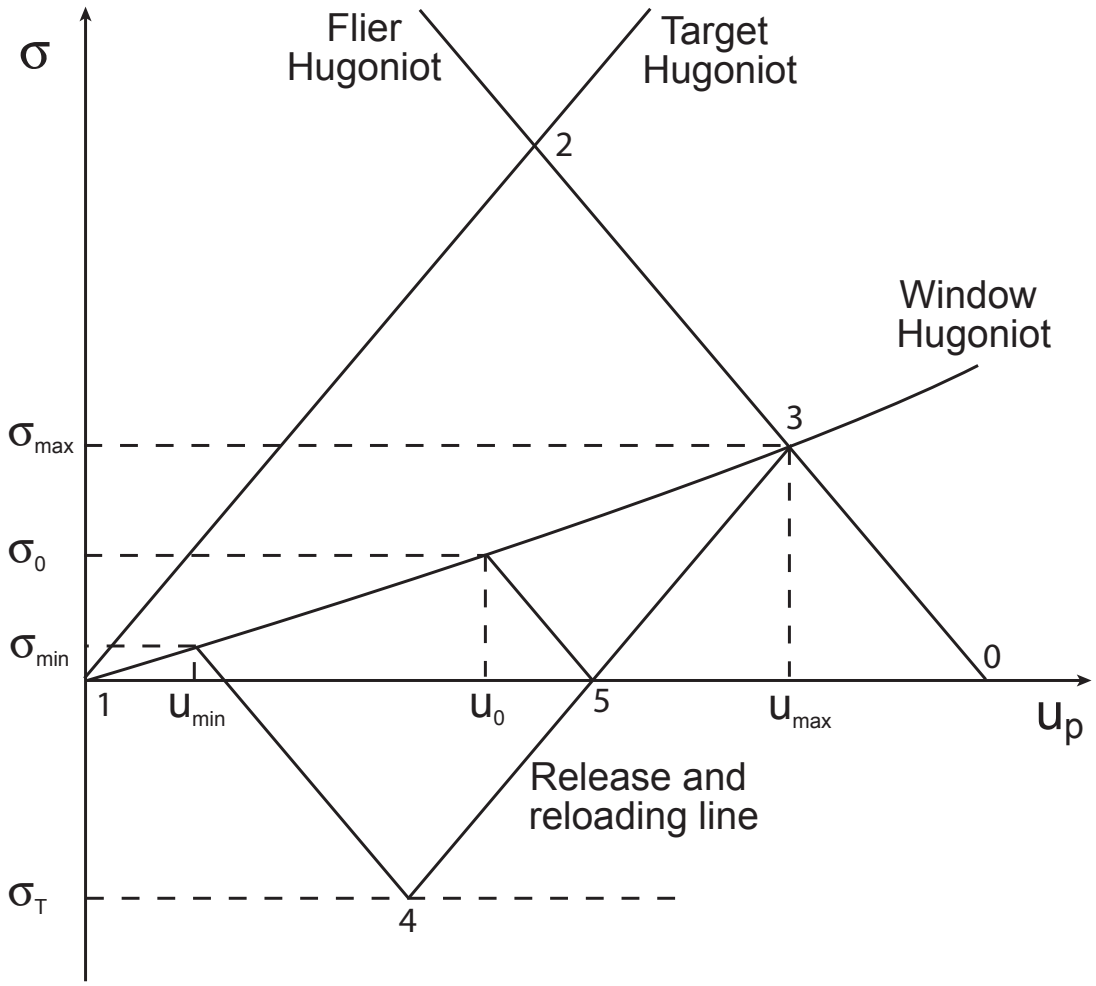

Figure 5.15: $\sigma - u_p$ diagram of a spall experiment with a window. The initial stress measured can be determined in the same way as in figure 5.7. After this point there is a release and a reloading, as shown in figure 5.13. The important thing to remember is that while the goes from state 3, to 4 and the to 5, the diagnostics can only measure interactions within the PMMA backing material. Such interactions can only occur along the PMMA Hugoniot, and therefore the diagnostics measure σ_{min} and σ_0 or u_{min} and u_0.

An example of a spall trace is shown in figure 5.16. The levels that would be used in calculating the spall strength are shown in the enlarged section of the diagram. While this is a trace from the VISAR with no window material present, the identification of the levels is the same in the case of a gauge and with a window material.

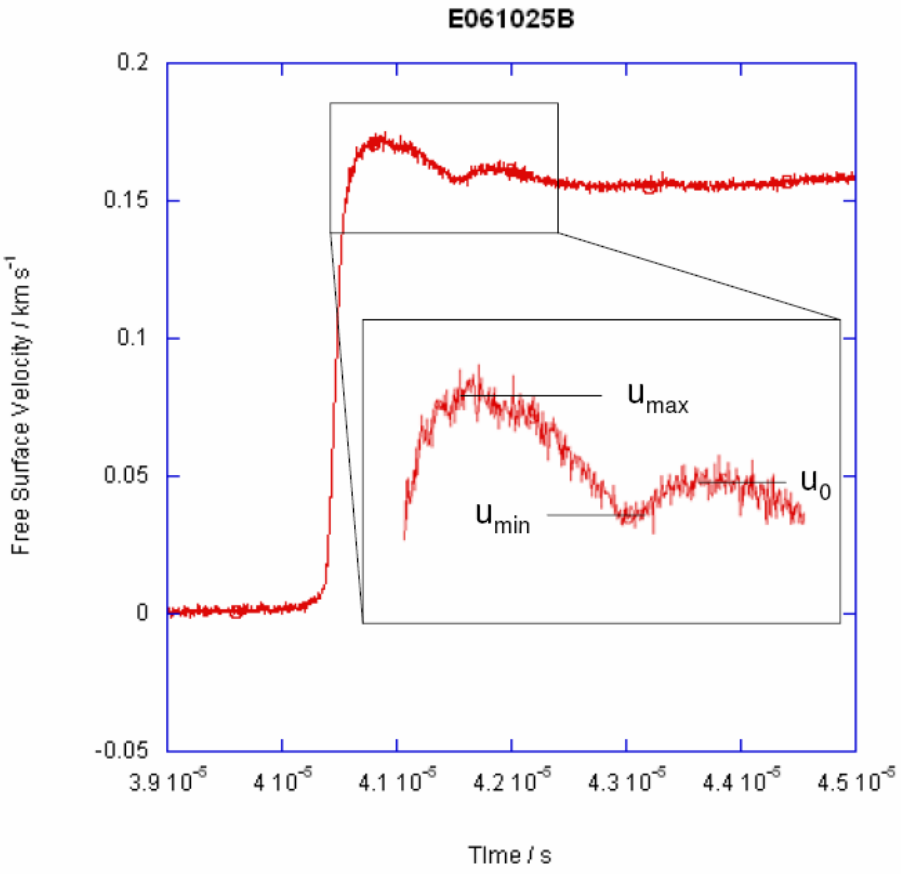

Figure 5.16: A typical spall trace showing identification of the levels for analysis. The levels as identified in figure 5.15 are labelled in the inset.

As a final point it is also possible to use data from the spall experiments with window materials and a flier of known properties to derive points on the Hugoniot of the material. In figure 5.15 it can be seen that the measured peak stress or particle velocity corresponds to a point that is both on the release of the rock material and the PMMA Hugoniot. As we have a knowledge of the PMMA

Hugoniot this allows us to fix a definite point on the release path of the rock. The release path must also intersect the flier Hugoniot, which if it is a standard material, is also known. To determine the exact point of the intersection (which will also be the Hugoniot point as it is the intersection of the flier Hugoniot and the rock target Hugoniot) it is necessary to assume that the material is behaving in an elastic manner (an assumption which is likely to be valid given the low stresses involved in the spall experiments). This assumption means that the slope of the release will simply be the negative of the slope of the Hugoniot. This fact means that a unique point on the flier Hugoniot can be determined, thus giving a further point on the rock Hugoniot.

5.3 Summary

- The mathematical and theoretical underpinning of shock physics is well understood and established.
- It is possible to measure the Hugoniot (locus of all states it is possible to reach through a single shockloading) by a series of experiments.
- The measurement of release properties can be achieved through the use of a reverse ballistic configuration.
- Embedding of gauges in a lateral orientation means that one can determine shear strengths.
- Through a slightly more involved analysis the tensile strength of the material can be found through the use of spall experiments.
- If both the compression and release behaviour of the material has been measured then it is possible to calculate the energy loss in such a cycle.

References

[1] Willmott, G.R., *Shock Studies of Kimberlite, Diamond and Brittle Embedded Particles*, Phd, Cambridge (2004)

[2] Asay, J.R. and Shahinpoor, M., *High-Pressure Shock Compression of Solids*, Springer-Verlag, New York (1993)

[3] Marsh, S.P., *LASL Shock Hugoniot Data*, University of California Press, Berkeley, California (1980)

[4] Nicholas, T and Recht, R.F., "Introduction to Impact Phenomena", in *High Velocity Impact Dynamics*, J. Zukas, ed., John Wiley and Sons, New York (1990), pp. 1–64

[5] Rosenberg, Z., "On the relation between the Hugoniot elastic limit and the yield strength of brittle materials", *J. Appl. Phys.*, **74**, (1993), 752–753

[6] Ruoff, A.L., "Linear Shock-Velocity-Particle-Velocity Relationship", *J. Appl. Phys.*, **38**, (1969), 4976–4980

[7] Swift, D.C. and Kraus, R.G., "On the Properties of Plastic Ablators in Laser-Driven Material Dynamics Experiments", *Phys. Rev. E*, (2008), In Press

[8] Chapman, D.J., Phd, Cambridge (2009)

[9] Grady, D.E. and Hollenbach, R.E., "Dynamic fracture strength of rock", *Geophys. Res. Letts*, **6**, (1979), 73–76

[10] Grady, D.E. and Kipp, M.E., "Dynamic fracture and fragmentation", in *High-Pressure Shock Compression of Solids*, J. Asay and M. Shahinpoor, eds., Springer-Verlag, New York (1993), pp. 265–322

Chapter 6

Compressional Strength and Release Behaviour

6.1 Observations on Experimental Method

6.1.1 Introduction

Obtaining the Hugoniots for the materials in this thesis was the initial priority for the investigation, and therefore naturally became something of a proving ground for the experimental techniques described earlier. Before presenting the results themselves therefore, it is instructive to look at some of the issues that arose in obtaining reliable data on geological materials. Not only does examining the problems give an insight into the methodology employed, but also provides additional information about the material response, and probes some of the fundamental issues with making high strain rate measurments.

6.1.2 Gauge Traces

Initial experimental work was carried out using embedded stress gauges as the main diagnostic as described in section 5.2.3. Accuracy of the results varied and appeared to correlate with the level of heterogeneity within the samples. This can be seen in figures 6.1 - 6.3, which show the stress/time histories of the gauges. These should be compared with the photographs of the rock types in section

2.4. It can be seen that the smaller grained amphibolite behaved in a manner that allowed fairly easy determination of plateau stresses from the gauge traces, whereas the larger grained materials did not allow for this to be done so easily. For the gneiss, it was possible to derive a Hugoniot with a reasonable degree of certainty, however the results for the kimberlite did not allow a Hugoniot to be constructed. Certainly experimental results obtained using gauges in kimberlite were not in agreement with the VISAR data obtained on the same material.

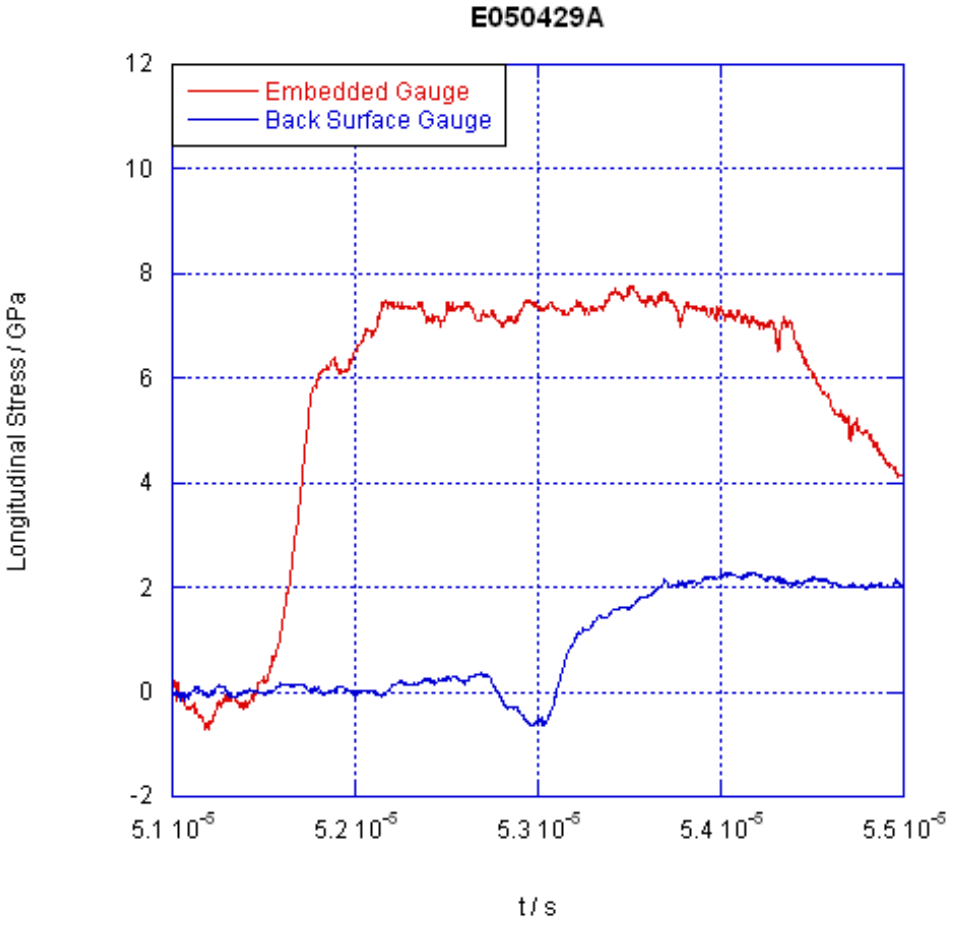

Figure 6.1: Gauge traces from an amphibolite experiment. While there is obviously noise present in the traces, it is still possible to determine plateau levels and times of arrival with confidence.

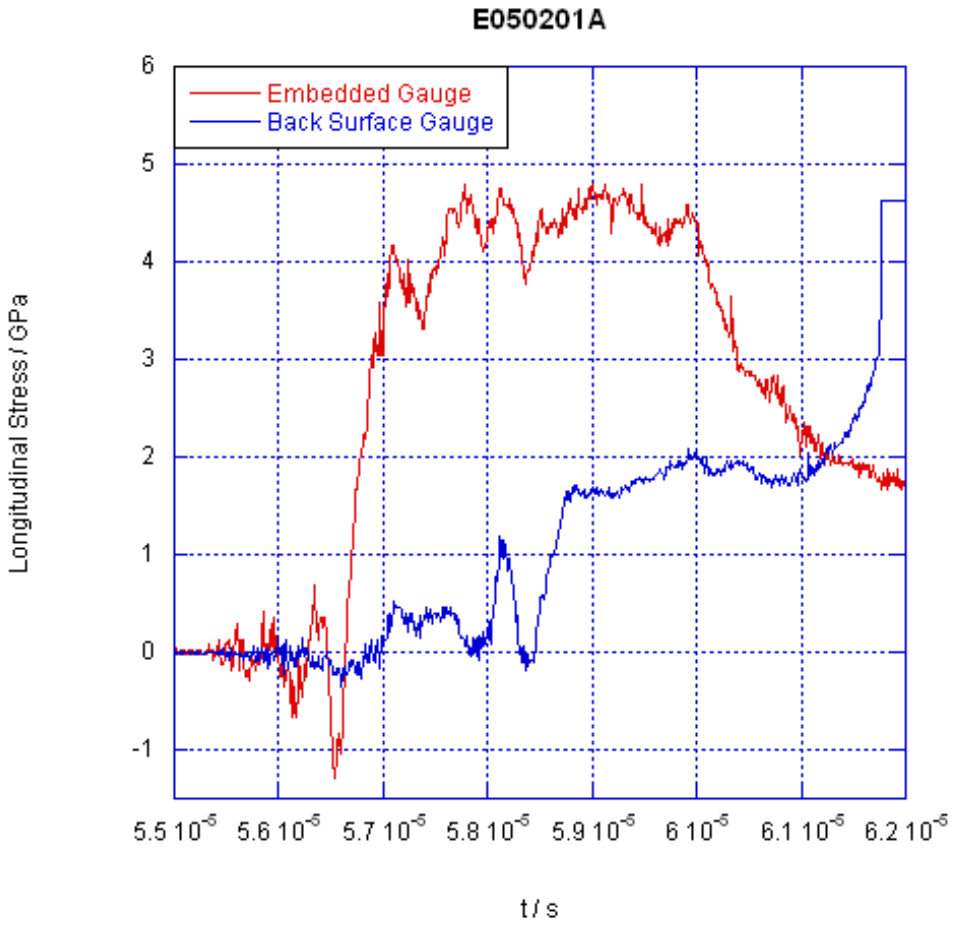

Figure 6.2: Gauge traces from a quartz/feldspathic gneiss experiment. When compared to figure 6.1, it can be seen that the noise is greater in amplitude and determination of the plateau levels and times of arrival are more difficult (although still possible).

The reduced accuracy of stress gauges in certain geological materials, as shown, could be due to a number of factors. The two most likely reasons are electromagnetic emission and local straining of the gauge element. Many geological materials, including some of those tested in this investigation contain quartz or other piezoelectric materials. Upon compression it is possible therefore that electromagnetic emissions from the quartz are picked up by the circuit made by the gauges and their power supplies. This would potentially lead to a noisy sig-

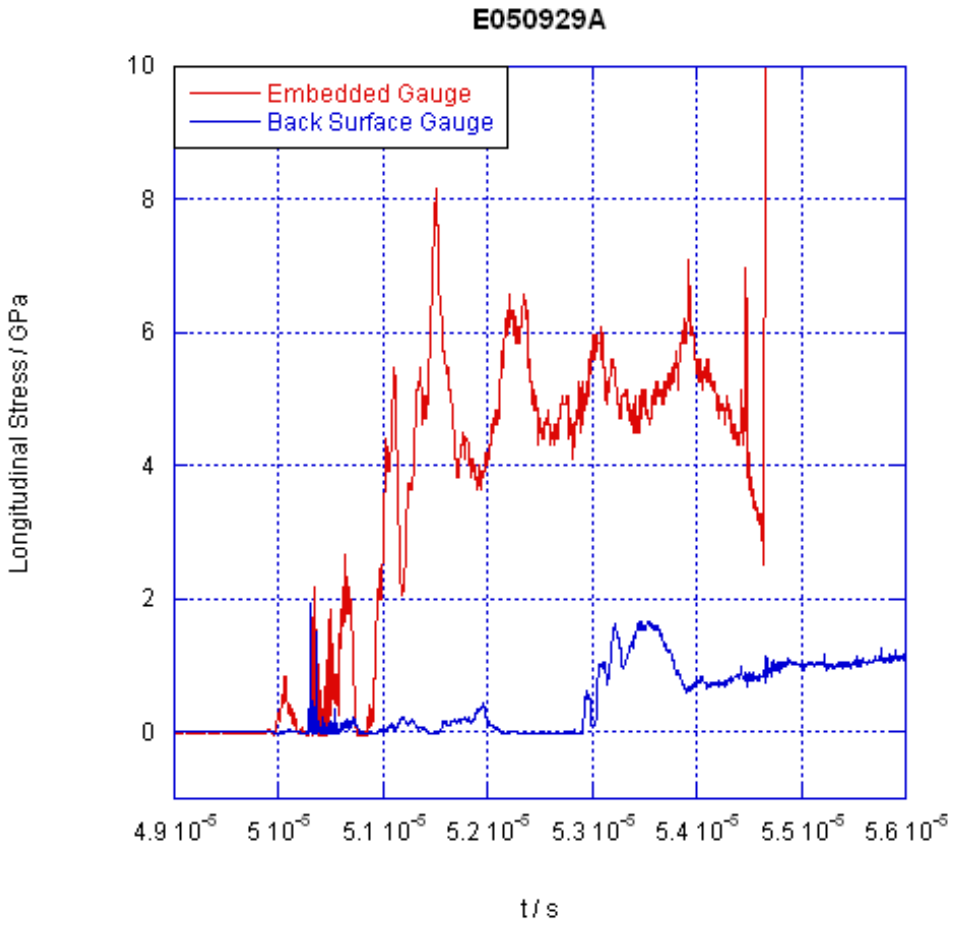

Figure 6.3: Gauge trace from a kimberlite experiment. It can be seen from the figure, that the noise, when compared with figures 6.1 and 6.2, is of a much greater amplitude, and one can no longer (in particular in the front gauge) be sure of either the plateau levels or the time of arrival. At this level of noise the use of gauges to determine the Hugoniot is unwise.

nal. The quartz/feldspathic gneiss is certainly rich enough in quartz for this phenomenon to potentially affect results. An example of a paper demonstrating electromagnetic emissions from rock material is Yoshida and Ogawa [1] who examined granite under triaxial deformation. An attempt has been made to examine this phenomenon briefly within the context of this thesis. Two samples were prepared from materials of differing quartz content, namely amphibolite and

quartz/feldspar gneiss (the gneiss having a much higher quartz content as can be seen in the MLA pictures). These materials were then impacted at velocities which generated a similar level of stress in each material. As well as the lateral gauges which were intended to be the primary diagnostic for the experiments concerned, each sample had a standard grid gauge connected to the rear surface of the sample. This was then not powered, and left in an essentially passive state to pick up any electromagnetic emissions that should occur. The traces for the two experiments are shown in figures 6.4 and 6.5.

It can be seen that the amphibolite signal is of a lower amplitude than the signal from the gauge in the gneiss. It is certainly noticeable that both of the non-powered gauges recorded fairly significant signals. It is unlikely that this is due to an electrical connection within the system, as this sort of noise amplitude is not seen on other gauge traces obtained through the use of the same system. The difference in noise between this and other amphibolite experiments can almost certainly be attributed to a non-uniform distribution of quartz (or other piezo-electric materials) throughout the cores supplied. It is possible to examine the effect that this electromagnetic emission is having on the diagnostic gauges in the material by examining them together, as in figure 6.6. Some of the features of the traces seem to coincide, and from this it is certainly a reasonable assumption that the emission of electromagnetic waves from the compression of piezoelectric components of the geological materials is affecting the performance of the manganin stress gauge diagnostics contained within these materials.

Another possible cause of the noise seen in the gauge traces (especially in the case of materials without significant piezoelectric elements) is local straining of the manganin gauge element. The gauges used in these experiments are designed to give a measurable and calibrated change in resistance with the application of a planar stress. As it is the resistivity of the gauge that is changing, any deviation from a planar stress pulse will cause erroneous results. This is partially the reason why such care is taken with both sample preparation and target alignment. In a homogeneous material, provided target alignment and preparation is acceptable,

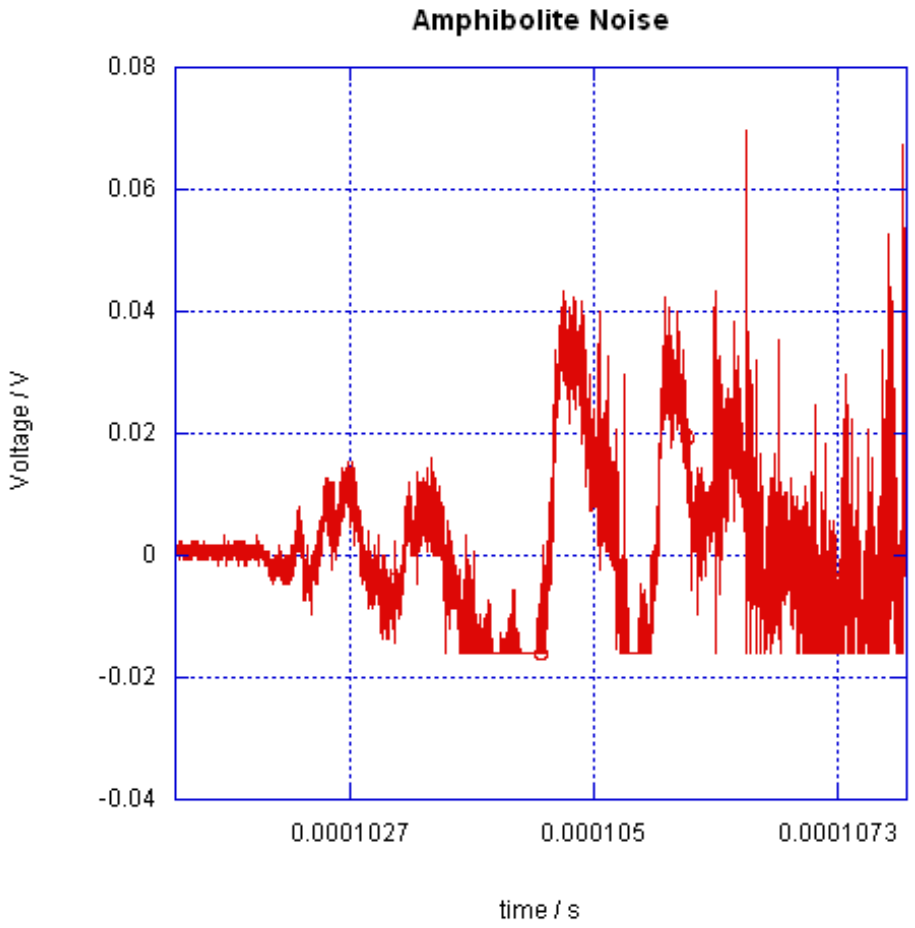

Figure 6.4: Non powered gauge trace from an amphibolite experiment. The maximum positive amplitude of the noise is approximately 40 mV (barring one spike at about 70 mV). The gauge is picking up a signal from the compression of the quartz in the material. The bottom part of the gauge trace is clipped owing to an underestimation fo the negative amplitude of the noise when setting the scales on the oscilloscope.

it is likely that a planar loading of the gauge will occur. In a heterogeneous geological material however, this is not necessarily the case.

Different grains within the whole will have different properties under dynamic loading. If we imagine two grains side by side in a flat disc, with different shock

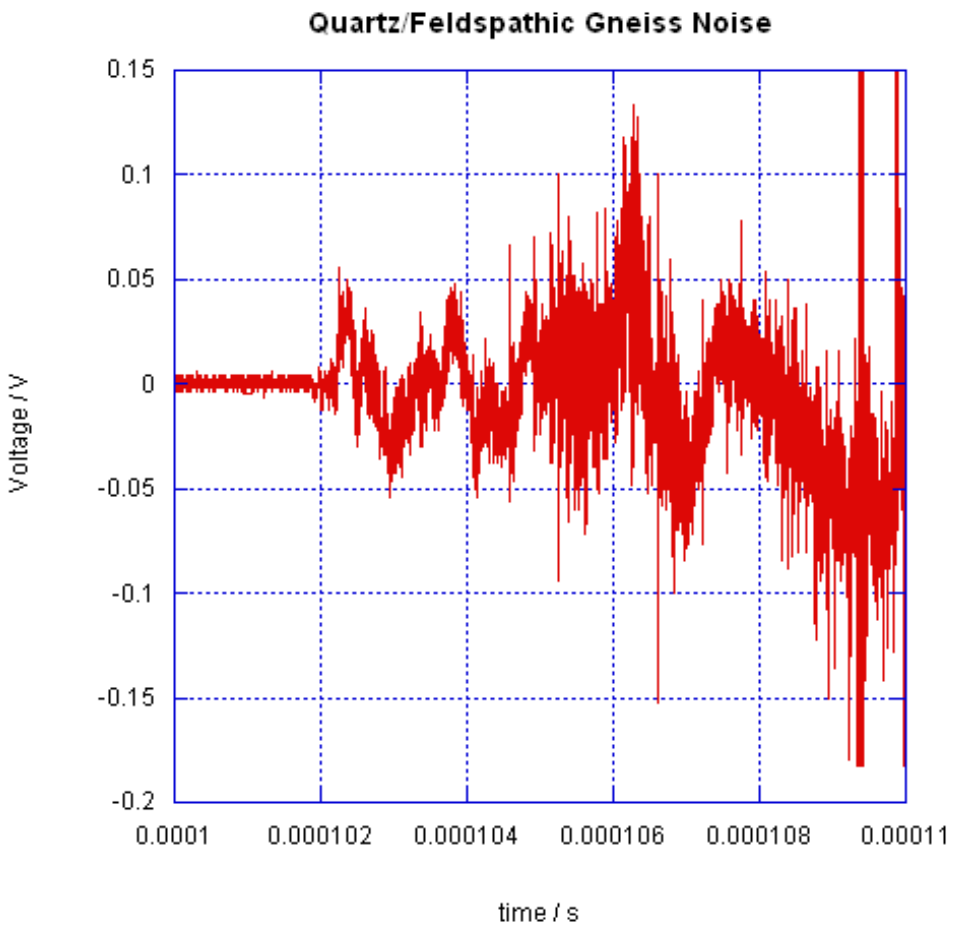

Figure 6.5: Non powered gauge trace from quartz/feldspathic gneiss experiment. Again the gauge is picking up a signal from the compression of the quartz in the material. In this case the maximum noise amplitude is in the region of 130 mV. This is significantly higher than that seen in figure 6.4, and can be linked to the higher quartz content of the gneiss over the amphibolite.

speeds for a given pressure, it is clear that a shock incident on one side of the two grains at the same time, will not reach the other side simultaneously. If two or more grains sit across the gauge element then one side of the gauge will experience a pressure before the other. This uneven pressure will cause the gauge to deform, giving an anomalous result as the resistivity changes. It has been demonstrated that shock fronts can become distorted by different orientations of

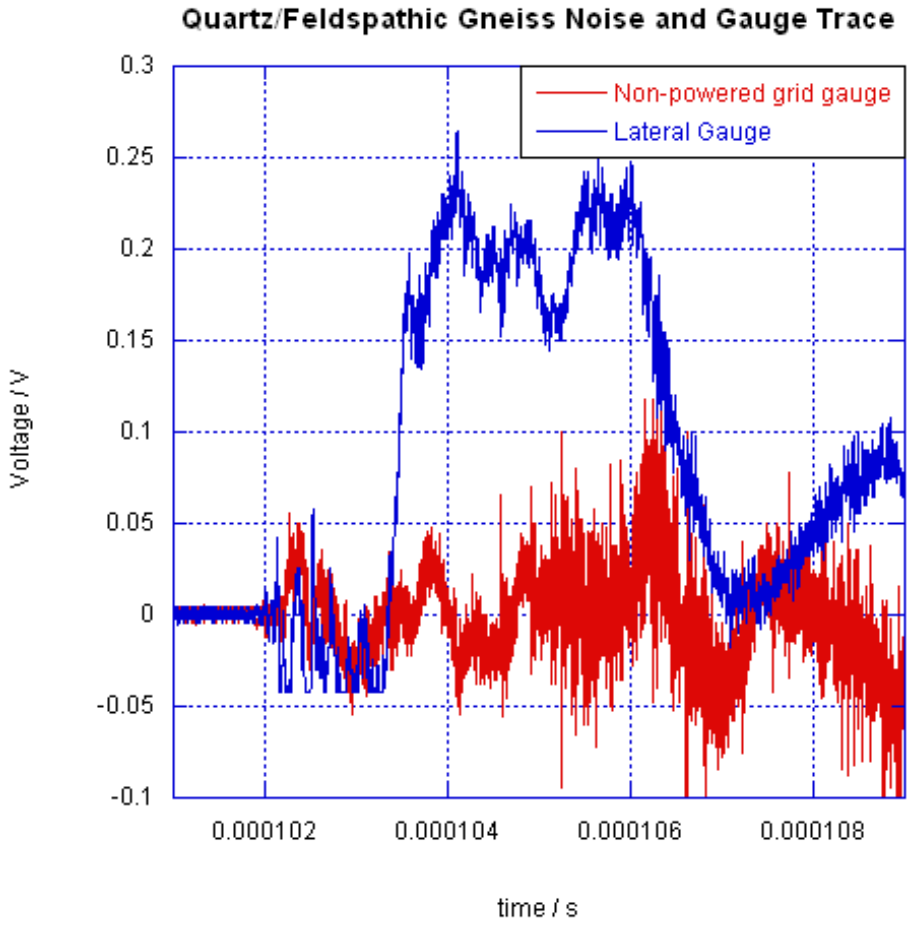

Figure 6.6: Non powered and powered (lateral) gauge traces from a quartz/feldspathic gneiss experiment. It is noticeable that at certain points, the noise in both traces appears to coincide. This would suggest that the electromagnetic emission from quartz is causing a significant amount of the noise in the gauge traces for quartz rich materials.

grains of the same material in a polycrystal. Barber and Kadau [2] calculate that the shock width increases as the half power of front penetration distance into the polycrystalline sample. Obviously if the grains have intrinsically different properties (owing to being made of different materials) then the effect will be enhanced.

6.1.3 Further Gauge Experiments

While only two of the rocks presented in this thesis have had their Hugoniots explicitly measured via the use of gauges, there are other data from gauges that have contributed to the overall knowledge of the Hugoniots of the remaining rock materials. These data are incidental data from the siltstone shock velocity measurements described previously and also the inclusion of longitudinal gauges in some of the samples designed to measure lateral stress and spall strength. In the case of the lateral experiments it is beneficial to measure the longitudinal stress directly in the experiment so that the shear strength can be determined without the need to infer the longitudinal stress from the Hugoniot of the material. However to include a longitudinal gauge two issues need to be considered.

Firstly the material should be of a sufficiently fine grain size as to avoid the worst of possible gauge straining effects described earlier (also the material should be as quartz free as possible). Secondly to ensure that the lateral gauges are still in a state of one dimensional strain when they are recording data, it is necessary that any "cover plate" attached to the front of the material (behind which a longitudinal gauge would be located) is thin, of the order of 2 mm thick. To cut samples of this thickness is not possible in some of the softer materials available, such as the sandstone and the kimberlite, and so for these materials a copper coverplate and no longitudinal gauge were used. Additionally the longitudinal gauges were only used in the finer grained materials such that even a thin sample was likely to be representative of the bulk material. To use the data from the spall experiment an impedance match method was used, coupled with an assumption that the material was behaving in an elastic manner. This is described in section 5.2.7. The results of gauges placed in siltstone for various experiments also (as the VISAR results do) point to it having a linear Hugoniot, as the results plotted in figure 6.7 demonstrate.

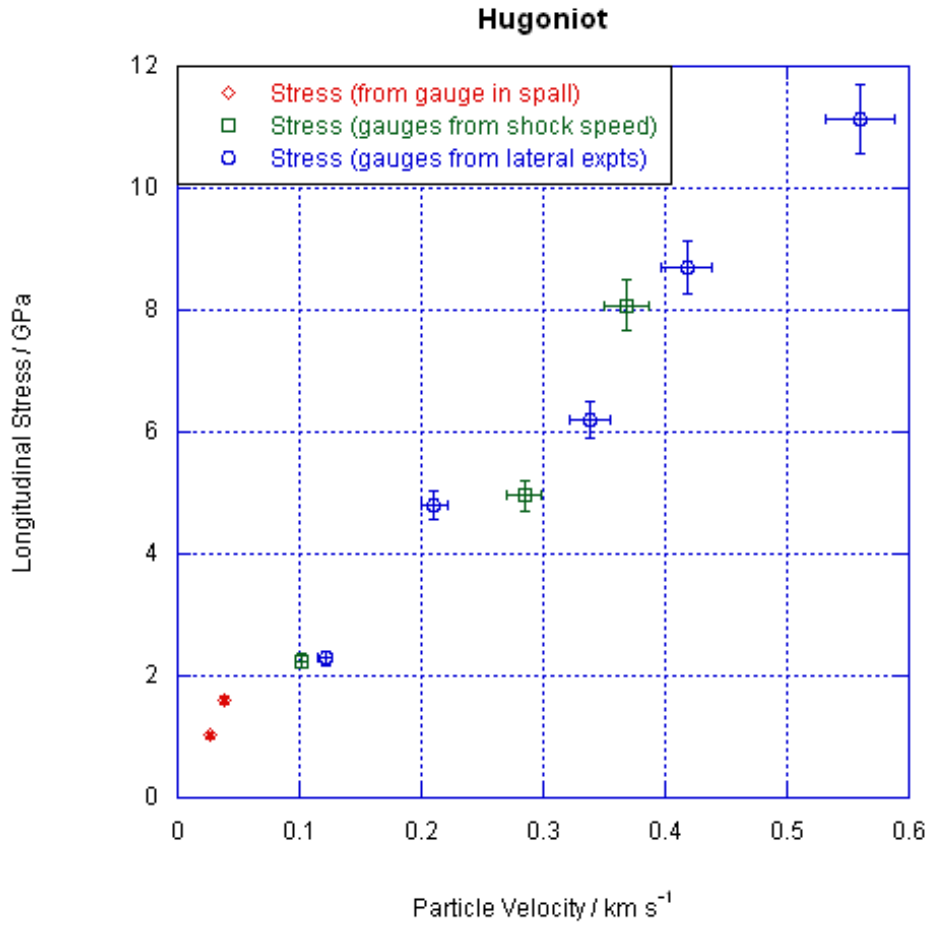

Figure 6.7: Hugoniot of siltstone in $\sigma - u_p$ space determined from gauges in shock velocity, spall and lateral stress experiments. There is a good consistency between the results, all seem to be describing a linear relationship between stress and particle velocity.

6.1.4 VISAR

As noted in section 5.2.3, there have been a number of experimental designs used in this thesis to determine the compressional behaviour of rock materials and derive their principal Hugoniot. The investigations described in the previous section represented an initial attempt to use gauges to achieve this aim. While there was a level of success in this, it was noted that the method was not without its difficulties. A reverse ballistic configuration was then suggested as a solution to

some of the problems posed by the gauges. The fact that the measurements in the reverse ballistic configuration are taken on a well-characterised, homogeneous and "well-behaved" material means that some of the heterogeneous nature of the rock materials can be averaged out. In this way, one can be more confident that a result representative of the bulk behaviour can be obtained. It is certainly less likely that a VISAR probe point will be unduly affected by grain structure. A comparison between the best estimate of Hugoniot points for kimberlite using the gauge data and the Hugoniot as determined by the VISAR data is shown in figure 6.8.

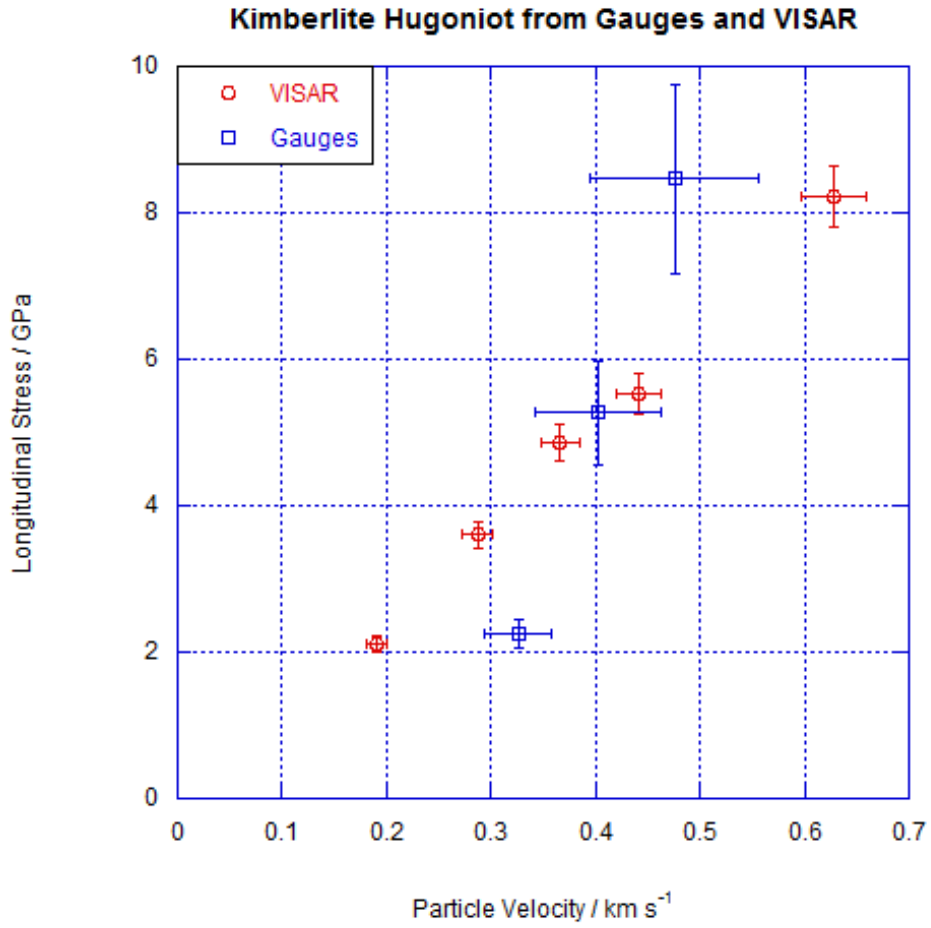

Figure 6.8: Hugoniot of kimberlite in $\sigma - u_p$ space as determined from gauges and VISAR. It is clear that the results from the gauge experiments and the VISAR experiments do not agree. Owing to the problems with the gauges, as shown in figure 6.3, it is assumed that the VISAR data accurately describes the Hugoniot of the material. This leads to the conclusion that in certain geological materials, the use of gauges is inappropriate.

The data analysis and experimental design suggested in section 5.2.3 indicates that some knowledge of the release states in the rock material can also be elucidated from the reverse ballistic experiments. It is possible to look at releases through gauge experiments as well, but this does rely on the gauge record being readable past the original passage of the stress pulse. In the data shown

previously, this would not be easily possible. Additionally, the reverse ballistic experimental design used (which could be described as a "ring-up" in terms of particle velocity, or perhaps more accurately as a "ring-down" in terms of stress) in this thesis allows for multiple points on the release curve to be determined, in contrast to a gauge experiment where one release point is most likely the limit of technical capability. As well as giving a fuller picture of the release in the material, additional release points permit an estimation of "waste heat" to be made, as outlined in section 5.2.5. The error associated with the individual release points is due, as with the Hugoniot points measured with VISAR, to the accuracy of the copper Hugoniot and the error in the VISAR record itself. These errors however have not been plotted as the major use of the releases is in the waste heat measurements and the inhomogeneity of the samples gives rise to sufficient scatter in the release data to make this rather than anything else the major source of error when calculating the waste heat.

6.2 Hugoniot Data

6.2.1 Quartz/Feldspathic Gneiss

Shot Code	Experiment Type (Major Diagnostics)	Impactor/Target Materials	Impact Velocity $m\ s^{-1}$	Useful Data
E041217A	Hugoniot (Gauges)	Copper/Gneiss	800	No
E050111A	Hugoniot (Gauges)	Copper/Gneiss	810	Yes
E050112A	Hugoniot (Gauges)	Copper/Gneiss	256	Yes
E050112B	Hugoniot (Gauges)	Copper/Gneiss	499	Yes
E050113A	Hugoniot (Gauges)	Copper/Gneiss	957	Yes
E050119A	Hugoniot (Gauges)	Copper/Gneiss	656	Yes
E050201A	Hugoniot (Gauges)	Copper/Gneiss	400	Yes
E050303A	Hugoniot/Release (VISAR)	Gneiss/Copper	778	Yes
E050412A	Hugoniot (Gauges)	Aluminium/Gneiss	324	No

Table 6.1: Experiments on quartz/feldspathic gneiss

The Hugoniot of the gneiss was primarily determined using the stress gauge method, the experiments carried out on this material are tabulated in table 6.1. The agreement of the gauge data with the VISAR experiment on the same material, and the fact that the linear Hugoniot derived is similar to the elastic impedance (as with a number of the other materials presented) indicate that for this material the Hugoniot has been adequately determined through the use of gauges. As noted previously, this is not the case for the kimberlite. The Hugoniot derived from the gauge records for the gneiss is shown in figures 6.9. It can be seen that the Hugoniot is well-fitted by a linear relationship between longitudinal stress and particle velocity.

Some of the larger differences of the points from the fit line can be attributed to the large errors in the determination of the plateau levels in noisy gauge traces. It should also be noted that as two gauges were used in these experiments further data analysis is possible. It is possible for example to cross the Hugoniots further to determine whether the stress states in the PMMA backing material matches the Hugoniot. The fact that this analysis requires the reading of the noisy stress gauge traces from two different gauges however means that the accuracy is likely to be limited.

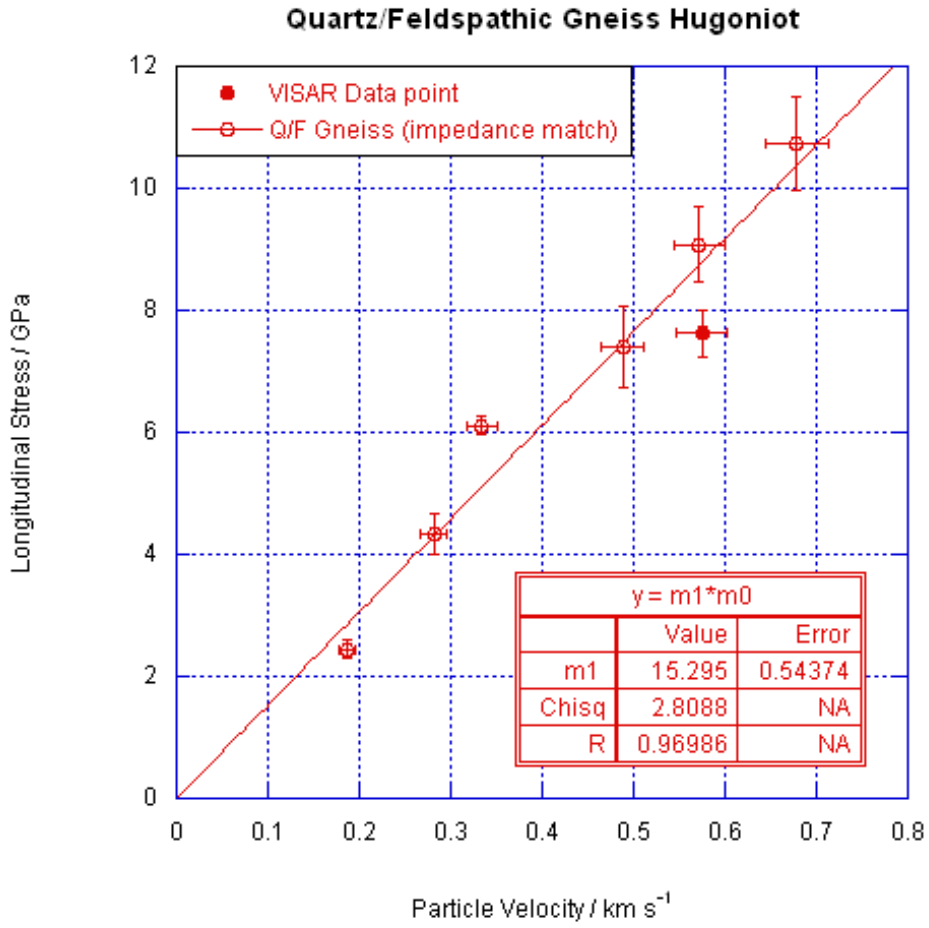

Figure 6.9: Quartz/Feldspathic Gneiss Hugoniot. The closed circle datum is from a VISAR experiment, whereas the other data are derived from stress levels measured by in-material gauges (the particle velocity was found by impedance matching with the copper Hugoniot). The data are well described by the fitted linear relationship. Where the data deviate from this fit to an extent greater than experimental error, this is attributed to sample to sample variation.

As described in detail in section 6.4.2, it is possible to use the transit time between the two gauges to derive a shock speed for the material. If we assume that the relationship in equation 6.1 holds then this allows us to calculate u_p given the density for a given stress.

$$\sigma_x = \rho_0 U_s u_p. \tag{6.1}$$

The advantage of this method is that it uses only information directly measured from the material and therefore gives additional material information. However this is also the weakness, in that a material with sample to sample variation will then likely include more errors in the result. It is not always possible to account for these sample issues within the quoted errors as they may merely manifest themselves as data points that are different from the general trend. The data derived from shock speed can be seen, plotted with the original data in figure 6.10. Also included are a line denoting elastic behaviour and the release data from the VISAR experiment. It can be seen that the data from the shock speed derivation agrees to within the experimental error with the impedance match data. In addition the material would appear to have a good fit to the expected elastic behaviour.

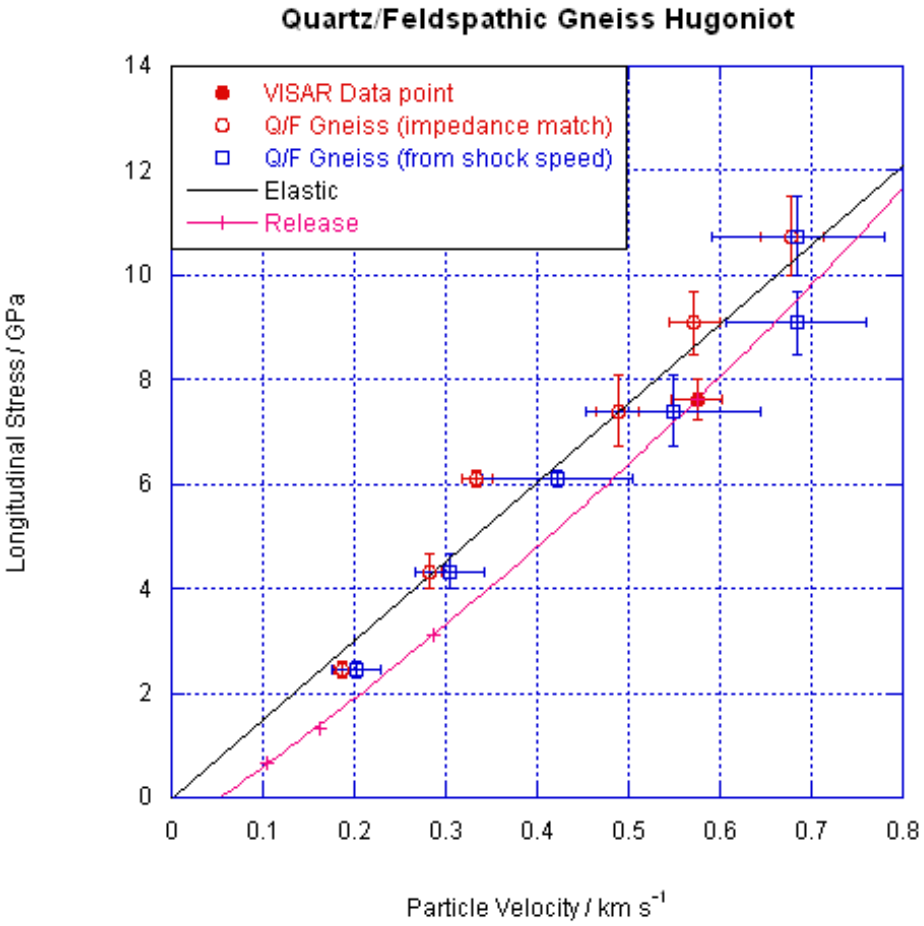

Figure 6.10: Quartz/Feldspathic Gneiss Hugoniot. The data shown in figure 6.9 are reproduced along with an equivalent set of data where particle velocity has been calculated from the measured shock velocity (using equation 6.1). The results agree to within experimental error. Also shown is a line of theoretical elastic behaviour, this is a good representation of the data. Finally, the release data (and a polynomial fit to it) from the VISAR experiment are plotted.

6.2.2 Amphibolite

Shot Code	Experiment Type (Major Diagnostics)	Impactor/Target Materials	Impact Velocity $m\ s^{-1}$	Useful Data
E050428A	Hugoniot (Gauges)	Copper/Amphibolite	217	Yes
E050428B	Hugoniot (Gauges)	Copper/Amphibolite	398	Yes
E050429A	Hugoniot (Gauges)	Copper/Amphibolite	555	Yes
E050429B	Hugoniot (Gauges)	Copper/Amphibolite		No
E050506A	Hugoniot (Gauges)	Copper/Amphibolite		No
E050506B	Hugoniot (Gauges)	Copper/Amphibolite		No
E050527A	Hugoniot (Gauges)	Copper/Amphibolite	705	Yes
E050527B	Hugoniot (Gauges)	Copper/Amphibolite		No
E050530A	Hugoniot (Gauges)	Copper/Amphibolite	1038	Yes

Table 6.2: Amphibolite experiments providing compressional data

The Hugoniot for amphibolite (data tabulated in table 6.2 has a number of similarities with the gneiss described in the previous section. As can be seen in figure 6.11 the data are again well represented by a linear fit, though the errors in the measurements are smaller owing to the better quality of the gauge traces.

In figure 6.12 a similarity between the fitted Hugoniot data and the theoretical elastic behaviour can be seen. It should also be remembered that there is an error associated with the calculated elastic line (the gradient of the line is 19.84 $\pm$ 0.2) which is not shown in the figure. There is additionally agreement to within experimental error with the data where the particle velocity has been calculated from the gauge transit times, as opposed to being inferred from the copper Hugoniot.

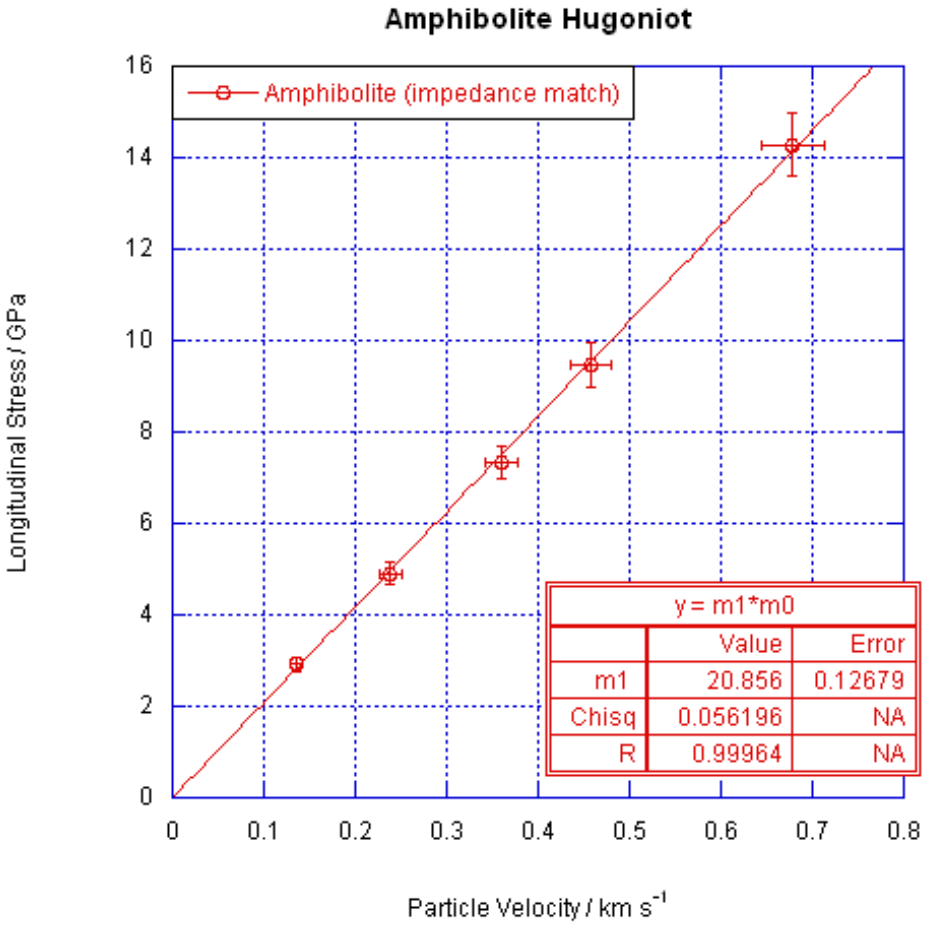

Figure 6.11: Amphibolite Hugoniot, derived from measured gauge stresses (and impedance matched with copper). The data are well described by the linear fit shown in the figure. The more homogeneous nature of the amphibolite over some of the other materials is demonstrated by the lack of any data points that do not agree, due to sample to sample variation, with the general trend .

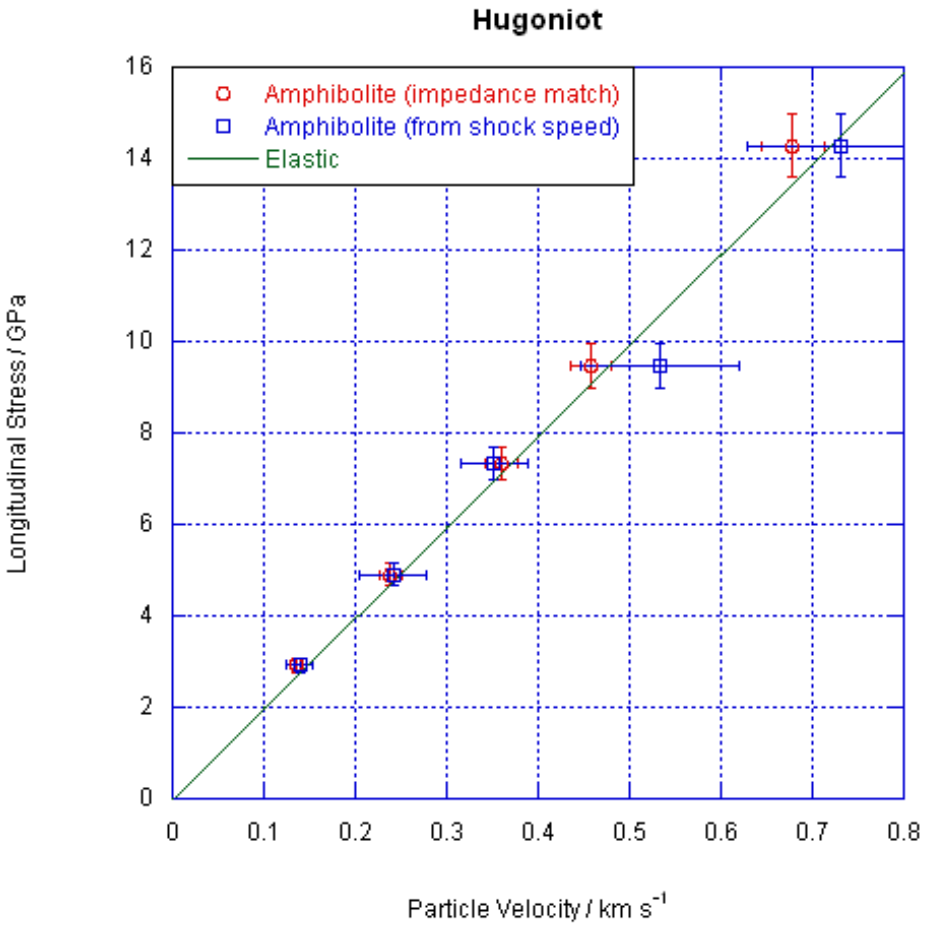

Figure 6.12: Amphibolite Hugoniot with an elastic line and data derived from shock speed. The agreement between the two different methods of arriving at the final result agree to within experimental error. Additionally the data are well described by the theoretical elastic line and there is no distinct HEL visible in the longitudinal data.

6.2.3 Kimberlite

Shot Code	Experiment Type (Major Diagnostics)	Impactor/Target Materials	Impact Velocity $m\ s^{-1}$	Useful Data
E050928A	Hugoniot (Gauges)	Copper/Kimberlite	389	No
E050929A	Hugoniot (Gauges)	Copper/Kimberlite	546	No
E050929B	Hugoniot (Gauges)	Copper/Kimberlite	699	No
E051028A	Hugoniot/Release (VISAR)	Kimberlite/Copper	845	Yes
E051028B	Hugoniot/Release (VISAR)	Kimberlite/Copper		No
E051031A	Hugoniot/Release (VISAR)	Kimberlite/Copper	250	Yes
E051104A	Hugoniot/Release (VISAR)	Kimberlite/Copper		No
E060125A	Hugoniot/Release (VISAR)	Kimberlite/Copper	387	Yes
E060125B	Hugoniot/Release (VISAR)	Kimberlite/Copper	591	Yes
E070809A	Spall (Gauge/VISAR)	Aluminium/Kimberlite	128	No
E070809B	Spall (Gauge/VISAR)	Aluminium/Kimberlite	131	No
E090119D	Hugoniot/Release (VISAR)	Kimberlite/Copper	499	Yes

Table 6.3: Kimberlite experiments potentially yielding compressional data

Shot data for kimberlite experiments which could have (if they had been successful) yielded compressional data are shown in table 6.3. The kimberlite Hugoniot is shown in figure 6.13 along with the associated release points (denoted by the impact velocity of the shot).

It can be seen that at low levels the release appears to be indistinguishable from the Hugoniot, and in fact it is only the release from the highest pressure state that shows an obvious deviation. It was initially speculated that this would give an indication of the onset of plastic, or non-elastic behaviour in the material, but in view of the lateral results presented subsequently for this material this would seem not to be the case. The onset of obvious deviation from the Hugoniot on release is at a much higher stress than the deviation from elastic behaviour in the lateral stress data. In fact the waste heat measurements suggest that in fact the difference in release does exist at a lower stress but is just more difficult to see with the noise in the data. Even so, this does not allow a firm conclusion to be drawn. An elastic behaviour line has also been added to show that the behaviour of the material is not too dissimilar to that which would be expected from idealised elastic behaviour. This has been calculated as the elastic or acoustic impedance of the material.

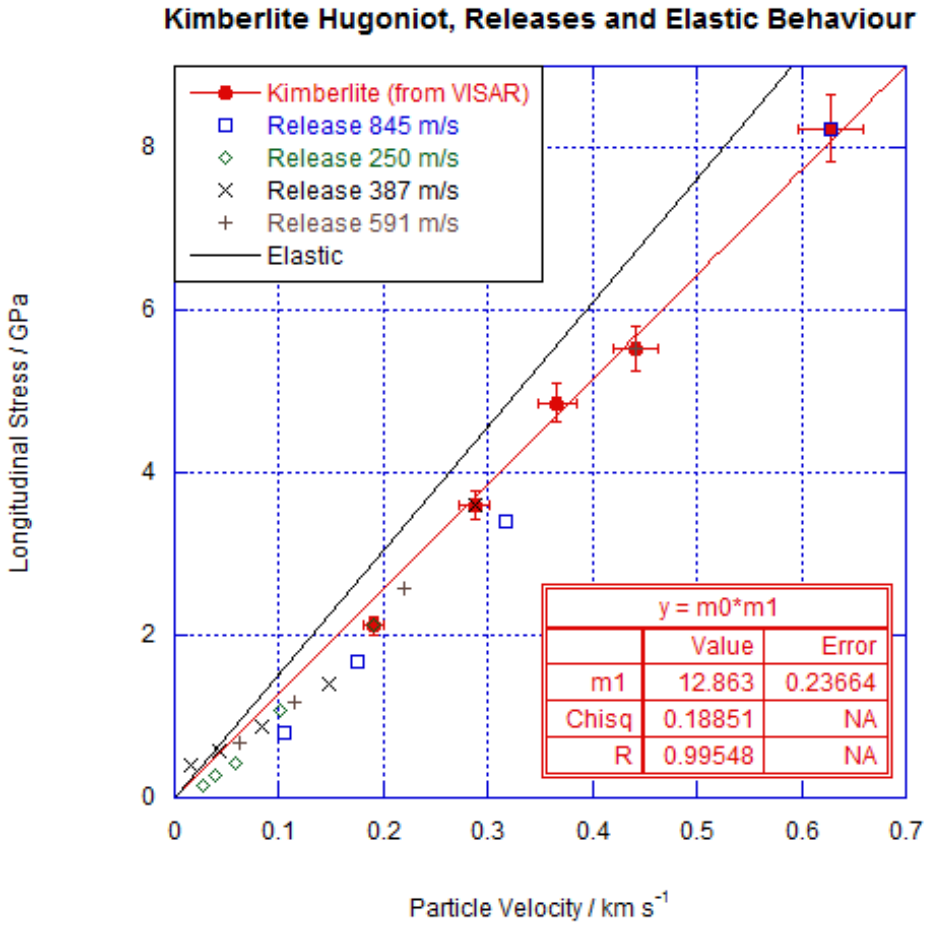

Figure 6.13: Hugoniot of kimberlite in $\sigma - u_p$ space determined from VISAR results. The data, which are the solid circles, are well described by a linear Hugoniot relationship. The theoretical elastic line however does not fit the points accurately. Also shown are the release points from each experiment, it can be seen that in general these lie below the Hugoniot.

Figure 6.14 shows similar data to that shown in figure 6.13. However some of the lower release data have been removed to make it easier to see the release that more obviously deviate from the Hugoniot at higher stress. A second order polynomial has also been fitted to this release.

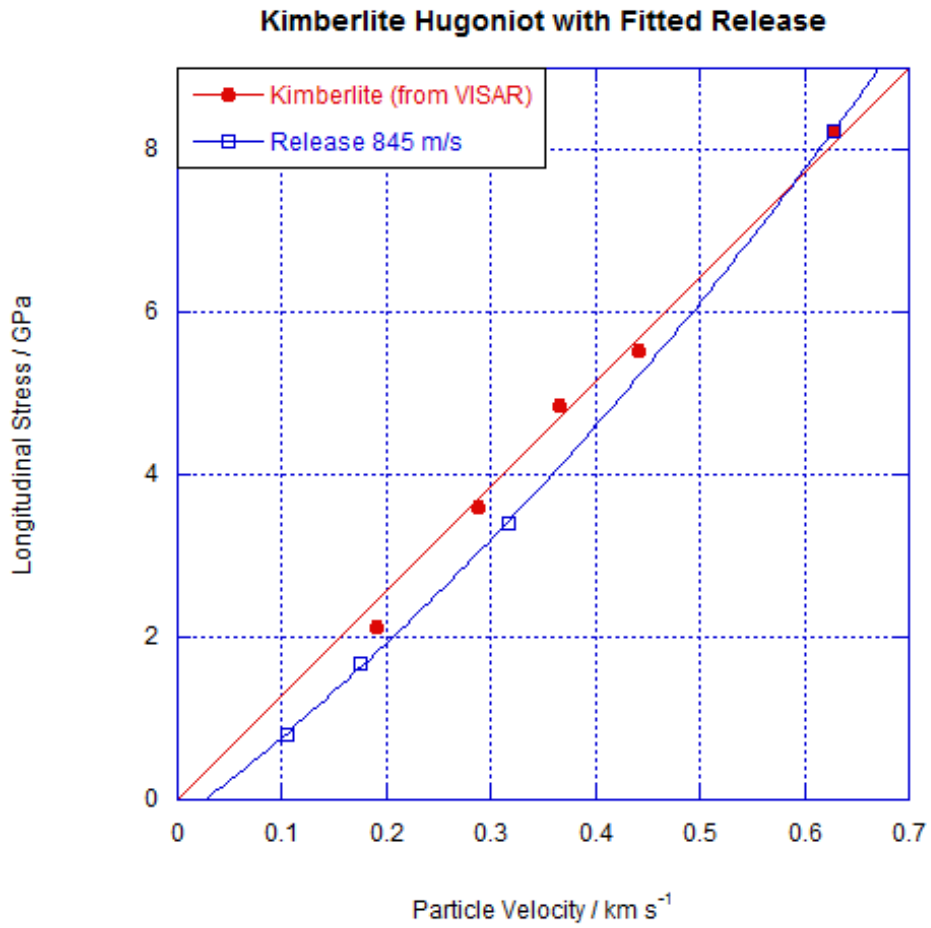

Figure 6.14: Hugoniot of kimberlite in $\sigma - u_p$ space showing a fit to release data. It can be more clearly seen with some of the data removed that the release shown is both below the Hugoniot, and below the loading line (although this line is not plotted) for the experiment.

6.2.4 Amphibolitic Gneiss

Shot Code	Experiment Type (Major Diagnostics)	Impactor/Target Materials	Impact Velocity $m\ s^{-1}$	Useful Data
E060226A	Hugoniot/Release (VISAR)	Amph Gneiss/Copper	498	Yes
E060202A	Hugoniot/Release (VISAR)	Amph Gneiss/Copper	732	Yes
E060208B	Hugoniot/Release (VISAR)	Amph Gneiss/Copper	251	Yes
E060321A	Hugoniot/Release (VISAR)	Amph Gneiss/Copper	986	Yes

Table 6.4: Amphibolitic gneiss compression experiments

The general form of many of the Hugoniot and release plots are similar across the range of geological materials investigated in this thesis. As the rocks are very similar in the most part, being a collection of mineral crystals with little or no porosity, this is perhaps not a surprise. Furthermore, the range of densities available is not particularly large. The Hugoniot of amphibolitic gneiss (for which the shot data are presented in table 6.4) and the release points are shown in figure 6.15. The fit to a straight line is good and a number of the points also agree with the plotted elastic line.

Figure 6.16 shows the fits to releases that are noticeably different to the Hugoniot. With further experimentation involving many more release shots it might be possible to average out some of the random errors in the release measurements (and thus obtain a more accurate description of the release at all pressures) but this is unlikely to be practical. It is additionally noted that the fit to the release from the shot at 732 m s^{-1} is different in shape to the releases from the 986 and 498 m s^{-1} though this is more likely due to a sample variation than any meaningful trend.

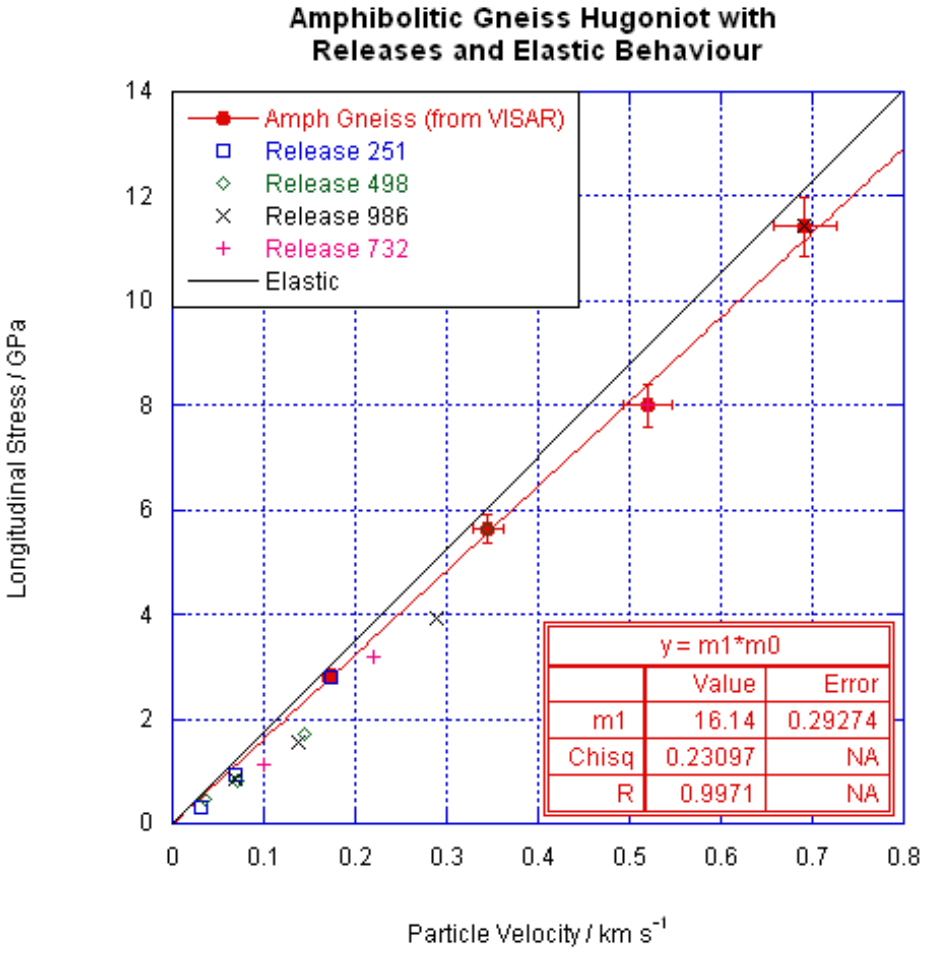

Figure 6.15: Hugoniot of amphibolitic gneiss in $\sigma - u_p$ space. The Hugoniot is fitted as a linear relation, and describes the data well. The Hugoniot lies slightly below the line that is predicted by the theoretical elastic behaviour, although it is noted that it is within the experimental error of three of the data points. The release points lie slightly below the Hugoniot.

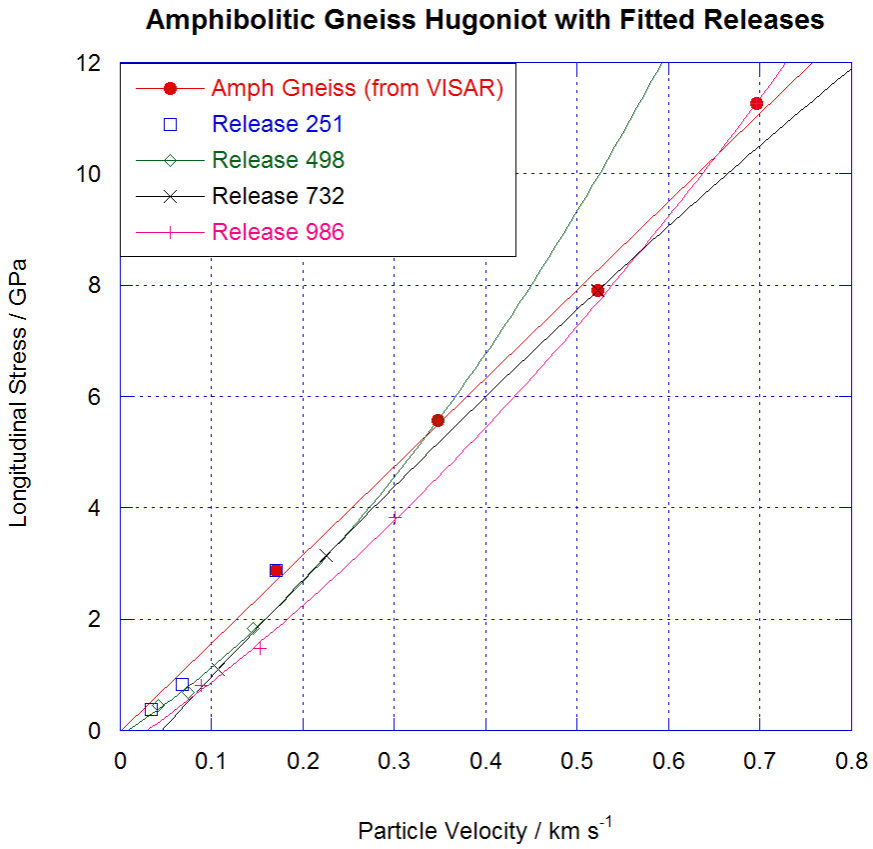

Figure 6.16: Hugoniot of amphibolitic gneiss in $\sigma - u_p$ space. The release data are reproduced and the three highest pressure releases have had polynomial lines fitted. The release fits show a clear deviation from the Hugoniot.

6.2.5 Siltstone

Shot Code	Experiment Type (Major Diagnostics)	Impactor/Target Materials	Impact Velocity $m\ s^{-1}$	Useful Data
E060126B	Hugoniot/Release (VISAR)	Siltstone/Copper	493	Yes
E060203B	Hugoniot/Release (VISAR)	Siltstone/Copper	715	Yes
E060208A	Hugoniot/Release (VISAR)	Siltstone/Copper	244	Yes
E060216A	Hugoniot/Release (VISAR)	Siltstone/Copper	927	Yes
E060228A	Hugoniot/Release (VISAR)	Siltstone/Copper	743	Yes
E070513B	Spall (Gauge/VISAR)	Aluminium/Siltstone	115	Yes
E070513C	Spall (Gauge/VISAR)	Aluminium/Siltstone	96	Yes
E070516B	Lateral (Gauges)	Copper/Siltstone	183	Yes
E070516C	Lateral (Gauges)	Copper/Siltstone	339	Yes
E070517A	Lateral (Gauges)	Copper/Siltstone	499	Yes
E070517B	Lateral (Gauges)	Copper/Siltstone	647	Yes
E070517C	Lateral (Gauges)	Copper/Siltstone	847	Yes
E070519B	Shock Speed (Gauges)	Siltstone/Al+Silt	249	Yes
E070519C	Shock Speed (Gauges)	Siltstone/Al+Silt	602	Yes
E070519D	Shock Speed (Gauges)	Siltstone/Al+Silt	864	Yes
E070616B	Spall (Gauge/VISAR)	Aluminium/Siltstone	139	Yes
E070616C	Spall (Gauge/VISAR)	Aluminium/Siltstone	146	Yes
E070808A	Spall (Gauge/VISAR)	Aluminium/Siltstone	132	Yes

Table 6.5: Siltstone experiments potentially yielding Hugoniot information

The Hugoniot of siltstone as derived from the results of VISAR experiments as opposed to the gauges experiments shown previously (all of the shot data are tabulated in table 6.5) is represented in figure 6.17. The data are well represented by a linear fit.

The fits to the release data in figure 6.18 have only been applied to the two highest stress releases as these showed the most notable deviation from the Hugoniot.

Figure 6.19 shows the complete siltstone Hugoniot, with the data from both gauges and VISAR experiments. There is some scatter as would be expected. Even though the siltstone is reasonably homogeneous, there are significant quartz inclusions in some of the samples that would likely give slightly spurious results. Despite this there is agreement between all of the experimental methods to within experimental error, and certainly reinforces the conclusion that in $\sigma - u_p$ space, the Hugoniot is indeed linear.

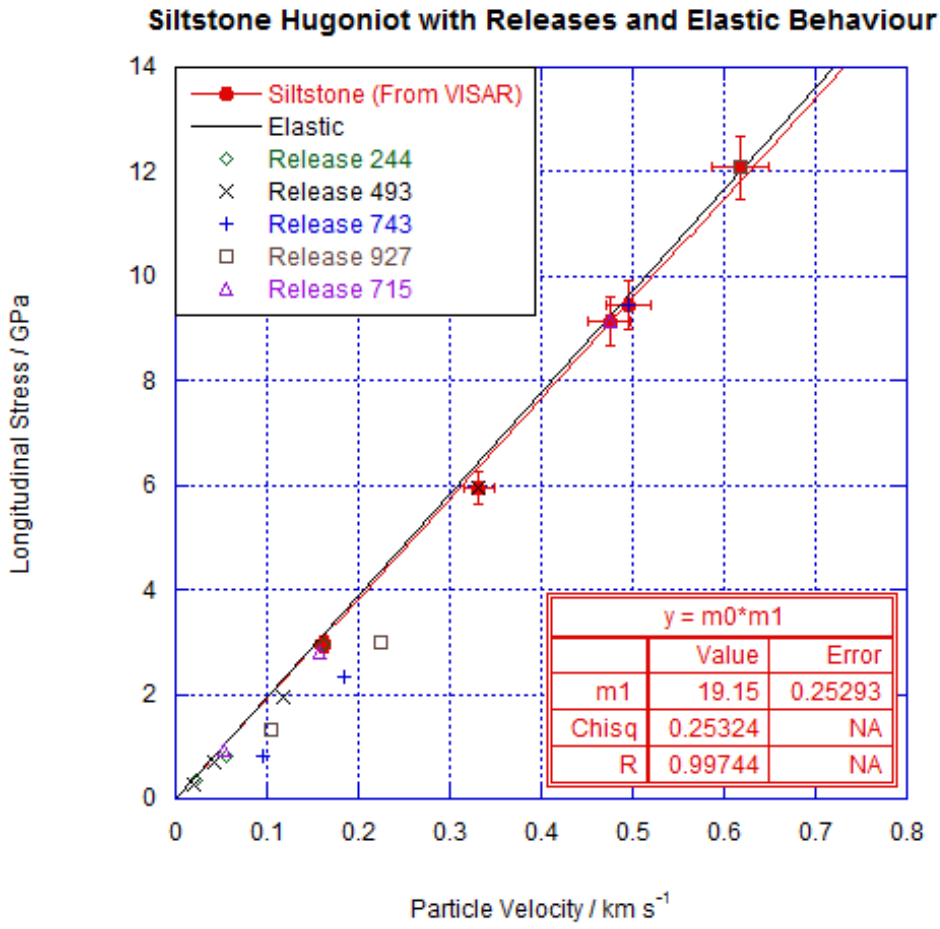

Figure 6.17: Hugoniot of siltstone (as derived from VISAR experiments) in $\sigma - u_p$ space. The theoretical elastic line plotted agrees well with both the data and the fitted Hugoniot, which is also plotted. The release points lie below the Hugoniot, seemingly more so at the higher stresses.

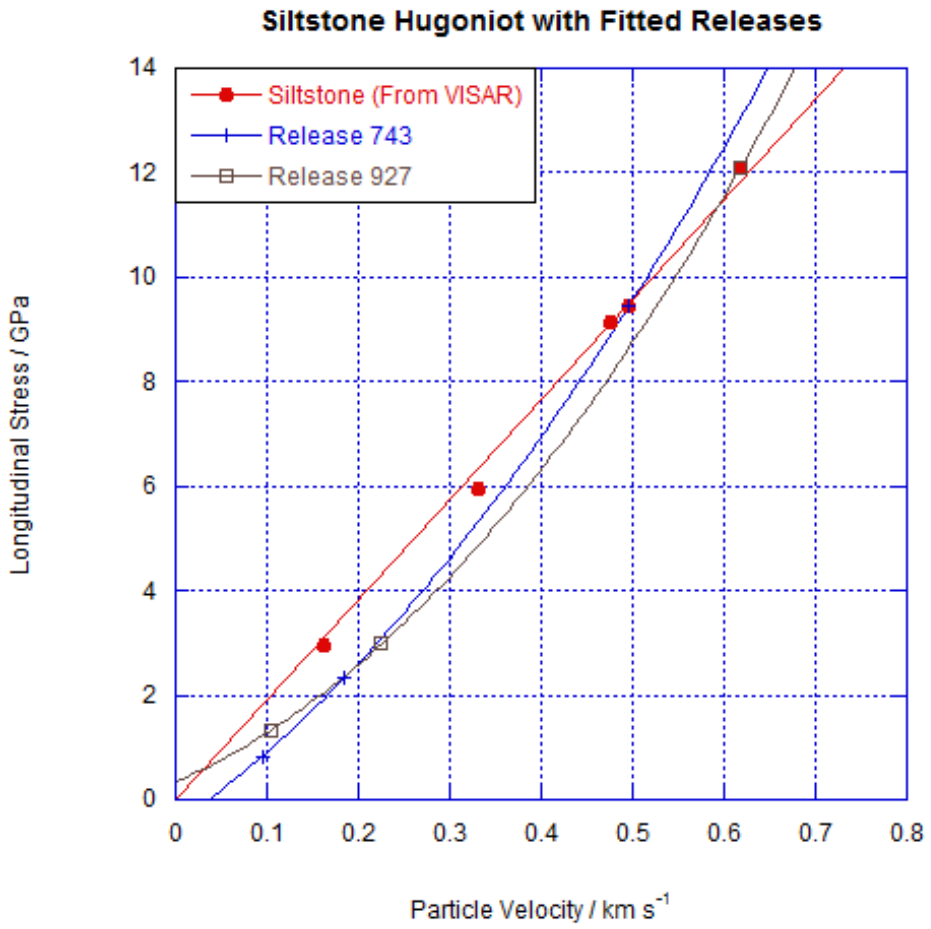

Figure 6.18: Hugoniot of siltstone in $\sigma - u_p$ space showing fits to release data. Some data have been removed when compared with figure 6.17, to make it easier to interpret the graph. There are clear deviations in the releases from the Hugoniot, suggesting some energy loss in a loading/unloading cycle.

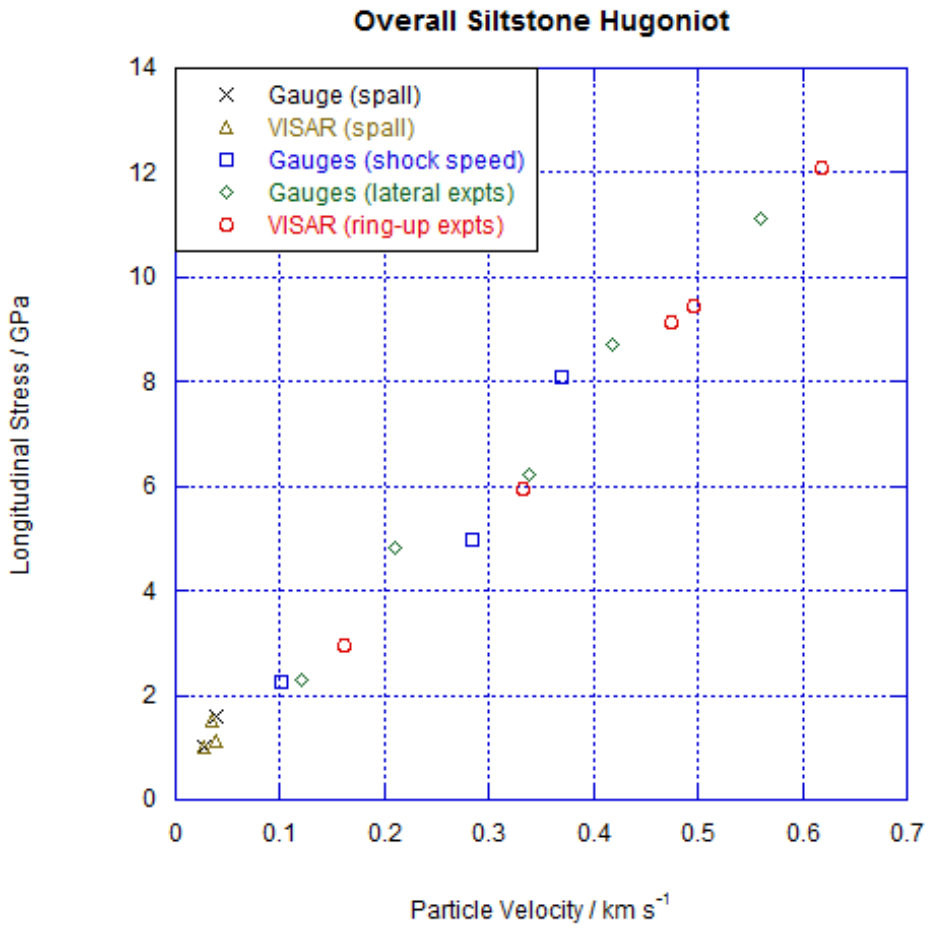

Figure 6.19: Hugoniot of siltstone in $\sigma - u_p$ space showing data from all longitudinal experiments. Note that error bars have not been plotted so as not to obscure the graph. While sample to sample variation and experimental error mean that there is some scatter to the data, the data describe a linear relationship between stress and particle velocity. The same trend is shown whichever diagnostic method is utilised.

6.2.6 Biotite Schist

Shot Code	Experiment Type (Major Diagnostics)	Impactor/Target Materials	Impact Velocity $m\ s^{-1}$	Useful Data
E070423A	Spall (VISAR)	PMMA/Biotite Schist	105	No
E070423B	Spall (VISAR)	PMMA/Biotite Schist	105	No
E070518A	Hugoniot/Release (VISAR)	Biotite Schist/Copper	250	Yes
E070518B	Hugoniot/Release (VISAR)	Biotite Schist/Copper	501	Yes
E070518C	Hugoniot/Release (VISAR)	Biotite Schist/Copper	742	Yes
E070519A	Hugoniot/Release (VISAR)	Biotite Schist/Copper	986	Yes
E090119A	Hugoniot/Release (VISAR)	Biotite Schist/Copper	90	Yes
E090119B	Hugoniot/Release (VISAR)	Biotite Schist/Copper	199	Yes
E090119C	Hugoniot/Release (VISAR)	Biotite Schist/Copper	476	Yes

Table 6.6: Biotite schist compression experiments

In table 6.6 there is a list of all the experiments that could potentially have provided Hugoniot information. The Hugoniot for biotite schist is slightly different to many of the other Hugoniots. While the data can conceivably be fitted with a straight line fit, as shown in figure 6.20 it is in fact best fitted with a second order polynomial fit as shown in figure 6.21. While it was initially considered that this could be due to data scatter, it seems unlikely that with the number of points determined from experiments that this is in fact the case. In any case the fact that none of the other "linear" Hugoniots show such a clear curved trend leads to the conclusion that there is probably an underlying physical reason for this. One possible reason is shown in the MLA data. While the majority of the components within the rock samples are mineral crystals, there is a percentage of clay in the biotite schist samples. This might induce some additional compressibility in the biotite schist samples that is not present in the other "hard rock" materials presented. This additional compressibility may well manifest itself in a similar manner to small amounts of porosity and produce an upwards curving Hugoniot.

The fits to the release data in the biotite schist samples are shown in figure 6.22. There is a clear difference from the Hugoniot for a number of cases, although due to the curve in the Hugoniot this appears to be less than the difference for the materials with linear Hugoniot relations. Owing to the curved nature of the Hugoniot and the fact that it is unclear whether at any point the material

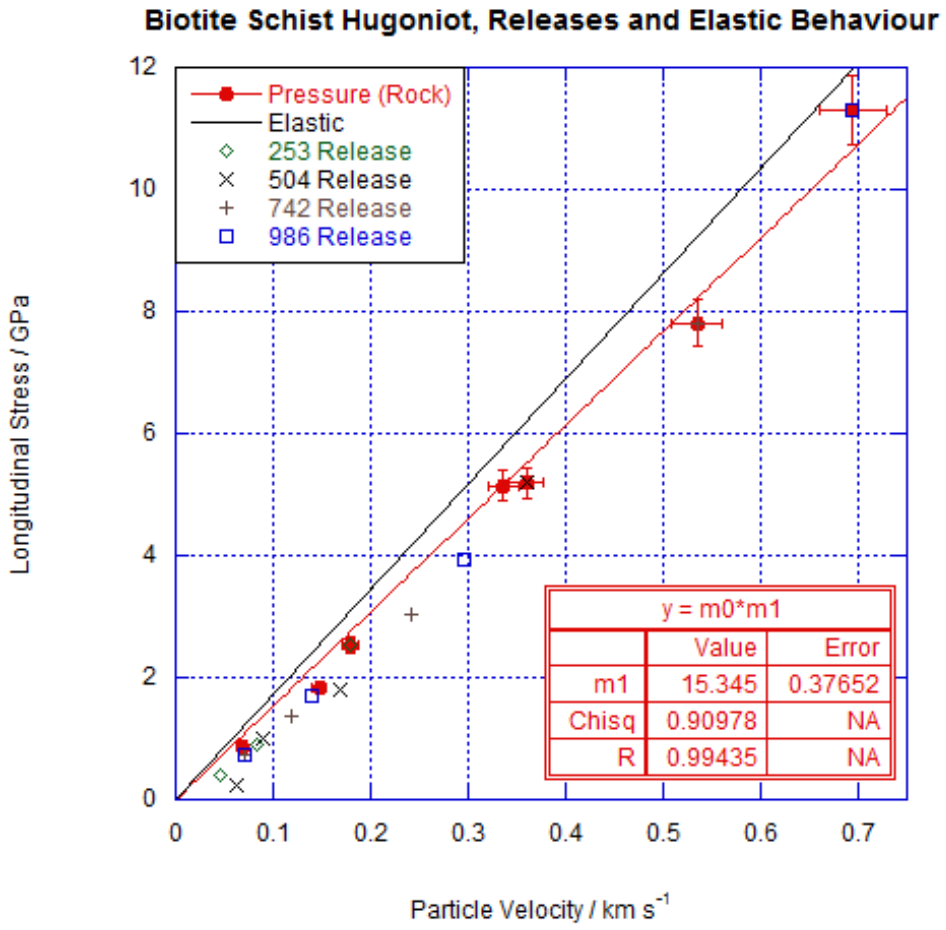

Figure 6.20: Hugoniot of biotite schist in $\sigma - u_p$ space showing a linear fit to the data and elastic behaviour. The elastic behaviour lies above the Hugoniot, which is reasonably well described by the linear fit. As is usual in this investigation, the release data lie below the fitted Hugoniot relationship.

behaves in an elastic manner, data derived from spall experiments (where the analysis requires an assumption of elastic behaviour) have not been plotted.

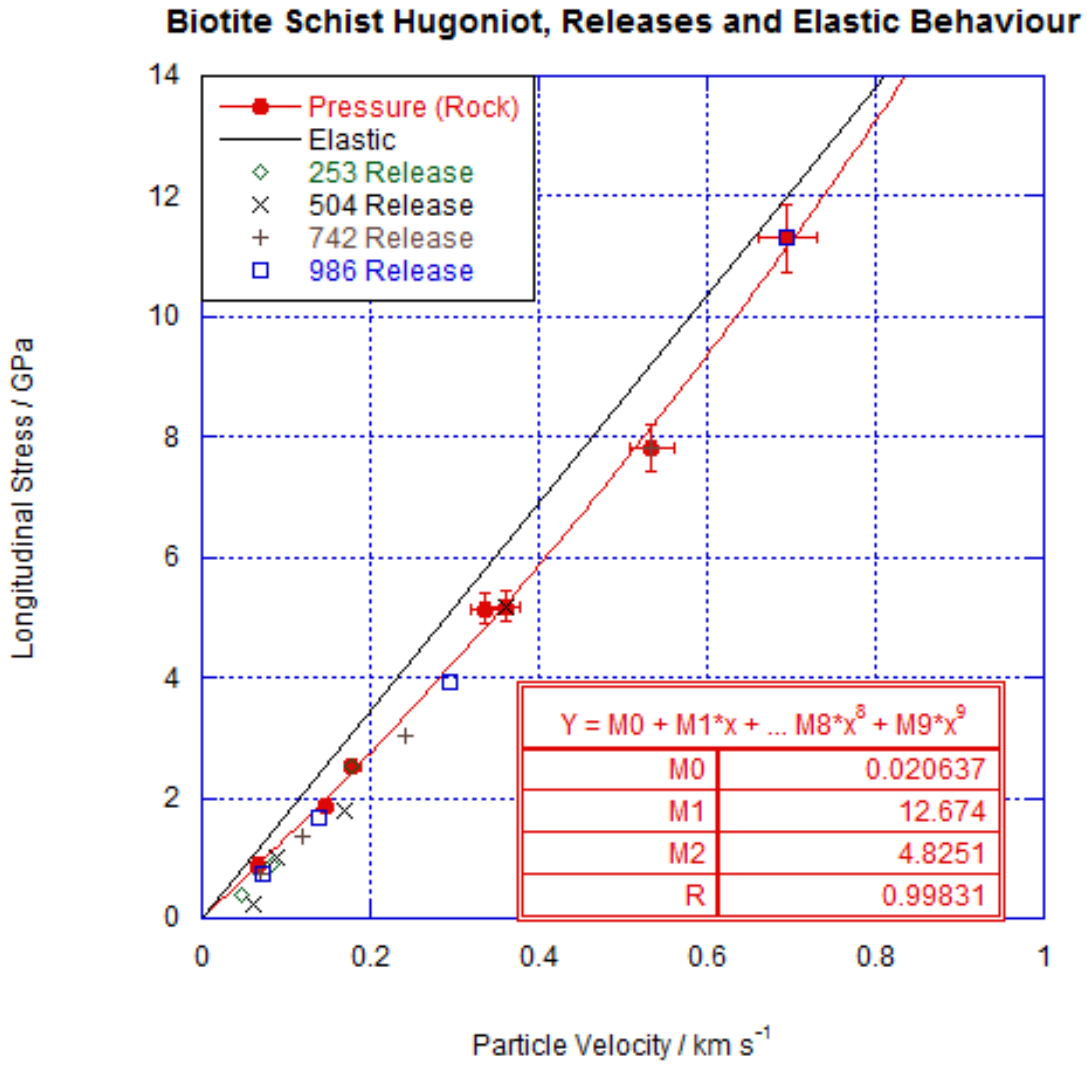

Figure 6.21: Hugoniot of biotite schist in $\sigma - u_p$ space showing a second order polynomial fit to the data. This figure is essentially the same as figure 6.20, but with an improved fit to the Hugoniot data.

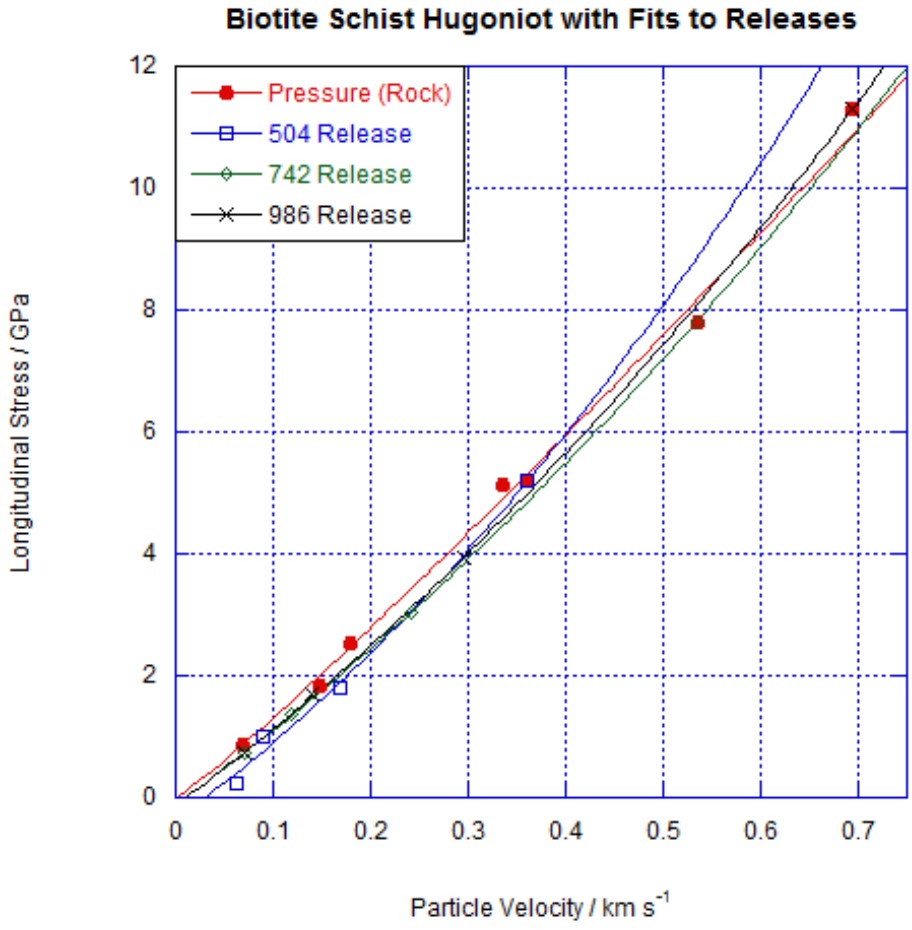

Figure 6.22: Hugoniot of biotite schist in $\sigma - u_p$ space showing fits to releases. While it can be seen that the deviation of the releases from the Hugoniot in this plot seems less than for many of the other Hugoniots, it should be noted that for waste heat measurements it is the loading line rather than the Hugoniot that is important.

6.2.7 Sandstone

Shot Code	Experiment Type (Major Diagnostics)	Impactor/Target Materials	Impact Velocity $m\ s^{-1}$	Useful Data
E060328A	Hugoniot/Release (VISAR)	Sandstone/Copper	505	Yes
E060404A	Hugoniot/Release (VISAR)	Sandstone/Copper	742	Yes
E060404B	Hugoniot/Release (VISAR)	Sandstone/Copper	991	No
E060428A	Hugoniot/Release (VISAR)	Sandstone/Copper	247	Yes
E060627B	Hugoniot/Release (VISAR)	Sandstone/Copper	1007	No
E060911A	Hugoniot/Release (VISAR)	Sandstone/Copper	979	Yes

Table 6.7: Sandstone longitudinal experiments

The sandstone (for which shot data are shown in table 6.7) is a distinctly different material, and this is seen in the Hugoniot. The Hugoniot is dominated by the porosity in the material and the fact that the pores can collapse under pressure. As the pores collapse the material loses structural integrity. The fact that the shock speed in the material is strongly dependent on the density means that as the pores are crushed, the shock speed increases. The consequence of this is a lack of distinct levels in the VISAR traces, figure 6.23 is an example.

The pore collapse process means that the material density rapidly increases with pressure as it is compressible, in contrast to the non porous materials where any increase in density is less dramatic. The increased density allows for the material to sustain a higher pressure, and hence the Hugoniot has an upward curve. Figure 6.24 shows the Hugoniot and also one set of release points, where there was sufficient definition in the VISAR trace to allow them to be elucidated. The release fit is a linear fit rather than a higher order polynomial. This is typical for a porous material.

The release fit demonstrates that the material has absorbed much more energy due to the pore collapse than the other materials in this thesis. Even accounting for the curve in the Hugoniot, the difference between the release and the Hugoniot (although it is noted that the Hugoniot is not the loading path of the material) is substantial, much greater than for the other rocks. Additionally, the elastic line lies above the Hugoniot in the low pressure regime suggesting that at no point in the stress regime investigated is the sandstone behaving in an elastic

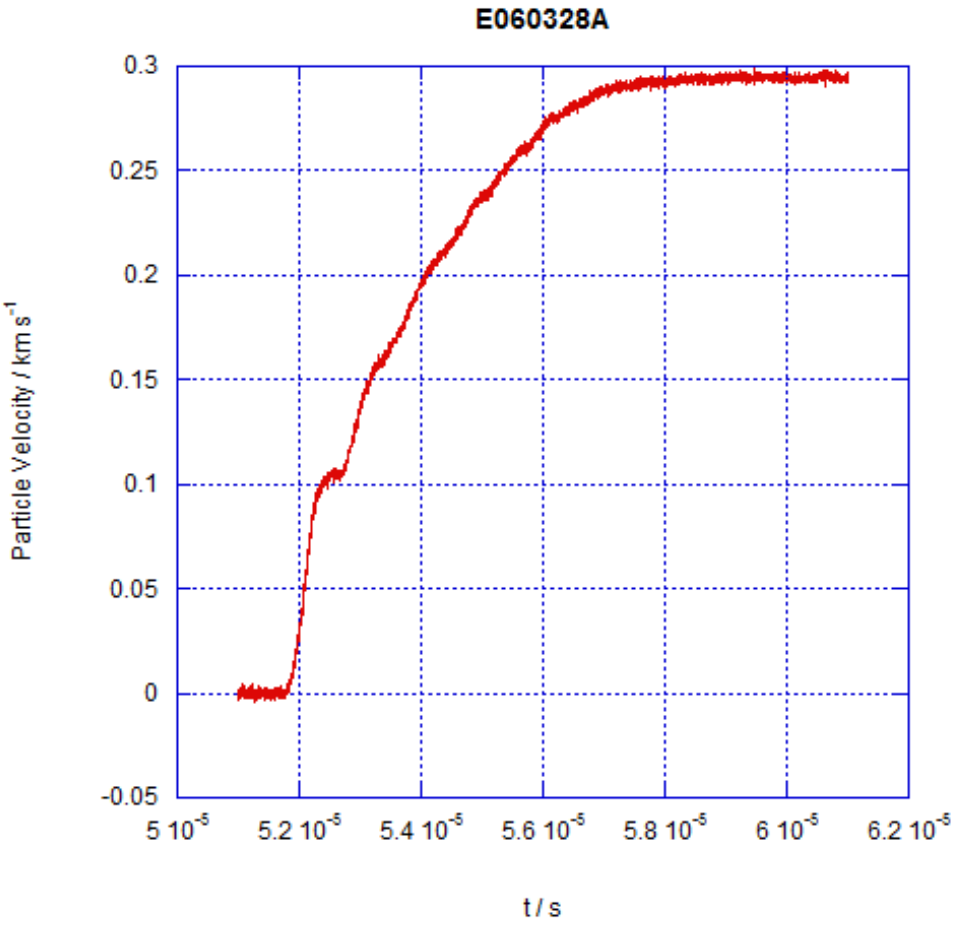

Figure 6.23: VISAR trace from a sandstone experiment. This should be compared with the example trace for this type of experiment shown in figure 5.10. The porous nature of the sandstone means that the levels are poorly defined, making both the Hugoniot points and especially the release characteristics difficult to determine.

manner. This result is consistent with the extreme softness of the material which is obvious on handling. At higher stresses the Hugoniot lies above the elastic line. This is again to be expected as the compressed material is significantly different from the material for which the elastic properties have been calculated. The fit to the Hugoniot data, while extrapolated in the figure should not be taken as a prediction of behaviour below the stress regime investigated. It is possible that

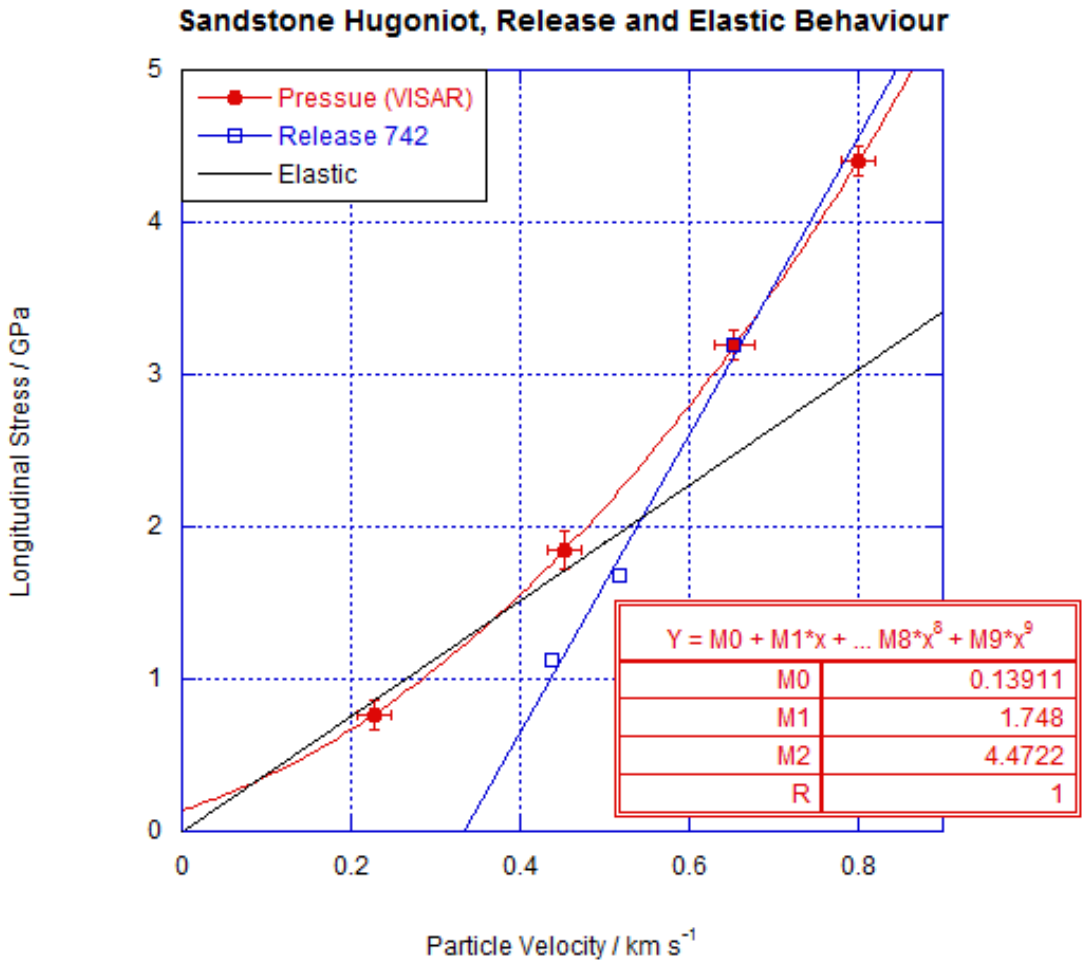

Figure 6.24: Hugoniot of sandstone in $\sigma - u_p$ space, elastic behaviour and release data. The release, as is typical for a porous material is fitted with a linear relationship. The Hugoniot is fitted with a second order polynomial, however without further data it is impossible to comment accurately on the lower pressure response of the sandstone. It may be that there is a low pressure HEL (giving a kink in the Hugoniot), or the response could converge smoothly on the origin. The Hugoniot lies below the elastic behaviour initially and then climbs above it as the material compacts at higher pressures.

there could be a very low pressure HEL (as the fit indicates) or the response could converge smoothly to the zero pressure, zero particle velocity state.

6.2.8 Basalt

Shot Code	Experiment Type (Major Diagnostics)	Impactor/Target Materials	Impact Velocity $m\ s^{-1}$	Useful Data
E080716A	Hugoniot/Release (VISAR)	Basalt/Copper	211	Yes
E080718A	Hugoniot/Release (VISAR)	Basalt/Copper	392	Yes
E080723A	Hugoniot/Release (VISAR)	Basalt/Copper	594	Yes
E080725A	Hugoniot/Release (VISAR)	Basalt/Copper	791	Yes
E080730A	Hugoniot/Release (VISAR)	Basalt/Copper	1000	Yes
E081104A	Spall (Gauge/VISAR)	Aluminium/Basalt	162	No
E081105A	Spall (Gauge/VISAR)	Aluminium/Basalt	156	No
E081216A	Lateral (Gauges)	PMMA/Basalt	341	Yes
E090118B	Lateral (Gauges)	Aluminium/Basalt	257	Yes
E091221B	Lateral (Gauges)	Aluminium/Basalt	357	Yes
E091221C	Lateral (Gauges)	Aluminium/Basalt	500	Yes
E091221G	Lateral (Gauges)	Copper/Basalt	447	Yes

Table 6.8: Shot data for basalt experiments relevant tot he determination of the Hugoniot

The basalt Hugoniot again shows a difference between the loading and unloading paths. With a linear Hugoniot the Rayleigh line will follow a similar line to the Hugoniot, although this is not true as a general statement regardless of the form of the Hugoniot. All of the relevant basalt data are presented in table 6.8. There is in fact a discernable deviation of the release from the Hugoniot at all stress levels, although it is questionable whether this is a true representation of the material or merely noise and/or error. It is noticeable from figure 6.25 that the lowest stress point (determined by VISAR) does not agree with the fit line particularly well. It is viewed as a slight anomaly, but lack of samples made repeating the experiment an impossibility. The remaining Hugoniot points however show a good agreement.

In fitting curves to the release points for the three highest stress values we can see more clearly the deviation from the fitted Hugoniot, see figure 6.26. The elastic line derived from the acoustic impedance also shows a very close agreement with the data, suggesting that the material is behaving in the way that one would expect it to if it were behaving elastically on compression. Obviously the deviation from the Hugoniot on release indicates some level of non-elastic behaviour, but

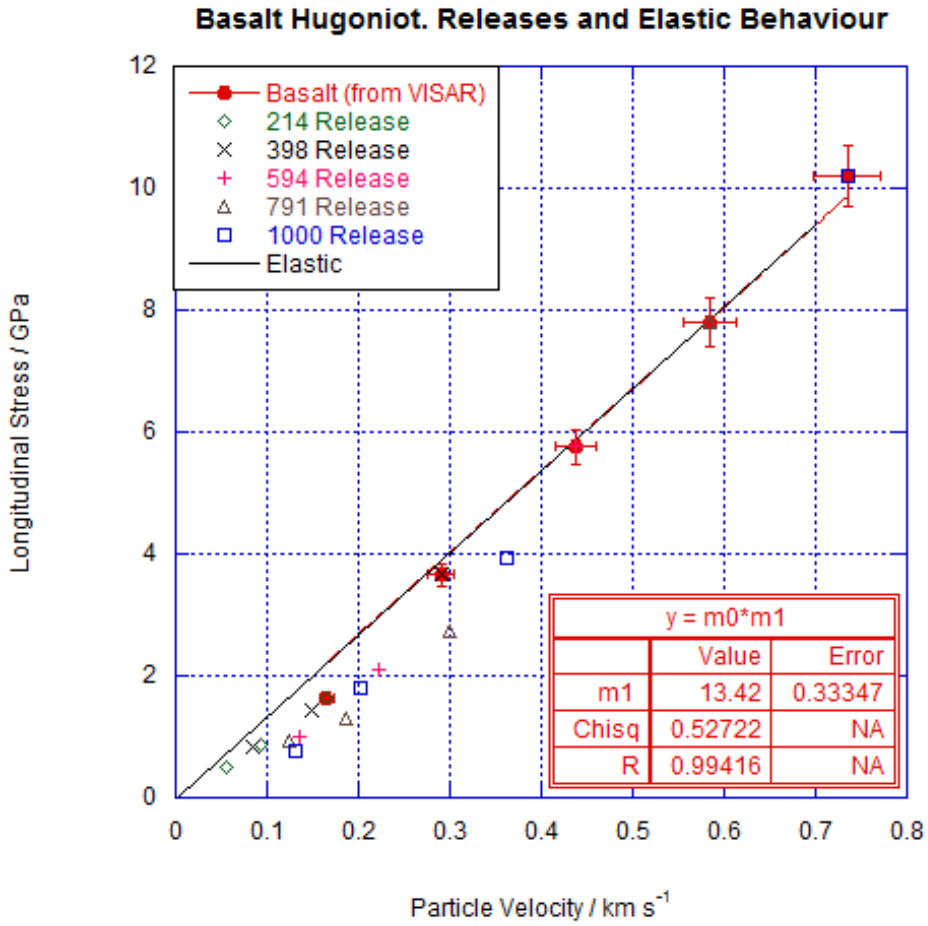

Figure 6.25: Hugoniot of basalt in $\sigma - u_p$ space. The fit to the Hugoniot data is based on an assumption of a linear Hugoniot relationship. While it is not entirely clear from the purely VISAR data shown that a linear fit is appropriate, referring to figure 6.27 suggests the conclusion that the low stress VISAR datum is an anomaly caused by sample to sample variation. The assumed fit shows a strong similarity to the theoretical elastic behaviour. The release data all lie below the Hugoniot as it is plotted.

this is not noticeable on the loading part of the cycle.

In addition to the VISAR data, gauges were included in the lateral samples for the basalt, and therefore it is possible to add these to the Hugoniot. This has

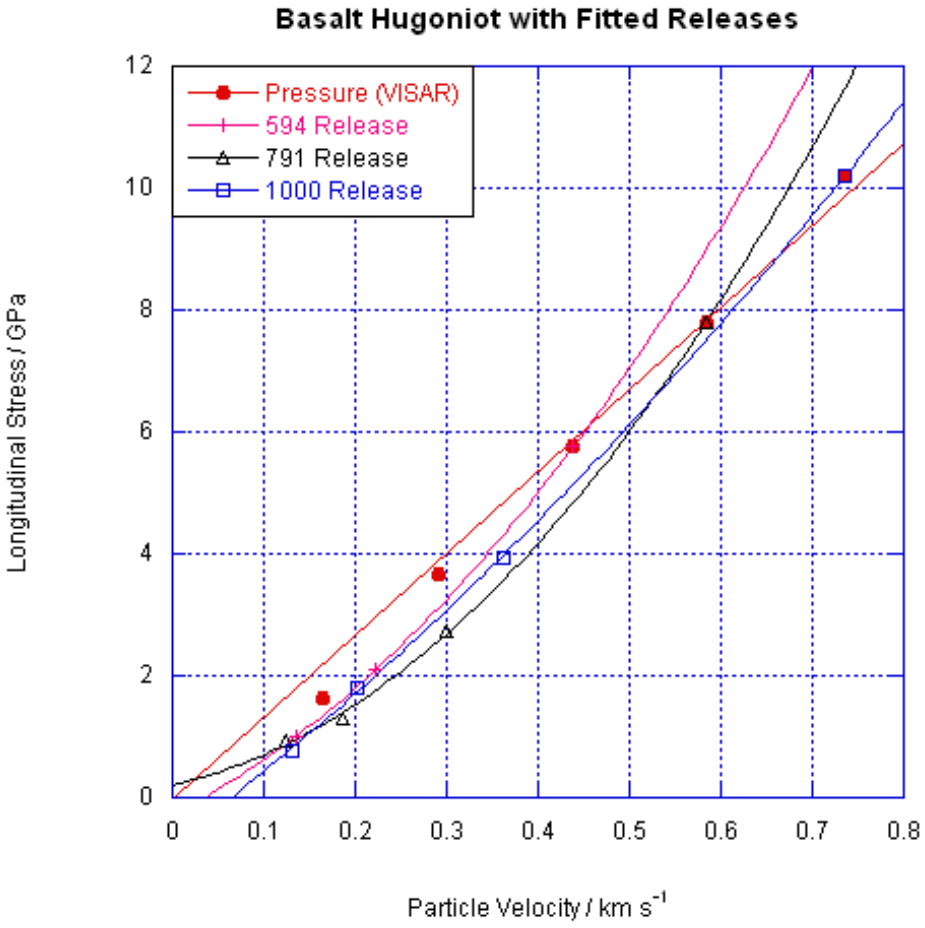

Figure 6.26: Hugoniot of basalt in $\sigma - u_p$ space. Some of the lower release data have been removed to make viewing of the graph easier. It is clear from the fits to the releases that there are large deviations from the Hugoniot as plotted and also from the loading lines (which are not shown).

been done in figure 6.27. It can be seen that there is agreement between the two sets of data. Data from spall experiments has not been included as there was no clear plateau in the diagnostics, suggesting the material has been released before reaching the peak stress.

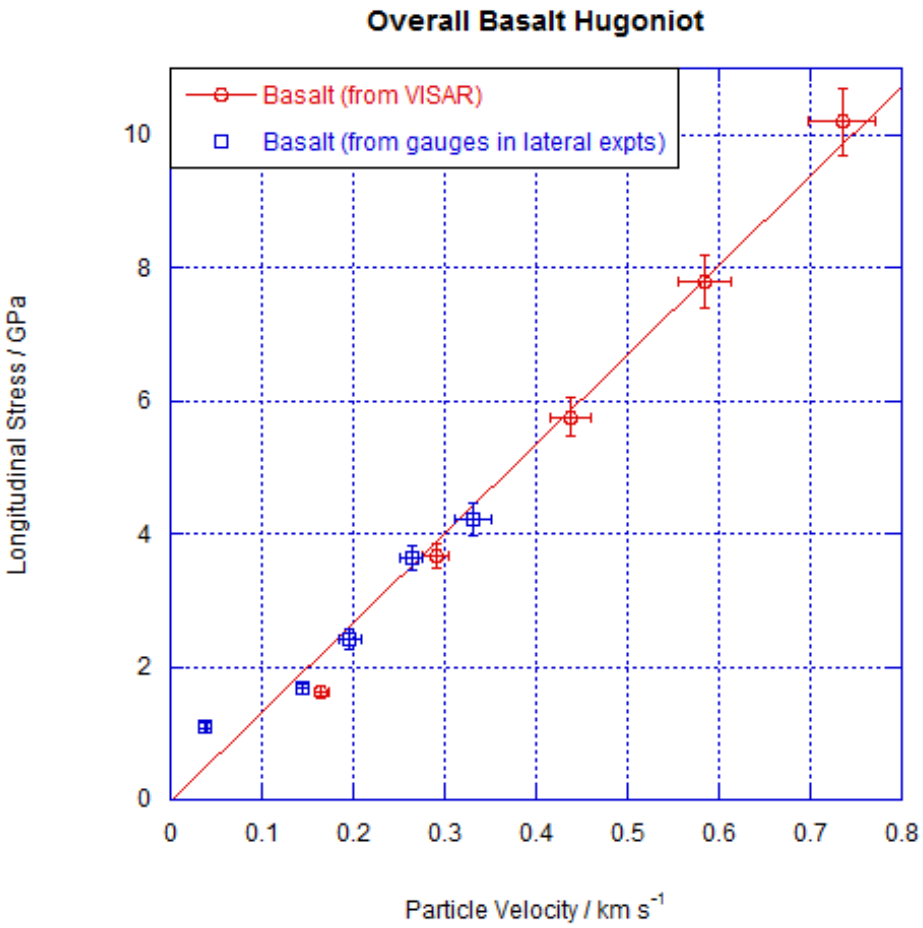

Figure 6.27: Hugoniot of basalt in $\sigma - u_p$ space showing both VISAR and gauge data. From these data it becomes clearer that the lowest stress VISAR datum is slightly anomalous. The linear relationship fitted to the data is a good description of the data, although there are some places where, through sample to sample variation, the data not agree with the fit to within the experimental error.

6.2.9 Iron Ore

Shot Code	Experiment Type (Major Diagnostics)	Impactor/Target Materials	Impact Velocity $m\ s^{-1}$	Useful Data
E080717A	Hugoniot/Release (VISAR)	Iron Ore/Copper	204	Yes
E080721A	Hugoniot/Release (VISAR)	Iron Ore/Copper	393	Yes
E080724A	Hugoniot/Release (VISAR)	Iron Ore/Copper	595	Yes
E080729A	Hugoniot/Release (VISAR)	Iron Ore/Copper	799	Yes
E080731A	Hugoniot/Release (VISAR)	Iron Ore/Copper	975	Yes
E081104B	Spall (Gauge/VISAR)	Aluminium/Iron Ore	172	No
E081217A	Lateral (Gauges)	Copper/Iron Ore	146	No
E090121A	Lateral (Gauges)	Copper/Iron Ore	140	Yes
E070112B	Lateral (Gauges)	Copper/Iron Ore	262	Yes
E091221D	Lateral (Gauges)	Aluminium/Iron Ore	493	Yes
E091221E	Lateral (Gauges)	Copper/Iron Ore	495	Yes
E091221F	Lateral (Gauges)	Copper/Iron Ore	497	Yes

Table 6.9: Iron ore experiments with potential to contribute to knowledge of the Hugoniot

Data for iron ore experiments are tabulated in table 6.9. The iron ore has a distinctive structure and this is shown up in the loading characteristic as seen in the VISAR trace in figure 6.28. There is no distinctive step structure as seen in the fully dense rocks. The trace is much noisier and does not allow for a release to be determined. As with the sandstone, the shock speed will increase as the pores collapse. Additionally the iron ore is much closer in impedance to the copper than the other materials examined. This could also lead to a lack of distinct steps, a problem which could be overcome through the use of a higher impedance witness plate.

The iron ore itself is a high impedance material but has significant macroscale porosity. The Hugoniot, figure 6.29, has an initially linear structure which reflects the fact that the material behaves elastically up until the point where the pores can collapse and the material can fail. The elastic nature of the low pressure region is demonstrated by the close agreement with the line derived from the acoustic impedance. Above an HEL of approximately 3 GPa the pore collapse means that the material does not continue to behave in an elastic manner. This corresponds to a deviation in the Hugoniot.

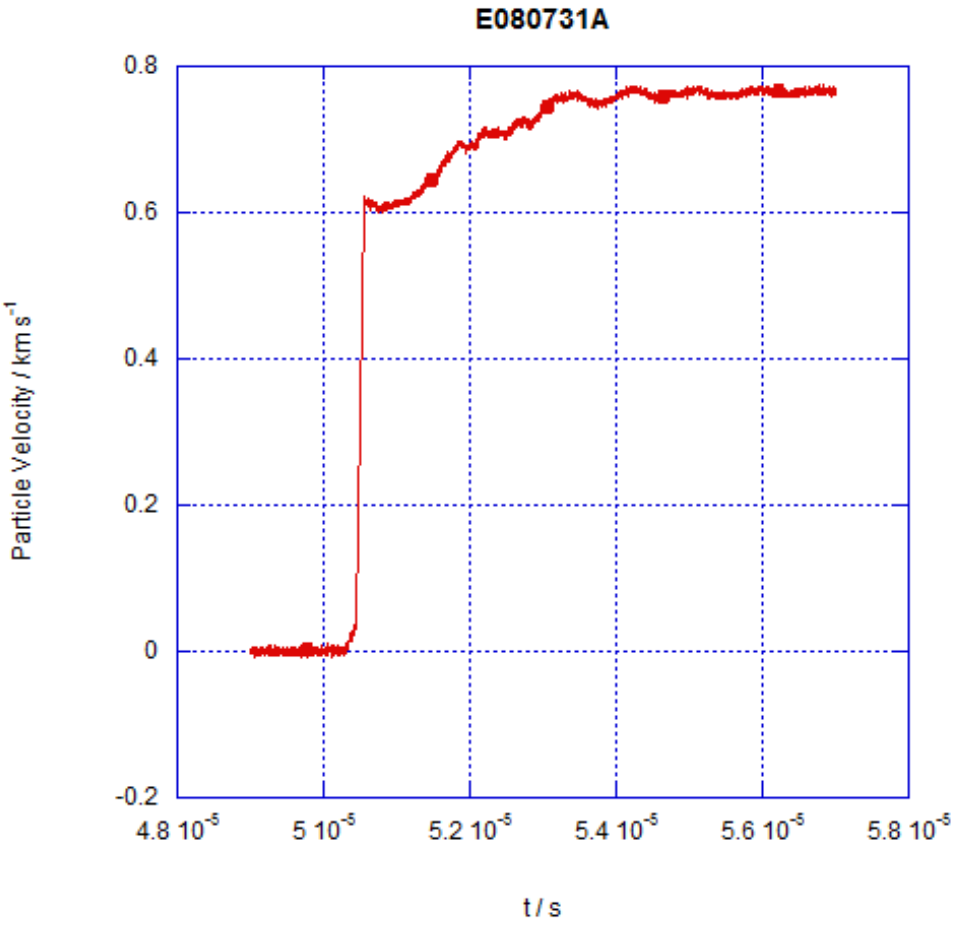

Figure 6.28: VISAR trace from iron ore experiment. While it is possible to discern an initial plateau level from this trace, it is not possible to obtain any meaningful release data, as there are no subsequent levels of the sort seen in figure 5.10.

In order to clarify the Hugoniot as derived from the VISAR traces, data from longitudinal gauges included in the lateral experiments have been added to figure 6.29. It can be seen that the data is somewhat variable in the agreement with the fit lines (in fact this is true of the VISAR data as well). The reason for this is the large sample to sample variation in the material. The distribution of macroscopic flaws in the material was not uniform between samples and it is likely that this contributed to the scatter in the data. Additionally, the presence of large macroscopic flaws can modify the loading characteristics and adversely

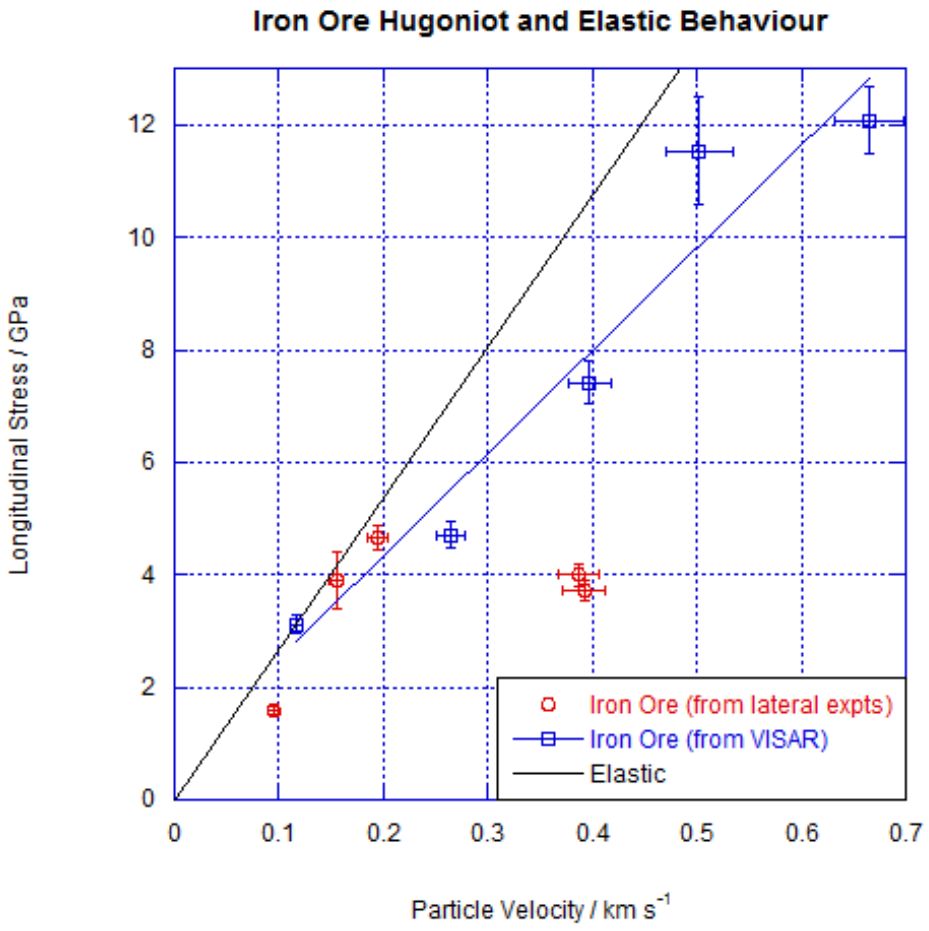

Figure 6.29: Hugoniot of iron ore in $\sigma - u_p$ space. It is assumed that the material behaves elastically up to a point around 3-4 GPa, where a deviation in the Hugoniot is observed. Unfortunately sample to sample variation, and especially large flaws in the material, meant that the data do not sit, in many cases, within experimental error of the fitted line. The two data points around 4 GPa and 0.4 km s^{-1} are from experiments where the gauge traces showed that the stress pulse had been prematurely released.

affect the results. A particular stress state arising from the loading characteristics of a particular velocity will only be maintained as long as the material is not released. A large macroscopic flaw can act as just such a point of release. The gauge data that sits nearest to the fit line were derived from gauge traces

where it is clear the full loading of the material has occurred, and the material has not been released prematurely. An example of a gauge trace where there has been a full loading is shown in figure 6.30. The flat top is what is expected in a normal plate impact loading, i.e. that the loading pulse is of finite duration. The data points that are significantly further from the Hugoniot fit were derived from data where it is obvious that premature release of the material has occurred. An example of premature release is shown in figure 6.31. There is no flat topped loading pulse, merely a spike where the release from a flaw has reduced the pressure in the material before it can reach the level that would be expected given the impact conditions. The releasing caused by flaws in the material is a limitation of the material and one that could not be overcome with the limited availability of samples. It should also be noted that if the flaws in a material are sufficiently large then the ability of a 50 mm bore gas gun with the diagnostics available for this investigation to accurately sample the material is limited. This mismatch in samples and equipment is obviously something that should ideally be avoided, but in this case it was impossible to do so.

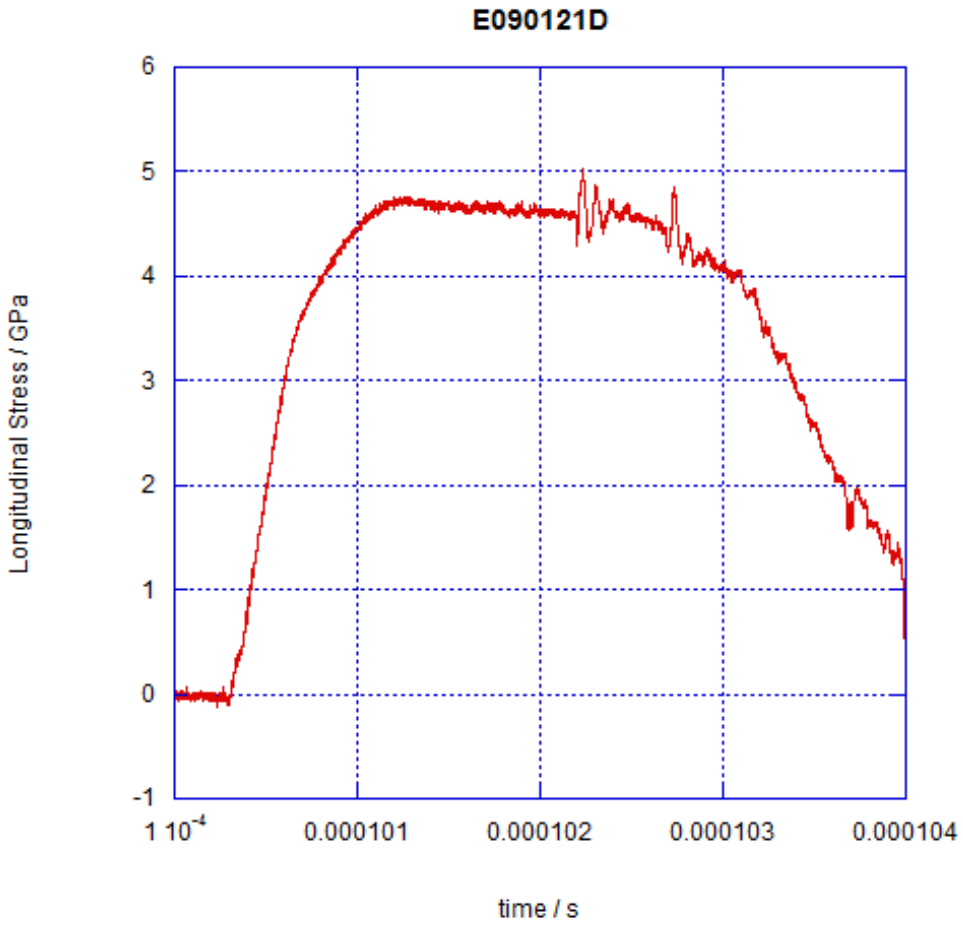

Figure 6.30: "Good" gauge trace from iron ore experiment. The relatively flat topped plateau indicates that the sample has been loaded in the manner intended by the experimental design and has not been released prematurely from flaws within the sample.

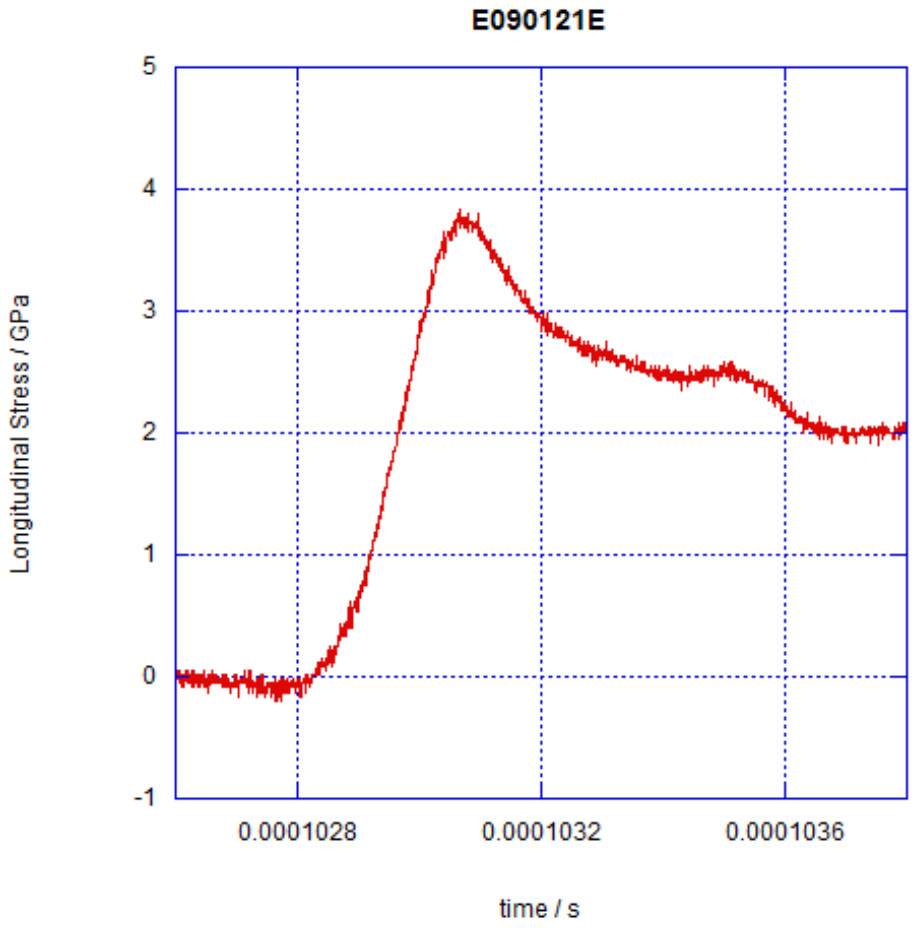

Figure 6.31: "Bad" gauge trace from iron ore experiment. In this case there is no flat topped pulse as one would expect in a plate impact experiment of this sort. Instead, the presence of flaws in the material have caused the material to be released prematurely, so the peak stress reached is below what would be expected for the material.

6.3 Overall Hugoniot Summary

To give an idea of the overall range of Hugoniots that are covered in this thesis, figure 6.32 plots all of the fits to the Hugoniot data on the same axes. The lines are only plotted to roughly the limit of the experimental data to avoid significant extrapolation. Figure 6.33 shows an enlarged version of the same plot focussing on the low stress region. The fact that there are clear differences between the rock types means that in modelling the materials for the HSBM, the different materials can be given appropriately different compressional behaviours.

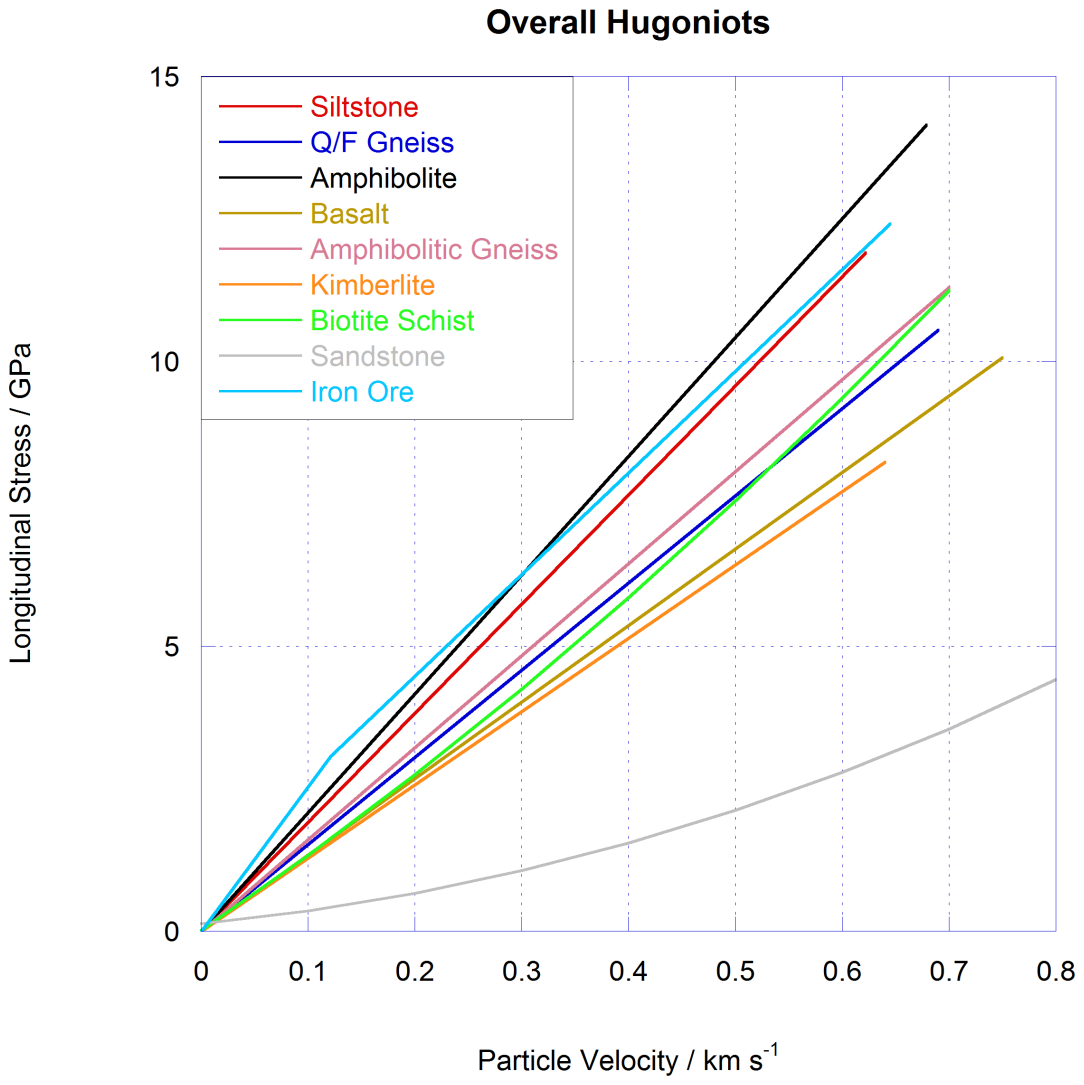

Figure 6.32: Hugoniots from all materials in $\sigma - u_p$ space. A range of material behaviours can be seen. The biotite schist and the sandstone both have curved Hugoniots with no obvious HEL from the data obtained. The iron ore has a distinct kink, where there is a deviation from elastic behaviour. While the remainder of the Hugoniots show a linear relationship, there is a wide variety of slopes.

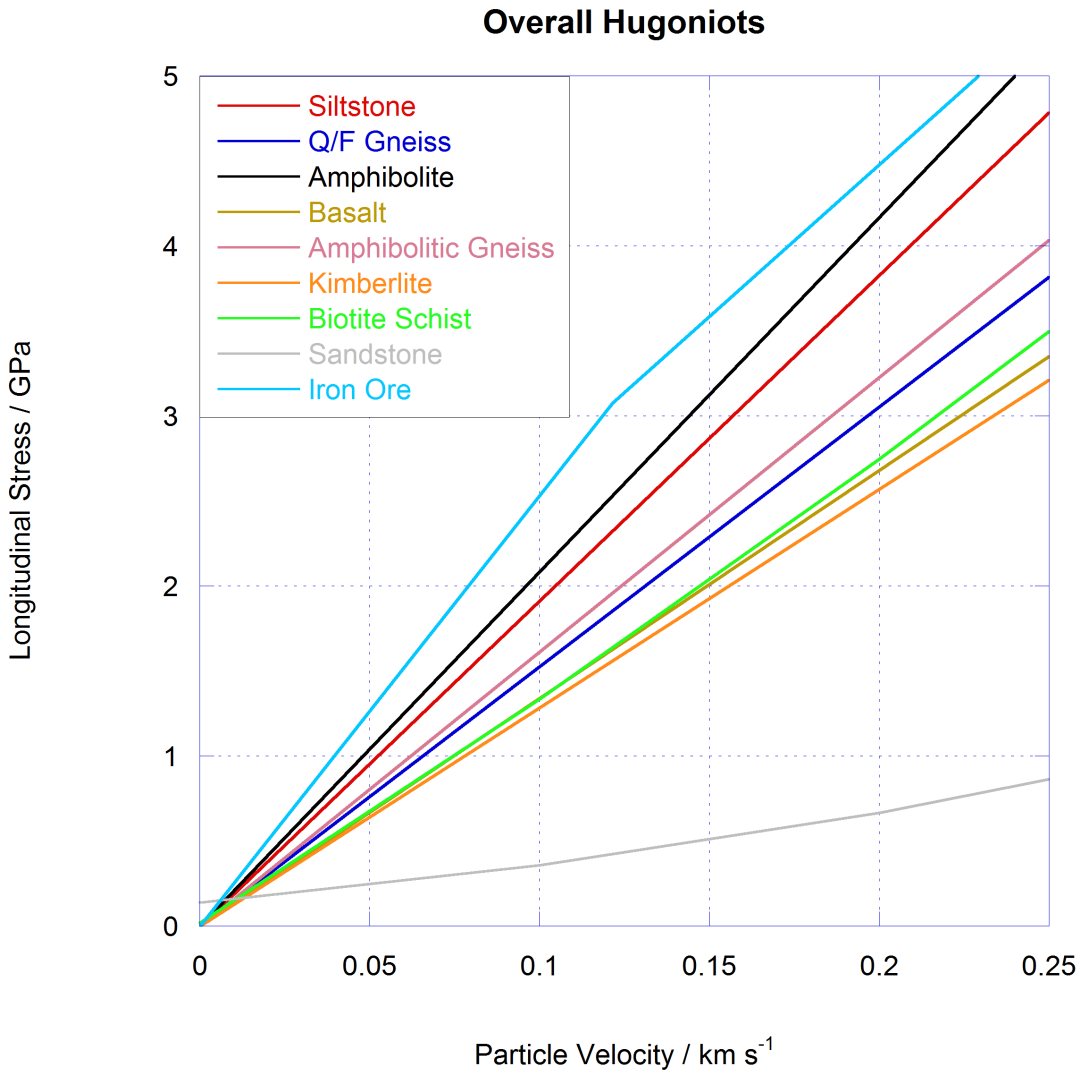

Figure 6.33: Hugoniots from all materials in $\sigma - u_p$ space (enlarged). This plot is the same as that in figure 6.32 but enlarged so that the low pressure response can be seen more easily.

6.4 Further Results from Compressional Experiments

6.4.1 Waste Heat Measurements

Section 5.2.5 described a method which when applied to release measurements could give an estimate of the energy that is irretrievably lost in the loading and unloading cycle. When the data from the experiments are processed it becomes clear that at best this method gives a fairly rough estimate. In many cases other factors such as sample to sample variability seem to affect the results, and as mentioned previously, one anomalous point in the release curve can make a substantial difference to the output of the formulae. It is certainly the case that the results however broadly follow the trend that can be seen graphically in the Hugoniot and release plots. If the release is further from the Hugoniot then the method calculates a greater waste heat. This is as it should be, so it is perhaps more accurate to say that the failure is less in the method of waste heat calculation and more in the variability of the experimental data.

A valid question therefore is whether the data could have been better obtained to allow for greater accuracy in the waste heat measurements. The answer is almost certainly yes, but the practicalities of this are more questionable. Removing the sample to sample variation is possible (through the careful selection of samples), but probably not desirable, as this would lead to an inaccurate conclusion as to the physical properties of the material under investigation. In so far as obtaining more points on the release curve through the determination of more levels in the VISAR trace; the trace will inevitably be hard to interpret at the end of the experiment as the time difference and the particle velocity difference between steps becomes small. The signal will always eventually become lost in the noise. In the early part of the trace however an improvement could be made by simply replacing the copper with a higher impedance material. A higher impedance material would mean that the height of the initial steps on the trace would be smaller in particle velocity. Thus more steps would be able to be fitted in before they became indistinguishable, leading to an increased amount of release data and an

improved fit to this data. This is impractical due to the availability, cost and in some cases difficulty in machining higher impedance materials when compared to the ease of using copper as the well-characterised witness material.

Despite the limitations of the method and the results in these calculations, it is certainly of benefit for the purposes of blast modelling to have some indication of the energy absorbed on blast loading the rock mass in a mining situation. Table 6.10 tabulates the results of the calculations. Energy recovered refers to the energy that is not lost in the loading/unloading cycle and is released back to the environment on unloading.

There are a number of points that are worth making with regards to the results in the table. Firstly it should be noted that there is in fact no experiment where the waste heat is zero. The reasons for this are that in any impact process, even an elastic one, there will be processes that use energy, such as heating of the material. It should be remembered that the loading along the Rayleigh line is not an isentropic loading. This will mean that this energy is unavailable to be released back to the environment during unloading. While the absolute values should not be read too carefully (as there are large sources of error associated with the calculations, not least a 5-7% error on the initial data points) there are some useful trends. In the linear Hugoniot materials (basalt, kimberlite, siltstone and amphibolitic gneiss) there is generally less energy recovery at the higher stresses (in the non-elastic regime) than in the low stress regime. This is as would be expected. The biotite schist shows the oposite trend which is further evidence of the non typical behaviour of this material. The sandstone, as would be expected, shows a significantly reduced amount of energy recovered compared with the other materials. Finally it should be noted that across the materials, the overall agreement is reasonable, showing that for these materials the energy loss during loading/unloading cycles is fairly similar.

Table 6.10: Table of Calculated Energy Loss in Loading/Unloading Cycles. An error of around 5-7% is appropriate of the energy recovery values

Rock Type	$\boldsymbol{\sigma_x}$ **GPa**	**Energy Recovered % - Parabolic Fit**	**Energy Recovered % Trapezium Rule**	**Impact Velocity** $(\boldsymbol{m\ s^{-1}})$
Kimberlite	8.2	78	80	845
Kimberlite	5.5	90	92	591
Kimberlite	3.6	85	90	387
Kimberlite	2.1	80	88	250
Amph Gneiss	11.4	81	84	986
Amph Gneiss	8.0	91	91	732
Amph Gneiss	5.6	77	81	498
Amph Gneiss	2.8	95	85	251
Siltstone	12.1	73	77	927
Siltstone	9.6	70	73	743
Siltstone	6.0	94	95	493
Siltstone	3.0	77	86	244
Basalt	10.2	72	73	1000
Basalt	7.8	63	67	791
Basalt	5.8	65	66	594
Basalt	3.7	74	76	392
Basalt	1.6	86	86	211
Q/F Gneiss	7.6	74	75	778
Sandstone	3.2	25	25	742
Biotite Schist	11.3	81	83	986
Biotite Schist	7.8	84	85	742
Biotite Schist	5.2	73	77	501
Biotite Schist	2.5	71	73	250

6.4.2 Shock Velocity

Shot Code	Experiment Type (Major Diagnostics)	Impactor/Target Materials	Impact Velocity $m\ s^{-1}$	Useful Data
E041217A	Hugoniot (Gauges)	Copper/Gneiss	800	No
E050111A	Hugoniot (Gauges)	Copper/Gneiss	810	Yes
E050112A	Hugoniot (Gauges)	Copper/Gneiss	256	Yes
E050112B	Hugoniot (Gauges)	Copper/Gneiss	499	Yes
E050113A	Hugoniot (Gauges)	Copper/Gneiss	957	Yes
E050119A	Hugoniot (Gauges)	Copper/Gneiss	656	Yes
E050201A	Hugoniot (Gauges)	Copper/Gneiss	400	Yes
E050428A	Hugoniot (Gauges)	Copper/Amphibolite	217	Yes
E050428B	Hugoniot (Gauges)	Copper/Amphibolite	398	Yes
E050429A	Hugoniot (Gauges)	Copper/Amphibolite	555	Yes
E050429B	Hugoniot (Gauges)	Copper/Amphibolite		No
E050506A	Hugoniot (Gauges)	Copper/Amphibolite		No
E050506B	Hugoniot (Gauges)	Copper/Amphibolite		No
E050527A	Hugoniot (Gauges)	Copper/Amphibolite	705	Yes
E050527B	Hugoniot (Gauges)	Copper/Amphibolite		No
E050530A	Hugoniot (Gauges)	Copper/Amphibolite	1038	Yes
E070519B	Shock Speed (Gauges)	Siltstone/Al+Silt	249	Yes
E070519C	Shock Speed (Gauges)	Siltstone/Al+Silt	602	Yes
E070519D	Shock Speed (Gauges)	Siltstone/Al+Silt	864	Yes
E070519E	Shock Speed (Gauges)	Copper/Al+Silt	879	Yes

As mentioned previously, it is possible with two gauges to examine the shock speed of the material concerned by examining the transit time between the two stress gauges. In many cases the rise of the gauges is ill-defined, and therefore large errors are present in the analysis. However it can be seen from figures 6.34 and 6.35 that there is no clear trend in the data, even when the errors are taken into account. Essentially this means that over the range of stresses investigated the shock speed is effectively constant, and not dissimilar to the measured longitudinal sound speed (noting of course that there is also an error associated with the measured longitudinal sound speeds). This is in good agreement with much of the literature data [3], such as that shown in figure 6.36.

Note that the literature data presented here are subsets of the full data showing merely that at certain low velocities there is no dependence of shock velocity on particle velocity.

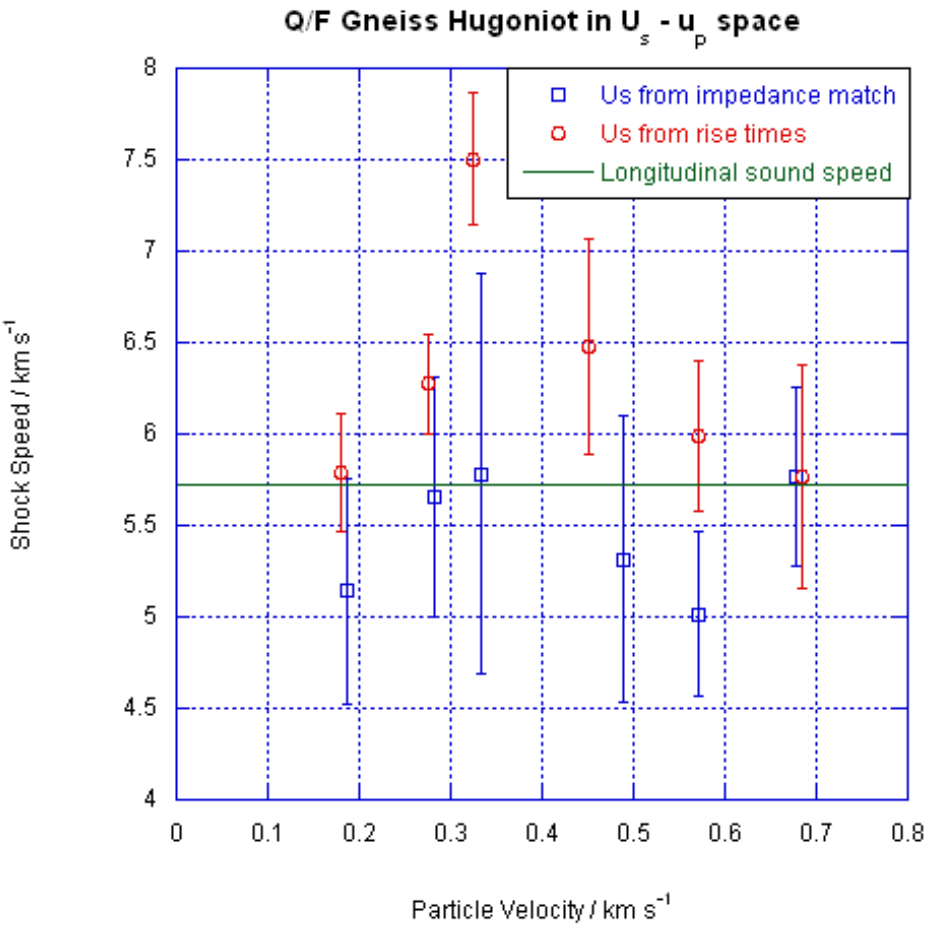

Figure 6.34: Shock velocity in quartz/feldspathic gneiss experiments. Data are shown both from measured shock velocity (using the time of arrival method) and from impedance matching with the copper Hugoniot. There is no obvious trend to the shock velocity with particle velocity. The static longitudinal sound speed is also plotted and shows some similarity with the data. It should be noted that the noise in the gauge traces for the gneiss made the determination of time of arrival difficult.

As mentioned in section 5.2.4 some further experiments were carried out using rocks sandwiched between aluminium anvils. As expected the times of arrival of the shock in the gauges in the anvils were much more accurately determined than for the gauges embedded directly in the rocks. An example of this increase in

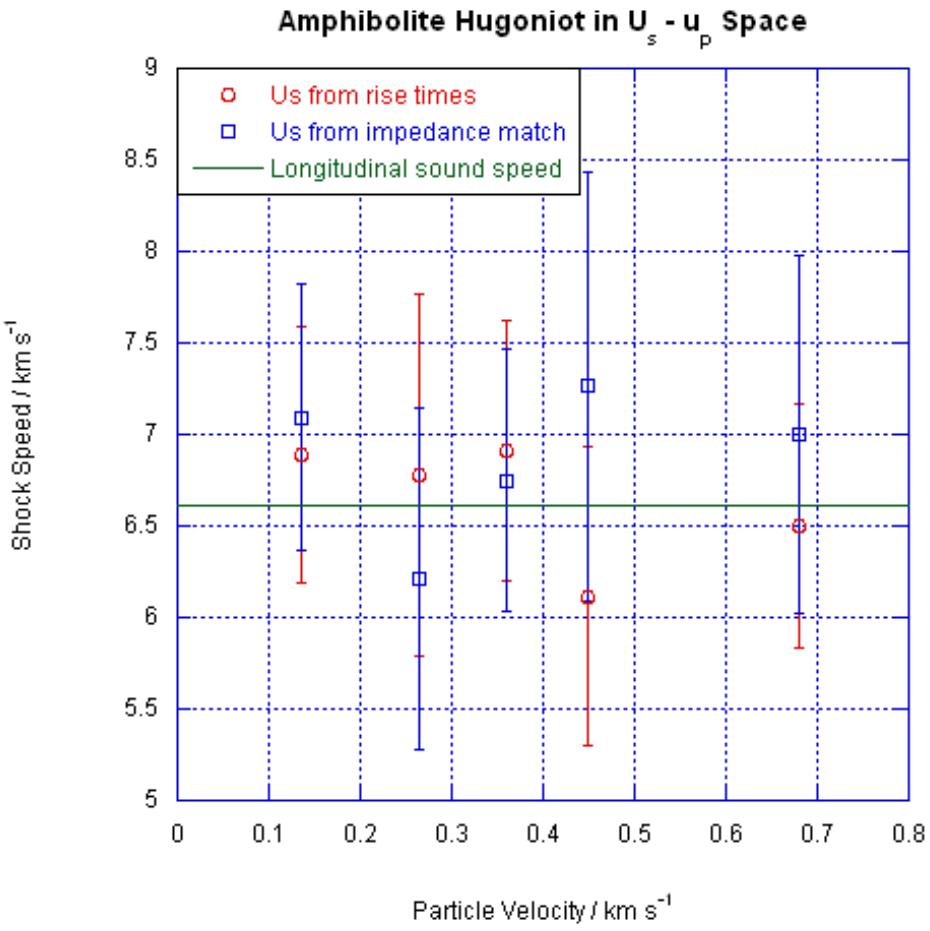

Figure 6.35: Shock velocity in amphibolite experiments. As with figure 6.34 both measured and impedance matched data are plotted. Owing to the lower noise in the gauges when used in amphibolite, the determination of the shock velocity was significantly easier. The results demonstrate that there is no discernable trend in shock velocity with increasing particle velocity for amphibolite. The data also agree well with the measured static longitudinal sound speed.

accuracy can be seen in Figure 6.37.

It is necessary to use data from the literature to account for the shock speed in the epoxy and aluminium components of the experiment, but a good measurement of the shock speed in the rock can be obtained. There are a couple of issues

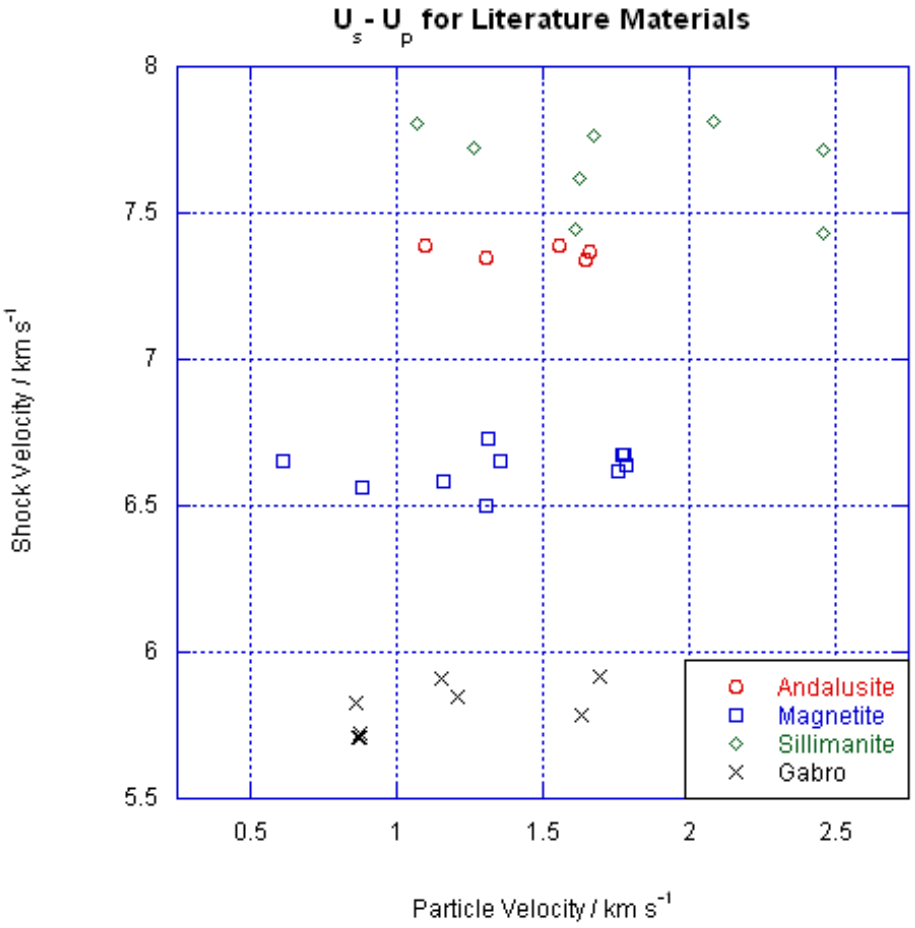

Figure 6.36: Shock speed and particle velocities from [3]. The data demonstrate that for a range of different geological materials, with differing shock velocities, it is possible to find a similar relationship in the literature to the one found in this investigation between shock and particle velocities (i.e. that there is no discernable trend).

which affect the accuracy of this method however. Firstly there is still a finite rise time and it is appropriate therefore to give some uncertainty due to this to the time of arrival in the gauge. Additionally the exact position of the gauge within the epoxy layer (which has a finite thickness) is unknown and therefore must be estimated. After accounting for these inaccuracies as error bars, it allows for a plot such as the one shown in figure 6.38 to be constructed.

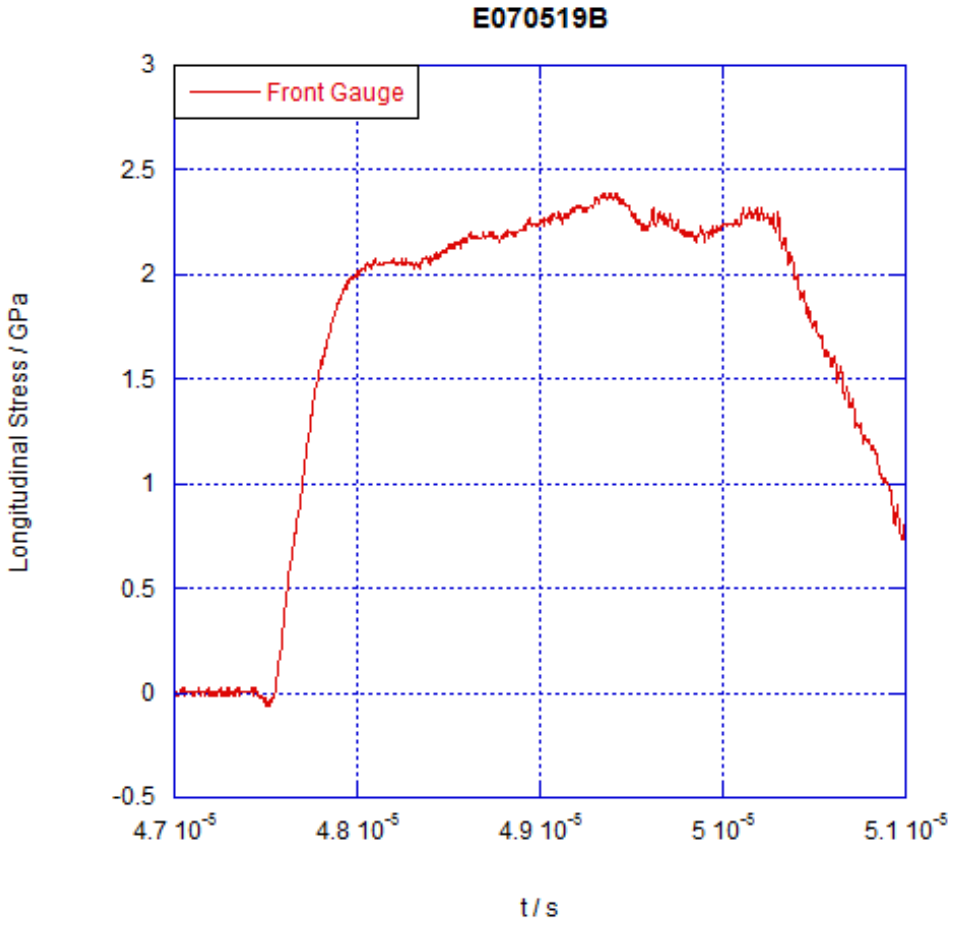

Figure 6.37: Gauge trace from an aluminium anvil experiment. The purpose of using the aluminium anvils in these experiments was to provide more reliable time of arrival data. When comparing this trace to the one shown in figure 6.1 it can be seen that this aim was acheived.

Figure 6.38 shows a similar trend to figures 6.34, 6.35 and 6.36, i.e. a lack of a definite trend between shock velocity and particle velocity or longitudinal stress. There is also good agreement with the measured longitudinal sound speed for siltstone.

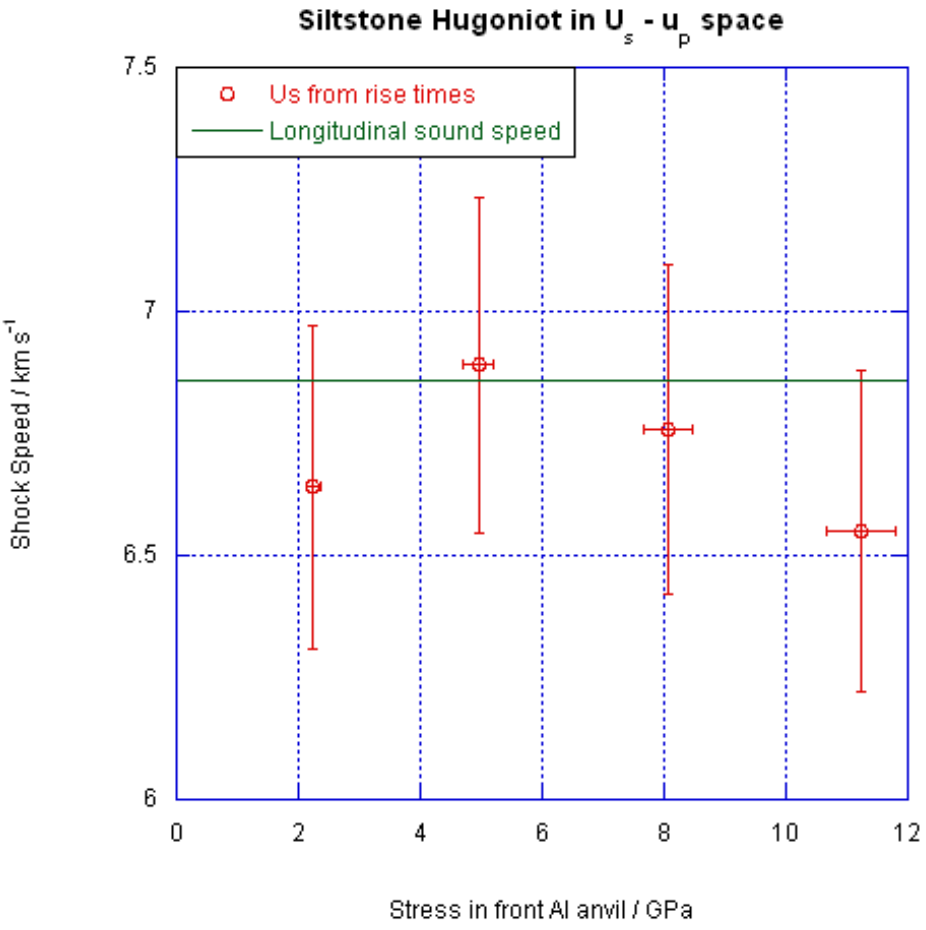

Figure 6.38: Variation of shock speed with longitudinal stress in siltstone. The data show that there is agreement to within experimental error between the measured shock velocity and the static longitudinal sound speed. There is also no discernable trend to the data. The accuracy of the data is improved over the other materials where shock velocity has been measured. This is through the use of the aluminium anvils.

6.5 Summary

- The Hugoniot properties of a number of materials have been measured.
- The use of gauges was found to be problematic in the more inhomogeneous of the materials, a problem which was overcome using the reverse impact

configuration and VISAR

- Sandstone and biotite schist were found to exhibit no measurable elastic behaviour under shock conditions.
- The iron ore was shown to exhibit elastic behaviour up to a defined HEL, beyond which the Hugoniot showed indications of non-elastic deformation within the material.
- The remainder of the materials showed "elastic" behaviour over the entire stress regime investigated. This is to say that the Hugoniot was linear in $\sigma - u_p$ space.
- Many of the Hugoniots agreed well with the measured elastic impedances of the materials.
- The materials which exhibit a linear relationship in stress - particle velocity space also have constant shock velocity across the stress range examined. This has been confirmed through specific experiments in the case of siltstone.

References

[1] Yoshida, S. and Ogawa, T., "Electromagnetic Emissions from Dry and Wet Granite Associated with Acoustic Emissions", *Journal of Geophysical Research*, **109**, (2004), B09,204

[2] Barber, J.L. and Kadau, K., "Shock-front broadening in polycrystalline materials", *Physical Review B*, **77**, (2008), 144,106

[3] Marsh, S.P., *LASL Shock Hugoniot Data*, University of California Press, Berkeley, California (1980)

Chapter 7

Shear Strength, Lateral Stress and Dynamic Tensile Strength

7.1 Shear Strength and Lateral Stress

7.1.1 Kimberlite and General Principals

Shot Code	Inferred/Measured Longitudinal Stress	Impactor/Target Materials	Impact Velocity $m\ s^{-1}$	Useful Data
E061026B	Inferred	Copper/Kimberlite	395	Yes
E061006C	Inferred	Copper/Kimberlite	594	Yes
E061027A	Inferred	Copper/Kimberlite	835	Yes
E070615A	Inferred	Copper/Kimberlite		No
E070618A	Inferred	Copper/Kimberlite		No
E090118A	Inferred	Copper/Kimberlite	166	Yes

Table 7.1: Kimberlite lateral experiments

The manganin gauges used in the samples gave voltage traces that were reduced to stress via the calibration due to Rosenberg [1] described in section 4.2.1. Overall the quality of the gauge traces was superior to that seen in the longitudinal experiments. A couple of reasons could be suggested to explain this. It is possible that the specifics of the loading geometry in some way limit the straining of the gauge. However more likely is that the 't' gauge design is mitigating strain effects. It has a much smaller gauge element and is also encapsulated in a layer of thin plastic as part of the manufacturing process. The grid gauges used in the longitu-

dinal orientation have both a larger gauge area and no plastic encapsulation. An example gauge trace showing the fact that noise is reduced and levels easier to determine is shown in figure 7.1 (this should be compared to figure 6.3). It should also be noted that agreement in stress level between the front and back gauges in the kimberlite is good. The relevant lateral data for kimberlite is tabulated in table 7.1. This demonstrates not only that there is no significant attenuation in the material over the distance concerned, but also that the one dimensional strain condition has not been released from the sides in the time frame of this experiment.

After working out the stress level, it is then possible to calculate the shear strength using equation 5.14 and then plot the variation of shear strength with changing longitudinal stress. The longitudinal stress can either be found from the inclusion of a longitudinal gauge in the experimental set-up for examining lateral stress, or by using a previously determined experimental Hugoniot. An elastic line can be plotted using equation 5.15. It is therefore possible to see where the shear behaviour departs from the elastic, namely the HEL. The kimberlite has an HEL of 1.6 GPa as can be seen from the plot in figure 7.2. Above the HEL, a line has been fitted to the data points. This line has been used to determine the HEL. There is of course an error associated with the fitting of the line. This would encompass both the errors on the points themselves (arising from errors in the calibrations, determination of levels and the knowledge of the well-characterised materials) but also the sample to sample variation. It should therefore be taken that the fit line gives a reasonable indication of potential behaviour rather than anything more accurate. It is noticeable that there is little increase in shear strength above the HEL.

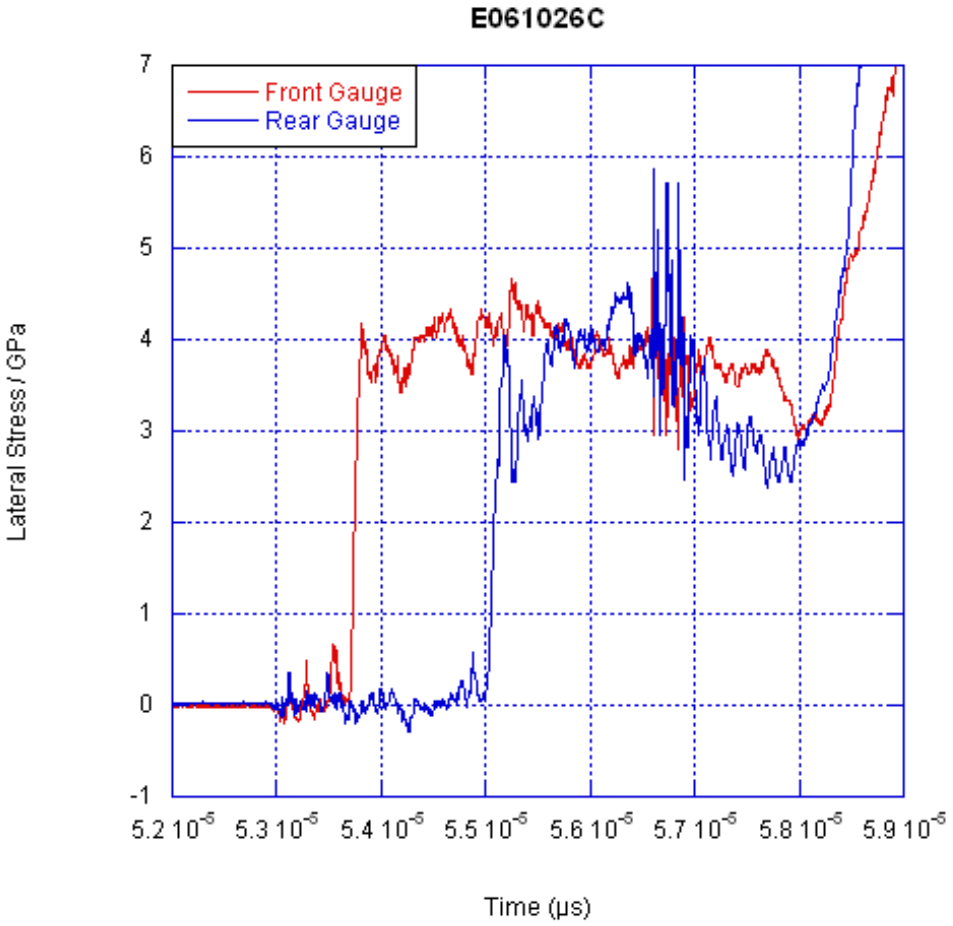

Figure 7.1: Lateral gauge trace from a kimberlite experiment. Accurate determination of plateau levels is possible owing to the reduced noise when compared for example with the traces shown in figure 6.3. It is likely that this improvement is due to improved gauge encapsulation in the 't' gauges compared with the grid gauges.

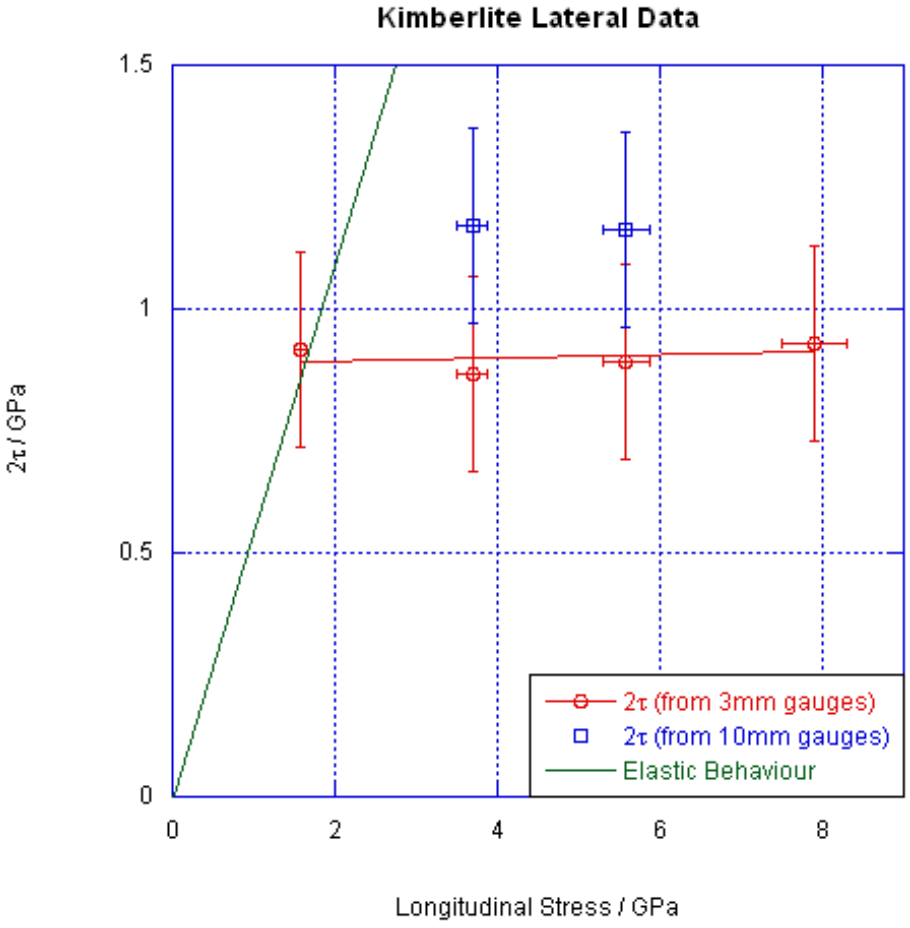

Figure 7.2: Lateral data and elastic line showing HEL from kimberlite experiments. Data are plotted for both the 3 mm and 10 mm gauges, although for consistency only the 3mm gauges have been used in determining the HEL (as two of the 10 mm gauges failed). The HEL is approximately 1.6 GPa and the data suggest that above this level there is little increase in shear strength with pressure.

7.1.2 Siltstone

Shot Code	Inferred/Measured Longitudinal Stress	Impactor/Target Materials	Impact Velocity $m\ s^{-1}$	Useful Data
E070516B	Measured	Copper/Siltstone	183	Yes
E070516C	Measured	Copper/Siltstone	339	Yes
E070517A	Measured	Copper/Siltstone	499	Yes
E070517B	Measured	Copper/Siltstone	647	Yes
E070517C	Measured	Copper/Siltstone	847	Yes

Table 7.2: Siltstone Lateral Data

The siltstone HEL (shot data in table 7.2) is shown to be approximately 5 GPa in figure 7.3. The low pressure data sit well on the elastic line below the HEL. Above the HEL there is not as clear a trend as with the kimberlite. However it is certainly clear that there is a departure from the elastic behaviour. Additionally there is no clear trend of falling or rising stress between the front and rear gauges in the samples. This suggests no significant or detectable attenuation across the sample size used in this investigation.

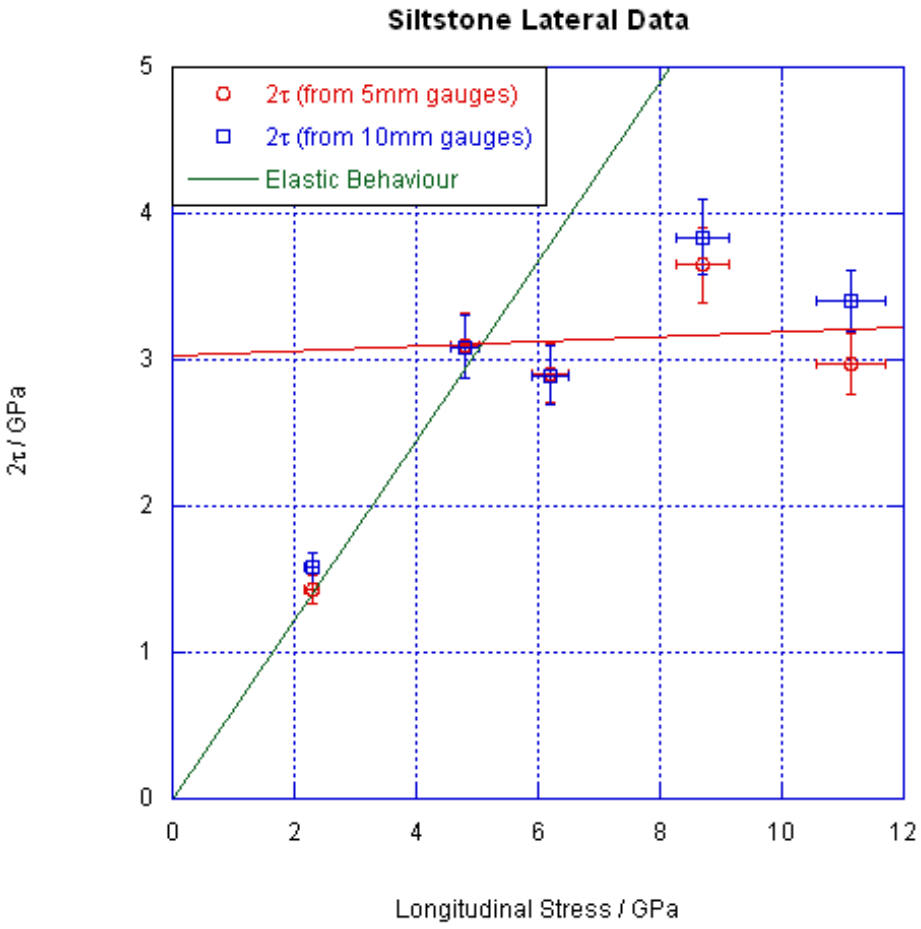

Figure 7.3: Lateral data and elastic line showing HEL from siltstone experiments. The 5 mm and 10 mm gauges show no systematic difference and agree to within experimental error. There is little evidence of a large increase in shear strength above the HEL of 5 GPa. A line has been added to give an indication of the likely behaviour of the material above the HEL.

7.1.3 Amphibolite

Shot Code	Inferred/Measured Longitudinal Stress	Impactor/Target Materials	Impact Velocity $m\ s^{-1}$	Useful Data
E090120A	Inferred	Copper/Amphibolite	498	Yes
E090120B	Inferred	Copper/Amphibolite	369	Yes
E090120C	Inferred	Aluminium/Amphibolite	397	Yes
E091221H	Inferred	Copper/Amphibolite	582	Yes

Table 7.3: Amphibolite lateral data

Four experiments were performed in the lateral configuration on the amphibolite, as can be seen in table 7.3. There is some experimental uncertainty in the data above the experimentally determined HEL. However by roughly fitting a line to the data by eye, as shown in figure 7.5 an HEL can be determined. The value of the HEL is approximately 4.2 GPa. Below the HEL the single point indicates elastic behaviour. It should be noted that while the gauge traces (an example of which is shown in figure 7.4) for these experiments were better than those for the quartz/feldpathic gneiss and the kimberlite, they were not quite as noise free as the longitudinal data for the amphibolite. Whether this is something intrinsic to the lateral gauge orientation, the type of gauge used, or merely a variation in the amphibolite cores is hard to determine. Bearing in mind that some of the other materials saw a reduction in the noise in the lateral gauges, it is most likely that the amphibolite samples used in the lateral experiments had a higher quartz content than the ones used in the longitudinal experiments..

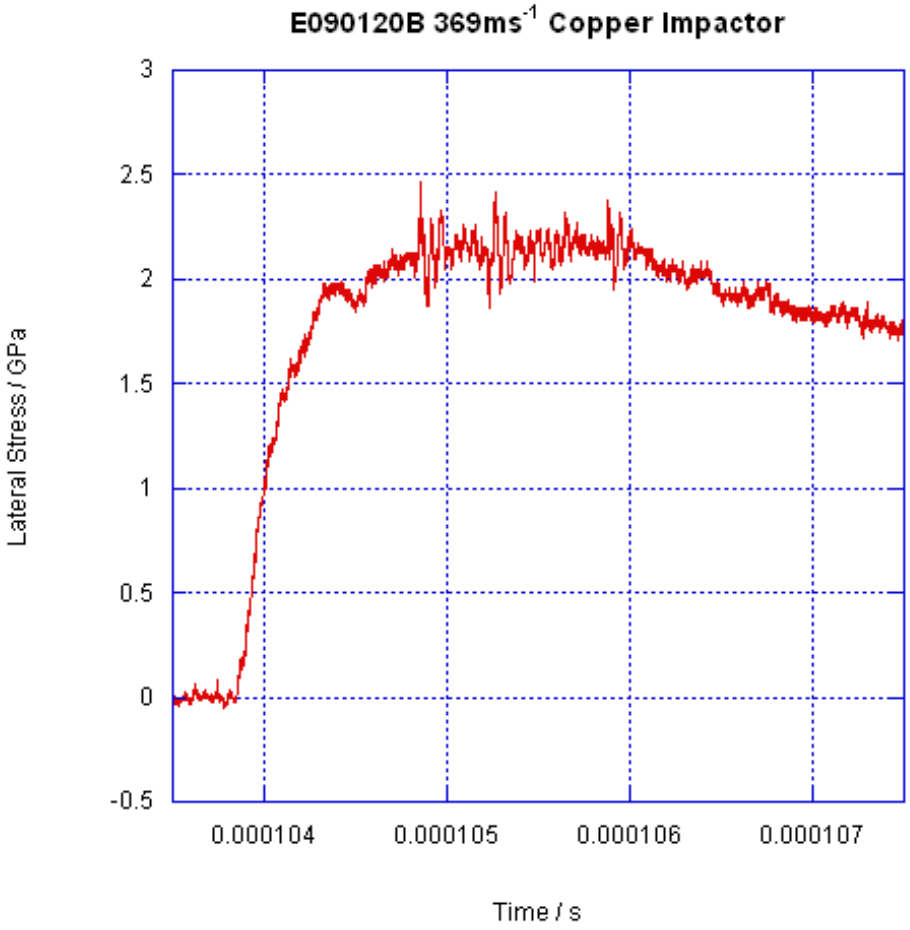

Figure 7.4: Gauge trace from an amphibolite lateral experiment. There is an increase in noise over the longitudinal gauge traces from the same material, see figure 6.1. This is probably due to increased quartz content in the samples used for the lateral experiments.

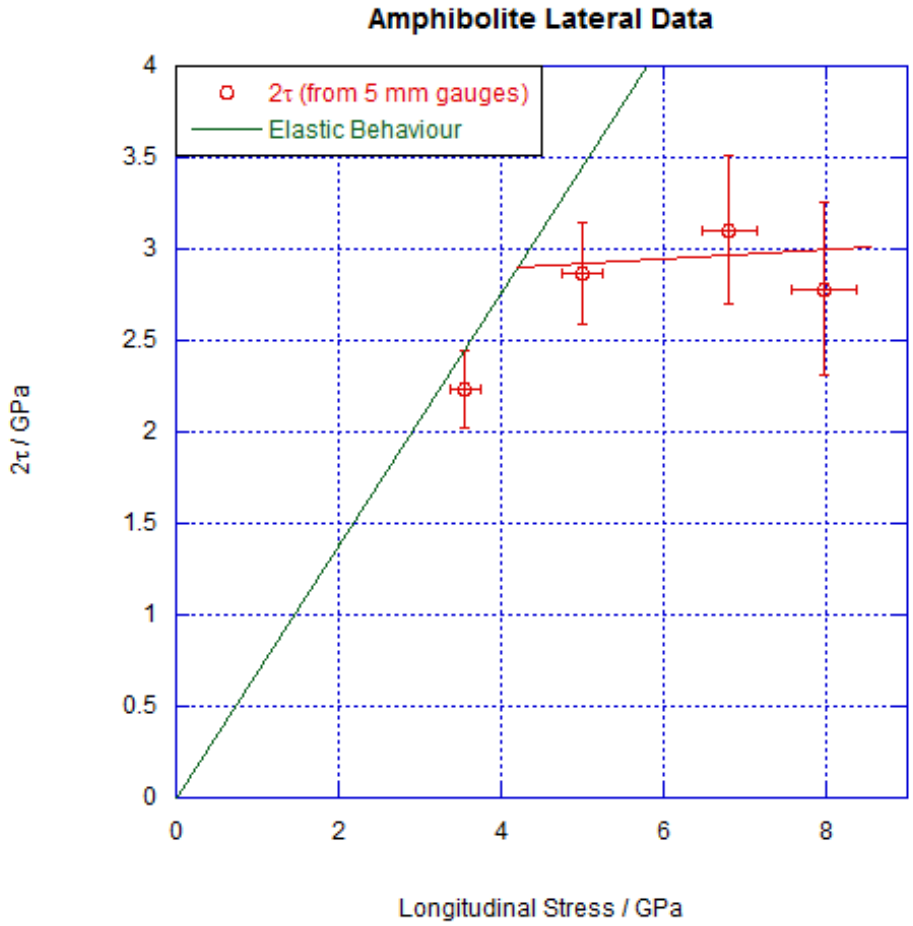

Figure 7.5: Lateral data and elastic line showing the HEL from amphibolite experiments. The fit above the HEL is fitted by eye to give an indication of likely behaviour above the HEL. The experimental uncertainty means that with only three points fitting by eye is the most informative method, it allows for determination of the HEL (approximately 4.2 GPa) without implying any physically unlikely behaviour (as might be the case if a strict mathematical fit to the data is used).

7.1.4 Quartz/Feldspathic Gneiss

Shot Code	Inferred/Measured Longitudinal Stress	Impactor/Target Materials	Impact Velocity $m\ s^{-1}$	Useful Data
E081030A	Inferred	Copper/Gneiss	394	Yes
E081217B	Inferred	PMMA/Gneiss	337	Yes
E081222B	Inferred	Aluminium/Gneiss	314	Yes
E090112C	Inferred	PMMA/Gneiss	560	Yes
E091221A	Inferred	Aluminium/Gneiss	446	Yes

Table 7.4: Quartz/feldspathic gneiss lateral data

The lateral data for quartz/feldspathic gneiss (shot data are tabulated in table 7.4) are shown in figure 7.6. The gauge traces for these experiments were still rather noisy (as can be seen in figure 7.7), owing probably to the electromagnetic emission issue, though there is also the potential for straining of the gauge element. The consequences of this are that the points have large errors associated with them, and the data point with the highest stress seems to be somewhat anomalous (possibly for example due to gauge straining). In the low stress regime there is a single datum, which to within experimental uncertainty is well-described by the theoretical elastic model. To confirm elastic behaviour below the HEL further investigation would be required. Above the HEL (and to determine the value of the HEL) the data have been fitted with a line by eye, assuming that it is likely the high stress point is anomalous, and it is unlikely that this datum accurately describes the general material behaviour. The HEL is approximately 1.3 GPa.

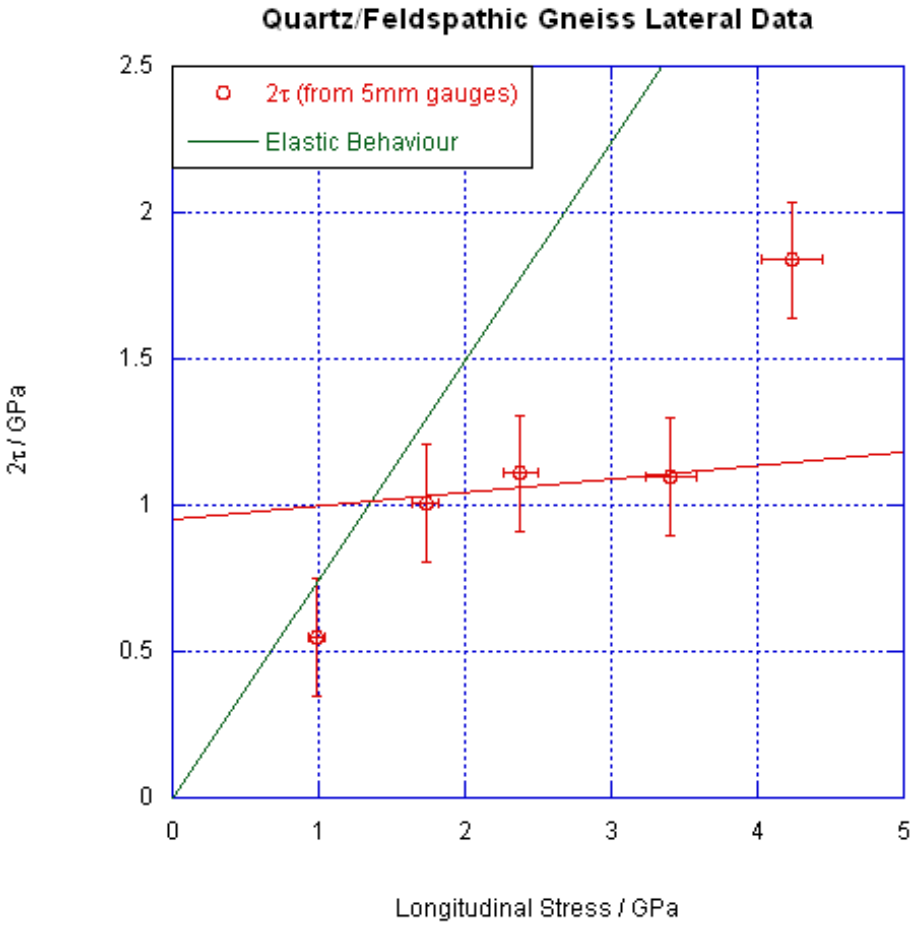

Figure 7.6: Lateral data and elastic line from quartz/feldspathic gneiss experiments. The line fitted to the data that do not lie (within experimental error) on the elastic line has been fitted by eye, to give an indication of the likely behaviour of the material above the HEL. This line suggests that the value of the HEL is 1.3 GPa

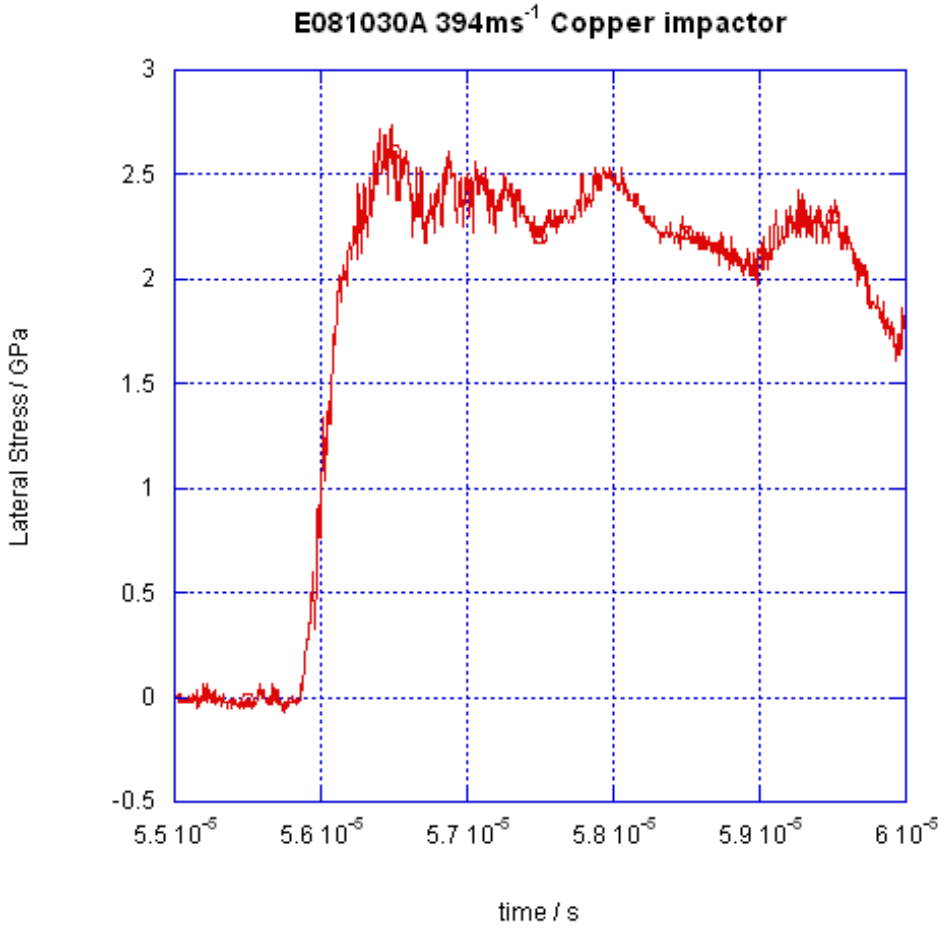

Figure 7.7: Lateral gauge trace from a quartz/feldspathic gneiss experiment. While the noise is not as severe as in the longitudinal case for the same material (shown in figure 6.2) there is still a reasonable amount of noise present in the gauge trace. It is likely that the source of the noise is electromagnetic emissions from quartz within the material.

7.1.5 Sandstone

Shot Code	Inferred/Measured Longitudinal Stress	Impactor/Target Materials	Impact Velocity $m\ s^{-1}$	Useful Data
E070510A	Inferred	Copper/Sandstone	206	Yes
E070513D	Inferred	Copper/Sandstone	400	Yes
E070513E	Inferred	Copper/Sandstone	608	Yes
E070513F	Inferred	Copper/Sandstone	801	Yes
E070513G	Inferred	Copper/Sandstone	922	Yes

Table 7.5: Sandstone lateral data

The data in table 7.5 give details of the the lateral stress experiments performed on sandstone. The shear behaviour of the sandstone is different to the other materials in that there is no discernable HEL at all. None of the data points lie on the elastic line, as shown in figure 7.8. The other key feature of the sandstone data is that the front gauge records a higher value of stress than the rear gauge. A plot of two typical gauge traces is shown in figure 7.9. This is systematic across the stress range. The reason for this is either attenuation or lateral releases.

It seems logical given the material properties in general that there is some attenuation in the wave as it passes through the material. However it is possible to use equation 7.1 to establish whether the gauge location has been laterally released (using the slope of the release fit to determine the value of c_a).

$$tan\ \phi = \frac{1}{U_s}\sqrt{c_a^2 - (U_s - u_p)^2}, \tag{7.1}$$

The porosity present in the material means that the release speed will be substantially higher than the shock speed (making it likely that the extent of 1D strain in sandstone will be reduced compared with the other materials). The high release speed is demonstrated by the steepness of the release fit in the lateral data. It is possible through the use of equation 5.6 to calculate the shock speed in the material, as the slope of the loading path to the Hugoniot point (the Rayleigh line) is known, and the density has been previously calculated. For the sandstone experiment which yielded release data this gives a value of shock speed of 2.54 km s^{-1}. In the same manner it is possible to calculate c_a, provided that the density

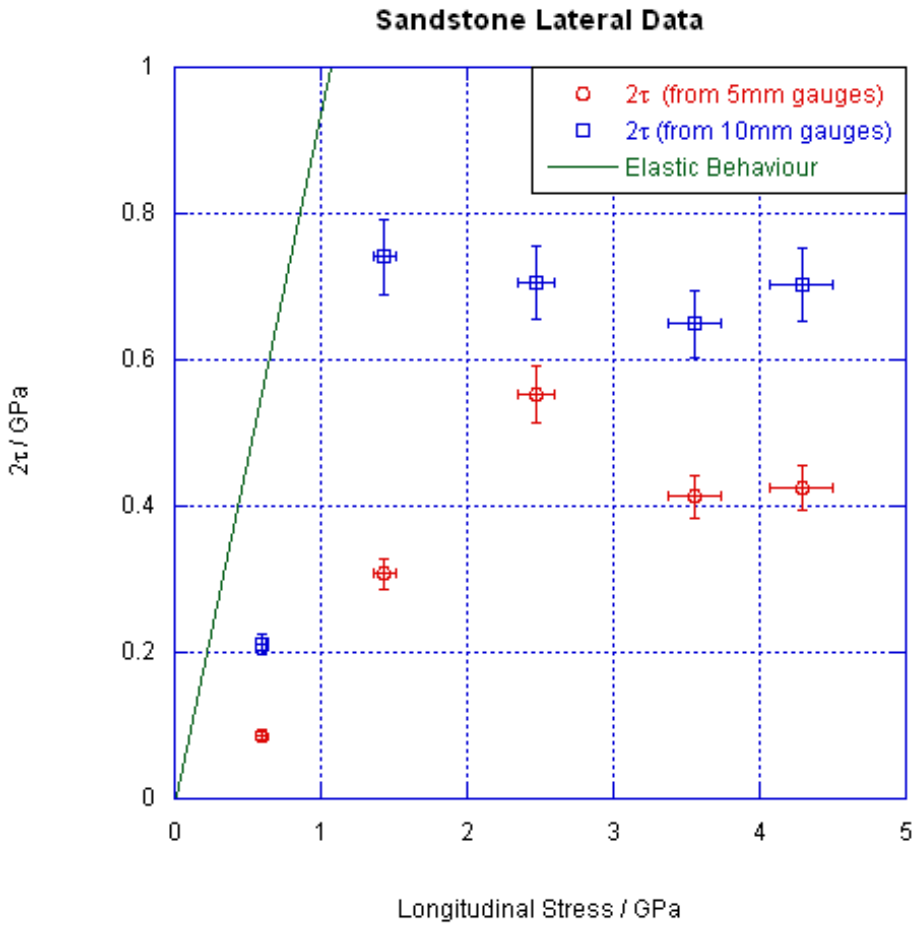

Figure 7.8: Lateral data and elastic line from sandstone experiments. It is clear that within the stress regime investigated, none of the sandstone samples have behaved in an elastic manner, and there is no clear HEL. Additionally there is a systematic difference between the 5 mm and 10 mm gauges. The 5 mm gauges consistently recorded higher values of stress than the 10 mm gauges.

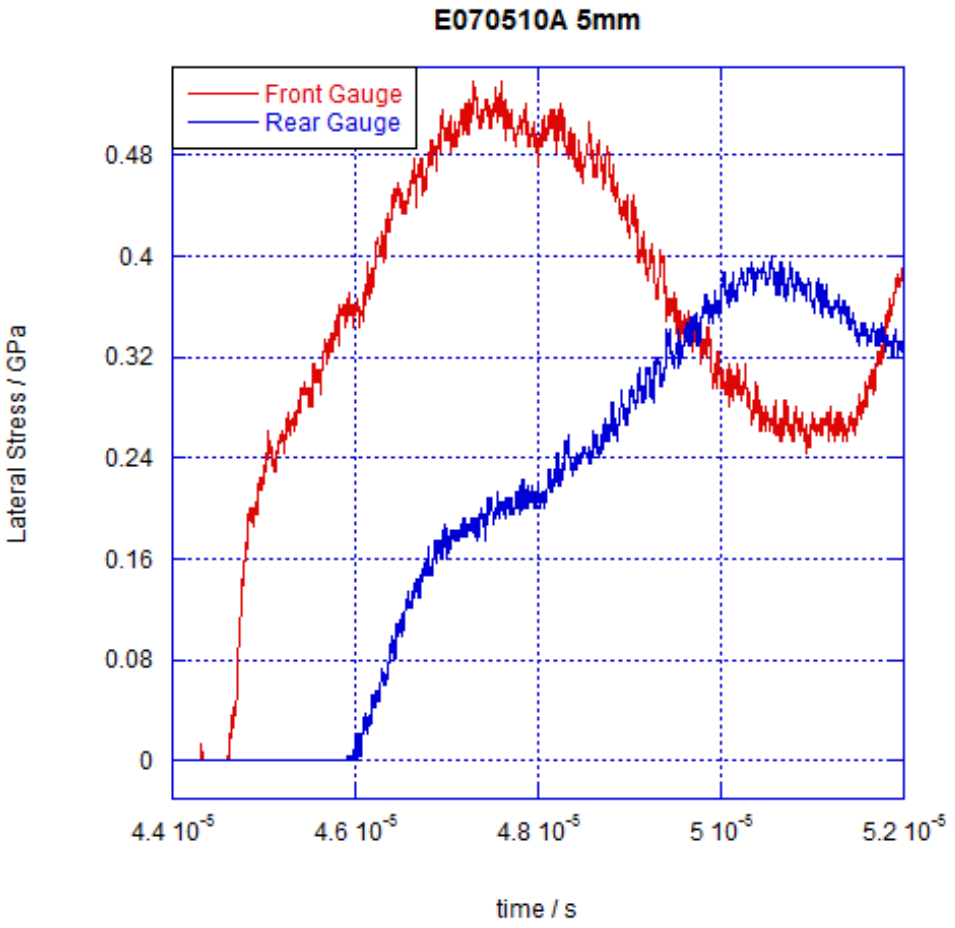

Figure 7.9: Lateral traces from sandstone experiment, it is clear there is a plateau in the front gauge trace which is absent from the rear trace

of the material can be determined post loading. Equation 5.19 allows for this to be done, noting that the specific volume calculated is the inverse of the density. The release wave speed is 3.77 km s^{-1}. This is significantly larger than the shock speed, and indicated that the sandstone will be laterally released at a greater rate (proportional to the shock speed) than the other materials presented in this thesis. The proportionally higher release velocity is reflected in the calculated angle in equation 7.1 of 52 degrees. It should be noted that 52 degrees will be almost certainly one of the better cases for sandstone as at the lower pressures it is probable that the discrepancy between the release and the shock speed will be

higher. For the case in question however we can relate the calculated angle to the depth at which gauges will no longer be in a state of 1D strain. A graphical representation of the experiment is shown in figure 7.10. If we assume that the copper cover-plate will have a decay angle of 45 degrees (a not unreasonable assumption given that the release in copper is well-approximated by the Hugoniot) then the 2.2 mm coverplate will have reduced the 1D strain area (going into the sandstone sample) from a circular area of diameter 48 mm (the flier diameter) to a circle of diameter 43.6 mm. It can be seen that at 10 mm into the sandstone sample the 1D strain area will be approximately a circle of diameter 18 mm. While this is in theory enough to accommodate a 15 mm gauge element, it should be considered that the gauges are positioned by eye to a measured (using a pair of vernier calipers) mark on the sample. They are then glued in place using a slow setting epoxy. During the epoxy cure time, some, albeit minimal, gauge movement may be possible. Additionally the fixing of the sandstone to the copper plate and the plate to the sample ring may have introduced a small amount of error. In this case a movement of 1.5 mm from the centre line would have been sufficient to cause releasing in the gauge during the experiment. Hence it can be concluded that in addition to the possibility of attenuation in the material, there is almost certainly an element of the stress in the gauge being reduced through the action of lateral releases.

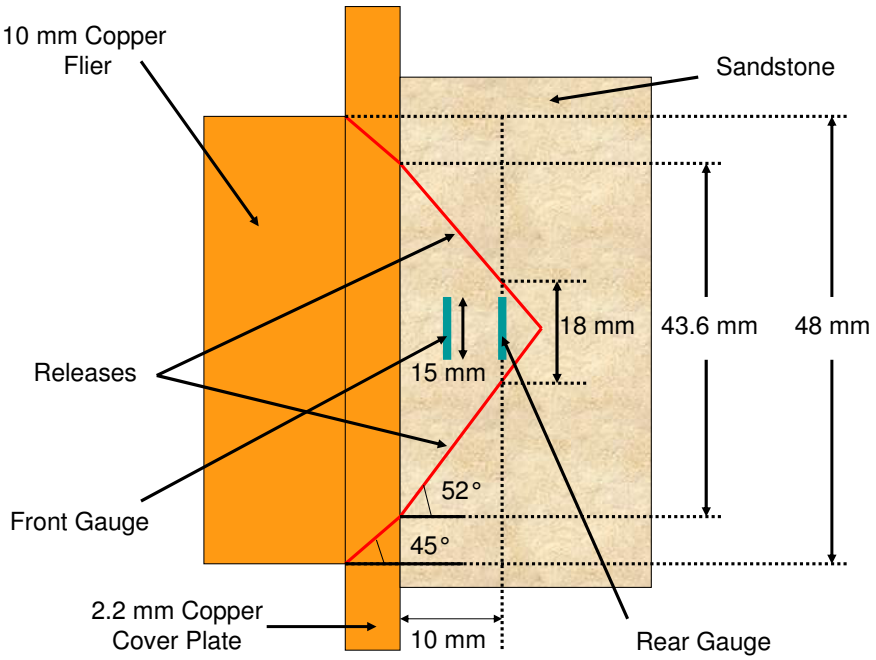

Figure 7.10: Schematic of releases in sandstone experiments. Through a careful examination of the Hugoniot and release characteristics of the material, it is possible to calculate the angle (with respect to the normal) of the release in the sandstone. In the figure, the releases have been superimposed on a diagram of the experimental set-up. It is shown that there is very little room (approximately 3 mm) for error in placement of the rear gauge, if lateral releases are to be prevented from affecting the output of the gauge.

7.1.6 Basalt

Shot Code	Inferred/Measured Longitudinal Stress	Impactor/Target Materials	Impact Velocity $m\ s^{-1}$	Useful Data
E081216A	Measured	PMMA/Basalt	341	Yes
E090118B	Measured	Aluminium/Basalt	257	Yes
E091221B	Measured	Aluminium/Basalt	357	Yes
E091221C	Measured	Aluminium/Basalt	500	Yes
E091221G	Measured	Copper/Basalt	447	Yes

Table 7.6: Basalt Lateral Data

In this investigation, owing to limited sample availability (shots involving the five available samples are tabulated in table 7.6), it is not entirely clear that the basalt has been shocked above the HEL of the material in the lateral gauge configuration. From figure 7.11 it is obvious that the data presented are well described by the theoretical elastic behaviour. It is possible however that the highest stress point does indicate a deviation from elastic behaviour. If this is the case, one might sensibly suggest that the value of the HEL in basalt is above about 4.2 GPa. A further point to consider however is that the HEL may in fact be slightly lower, of the order of 3.6 GPa. The reason for suggesting this is that a significantly smaller range of sample thicknesses were available for the measurements of sound speed. This could in turn lead to an error in the determination of the theoretical elastic behaviour line that is drawn in figure 7.11. If the gradient of the line was slightly steeper it would provide a slightly better representation of the "elastic" data, and the final point would more obviously be a deviation from the elastic regime.

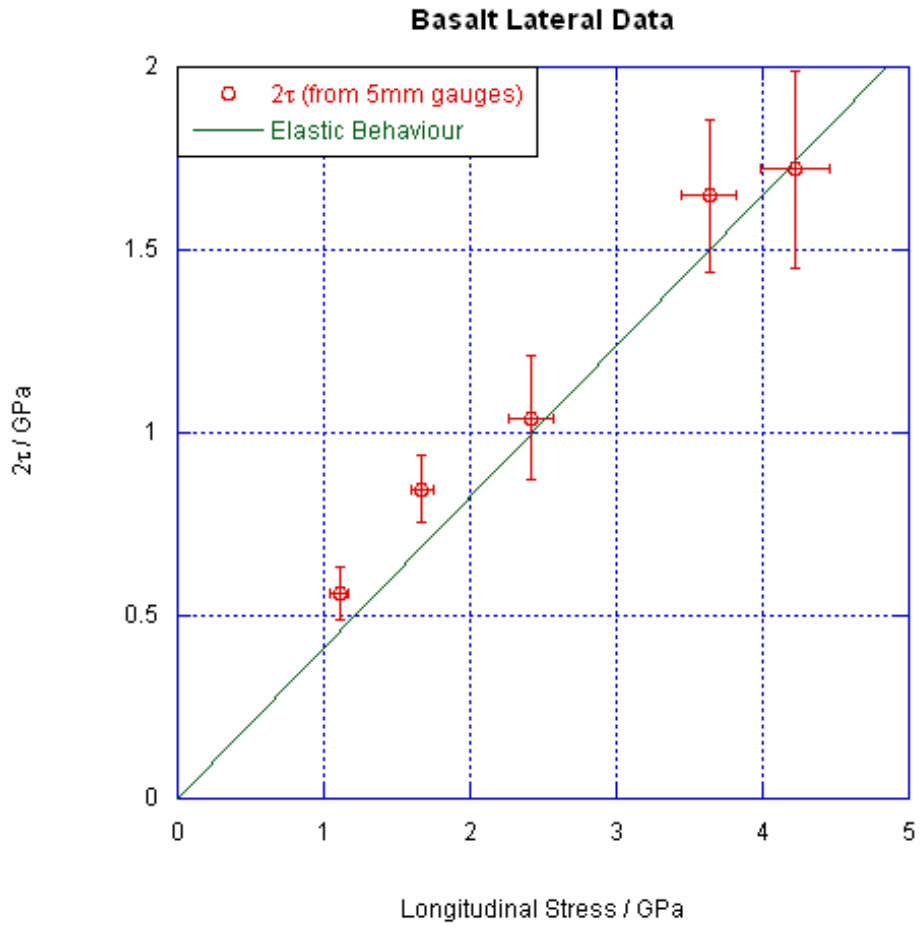

Figure 7.11: Lateral data and elastic line from basalt experiments. As all of the data shown, to within experimental uncertainty, lie on the line of theoretical elastic behaviour, it is not possible to determine whether the HEL has been exceeded in the material.

7.1.7 Iron Ore

Shot Code	Inferred/Measured Longitudinal Stress	Impactor/Target Materials	Impact Velocity $m\ s^{-1}$	Useful Data
E081217A	Measured	Copper/Iron Ore	146	No
E090121A	Measured	Copper/Iron Ore	140	Yes
E070112B	Measured	Copper/Iron Ore	262	Yes
E091221D	Measured	Aluminium/Iron Ore	493	Yes
E091221E	Measured	Copper/Iron Ore	495	Yes
E091221F	Measured	Copper/Iron Ore	497	Yes

Table 7.7: Iron ore lateral data

The lateral data for the iron ore samples (shot data are shown in table 7.7 shows similarity with the longitudinal data (figure 7.12). There is significant scatter in the results, owing to sample to sample variation and the effect of releases from flaws in the material. Above the HEL, which appears slightly lower (about 2.6 GPa) in the lateral data as opposed to the longitudinal data (about 3 GPa) there are two distinct groupings of points. The more reliable set are likely to be the two points with the higher values of shear strength. These points correspond to the experiments where the longitudinal gauges showed a distinct plateau as shown in figure 6.30. The lower shear strength data points were derived in part from longitudinal gauges that had been released from flaws within the material, as in figure 6.31. It is in theory possible to ignore the longitudinal gauge and derive the longitudinal stress from the Hugoniot, but there is little value in this if it is evident that the stress state in the material is not actually on the Hugoniot for the material. There were insufficient samples available to allow for repeat testing or the selection of samples without large flaws present.

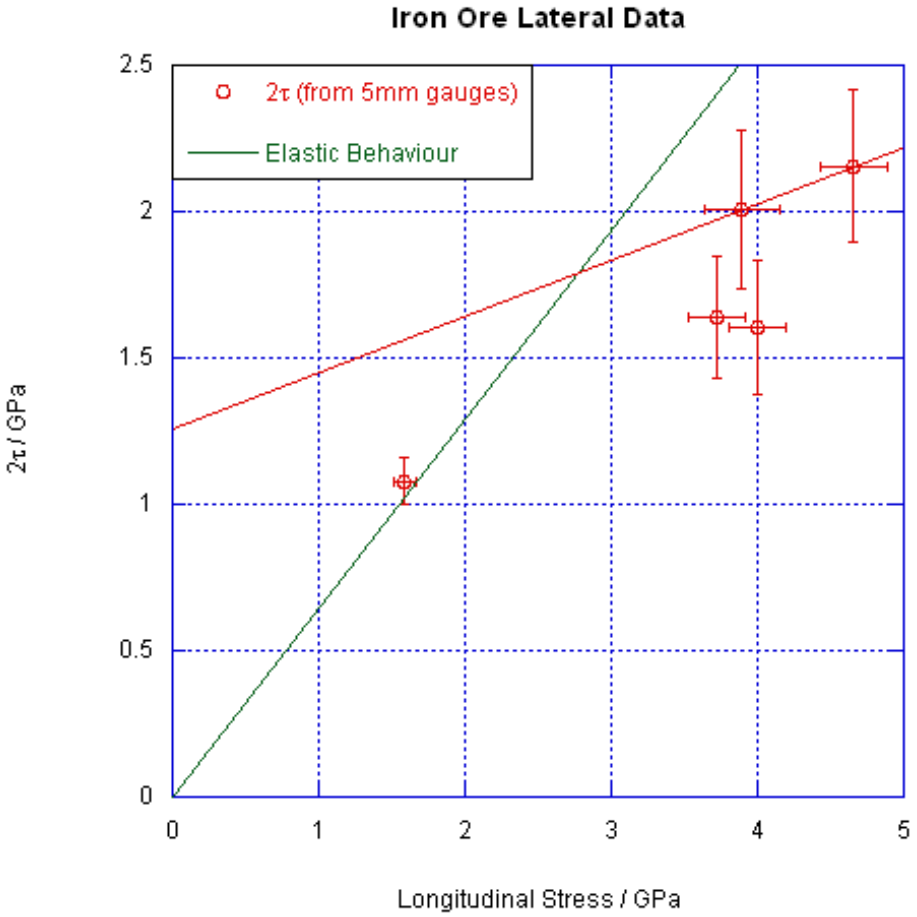

Figure 7.12: Lateral data and elastic line from iron ore experiments. Above the HEL (approximately 2.6 GPa) the line showing likely material behaviour has only been fitted to the two higher shear strength points. The reason for this fitting choice is that in both of the lower shear strength points there is evidence that the material was released prematurely due to flaws in the samples.

7.1.8 Supporting Literature Data

As mentioned in section 3.8 the determination of HEL values in the literature is done by a variety of methods. The results obtained in this thesis are in broad agreement with the range of values quoted in the literature. For a specific comparison it is worth comparing the current series of experiments with HELs measured in the same way, i.e. through the use of lateral stress gauges. Additionally it is possible in these cases [2, 3] to examine whether the shear strength of the materials investigated show comparable trends to the materials in this thesis. One slight problem with making these comparisons is that the literature data referred to was carried out before the publication of the most recent calibration for the gauges used in the experiments [1]. However in the case of the Tsembelis work on dolerite it has been possible to re-analyse the data using the new calibration. For the Millett work on gabbro, the best that can be done is to estimate (by using the corrections in the new calibration) the change in the final data values, as the raw traces were unavailable. In figures 7.13 and 7.14 the shear strength is shown plotted against the longitudinal stress both for the original published values and the re-analysed data.

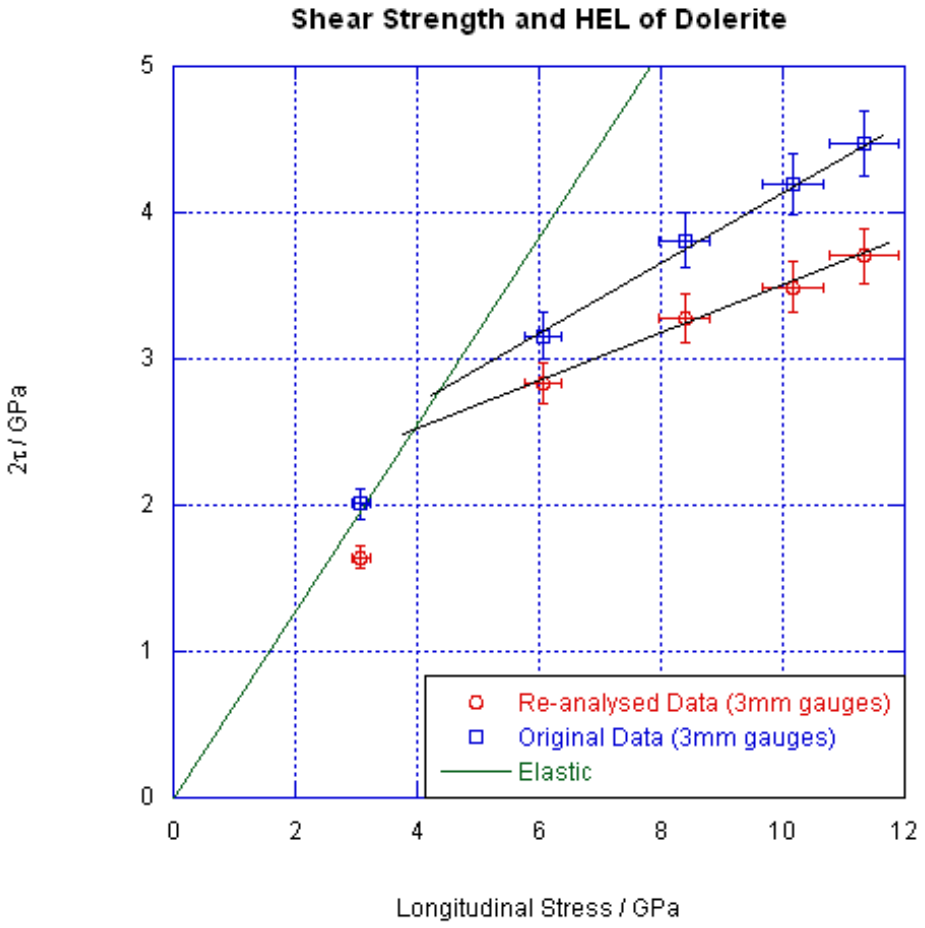

Figure 7.13: Lateral data and elastic line from Tsembelis et al. [3] plus re-analysis. Above 6 GPa (longitudinal) the data have been fitted with lines in order to allow for the determination of the HEL. it can be seen that the effect of the re-analysis is to lower the HEL slightly, and decrease the extent to which the shear strength increases above the HEL. The HEL is approximately 3.8 GPa.

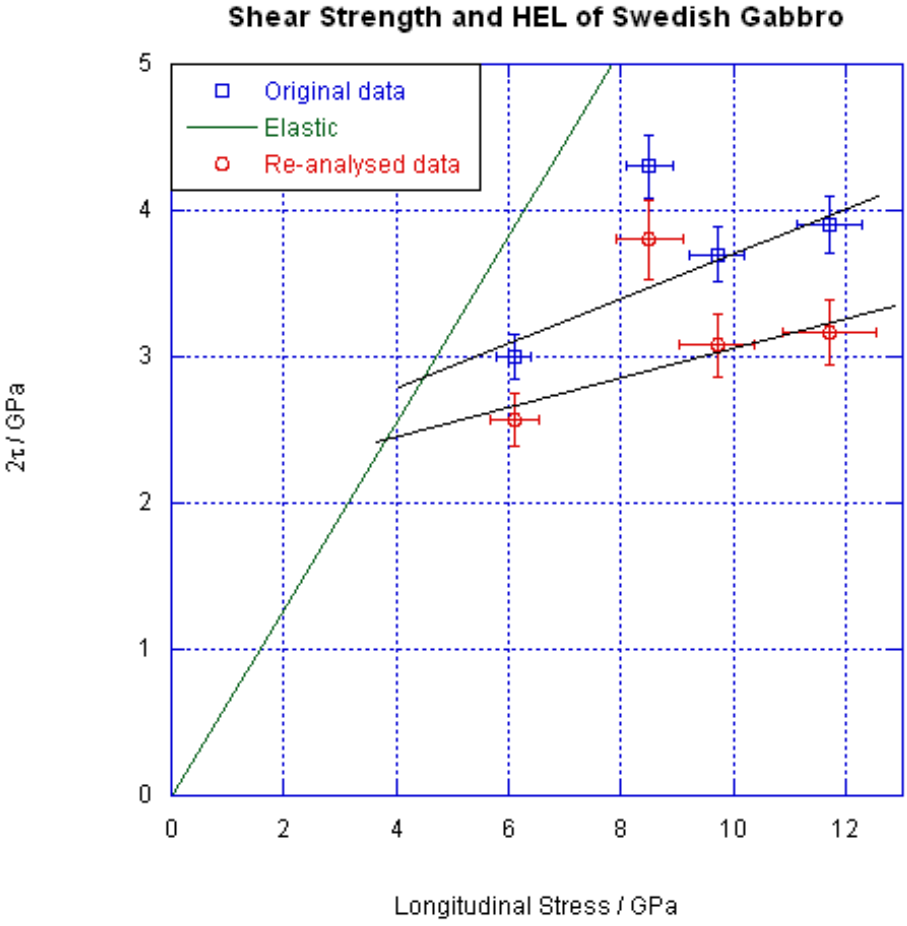

Figure 7.14: Lateral data and elastic line from Millett [2]. The lines through the data have been fitted by eye and are intended to provide an indication of likely behaviour above the HEL (determined to be 3.9 GPa). The high shear strength point has been assumed to be anomalous for the purposes of this fitting. As with figure 7.13 the effect of the re-analysis is to lower the HEL slightly, and decrease the extent to which the shear strength increases above the HEL.

It can be seen that the main effect of the recalibration is to reduce the value of the measured shear strength (in another way the value of the lateral stress has increased). This gives a reduction in the HEL. It is also noticeable that the slopes of the fit lines to the higher stress data points are reduced in the re-analysed data, implying that the increase in shear strength with pressure is also reduced. The fit lines are estimates made for this thesis and are separate to the published values. In fitting the data, as the general trend seemed to be gradually increasing shear strength after the HEL, the high point in the Millett data was taken to be the result of either unrepresentative sample to sample variation or gauge straining and not included. The low stress point in the Tsembelis data has also been ignored for the purposes of fitting and has been assumed to be elastic. The fact that it does not lie on the elastic line may be either due to sample to sample variation or to errors in the measurements of sound speed which are not shown in the figure. In general however the pattern of the shear strength is in agreement with the materials presented as new data for this thesis.

7.1.9 Discussion of the HEL in Geological Materials

A general trend appears to be that above the HEL of the material (or above a certain already non-elastic point in the sandstone), the shear strength does not increase significantly. As the method of failure in a geological material is likely to be brittle fracture, this should not be too surprising. A powder, such as sand or silica dust has a low value of shear strength, the same is true of a liquid. A geological material which is extensively fractured may well behave in the same manner. The fact that the experiments suggest a value of shear strength above the HEL is possibly more to do with the loading method in these experiments. It should be remembered that the experiments are inertially confined and therefore there will always be some value of lateral stress measured (i.e. there will always be a resistance to movement in the y direction). As the method of calculating the shear strength is in this case reliant on a measurement of the lateral stress, the value of shear strength calculated is unlikely to be the same as a value measured if the material could be returned to ambient conditions. Above the HEL therefore the shear strength is in fact the shear strength of an inertially confined “3D rock

jigsaw".

The "3D rock jigsaw" effect also gives a possible insight into the reason why there is no detectable change in the slope of the Hugoniot in σ - u_p space for many of the materials in this thesis. An inertially confined fractured rock mass of interlocking grains will, in compression with no opportunity for movement of material out of the direction of loading, behave in much the same way as an intact rock mass does. Thus as Tsembelis notes, the elastic and the shock impedances can often seem similar. In a metal or other material where the main method of non-elastic deformation is flow or dislocation movement, above the HEL the fundamental character of the material is changed (dislocations have moved and piled up, there could also be strain hardening effects for example). In these materials one might expect to see a change in the Hugoniot at a value corresponding to the HEL.

In a similar way, a material with porosity, or in the case of the biotite schist, a material where there is a softer component that is less likely to fail through brittle fracture (as with a completely crystalline rock material), the "rock jigsaw" model fails to accurately describe the situation. More "flow" of material is possible such that above the HEL there is essentially a "different" material being compressed, rather than the same material but merely broken up into interlocking pieces. Hence in these materials, such as the iron ore, the sandstone (which in fact is sufficiently weak to display no HEL in the data collected) and the biotite schist, it is possible to discern an HEL, or the complete absence of one from the longitudinal data.

7.2 Dynamic Tensile Strength

Shot Code	Diagnostics (Window)	Impactor/Target Materials	Impact Velocity $m\ s^{-1}$	Useful Data
E060627A	VISAR (None)	Amphibolite/Copper	247	No
E061024A	VISAR (None)	Kimberlite/Kimberlite	139	Yes
E061025A	VISAR (None)	Kimberlite/Kimberlite	183	Yes
E061025B	VISAR (None)	Kimberlite/Kimberlite	175	Yes
E061025C	VISAR (None)	Kimberlite/Kimberlite	147	Yes
E061026A	VISAR (None)	Kimberlite/Kimberlite	151	Yes
E070209A	VISAR (None)	Amph Gneiss/Amph Gneiss	113	No
E070209B	VISAR (None)	Amph Gneiss/Amph Gneiss	140	No
E070209B	VISAR (None)	Amph Gneiss/Amph Gneiss	113	No
E070417A	VISAR (None)	Biotite Schist/Biotite Schist	143	Yes
E070418A	VISAR (None)	Biotite Schist/Biotite Schist	125	No
E070418B	VISAR (None)	Biotite Schist/Biotite Schist	102	No
E070423A	VISAR (PMMA)	PMMA/Biotite Schist	105	No
E070423B	VISAR (PMMA)	PMMA/Biotite Schist	105	No
E070513B	Gauge/VISAR (PMMA)	Aluminium/Siltstone	115	Yes
E070513C	Gauge/VISAR (PMMA)	Aluminium/Siltstone	96	Yes
E070616B	Gauge/VISAR (PMMA)	Aluminium/Siltstone	139	Yes
E070616C	Gauge/VISAR (PMMA)	Aluminium/Siltstone	146	Yes
E070808A	Gauge/VISAR (PMMA)	Aluminium/Siltstone	132	Yes
E070809A	Gauge/VISAR (PMMA)	Aluminium/Kimberlite	128	No
E070809B	Gauge/VISAR (PMMA)	Aluminium/Kimberlite	131	No
E081104A	Gauge/VISAR (PMMA)	Aluminium/Basalt	162	No
E081104B	Gauge/VISAR (PMMA)	Aluminium/Iron Ore	172	No
E081105A	Gauge/VISAR (PMMA)	Aluminium/Basalt	156	No

Table 7.8: Spall shots

The measurement of spall strength as a measure of dynamic tensile strength is one of the more difficult experiments to perform. As noted previously, multiple experiments are needed to determine a statistical average. A list of all the shots completed (though not necessarily providing useful data) is given in table 7.8. In addition, the experiments have a lower success rate than both the longitudinal and lateral experiments. While data are gathered from most experiments it is not always possible to derive a spall strength as either the diagnostics do not function as expected due to material break up, or a spall in the classic sense did not occur. The problem with the "classic" spall is that it requires the failure of the material to be a clean plane of fracture. This is unlikely to be the case in an inhomogeneous geological material. If material breakup is complicated, with multiple fractures, some of which reach the back surface of the rock material

(which does not occur in the "classic" spall experiment) then it is likely that the diagnostics which are located on this rear surface will be adversely affected by this.

Initial spall experiments on kimberlite were carried out with the most simple experimental arrangement. A rock impactor was used to impact a rock target of twice the thickness. The rear of the target was given a reflective coating and VISAR was used to monitor the rear of the target. This gave good results for kimberlite, producing VISAR traces such as the one shown in figure 7.15.

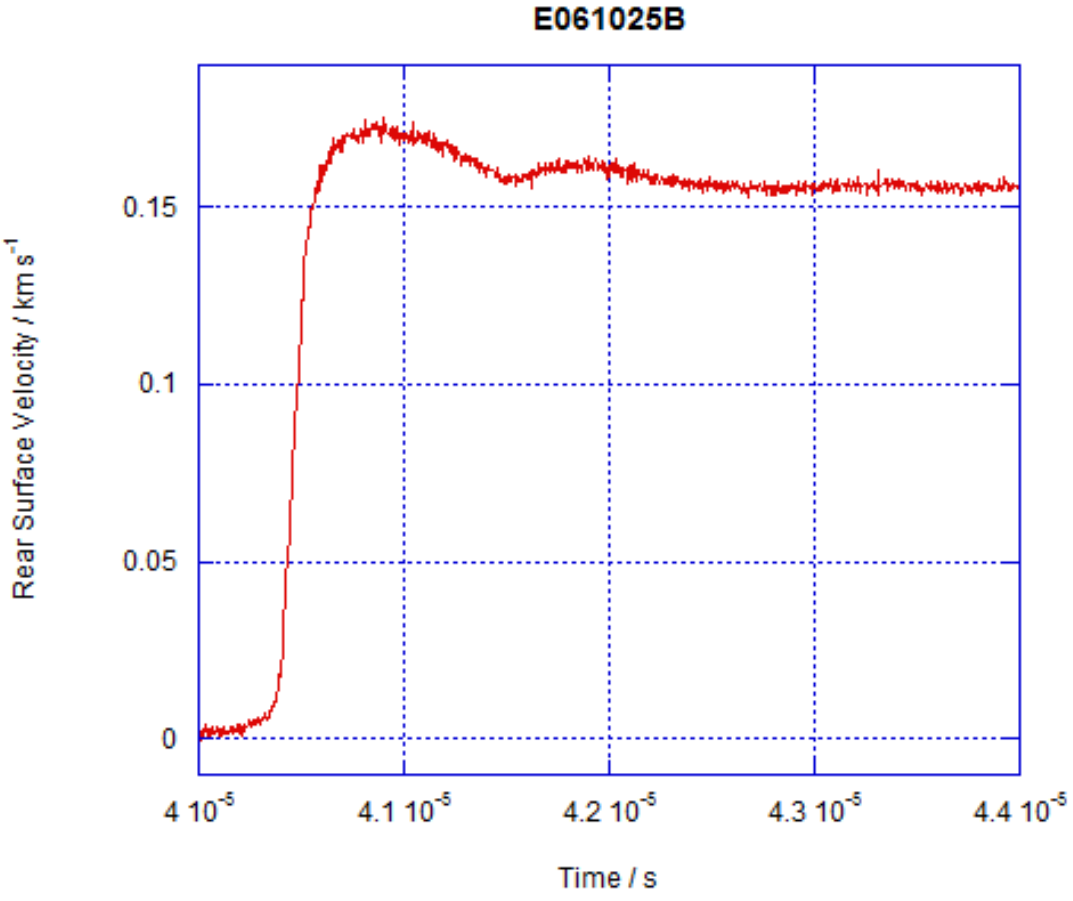

Figure 7.15: An example VISAR trace from a kimberlite spall experiment. The typical spall signal of release and rebound can clearly be seen and this allows for a spall strength to be derived.

The five successful experiments performed on kimberlite yielded a spall strength of 21 ± 4 MPa. When the method described above was attempted for biotite schist and amphibolitic gneiss the results failed to show the characteristic spall signal as shown in figure 7.15. It was speculated that a change in the experimental design might prove to be beneficial. To this end, the design was changed to the design in the bottom half of figure 5.14. This design is similar to that used by Grady [4] in his investigations into spall in geological materials. The benefits of this design included the thin PMMA plate potentially helping to contain fragments and additionally a reduction in the strength of the release passing back into the material (owing to the PMMA backing having a higher impedance than the rough vacuum of the previous experimental design). This second experimental design was also temperamental, but owing to the presence of two diagnostics, is more consistent in producing results. This gave a spall strength (if one outlying point is neglected from the 5 available data points) of 55 ± 6 MPa for siltstone. One spall experiment was successful for the biotite schist yielding a value of 26 MPa.

It is obvious from the range of results for any individual rock type that the process of dynamic tensile failure is not an easy one to measure accurately. In a homogeneous metal sample for example, spall tends to occur in a well-defined plane due to the overlap of the release waves propagating through the material. An example of a cross section of such a sample is given in figure 7.16. While the spall is ductile there is still a clear well-defined plane of spalled material.

In the geological materials investigated in this thesis, there is a lack of homogeneity. This is obvious from looking at the materials, but it is the unseen inhomogeneity which has the potential to cause the biggest issues for attempting this type of measurement. Weak grain boundaries will fail at a much lower stress than the bulk material failure. Therefore the presence of these grain boundaries will lead to an increased scatter in the results. While copper and other metals will have grain boundaries, the scale of the inhomogeneity in the geological materials is significantly greater. In addition, the grain boundaries are as likely to be misaligned to the usual spall plane orientation as they are to be aligned. This gives rise to the possibility of fracture occurring in a way that gives rise to a signal

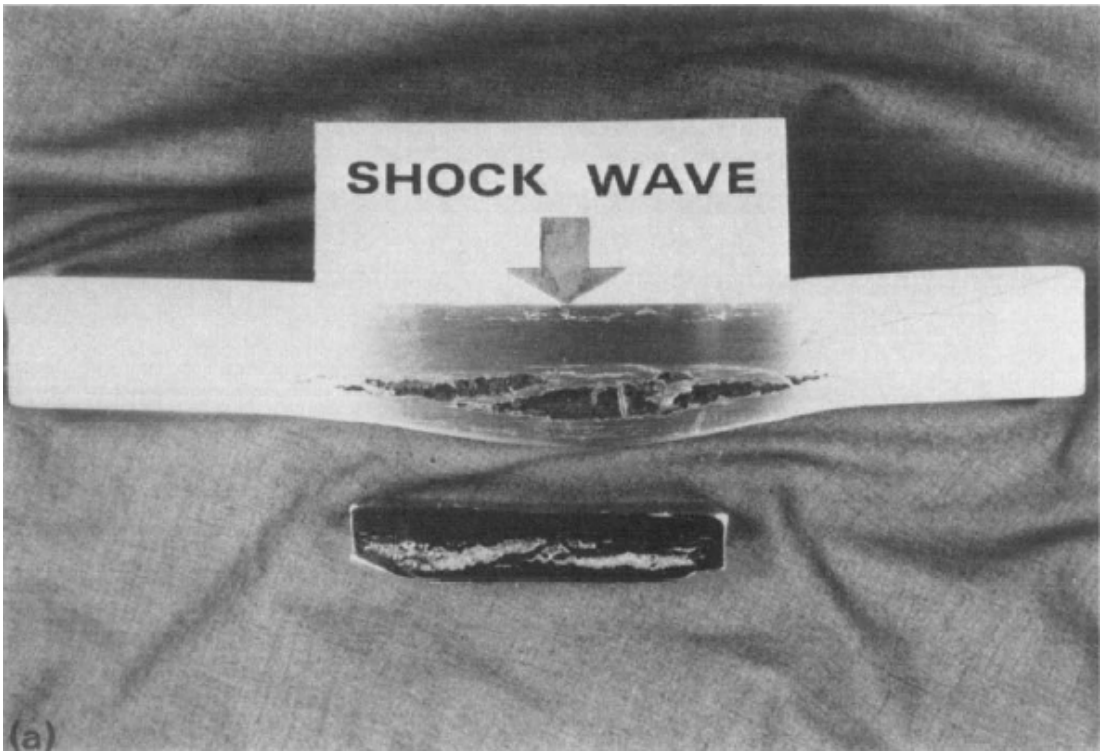

Figure 7.16: Incomplete (incipient) metal spall from [5]. Whilst the fracture is ductile, there is a clear plane of fracture, as would be expected in a planar impact spall experiment on a homogeneous material.

in the diagnostics that is not easily discernable as a signal indicating spall of the material. It is therefore difficult on occasion to correctly determine a value of the spall strength from the data records of the investigations conducted. This inhomogeneity can also help us to understand the reason why with two diagnostics it is possible for one diagnostic to function and the other not. As the diagnostics are slightly spatially separated, local fracture can occur and it is not unreasonable to suggest that even parts of the material in close proximity might be moving independently of each other. A final issue to consider is the small values of spall strengths in these materials. It can be hard in certain cases to discern the levels correctly in the gauge or VISAR traces.

7.3 Summary

- The HELs of various geological materials have been determined. The values are 1.3 GPa for quartz/feldspathic gneiss, 1.6 GPa for kimberlite, above 4.2 GPa for basalt, 4.2 GPa for amphibolite, 4.8 GPa for siltstone and around 3 GPa for iron ore.
- The measured values are shown to be consistent with literature data obtained in a similar manner.
- It is postulated that the compression of hard polycrystalline materials above their HEL causes failure such that no change in slope is seen in the longitudinal data (note that there is also no easily discernable two wave structure). This "3D rock jigsaw" effect explains why deviation from elastic behaviour is only seen in the lateral stress and shear strength data.
- Above the HEL in the materials investigated, the increase of shear strength with pressure is small.
- The spall strength of two of the materials has been investigated through a series of experiments, with the values found to be 21 ± 4 MPa for kimberlite and 55 ± 6 MPa for siltstone. A single experiment has also suggested a value of 26 MPa for biotite schist.

References

[1] Rosenberg, Z., Bourne, N.K. and Millett, J.C.F., "Calibration of commercial gauges of varying geometry to measure the lateral component of stress", in *Shock Compression of Condensed Matter - 2005*, M. Furnish, M. Elert, T. Russell and C. White, eds., American Institute of Physics, Melville, NY (2006), pp. 1207–1210

[2] Millett, J.C.F., Tsembelis, K. and Bourne, N.K., "Longitudinal and lateral stress measurements in shock-loaded gabbro and granite", *J. Appl. Phys.*, **87**, (2000), 3678–3682

[3] Tsembelis, K., Proud, W.G. and Field, J.E., "The principal Hugoniot and dynamic strength of dolerite under shock compression", in *Shock Compression of Condensed Matter - 2001*, M. Furnish, N. Thadhani and Y. Horie, eds., American Institute of Physics, Melville, NY (2002), pp. 1385–1388

[4] Grady, D.E. and Hollenbach, R.E., "Dynamic fracture strength of rock", *Geophys. Res. Letts*, **6**, (1979), 73–76

[5] Meyers, M.A. and Aimone, C.T., "Dynamic Fracture (Spalling) of Metals", *Progress in Materials Science*, **28**, (1983), 1–96

Chapter 8

Predicting Material Behaviour

8.1 Rationale

Each of the rock types in this thesis has taken a considerable amount of time and effort to characterise fully. As laid out in the introduction, the parameters investigated are considered important for the modelling of the blast mining process. To be a useful tool, the model has to be applicable to the situation as encountered in the mines of particular commercial companies. The fact that the geology of these mines is varied means that the model will only fulfill its potential if all necessary geology can be taken into account when making blasting predictions. This means that any rock type encountered must be either included in the model, or able to be added to the model. It is too time consuming and expensive to test every rock type that it might be necessary to blast and so some solution to easily predicting the properties of any given material is essential in achieving a workable commercial model.

The simplest solution is to use the rock types existing in the model and match rocks encountered to the nearest equivalent. While simple, this is also likely to be inaccurate in many cases, as there is no simple reasoning as to what makes the rocks "similar". A more involved method is to find some parameter which can be simply measured and use this to predict the behaviour which is more costly to investigate. This empirical method has the benefit of using the breadth of existing

knowledge in forming a relationship between the parameters, and also tailoring the result to the rock encountered (by means of some simple experiment).

8.2 Mine Data

Certain data were provided by the mines as examples of data routinely taken for internal investigation. This consisted of five measurements; density, ultimate compressive strength, triaxial compressive strength, brazilian disc, and slake durability index. These data were provided for the amphibolite, quartz/feldspathic gneiss and biotite schist. The density was in agreement with the measurements taken for this thesis and therefore will not be referred to further as it offers no additional information.

8.2.1 Slake Durability Index

The slake durability index is a measurement designed to quantify resistance to short term weathering [1]. The slake durability index in this case is not given as a numerical value. The value for all three of the rocks investigated is "very high". This is therefore of little use in making predictions for modelling. Additionally it is hard to see what physical connection there would be between dynamic strength and weathering.

8.2.2 Brazilian Disc

The brazilian disc test is a method of compressional testing which causes failure in tension. A disc of material is compressed between two anvils which are positioned opposite each other along one axis of the disc. As the material is compressed the free sides, that is the sides not constrained by the anvils are able to move outwards. When this happens, the material in the centre of the disc is put into tension. If the tensile strength of the material is exceeded, then the material will fail by fracturing. It is possible to derive the tensile strength by knowing the compressive force which caused the material to fail. A schematic of the setup for a Brazilian disc test is shown in figure 8.1.

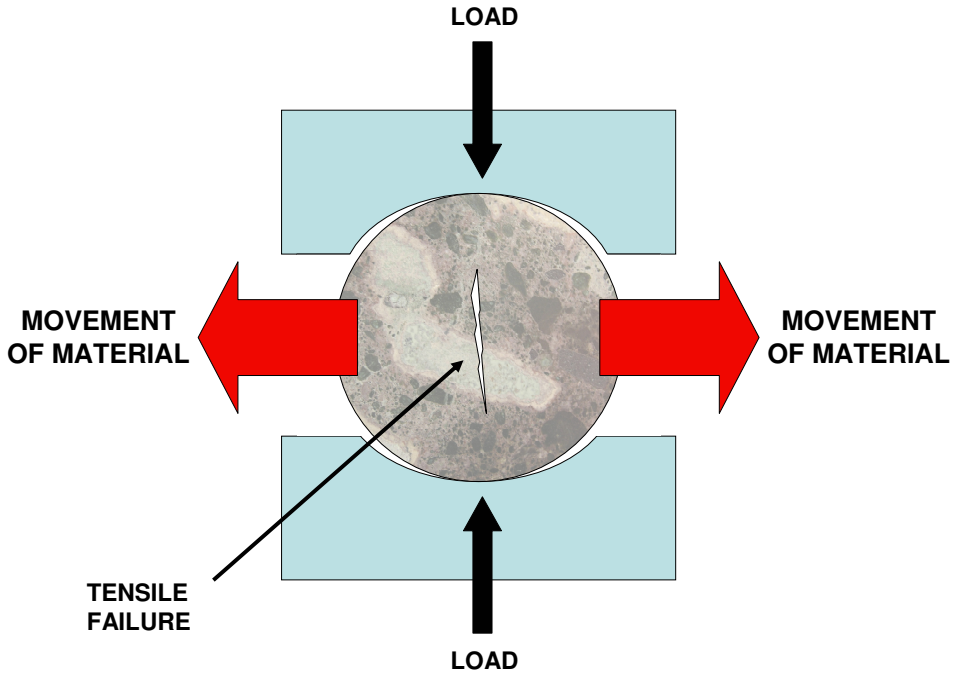

Figure 8.1: Schematic of Brazilian disc test. As the load is applied, the material moves out to the side leading to tensile cracking in the centre of the sample. The anvils are curved to prevent Hertzian cracking at the contact points

All three of the rock types tested have an associated Brazilian tensile strength. Unfortunately it has not been possible to examine the spall strengths for these materials, other than for the biotite schist. However, it is possible that the amphibolite (being small grained, see the MLA data) would have a higher tensile strength than the large grained materials. Therefore it is possible that the Brazilian test values could be a useful predictive method for dynamic tensile strength. Further experimentation would be required to confirm this however.

8.2.3 Ultimate Compressive Strength

Ultimate compressive strength (UCS) is defined as the failure load divided by the original cross section of the material under test. Samples of rock are subjected to uniaxial compression and the failure force is recorded by a machine specifically designed to compress to well-calibrated loads. This has been carried out for the three rocks mentioned, and a significant amount of data have been generated. While the values of static or quasi-static strength are unlikely to be the same as dynamic values due to strain rate effects, there is a possibility that a similar trend of compressive strength in the dynamic and static regimes might be found. The aim of using these data would be to predict for example the slope of the Hugoniot (should it be a straight line) or the HEL of the material.

The first observation that is striking about the UCS data is the large scatter in the data. The mean and standard deviation of the data sets are as follows: amphibolite - 146 ± 53 MPa, quartz/feldspathic gneiss - 166 ± 73 MPa and biotite schist - 87 ± 36 MPa. This obviously creates an issue for using these data for predictions, namely that a significant number of experiments will have to be carried out in order to determine the mean to an acceptable accuracy. This is of course also time-consuming and expensive. A further point is that the UCS for the quartz/feldspathic gneiss is higher than that of the amphibolite, the opposite to the trend in both their Hugoniot slopes and their HEL values.

8.2.4 Triaxial Compressive Strength

Triaxial compression (TCS) , as the name suggest is compression along three perpendicular axes. The test specimens are intact cylinders of rock core. The aim of the testing is to obtain values for failure load at a particular confining pressure. As with UCS, if these data were to be used in predictions, one would be aiming to predict the Hugoniot slope (i.e. the compressive behaviour) and the HEL.

The problems with TCS seem to mirror the problems found with UCS. Again there is a significant amount of scatter in the data. The quoted strengths are as follows: amphibolite - 271 ± 89 MPa, quartz/feldspathic gneiss - 276 ± 67 MPa

and biotite schist - 136 ± 55 MPa. This is the same pattern in the values as for the UCS measurements, the quartz/feldspathic gneiss has the highest TCS value, something not reflected in the dynamic behaviour. The fact that the trend statically is the opposite of the dynamic trend makes TCS unsuitable for making predictions.

8.2.5 Base Friction Angle

The base friction angle (the angle of friction for smooth non-damaged surfaces [2]) is determined by the following method [3], or similar. Two blocks of saw cut material are placed on top of one another so that the "smooth" saw cut surfaces are in contact. The pair of blocks is then tilted and the angle to the horizontal at which the top block begins to slide is the base friction angle. While these data were not supplied with the intention of being able to make predictions, it is unclear exactly what physical relationship it would have to any of the parameters that need to be predicted. In addition to the fact that the results would seem to be somewhat dependent on the exact saw cut made on each sample and other considerations, the values for the amphibolite and the quartz/feldspathic gneiss are the same to within the quoted experimental error. This obviously does not allow for the base friction angle to predict the differences that are found in the dynamic properties of these two materials.

8.2.6 Conclusion

The information provided by the mines contains a significant amount of data pertaining to the samples supplied for dynamic investigation. It appears however, that for the purposes of predicting the dynamic behavior, with the exception of the Brazilian test, these data are not particularly useful. While it would be expected that the low strain rate strengths of the materials would reflect the dynamic behaviour (albeit with some strain rate dependence) this does not seem to be the case, and there could be a number of reasons for this. One significant reason is the affect of flaws and sample to sample variation on the results. At the lower strain rates a sample with a significant flaw will have the time available for crack initiation and growth, leading to the failure of such samples at much lower

strengths then non flawed samples. The presence of flaws would account for some of the wide scatter in the data provided. The samples may be sufficiently large to be representative of the rock mass, excluding large flaws and jointing, but also large enough to conceal flaws that would be easily spotted in smaller samples such as those used for the dynamic testing. At higher strain rates the material is inertially confined in a state of one dimensional strain. Increased strain rate leads to a reduced effect from flaws and sample to sample variation. Additionally the time scale of the experiment is significantly shorter leading to a much smaller number of flaws that are able to grow into larger cracks.

8.3 Prediction Methodology

One of the key aspects to being able to make successful predictions is having a good understanding of the information available and applicable to the situation. In the case of predicting rock behaviour, the data presented in this thesis and also data from the literature are important. In particular any predictive capability must be able to fit data such as the experimental data presented here, where good information exists as to the exact rock types investigated. If predictions do not fit the data, then a good reason should be available to explain this failure. Obviously a perfect predictive capability should not be expected as it is is difficult, if not impossible, to accurately take account of all variations in the materials.

A good starting point for any prediction system is to examine the rock carefully by eye and then using some method determine the density across a reasonably wide number of samples. The reasoning behind doing this is that it can be seen from the compressional results and the Hugoniots that the presence of porosity can play a significant role in the response of a material to shock loading. The example of the response of the biotite schist also suggests that it is worth taking into account whether there is likely to be any soft components within the rock which could act in a similar way to porosity. A preliminary investigation such as this will allow the material to be roughly catagorised into one of the following groups:

- Very soft porous rocks, verging on powders, with low density and obvious porosity. Examples of this type of rock would be the sandstone in this thesis and TKB [4]. It would be expected that the HEL of these materials would be very low or essentially non-existent. The Hugoniot would be upward curving (likely after an initial downwards section) in σ - u_p space and be dominated by pore crushing. While these materials would have a tensile strength associated with them, it is unlikely that attempting to measure this via a spall technique would be profitable as the material would be broken sufficiently on compression as to have a very small spall strength.

- Harder rocks with some porosity, or elements of softer material, such as the iron ore or the biotite schist in this thesis. As the porosity in the material becomes important, such that pores are crushed, then the Hugoniot is likely to curve or deviate. As it is possible that the material will have an initial elastic region to the Hugoniot, this will be well-predicted by the acoustic impedance of the material. As the value of the HEL and the spall strength are likely to be affected both by the level of porosity and the bulk material these will be complex and difficult to predict.

- Hard, non-porous rocks with a density of roughly 2.5-3 g cm^{-3}. These constitute the majority of rocks in this study and therefore are significant in terms of the model as there are most representative of the rock types encountered by De Beers during mining. Predictions for this type of rock will be dealt with in more detail below.

- Hard, non-porous rocks with a density of greater than 3 g cm^{-3}. There have been none of this rock type in this thesis and therefore "hands on" knowledge of these rock types is limited. A thorough literature search would be necessary to be able to make predictions, although it is possible that a detailed mineralogy study of the materials would be needed to make accurate predictions.

8.3.1 Predicting the Hugoniot Slope

Predicting the Hugoniot slope if the Hugoniot is a straight line would be a useful tool for users of the model as the majority of rocks investigated follow this pattern. A logical parameter to use for the prediction would be the elastic (or acoustic) impedance. These data are tabulated in table 8.1. Indeed it is noticeable from the close agreement of the elastic behaviour plotted with the Hugoniots in chapter 6 that this is likely to achieve a positive result. Figure 8.2 shows the relevant data from this thesis in a plot of Hugoniot slope against acoustic impedance This data is tabulated along with some literature data in table 8.3.1.

Material	**Elastic Impedance** $g\ cm^{-3}\ km\ s^{-1}$	**Hugoniot Slope** $GPa\ km^{-1}\ s$
Siltstone	19.47	19.15
Kimberlite	15.24	12.86
Amph Gneiss	17.58	16.14
Amphibolite	19.84	20.90
Quartz/Feld Gneiss	15.16	15.30
Basalt	13.44	13.42
Granite [5]	13.59	13.67
Gabbro [5]	17.88	17.82
Granite [6]	15.54	18.18
Dolerite [7]	17.05	17.30
Basalt [8]	11.78	14.58
Diabase (Virginia) [9]	19.03	18.02
Diabase (Maryland) [9]	20.32	18.15
Granite [9]	14.00	14.24
Andalucite [9]	22.44	22.64
Haematite [9]	38.95	37.58
Magnetite [9]	35.82	34.05
Silliminite [9]	28.14	24.16

Table 8.1: Data from this thesis and literature with elastic impedances and Hugoniot slopes

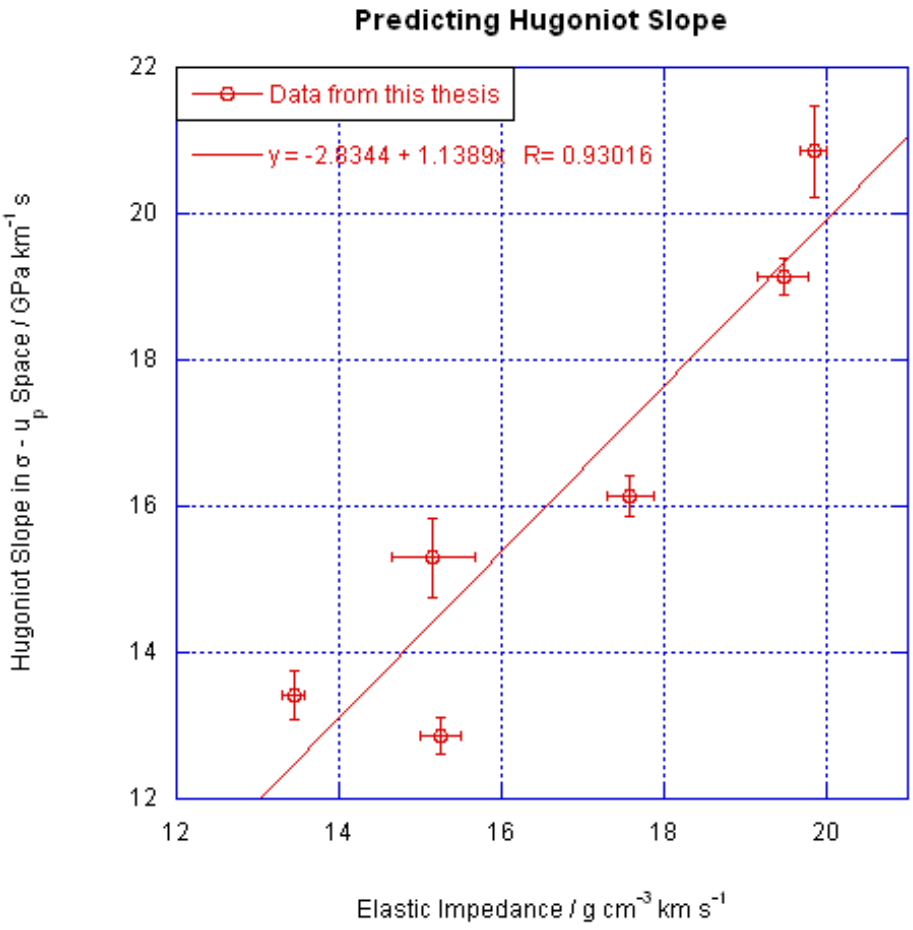

Figure 8.2: Plot of impedance against Hugoniot slope for data in this thesis. While the agreement is by no means perfect, a general trend is easily discernable. The line of best fit for these points only passes through one of them, but gives an indication as to a starting point for prediction of Hugoniot slope from elastic impedance.

While the agreement is in no way perfect there is certainly a trend discernable in the data. This can therefore form a good basis for predicting the Hugoniot slope. There will obviously be a fairly large potential for error, but it is unlikely that any more accurate method will be found. In figure 8.3, the same data as in figure 8.2 are reproduced along with some literature data. The fit to the total dataset is different, but shows a similar trend. This backs up the conclusion that this

method can be used in a predictive capacity. Additionally, it is not always clear how the measurements of the acoustic impedance were taken in the literature. In some cases these values, as they are not the main focus of the research may not be as accurate as is strictly necessary for predictive uses. A good example of this is the data in Marsh [9] where some of the sound speeds were, upon more thorough investigation, taken at pressure and are therefore slightly higher than one might expect for the rock types concerned. In an overall predictive capability however it may be better to consider the data in this thesis as an addition to the data in the literature, rather than separate from it. This allows for the use of a wider range of data when making predictions. It should also be noted that some of the materials from the literature are unusual in that their density is rather higher than 3 g cm^{-3} and yet still have a linear Hugoniot fit.

As has been shown previously, both in the compressional results and in figure 8.2, many of the linear Hugoniots in this thesis show a very good agreement with the proposed elastic behaviour calculated from their sound speeds and densities. Certainly in the low stress regime, this kind of agreement would be expected. It is a point worth considering therefore, as to why the other materials do not show such behaviour. The plate impact experiments give the response of the bulk material to shockloading, in that the pressure (or particle velocity) obtained is an equilibrium state involving the whole material and not merely certain components. It is not necessarily the case however that the measured elastic impedance is representative of the same bulk. The measured density is obviously representative of the density of the whole material as used in the Hugoniot measurements as the whole sample is weighed and measured to calculate the density. The sound speed however is measured by the first easily detectable arrival of an ultrasound pulse at the receiving transducer. This may not be representative of the bulk. The first arrival at the transducer will be determined by the route through the material containing the most high sound speed material. Clearly therefore this sound speed is not representative of the material as a whole. Indeed the effective sound speed when the whole material is compressed will be notably lower than this. Such an argument could be used to postulate why the amphibolitic gneiss

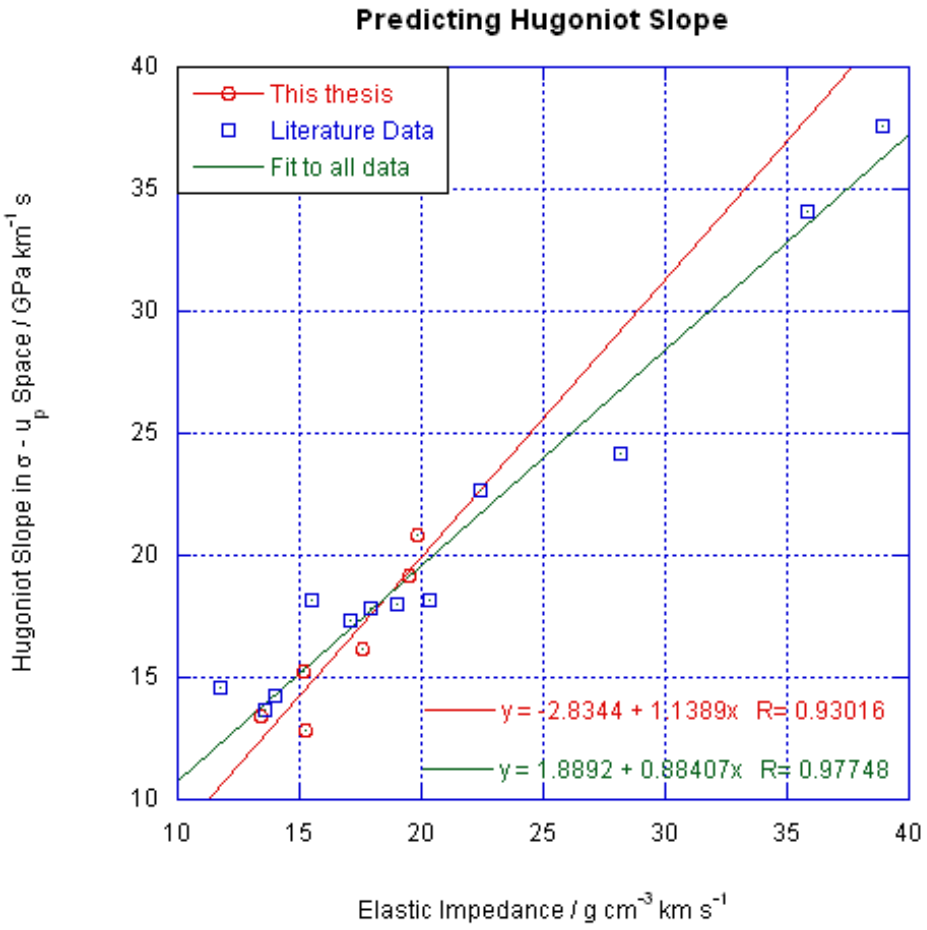

Figure 8.3: Plot of impedance against Hugoniot slope for data in this thesis and various literature data. The fits to the overall data set and the data from this thesis only are slightly different, but both indicate a similar trend. The trend suggests that for geological materials with linear Hugoniot relations in $\sigma - u_p$ space, the elastic impedance of the material is a reasonable predictor of the slope of the Hugoniot in $\sigma - u_p$ space.

and kimberlite have a Hugoniot that lies below the theoretical line of elastic behaviour. However, this does not explain the case of the amphibolite, which in figure 8.2 can be seen to display the opposite behaviour, namely that the effective sound speed in the Hugoniot experiments would appear to be higher than that measured in the static experiments. One possible explanation for this behaviour would be that the minerals that are not amphibole in the material are not present in sufficient quantities to cause a noticeable oscilloscope trace when measuring the sound speed. The sound speed measured therefore would effectively be the sound speed of amphibole or something near to it. In a shock the overall response of the material would include all of these materials and as opposed to making a judgment as to when the arrival occurs (as one has to do in the sound speed measurements) the measured stress would just be higher.

It would be instructive to try and show that the above explanation is indeed correct by examining the longitudinal sound speeds of the relevant minerals and comparing them. However a lack of data makes this an impossibility. A potential way around this is try and make the same adjustments by using a different (but linked parameter) for which data for the individual minerals is available. Such a parameter is the density. This is well tabulated for many minerals and is also related to the sound speed via the Young's Modulus. For a constant Young's Modulus the sound speed is proportional to the inverse of the square root of the density. Hence when making theoretical adjustments to the density, for a fall in effective sound speed we should be able to make an argument that the "effective density" is increased. It is worth noting that the two cuts of amphibolitic gneiss showed this relationship, with the lower density material exhibiting a higher sound speed.

Taking the amphibolitic gneiss and the amphibolite as examples (the mineral content of the kimberlite is too varied to be able to draw specific conclusions) we can calculate the following. The amphibolitic gneiss density is measured to be 2.8 g cm^{-3}. However the densities of the mineral components are somewhat more varied. A rough average of the densities (taken from http://webmineral.com) of the four major components of the sample in figure 2.8 is as follows: plagioclase -

2.68 g cm^{-3}, biotite - 3.09 g cm^{-3}, amphibole - 3.23 g cm^{-3} and quartz - 2.62 g cm^{-3}. A weighted average of these components (assuming that the other minor components were negligible) gives the correct density of 2.8 g cm^{-3}. However taking the sample in figure 2.8 63% of the material is made of material with an average density of 2.68 g cm^{-3} or below. If we assume that this material has a higher sound speed than the bulk this would quite possibly lead to the measurement of the sound speed by the transducers being high. To compensate for this if we use the weighted density of these lower density components instead of the bulk density on calculating the impedance the value obtained is 16.5 g cm^{-3} km s^{-1}, which is much closer to the measured Hugoniot slope of 16.1 GPa km s^{-1}.

If we consider the amphibolite, for example the MLA image in figure 2.2 then we can see that the inclusions of lower density materials in the amphibolite are small and possibly would, as suggested, give rise to a low signal that might then not be detected when measuring sound speeds. A mass average of the minerals using the average densities gives a density of 3.1 g cm^{-3}, which is clearly higher than the measured density of 3.0 g cm^{-3}. If we assume that all of this overestimate is due to the amphibole not being average, but actually below average density then we conclude an amphibole density of 3.1 g cm^{-3} which implies an impedance of 20.4 g cm^{-3} km s^{-1}. This is again an improvement towards predicting the Hugoniot slope of 20.9 GPa km s^{-1}. An alternative scenario would be to consider that the percentage of quartz for example was higher in the specimens where the density was measured. It is unlikely that this is entirely the case however as the quartz would have to occupy a 19% share of the material to correctly predict the measured density.

In conclusion therefore it is possible to demonstrate that potentially some of the discrepancies between the Hugoniots and measured elastic impedances can be explained through examination of the mineralogy. Ideally however, to make this a firm conclusion as opposed to a speculative thought experiment, a measurement of the sound speeds of the individual minerals would be required.

8.3.2 Predicting the HEL

The HEL is probably the single most important piece of information that is derived from the lateral gauge data. The HEL data are shown in table 8.2. In shear, it is important to be able to predict at what point the material will deviate from elastic behaviour. The acoustic impedance is an obvious starting point for predicting the compressional behaviour of the rock, but less obvious is a possible relation to the HEL. However if HEL is plotted against acoustic impedance (the data is tabulated in table 8.2) the result is as shown in figure 8.4

Material	**Elastic Impedance** $g\ cm^{-3}\ km\ s^{-1}$	**HEL** GPa
Siltstone	19.47	5.0
Kimberlite	15.24	1.6
Amphibolite	19.84	4.2
Quartz/Feld Gneiss	15.16	1.3
Basalt	13.44	4.2
Iron Ore	26.83	3
Gabbro [5]	17.88	3.9
Dolerite [7]	17.05	3.8

Table 8.2: Data from this thesis and literature with elastic impedances and HEL values

There is no clear trend to the data. Apart from the outlying iron ore point there does however appear to be two distinct groupings, around the 4 GPa level, and a lower grouping below 2 GPa. These data are seemingly independent of the acoustic impedance (and additionally the density, the basalt, the lowest density material other than the sandstone, seemingly has one of the higher HEL values). The most obvious similarity between the rocks within each group would appear to be the grain size of the material. The quartz/feldspathic gneiss and the kimberlite both have large grain sizes, when compared with the other materials for which HELs have been determined. These materials are also the low HEL materials.

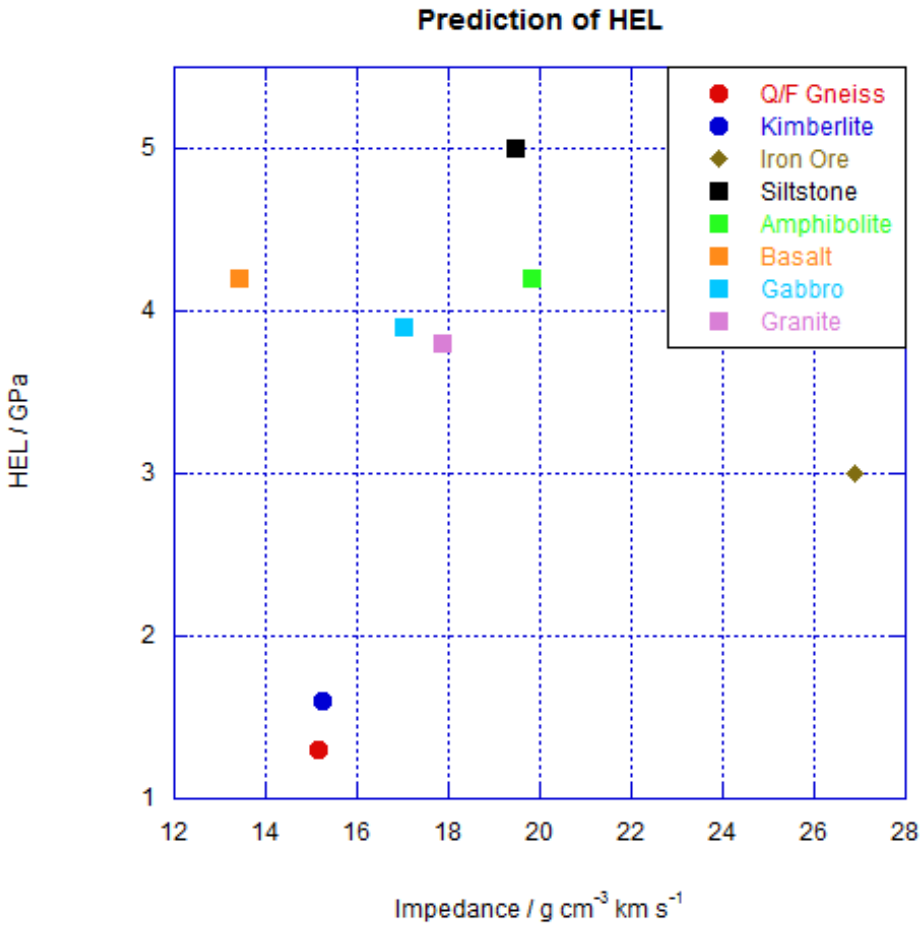

Figure 8.4: Plot of impedance against HEL value for data in this thesis and various literature data. The literature data are taken from Millett [5] and Tsembelis [7]. It can be seen that there is no trend to the data. However, excepting the iron ore, there are two distinct clumps of points, high HEL materials with small grain sizes and low HEL materials with high grain sizes.

The high HEL materials can all be described as fine grained (sub mm sized grains). This is also the case for the literature data, as both papers comment that the material grain size is small. It is likely that this is a dominant factor in determining the HEL. As the HEL is a measure of failure of the material, it is likely that large interlocking crystals will have weaker grain boundaries than the smaller grained, more homogeneous materials.

8.3.3 Predicting the Spall Strength

Owing to the fact that the spall of geological materials is such a statistical process and it is difficult to fix a value without a fairly substantial experimentation prediction is important. As there is a lack of spall data it is difficult to make a connection between the acoustic impedance and the tensile strength (though it is noted that the spall strength of the higher impedance siltstone is higher than that of kimberlite). It therefore makes sense to look for alternative predictive methods. One potential prediction methodology is the following formula (equation 8.1) due to Rosenberg [10].

$$\sigma_{HEL} = \left(\frac{1-\nu}{(1-2\nu)^2} \right) 10\sigma_T. \tag{8.1}$$

The HELs for kimberlite and siltstone have been calculated experimentally as described in chapter 7. The values are 1.6 GPa and 4.8 GPa respectively. It is possible that taking into account grain size, a rough estimate could be made of the HEL values without lengthy experimentation. The Poisson's ratio has been calculated from the shear and longitudinal wave speeds and is quoted in chapter 2. The determined experimental values for the spall strengths are 21 ± 4 MPa for the kimberlite and 55 ± 6 MPa for siltstone. Using equation 8.1 we calculate that the theoretical spall strength of these materials is approximately 33 MPa and 134 MPa respectively. This is an overestimate compared with the experimentally determined values, although it should be noted that the good agreement suggested by Rosenberg was for much more homogeneous ceramics. Clearly, again, the potential for preferential fracture along weakened grain boundaries is not accounted

for.

Another consideration is that the formula quoted by Rosenberg is actually an adaptation of a relationship derived from the Griffith Criterion. It is noted that the factor of ten in equation 8.1 is in fact a factor of 8 in the original expression. The reason given for altering the expression is to make it more appropriate to ceramics. If a similar argument is used for geological materials it is not unreasonable to suggest that the value might be different again. If the factor of 10 in the Rosenberg formula is back-calculated from the experimental values it is found to be 16 for the Kimberlite and 25 for the siltstone. This clearly implies that for the complex tensional failure in geological materials such a theoretical construct is not an accurate prediction method. It is likely that some direct measurement of tensile failure at a lower strain rate (for example the Brazilian test) would be a better method of predicting the higher strain rate behaviour. It is also worth noting that the higher spall strength in siltstone could also, as with the HEL, be a reflection of a grain size effect.

8.4 Summary

- It is important to be able to make predictions about the dynamic behaviour of geological materials for modelling purposes.
- Much of the data provided as standard mining data has proved of limited use in making predictions of dynamic behaviour.
- It is possible that the Brazilian test may provide useful predictive information about dynamic tensile strength, but due to a lack of available dynamic tensile data this has been impossible to demonstrate.
- The prediction of behaviour for any rock type should initially include examining density and porosity, as these have a significant impact on material response.
- For non porous materials in a density range of approximately $2.5-3\ g\ cm^{-3}$ the slope of the Hugoniot (which has been shown in this thesis to likely be

linear in σ - u_p space below about 15-20 GPa) is well predicted by the elastic impedance.

- The value of the HEL would appear to depend on grain size, with fine grained materials having a higher HEL than materials with large grains such as kimberlite and quartz/feldspathic gneiss.
- A theoretical construct derived from the Griffith criterion is inappropriate for the prediction of spall strengths.

References

[1] Singh, T.N., Verma, A.K., Singh, V. and Sahu, A., "Slake durability study of shaly rock and its predictions", *Environmental Geology*, **47**, (2005), 246253

[2] Homand, F., Belem, T. and Souley, M., "Friction and degradation of rock joint surfaces under shear loads", *Int. J. Numer. Anal. Meth. Geomech*, **25**, (2001), 973–999

[3] York, G., Canbulat, I. and Jack, B.W., "Coal pillar design procedures", Technical Report COL 337, Safety in Mines Research Advisory Committee (2000)

[4] Willmott, G.R., *Shock Studies of Kimberlite, Diamond and Brittle Embedded Particles*, Phd, Cambridge (2004)

[5] Millett, J.C.F., Tsembelis, K. and Bourne, N.K., "Longitudinal and lateral stress measurements in shock-loaded gabbro and granite", *J. Appl. Phys.*, **87**, (2000), 3678–3682

[6] Shang, J.L., Shen, L.T. and Zhao, J., "Hugoniot equation of state of the Bukit Timah granite", *Int. J. Rock Mech. Min. Sci.*, **37**, (2000), 705–713

[7] Tsembelis, K., Proud, W.G. and Field, J.E., "The principal Hugoniot and dynamic strength of dolerite under shock compression", in *Shock Compression of Condensed Matter - 2001*, M. Furnish, N. Thadhani and Y. Horie, eds., American Institute of Physics, Melville, NY (2002), pp. 1385–1388

[8] Nakazawa, S., Watanabe, S., Kato, M., Iijima, Y., Kobayashi, T. and Sekine, T., "Hugoniot equation of state of basalt", *Planet. Space Sci.*, **45**, (1997), 1489–1492

[9] Marsh, S.P., *LASL Shock Hugoniot Data*, University of California Press, Berkeley, California (1980)

[10] Rosenberg, Z., "On the relation between the Hugoniot elastic limit and the yield strength of brittle materials", *J. Appl. Phys.*, **74**, (1993), 752–753

Chapter 9

Conclusions

9.1 Fulfilling Aims

The object of the research for this thesis was the characterisation of the relevant properties of the provided geological materials. It was initially pertinent to discover what exactly the relevant properties were and identify methods of measuring them reliably. Drawing on the experience and needs of the sponsors, information from the literature, and the personal expertise of Prof. John Field it was possible to make this identification of relevant parameters. The methods used to make measurements were, to a large extent, standard experimental practice when examining shock properties of materials. However, the specifics and nuances of exactly which experimental configurations were most suited to geological materials had to be discovered through personal experience.

The series of experiments that has been conducted for this thesis, in support of the HSBM project, have provided much useful data for the modellers and has enhanced the understanding of the behaviour of geological materials under shock loading. This is true in the general sense as well as the specific case of the parameters required for the project. In some cases the investigations have gone beyond the initial scope of the research aims, for example in the calculation of waste heat and the characterisation of the release properties of the materials. While it has not been possible to fully investigate all of the materials provided the data obtained provide a significant contribution to the body of available

data on geological materials. In terms of low pressure data, this contribution is enhanced further. It should be noted that the reasons for not completing full characterisations for all of the materials were constraints of time and finance. It was deemed better to obtain reliable data for a smaller set of materials than to try and cover all materials, and miss important aspects of material response due to the lack of depth of the study. This is particularly true in the case of the spall strengths of the materials. Not only were repeat experiments required due to experimental failures, but also it was discovered that a significant number of experiments were needed to build up an accurate average value of the spall strength.

9.2 Static Data and Material Properties

It is clear that the characterisation of geological materials has to begin with collecting sufficient information about them in the non-shocked state to allow easy identification when compared with other materials, either in other studies, or in a mining environment. It is of course of minimal use if one has to conduct 20 plate impact experiments to decide whether two materials are similar. In examining the materials it was fortunate that Dr. Plint at Nottingham was able to provide such excellent data for the mineral analysis. In a number of cases, such as the relative quartz contents of different materials and the presence of clay in the biotite schist, this information has been invaluable and has allowed for conclusions to be drawn where otherwise they may not have been. The MLA data also aided in looking at grain size in the materials. While no formal calculations have been conducted there is a clear difference in grain sizes between the materials. Excluding large random inclusions in the cores (which are present in almost all of the materials) there are two materials with consistent occurrences of grains of the order of five or more mm, the kimberlite and the quartz/feldpathic gneiss. The biotite schist tended to have more inclusions than many of the materials but the average grain size was lower than that of the kimberlite for example. Amphibolite and amphibolitic gneiss samples showed grains on approximately mm scale in the photographs and to the naked eye, although the mineralogical variation between

these grains is less in the MLA images. For the basalt, the siltstone and the iron ore, some grain structure was discernable, but at a sub-mm scale. It is however worth noting that the colouring of the grains in the siltstone lead to patterns on the material of a much larger scale. The sand particles in the sandstone sample were also of sub mm scale.

The remaining static data are of a more standard nature and consisted of the relatively straight-forwardly measured densities and sound speeds. The densities ranged from 1.93 $g\ cm^{-3}$ for the sandstone to 4.5 $g\ cm^{-3}$ in the iron ore. However the materials were not evenly spaced over this range with the majority of the materials, seven in all, having densities between 2.6 and 3 $g\ cm^{-3}$. Only the sandstone and the iron ore exhibited any level of porosity involving interconnected pore networks. The range of sound speeds in the materials, with the exception of sandstone, was between 5 $km\ s^{-1}$ and 7 $km\ s^{-1}$ in the longitudinal orientation and 2-4 $km\ s^{-1}$ in the shear orientation. It was possible to measure both the density and the sound speed to a high degree of precision. It is certainly the case with these measurements that the sample to sample variation was the major source of experimental error on the values determined (additionally it is noted that at no point in this thesis was an effort made to address potential material anisotropy). The only real issue, other than the sample to sample variation, with the static measurements is exactly the extent to which they are truly representative of the bulk materials under dynamic loading. It has been suggested that this is not in fact always the case, in particular with reference to the sound speeds. Some success was had in potentially accounting for this using what essentially amounted to a thought experiment involving the individual mineral densities.

9.3 Compressional Results

Compressional data were obtained for all materials supplied for this investigation. In general the results were reliable and the methods used to obtain the final results were satisfactory. It was noted that the use of gauges was inappropriate for certain materials. Whilst not specifically investigated, it is likely that

straining of gauges played a large part in causing poor gauge results for some of the more inhomogeneous materials such as the quartz/feldspathic gneiss and the kimberlite. In addition experiments were conducted to investigate the possibility of electromagnetic emissions causing noise in gauge traces. The results of these shots indicated that it was probable that the materials that had higher quartz contents (or other piezoelectric materials) would be more susceptible to noisy gauge traces. The use of a reverse impact configuration and VISAR allowed for the releases of a number of the materials to be determined. The accuracy to which this could be done was limited in some cases by financial considerations, but also the effect of inhomogeneity. Sample to sample variations also limited the extent to which definite trends could be elucidated.

The Hugoniots of all of the materials with the exception of biotite schist, sandstone and iron ore were able to be described by a linear relationship in $\sigma - u_p$ space. Of these materials the basalt, the siltstone and the quartz/feldspathic gneiss all showed a great deal of similarity with the theoretical elastic behaviour calculated from the elastic impedance. The amphibolite Hugoniot lay above the elastic line, whereas the kimberlite and the amphibolitic gneiss lay below their respective elastic lines. For these linear materials there appears to be no strong relationship between shock and particle velocity in the stress regime investigated. Shock velocity was examined as part of the quartz/feldspathic gneiss and amphibolite Hugoniot measurements and was specifically examined through separate experiments for siltstone. Of the non linear materials, the iron ore and the sandstone had behaviour that was dominated by their porosity. There appeared to be no discernable elastic behaviour at all for the sandstone, which showed an upwards curving Hugoniot in $\sigma - u_p$ space in the stress range examined. The iron ore Hugoniot in contrast, showed an obvious linear elastic regime and an HEL of approximately 3 GPa. The strength of the material compared with the sandstone is the cause of this difference. Iron ore data were also subject to larger sample to sample variations, as a number of the samples had macroscopic cracks in them, leading to the premature release of the 1D strain condition. The biotite schist Hugoniot also demonstrated a slight curvature, which was unexpected owing to a lack of obvious porosity. However it is presumed that this curvature is caused

by the presence of clay in the material, as shown in the MLA data.

The releases in the materials were used to calculate the energy lost in a loading/unloading cycle. This is known as the waste heat. It was possible to calculate this for a number of the materials, and various potential trends were identified. The most obvious conclusion is that none of the materials retained 100% of the energy during the cycle, and this can be attributed to heating and other disipative mechanisms (it should be remembered that shockloading is not in general an inentropic process). Other trends included that in most materials (with the exception of biotite schist where the opposite occured) the energy recovered on unloading decreased at higher stresses. This was expected owing to the fact that greater damage is done to the material at higher stresses (above the HEL). It was also notable that the sandstone absorbed far more energy than the other materials, due to the crushing of the pores within the material.

9.4 Shear Strength and the HEL

Shear strength and lateral stress were measured using stress gauges for amphibolite, iron ore, sandstone, quartz/feldspathic gneiss, kimberlite, siltstone and basalt. In general the use of lateral gauges was easier, in terms of reliability of results and the noise in the gauge traces, than the use of longitudinal gauges. The likely reason for this is the increased padding and reduced surface area of the lateral gauges used (when compared with the longitudinal gauges). In some cases longitudinal gauges were used in conjunction with the lateral gauges. However in other materials (due to the unreliability of the gauges in that material or the need for a metal coverplate) the longitudinal stress was inferred from the previously measured Hugoniot for the material. The shear strengths of the materials were calculated by taking the difference of the longitudinal and lateral stresses. This difference is equal to twice the shear strength. With the exception of sandstone and the biotite schist, all of the materials were found to have an obvious HEL, as shown by a deviation from a line of elastic behaviour calculated from the Poisson's ratio. To obtain a value for the HEL a line was fitted to the data points above the

HEL and the intercept of this line with the line of elastic behaviour was taken as the HEL. The HELs ranged in value from 1.3 GPa (quartz/feldspathic gneiss) to 5 GPa (siltstone). With the exception of the iron ore the HEL was not obvious from the longitudinal data as it would be in many other materials. It is speculated that the nature of non-elastic deformation in rocks, namely brittle cracking would possibly account for this observation. It is suggested that the compression of the 3D "rock jigsaw" would be essentially the same as compressing the intact rock mass. This means that the shock impedance and the elastic impedance are essentially the same. In other materials, a metal for example, plastic flow and dislocation movement would mean that the elastic and shock impedance would not be the same above the HEL as the material is altered by the action of the shock wave. While the shock alters the rock material by cracking it, this does not seem to have a particular effect on the material impedance.

9.5 Spall, Dynamic Tensile Strength

Attempts were made to investigate the dynamic tensile properties of a number of the materials, however this was only successful for kimberlite (21 ± 4 MPa), siltstone (55 ± 6 MPa) and biotite schist (one experiment giving 26 MPa). For the kimberlite and siltstone (five and four experiments respectively) there is a reasonable confidence in the results presented. Two separate experimental designs were utilised in obtaining the results, one design with a buffer between the rock and the diagnostics, which were behind a PMMA window, and one where the VISAR probe was incident on a reflective layer painted directly on the rear surface of the specimen. The design with the buffer appeared marginally more successful, although it should be noted that results for the kimberlite were successfully obtained using the windowless technique. A number of problems arise when attempting to measure the spall strength of geological materials. Firstly the polycrystalline and inhomogeneous nature of rocks means that fracture is unlikely to occur in the well defined planes that are required for successful plate impact tensile failure experiments. The failure of the experiments partly arises owing to the inability of the diagnostics to record non planar events accurately.

Additionally, even if the diagnostics were to function perfectly (which is is often not the case owing to straining in gauges and break up of the material) it is not clear in some instances exactly what they are measuring. Unlike the compressional experiments, the idea is not to reach a plateau stress, but to release the stress and pull the material apart. Breakage of the material will be influenced by weak grain boundaries. A final problem is that the magnitude of the stresses or particle velocities involved are small, and this makes the determination of levels in the data (required for the calculation of the spall strength) difficult. A statistical approach is therefore necessary to determine a spall strength, and a significant number of unsuccessful shots should be expected.

9.6 Prediction of Material Behaviour

The material data are destined for use in a computer modelling programme it was essential to attempt to develop prediction methodologies to avoid the need for expensive dynamic characterisation of any new materials encountered in the mining environment. Initially it was supposed that some of the static data provided with the materials from De Beers, such as the UCS and TCS values could be used in making predictions. However this proved not to be the case as much of the data in fact showed the opposite trend to that shown in the dynamic experiments. In the case of the dynamic tensile strength not enough data was collected to compare with the mine supplied Brazilian test data. It is possible on future investigation that this will prove a useful prediction tool, but no such conclusion can be currently drawn.

To make predictions it was necessary to look away from the supplied data to other possible easy-to-measure physical properties that might be related to the dynamic properties in some way. From the compressional data it was clear that the elastic impedance was a good description for much of the linear fitted Hugoniots. A more formal plot of this showed good agreement between two and also with data from the literature. It was speculated that possible differences between the measured and the “representative” sound speeds could be the cause of discrepancies

between the Hugoniot slope in $\sigma - u_p$ space and the elastic impedance. A method of possibly accounting for this by varying the density (by way of a thought experiment of sorts) met with some success. This method involved examining the effects of individual mineral phases on the bulk response of the material. The elastic impedance and also the density were found to be of minimal use in predicting the HEL however, as no discernable trends were found with any measured static data. What was noticed was that the smaller grain size materials had higher values for the HEL (above 4 GPa) than the larger grain size materials (below 2GPa). Prediction of the spall strengths of the materials was not successful, though it was shown that a Griffiths criterion based approach using the Poisson's ratio to link HEL and spall strength was inappropriate. It is perhaps more likely that a prediction of spall strength from a low rate tensile test would be more successful.

9.7 Potential Areas for Future Research

A brief list of potential starting points for further investigation is presented below:

- Amphibolite release measurements could be performed.
- In general the release measurement experiments could be perfected through the use of different materials to give a fuller picture of the release of the material. Specifically the use of higher impedance materials would allow for a greater number of smaller steps in particle velocity to be determined. This would in turn allow for greater resolution of the release path (by increasing the number of data points available). Additionally even greater care could be taken with sample preparation to try and ensure sharp rises and plateaus.
- The HEL of amphibolite and biotite schist (if one is present) could be determined.
- Many more spall experiments need to be performed to build up a coherent picture of spall in geological materials. One suggestion that might aid this is to perform a series of experiments at varying strain rates. If these experiments were simpler to perform than plate impact experiments, they

could be done in a greater number. Experiments using different equipment would potentially allow for an idea of the rate dependence of strength to be determined, which in turn would be useful when examining the spall signals (as one would have an idea as to the expected value)

- As mentioned, many geological materials shown anisotropy, this has not been examined in the present thesis, but certainly should not be neglected. A series of samples cut at angles from the cores could be investigated both statically and dynamically to determine whether there are any differences when compared to the data already obtained.

- Further samples are needed to firm up some of the conclusions presented, especially for example in the case of the iron ore.

- It would be of use to find other geological materials (with certain desirable properties) which would allow for gaps in prediction methodologies to be filled. This would be coupled with further examination of the literature, to ensure that all available and relevant data have been considered and tabulated.

- In order to examine the "3D rock jigsaw" that has been proposed in this thesis, it would be preferable to design an experiment where the stresses reached in intact and pre-fractured samples are compared. One potential method of pre-cracking could be to encase the samples in a microwave transparent medium and crack the samples using microwave heating (so that no material is lost as a result of the fracturing process).

- The issue of noise in gauge traces has the potential to be of significant interest. A combination of modelling and the use of multipoint VISAR to examine the particle velocities of individual grains should help in gaining an understanding of potential gauge straining effects. The electromagnetic emissions could also benefit from further study. It is possible that with a good knowledge of the piezo-electric properties of quartz and sufficient sensors, to be able to reconstruct some size information about the sample from these electromagnetic pick-ups in unconnected gauges.

Appendix A

A.1 Table of Shots

The following table is intended to give a brief summary of all of the plate impact experiements conducted for this thesis. The information provided is not exhaustive, but does give important information regarding the main points of each experiment. As the results of experiments have been outined in the main body of the thesis no information about the results is provided in the table.

Shot Code	Experiment Type	Impactor Material	Target Material	Diagnositc 1	Diagnostic 2	Velocity $m\ s^{-1}$	Comments
E041217A	Hugoniot	Copper	Q/F Gneiss	Longitudinal Gauge	Longitudinal Gauge	800	Front Gauge Fail
E050111A	Hugoniot	Copper	Q/F Gneiss	Longitudinal Gauge	Longitudinal Gauge	810	repeat of E041217A
E050112A	Hugoniot	Copper	Q/F Gneiss	Longitudinal Gauge	Longitudinal Gauge	256	
E050112B	Hugoniot	Copper	Q/F Gneiss	Longitudinal Gauge	Longitudinal Gauge	499	
E050113A	Hugoniot	Copper	Q/F Gneiss	Longitudinal Gauge	Longitudinal Gauge	957	
E050119A	Hugoniot	Copper	Q/F Gneiss	Longitudinal Gauge	Longitudinal Gauge	656	
E050201A	Hugoniot	Copper	Q/F Gneiss	Longitudinal Gauge	Longitudinal Gauge	400	
E050303A	Hugoniot/Release	Q/F Gneiss	Copper	VISAR		778	
E050412A	Hugoniot	Aluminium	Q/F Gneiss	Longitudinal Gauge	Photo	324	
E050428A	Hugoniot	Copper	Amphibolite	Longitudinal Gauge	Longitudinal Gauge	217	
E050428B	Hugoniot	Copper	Amphibolite	Longitudinal Gauge	Longitudinal Gauge	398	
E050429A	Hugoniot	Copper	Amphibolite	Longitudinal Gauge	Longitudinal Gauge	555	
E050429B	Hugoniot	Copper	Amphibolite	Longitudinal Gauge	Longitudinal Gauge		Shot failed
E050506A	Hugoniot	Copper	Amphibolite	Longitudinal Gauge	Longitudinal Gauge		Shot failed
E050506B	Hugoniot	Copper	Amphibolite	Longitudinal Gauge	Longitudinal Gauge		Shot failed
E050527A	Hugoniot	Copper	Amphibolite	Longitudinal Gauge	Longitudinal Gauge	705	
E050527B	Hugoniot	Copper	Amphibolite	Longitudinal Gauge	Longitudinal Gauge		Vacuum Fail
E050530A	Hugoniot	Copper	Amphibolite	Longitudinal Gauge	Longitudinal Gauge	1038	Repeat of E050527B
E050928A	Hugoniot	Copper	Kimberlite	Longitudinal Gauge	Longitudinal Gauge	389	
E050929A	Hugoniot	Copper	Kimberlite	Longitudinal Gauge	Longitudinal Gauge	546	
E050929B	Hugoniot	Copper	Kimberlite	Longitudinal Gauge	Longitudinal Gauge	699	
E051028A	Hugoniot/Release	Kimberlite	Copper	VISAR		845	
E051028B	Hugoniot/Release	Kimberlite	Copper	VISAR			Projectile Fail
E051031A	Hugoniot/Release	Kimberlite	Copper	VISAR		250	
E051104A	Hugoniot/Release	Kimberlite	Copper	VISAR			Trigger fail
E060125A	Hugoniot/Release	Kimberlite	Copper	VISAR		387	
E060125B	Hugoniot/Release	Kimberlite	Copper	VISAR		591	
E060226A	Hugoniot/Release	Amph Gneiss	Copper	VISAR		498	
E060126B	Hugoniot/Release	Siltstone	Copper	VISAR		493	
E060202A	Hugoniot/Release	Amph Gneiss	Copper	VISAR		732	
E060203B	Hugoniot/Release	Siltstone	Copper	VISAR		715	
E060208A	Hugoniot/Release	Siltstone	Copper	VISAR		244	
E060208B	Hugoniot/Release	Amph Gneiss	Copper	VISAR		251	

Shot Code	Experiment Type	Impactor Material	Target Material	Diagnositc 1	Diagnostic 2	Velocity $m\ s^{-1}$	Comments
E060216A	Hugoniot/Release	Siltstone	Copper	VISAR		927	
E060228A	Hugoniot/Release	Siltstone	Copper	VISAR		743	Repeat of E060203B
E060321A	Hugoniot/Release	Amph Gneiss	Copper	VISAR		986	
E060328A	Hugoniot/Release	Sandstone	Copper	VISAR		505	
E060404A	Hugoniot/Release	Sandstone	Copper	VISAR		742	
E060404B	Hugoniot/Release	Sandstone	Copper	VISAR		991	
E060428A	Hugoniot/Release	Sandstone	Copper	VISAR		247	
E060627A	Spall	Amphibolite	Copper	Longitudinal Gauge		247	
E060627B	Hugoniot/Release	Sandstone	Copper	VISAR		1007	VISAR fail
E060911A	Hugoniot/Release	Sandstone	Copper	VISAR		979	Repeat of E060627B
E061024A	Spall	Kimberlite	Kimberlite	VISAR		139	
E061025A	Spall	Kimberlite	Kimberlite	VISAR		183	
E061025B	Spall	Kimberlite	Kimberlite	VISAR		175	
E061025C	Spall	Kimberlite	Kimberlite	VISAR		147	
E061026A	Spall	Kimberlite	Kimberlite	VISAR		151	
E061026B	Lateral	Copper	Kimberlite	2 Lateral Gauges		395	
E061006C	Lateral	Copper	Kimberlite	2 Lateral Gauges		594	
E061027A	Lateral	Copper	Kimberlite	2 Lateral Gauges		835	
E070209A	Spall	Amph Gneiss	Amph Gneiss	VISAR		113	
E070209B	Spall	Amph Gneiss	Amph Gneiss	VISAR		140	
E070209B	Spall	Amph Gneiss	Amph Gneiss	VISAR		113	Missed data
E070417A	Spall	Biotite Schist	Biotite Schist	VISAR		143	
E070418A	Spall	Biotite Schist	Biotite Schist	VISAR		125	
E070418B	Spall	Biotite Schist	Biotite Schist	VISAR		102	
E070423A	Spall	PMMA	Biotite Schist	VISAR		105	
E070423B	Spall	PMMA	Biotite Schist	VISAR		105	
E070510A	Lateral	Copper	Sandstone	2 Lateral Gauges		206	
E070513B	Spall	Aluminium	Siltstone	Longitudinal Gauge	VISAR	115	
E070513C	Spall	Aluminium	Siltstone	Longitudinal Gauge	VISAR	96	
E070513D	Lateral	Copper	Sandstone	2 Lateral Gauges		400	
E070513E	Lateral	Copper	Sandstone	2 Lateral Gauges		608	
E070513F	Lateral	Copper	Sandstone	2 Lateral Gauges		801	
E070513G	Lateral	Copper	Sandstone	2 Lateral Gauges		922	

Shot Code	Experiment Type	Impactor Material	Target Material	Diagnositc 1	Diagnostic 2	Velocity $m\ s^{-1}$	Comments
E070516B	Lateral	Copper	Siltstone	Longitudinal Gauge	2 Lateral Gauges	183	
E070516C	Lateral	Copper	Siltstone	Longitudinal Gauge	2 Lateral Gauges	339	
E070517A	Lateral	Copper	Siltstone	Longitudinal Gauge	2 Lateral Gauges	499	
E070517B	Lateral	Copper	Siltstone	Longitudinal Gauge	2 Lateral Gauges	647	
E070517C	Lateral	Copper	Siltstone	Longitudinal Gauge	2 Lateral Gauges	847	
E070518A	Hugoniot/Release	Biotite Schist	Copper	VISAR		250	
E070518B	Hugoniot/Release	Biotite Schist	Copper	VISAR		501	
E070518C	Hugoniot/Release	Biotite Schist	Copper	VISAR		742	
E070519A	Hugoniot/Release	Biotite Schist	Copper	VISAR		986	
E070519B	Shock Speed	Siltstone	Aluminium and Siltstone	Longitudinal Gauge	Longitudinal Gauge	249	
E070519C	Shock Speed	Siltstone	Aluminium and Siltstone	Longitudinal Gauge	Longitudinal Gauge	602	
E070519D	Shock Speed	Siltstone	Aluminium and Siltstone	Longitudinal Gauge	Longitudinal Gauge	864	
E070519E	Shock Speed	Copper	Aluminium and Siltstone	Longitudinal Gauge	Longitudinal Gauge	879	
E070615A	Lateral	Copper	Kimberlite	2 Lateral Gauges			Pin Fail
E070616B	Spall	Aluminium	Siltstone	Longitudinal Gauge	VISAR	139	
E070616C	Spall	Aluminium	Siltstone	Longitudinal Gauge	VISAR	146	
E070618A	Lateral	Copper	Kimberlite	2 Lateral Gauges			Pin Fail
E070808A	Spall	Aluminium	Siltstone	Longitudinal Gauge	VISAR	132	
E070809A	Spall	Aluminium	Kimberlite	Longitudinal Gauge	VISAR	128	
E070809B	Spall	Aluminium	Kimberlite	Longitudinal Gauge	VISAR	131	
E080716A	Hugoniot/Release	Basalt	Copper	VISAR		211	
E080717A	Hugoniot/Release	Iron Ore	Copper	VISAR		204	
E080718A	Hugoniot/Release	Basalt	Copper	VISAR		392	
E080721A	Hugoniot/Release	Iron Ore	Copper	VISAR		393	
E080723A	Hugoniot/Release	Basalt	Copper	VISAR		594	
E080724A	Hugoniot/Release	Iron Ore	Copper	VISAR		595	
E080725A	Hugoniot/Release	Basalt	Copper	VISAR		791	
E080729A	Hugoniot/Release	Iron Ore	Copper	VISAR		799	
E080730A	Hugoniot/Release	Basalt	Copper	VISAR		1000	
E080731A	Hugoniot/Release	Iron Ore	Copper	VISAR		975	
E081030A	Lateral	Copper	Q/F Gneiss	2 Lateral Gauges		394	
E081104A	Spall	Aluminium	Basalt	Longitudinal Gauge	VISAR	162	
E081104B	Spall	Aluminium	Iron Ore	Longitudinal Gauge	VISAR	172	

Shot Code	Experiment Type	Impactor Material	Target Material	Diagnositc 1	Diagnostic 2	Velocity $m\ s^{-1}$	Comments
E081105A	Spall	Aluminium	Basalt	Longitudinal Gauge	VISAR	156	
E081216A	Lateral	PMMA	Basalt	Longitudinal Gauge	2 Lateral Gauges	341	
E081217A	Lateral	Copper	Iron Ore	Longitudinal Gauge	Lateral Gauge	146	Delay fail no data
E081217B	Lateral	PMMA	Q/F Gneiss	2 Lateral Gauges		337	
E081222B	Lateral	Aluminium	Q/F Gneiss	Lateral Gauge		314	
E090121A	Lateral	Copper	Iron Ore	Longitudinal Gauge	Lateral Gauge	140	
E070112B	Lateral	Copper	Iron Ore	Longitudinal Gauge	Lateral Gauge	262	
E090112C	Lateral	PMMA	Q/F Gneiss	Lateral Gauge		560	
E090118A	Lateral	Copper	Kimberlite	Longitudinal Gauge	Lateral Gauge	166	
E090118B	Lateral	Aluminium	Basalt	Longitudinal Gauge	Lateral Gauge	257	
E090119A	Hugoniot/Release	Biotite Schist	Copper	VISAR		90	
E090119B	Hugoniot/Release	Biotite Schist	Copper	VISAR		199	
E090119C	Hugoniot/Release	Biotite Schist	Copper	VISAR		476	
E090119D	Hugoniot/Release	Kimberlite	Copper	VISAR		499	
E090120A	Lateral	Copper	Amphibolite	Lateral Gauge		498	
E090120B	Lateral	Copper	Amphibolite	Lateral Gauge		369	
E090120C	Lateral	Aluminium	Amphibolite	Lateral Gauge	Passive Gauge	397	
E091221A	Lateral	Aluminium	Q/F Gneiss	Lateral Gauge	Passive Gauge	446	
E091221B	Lateral	Aluminium	Basalt	Longitudinal Gauge	Lateral Gauge	357	
E091221C	Lateral	Aluminium	Basalt	Longitudinal Gauge	Lateral Gauge	500	
E091221D	Lateral	Aluminium	Iron Ore	Longitudinal Gauge	Lateral Gauge	493	
E091221E	Lateral	Copper	Iron Ore	Longitudinal Gauge	Lateral Gauge	495	
E091221F	Lateral	Copper	Iron Ore	Longitudinal Gauge	Lateral Gauge	497	
E091221G	Lateral	Copper	Basalt	Longitudinal Gauge	Lateral Gauge	447	
E091221H	Lateral	Copper	Basalt	Longitudinal Gauge	2 Lateral Gauges	582	

Appendix B

B.1 Mineralogical Glossary

The information in this glossary is intended as an aid to reading the thesis, in particular to clarify the meanings of various geological terms. There are extensive and fully reference mineral databases at http://webmineral.com and www.mindat.org, however as this section is aimed at giving a general overview, the descriptions are abstracted from www.wikipedia.org

Albite: Albite is a plagioclase feldspar mineral. It is the sodium endmember of the plagioclase solid solution series. As such it represents a plagioclase with less than 10% anorthite content.

Aluminosilicate: Aluminosilicate minerals are minerals composed of aluminium, silicon, and oxygen. They are a major component of kaolin and other clay minerals.

Akermanite: Akermanite ($Ca_2Mg[Si_2O_7]$) is a melilite mineral of the sorosilicate group, containing calcium, magnesium, silicon, and oxygen.

Amphibole: Amphiboles are generally dark-colored rock-forming inosilicate minerals of either igneous or metamorphic origin; in the former case occurring as constituents (hornblende) of igneous rocks, such as granite, diorite, andesite and

others. Those of metamorphic origin include examples such as those developed in limestones by contact metamorphism (tremolite) and those formed by the alteration of other ferromagnesian minerals (hornblende).

Anorthite: Anorthite is the calcium-rich endmember of the plagioclase solid solution series.

Apatite: Apatite is a group of phosphate minerals, usually referring to hydroxylapatite, fluorapatite, and chlorapatite, named for high concentrations of OH^-, F^-, or Cl^- ions, respectively, in the crystal.

Biotite: Biotite is a common phyllosilicate mineral within the mica group. More generally, it refers to the dark mica series, primarily a solid-solution series between the iron-endmember annite, and the magnesium-endmember phlogopite.

Calcite: Calcite is a carbonate mineral and the most stable polymorph of calcium carbonate ($CaCO_3$).

Chlorite: The chlorites are a group of phyllosilicate minerals. Chlorite is commonly found in igneous rocks as an alteration product of mafic minerals such as pyroxene, amphibole, and biotite.

Clay: Clay minerals are hydrous aluminium phyllosilicates, sometimes with variable amounts of iron, magnesium, alkali metals, alkaline earths and other cations. Clays are ultra fine grained (normally considered to be less than 2 micrometres in size on standard particle size classifications).

Diopside: Diopside is a monoclinic pyroxene mineral with composition $MgCaSi_2O_6$.

Dolomite: Dolomite is the name of a sedimentary carbonate rock and a mineral, both composed of calcium magnesium carbonate $CaMg(CO_3)_2$ found in crystals.

Epidote: Epidote is an abundant calcium aluminium iron sorosilicate rock-forming mineral, but one of secondary origin. It occurs in marble and schistose rocks of metamorphic origin.

Feldspar: Feldspars are a group of rock-forming tectosilicate minerals which make up as much as 60% of the Earth's crust. Feldspars crystallize from magma in both intrusive and extrusive igneous rocks, as veins, and are also present in many types of metamorphic rock.

Garnet: Garnets are nesosilicates having the general formula $X_3Y_2(SiO_4)_3$. The X site is usually occupied by divalent cations (Ca^{2+}, Mg^{2+}, Fe^{2+}) and the Y site by trivalent cations (Al^{3+}, Fe^{3+}, Cr^{3+}) in an octahedral/tetrahedral framework with $[SiO_4]^{4-}$ occupying the tetrahedra.

Goethite: Goethite is an iron oxyhydroxide.

Hematite: Hematite is a mineral, colored black to steel or silver-gray, brown to reddish brown, or red, and is the mineral form of Iron(III) oxide (Fe_2O_3).

Illite: Illite is a non-expanding, clay-sized, micaceous mineral. Illite is a phyllosilicate or layered alumino-silicate.

Ilmenite: Ilmenite is a weakly magnetic titanium-iron oxide mineral which is iron-black or steel-gray.

Mica: The mica group of sheet silicate (phyllosilicate) minerals includes several closely related materials having highly perfect basal cleavage. All are monoclinic with a tendency towards pseudo-hexagonal crystals and are similar in chemical composition. The highly perfect cleavage, which is the most prominent characteristic of mica, is explained by the hexagonal sheet-like arrangement of its atoms.

Muscovite: Muscovite (also known as Common mica, Isinglass, or Potash mica) is a phyllosilicate mineral of aluminium and potassium.

Oligoclase: Oligoclase is a high sodium plagioclase feldspar crystallizing in the triclinic system.

Orthoclase: Orthoclase (endmember formula $KAlSi_3O_8$) is an important tectosilicate mineral (potassium feldspar) which forms igneous rock.

Perovskite: A perovskite is any material with the same type of crystal structure as calcium titanium oxide ($CaTiO_3$), known as the perovskite structure.

Phlogopite: Phlogopite is a yellow, greenish, or reddish-brown member of the mica family of phyllosilicates. It is also known as magnesium mica.

Pigeonite: Pigeonite is a mineral in the clinopyroxene group. It has a general formula of $(Ca,Mg,Fe)(Mg,Fe)Si_2O_6$.

Plagioclase: Plagioclase is a very important series of tectosilicate minerals within the feldspar family. Rather than referring to a particular mineral with a specific chemical composition, plagioclase is a solid solution series, more properly known as the plagioclase feldspar series. The series ranges from albite to anorthite endmembers (with respective compositions $NaAlSi_3O_8$ to $CaAl_2Si_2O_8$), where sodium and calcium atoms can substitute for each other in the mineral's crystal lattice structure.

Prehnite: Prehnite is a phyllosilicate of calcium and aluminium with the formula: $Ca_2Al(AlSi_3O_{10})(OH)_2$. Limited Fe^{3+} substitutes for aluminium in the structure. Prehnite crystallizes in the orthorhombic crystal system. It is brittle with an uneven fracture and a vitreous to pearly lustre.

Pyroxene: The pyroxenes are a group of important rock-forming silicate minerals found in many igneous and metamorphic rocks. Pyroxenes have the general

formula $XY(Si,Al)_2O_6$ (where X represents calcium, sodium, iron(II) and magnesium and more rarely zinc, manganese and lithium and Y represents ions of smaller size, such as chromium, aluminium, iron(III), magnesium, manganese, scandium, titanium, vanadium and even iron(III)).

Quartz: Quartz is the second most abundant mineral in the Earth's continental crust (after feldspar). It is made up of a lattice of silica (SiO_2) tetrahedra.

Rutile: Rutile is a mineral composed primarily of titanium dioxide, TiO_2.

Saponite: Saponite is a monoclinic mineral of the montmorillonite group. It is soft, massive, and plastic, and exists in veins and cavities in serpentinite and basalt. The name is derived from the Greek sapo, soap. Other names include bowlingite; mountain soap; piotine; soapstone.

Serpentine: The serpentine group describes a group of common rock-forming hydrous magnesium iron phyllosilicate ($(Mg, Fe)_3Si_2O_5(OH)_4$) minerals; they may contain minor amounts of other elements including chromium, manganese, cobalt and nickel. In mineralogy and gemology, serpentine may refer to any of 20 varieties belonging to the serpentine group.

Spinel: $MgAl_2O_4$ crystallised in the cubic (isometric) crystal system.

Zircon: Zircon is a mineral belonging to the group of nesosilicates. Its chemical name is zirconium silicate and its corresponding chemical formula is $ZrSiO_4$.